Loughborough University

This item was submitted to Loughborough University as a PhD thesis by the author and is made available in the Institutional Repository (https://dspace.lboro.ac.uk/) under the following Creative Commons Licence conditions.

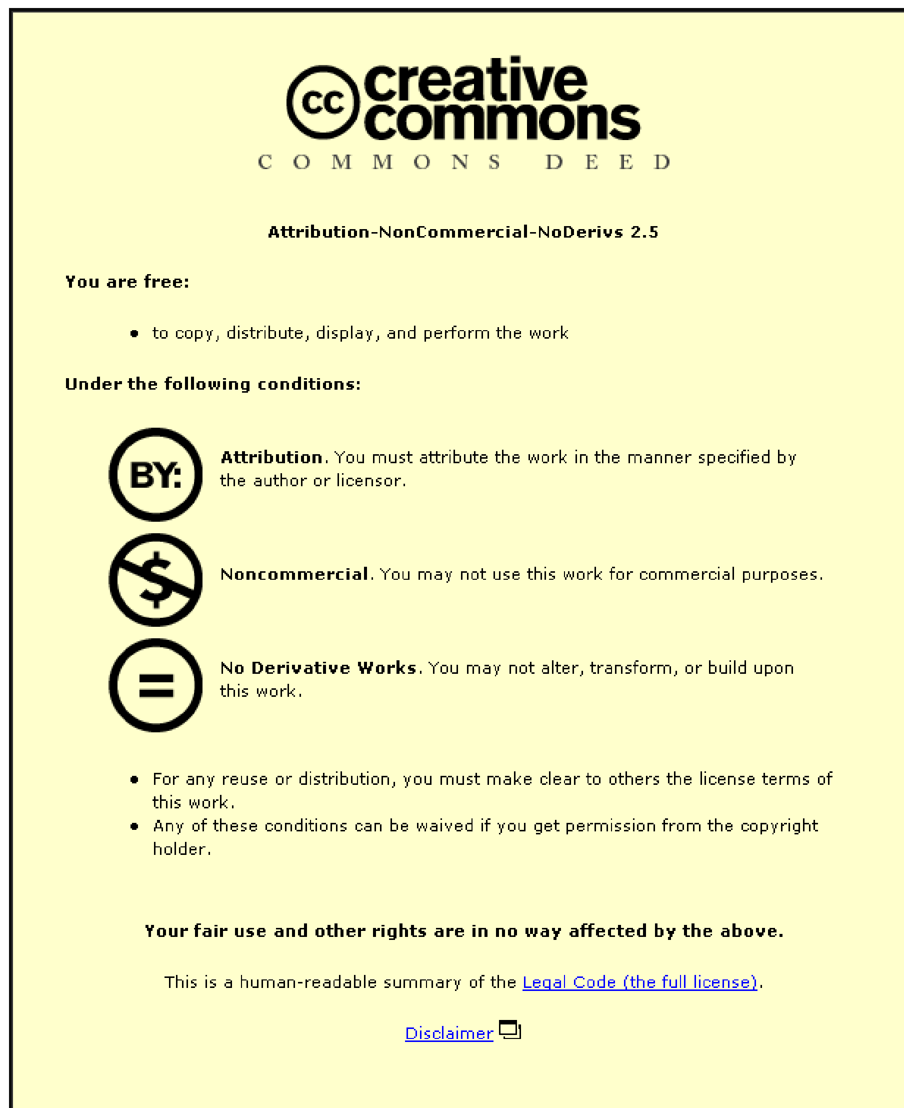

For the full text of this licence, please go to: http://creativecommons.org/licenses/by-nc-nd/2.5/

ELECTRODEPOSITION AND CHARACTERISATION OF LEAD-FREE SOLDER ALLOYS FOR ELECTRONICS INTERCONNECTION

By
Yi Qin

A DOCTORAL THESIS
SUBMITTED IN PARTIAL FULFILMENT OF THE REQUIREMENTS
FOR THE AWARD OF
DOCTOR OF PHILOSOPHY OF LOUGHBOROUGH UNIVERSITY

October 2010

© Yi Qin (2010)

ABSTRACT

Conventional tin-lead solder alloys have been widely used in electronics interconnection owing to their properties such as low melting temperature, good ductility and excellent wettability on copper and other substrates. However, due to the worldwide legislation addressing the concern over the toxicity of lead, the usage of lead-containing solders has been phased out, thus stimulating substantial efforts on lead-free alternatives, amongst which eutectic Sn-Ag and Sn-Cu, and particularly Sn-Ag-Cu alloys, are promising candidates as recommended by international parties. To meet the increasing demands of advanced electronic products, high levels of integration of electronic devices are being developed and employed, which is leading to a reduction in package size, but with more and more input/output connections. Flip chip technology is therefore seen as a promising technique for chip interconnection compared with wire bonding, enabling higher density, better heat dissipation and a smaller footprint. This thesis is intended to investigate lead-free (eutectic Sn-Ag, Sn-Cu and Sn-Ag-Cu) wafer level solder bumping through electrodeposition for flip chip interconnection, as well as electroplating lead-free solderable finishes on electronic components. The existing knowledge gap in the electrochemical processes as well as the fundamental understanding of the resultant tin-based lead-free alloys electrodeposits are also addressed.

For the electrodeposition of the Sn-Cu solder alloys, a methanesulphonate based electrolyte was established, from which near-eutectic Sn-Cu alloys were achieved over a relatively wide process window of current density. The effects of methanesulphonic acid, thiourea and OPPE (iso-octyl phenoxy polyethoxy ethanol) as additives were investigated respectively by cathodic potentiodynamic polarisation curves, which illustrated the resultant electrochemical changes to the electrolyte. Phase identification by X-ray diffraction showed the electrodeposits had a biphasic structure (β-Sn and Cu_6Sn_5). Microstructures of the Sn-Cu electrodeposits were comprehensively characterised, which revealed a compact and crystalline surface morphology under the effects of additives, with cross-sectional observations showing a uniform distribution of Cu_6Sn_5 particles predominantly along β-Sn grain boundaries.

The electrodeposition of Sn-Ag solder alloys was explored in another pyrophosphate based system, which was further extended to the application for Sn-Ag-Cu solder alloys. Cathodic potentiodynamic polarisation demonstrated the deposition of noble metals, Ag or Ag-Cu, commenced before the deposition potential of tin was reached. The co-deposition of Sn-Ag or Sn-Ag-Cu alloy was achieved with the noble metals electrodepositing at their limiting current densities. The synergetic effects of polyethylene glycol (PEG) 600 and formaldehyde, dependent on reaching the cathodic potential required, helped to achieve a bright surface, which consisted of fine tin grains (~200 nm) and uniformly distributed Ag_3Sn particles for Sn-Ag alloys and Ag_3Sn and Cu_6Sn_5 for Sn-Ag-Cu alloys, as characterised by microstructural observations. Near-eutectic Sn-Ag and Sn-Ag-Cu alloys were realised as confirmed by compositional analysis and thermal measurements.

Near-eutectic lead-free solder bumps of 25 μm in diameter and 50 μm in pitch, consisting of Sn-Ag, Sn-Cu or Sn-Ag-Cu solder alloys depending on the process and electrolyte employed, were demonstrated on wafers through the electrolytic systems developed. Lead-free solder bumps were further characterised by material analytical techniques to justify the feasibility of the processes developed for lead-free wafer level solder bumping.

Key words: Lead-free solder alloys, electrodeposition, wafer level solder bumping, flip chip interconnection.

ACKNOWLEDGEMENTS

I would like to take this opportunity to express my sincere gratitude and deep appreciation to my supervisors, Dr Geoffrey D. Wilcox and Dr Changqing Liu, for their support and invaluable tuition throughout my PhD study.

I am grateful to Dr Yi Zhang, Dr Yingtao Tian, Dr Hui Xu, Dr Gary W. Critchlow, Mr Andy J. Ebbage and Mr Dane E. Walker for their advice and discussions for the project. Deep gratitude is expressed to Mr Andrew P. Sandaver and Mr Andrew Lau for their continuous help with experiments, as well as Dr Geoff West, Mr John S. Bates and Mr Ray P. Owens in Department of Materials for their assistance and discussion on material characterisations using focused ion beam, transmission electron microscopy, scanning electron microscopy and other facilities.

Thanks are also extended to all of my colleagues in both the Interconnection Group and the Surface Engineering Group in Wolfson School and Department of Materials respectively for their help and knowledge.

In particular, I would like to acknowledge the help with sample preparation from Mr Kun Zhao and Dr Changhai Wang in Heriot-Watt University.

Besides, special thanks for the financial support of Loughborough University studentship for my PhD study.

Finally, I would like to express my deepest gratitude to my family for their great love, deep understanding, endless patience and encouragement during all the years of this education.

Table of Contents

Abstract .... **I**

Acknowledgements .... **III**

List of Figures .... **IX**

List of Tables .... **XIX**

Glossary of Symbols .... **XX**

Context of the Research .... **XXII**

1 Electronics Packaging **1**

1.1 Introduction 1

1.2 Packaging Hierarchy 2

1.3 Standard IC Packages 4

2 Chip Interconnection and Solder Bumping **6**

2.1 Chip Interconnection Techniques 6

2.1.1 Wire Bonding 8

2.1.2 Tape Automated Bonding 9

2.1.3 Flip Chip Bonding 10

2.2 Flip Chip Interconnection 11

2.2.1 Wafer Level Packaging 11

2.2.2 Flip Chip Interconnection Trend 13

2.2.3 Flip Chip Interconnection Configuration 14

2.3 Solder Bumping Process 16

2.3.1 Stencil Printing 16

2.3.2 Evaporation 18

2.3.3 Electrodeposition 19

2.4 Summary 21

3 Lead-Free Solder Alloys **22**

3.1 Introduction 22

3.2 Global Legislation 23

3.2.1 European Union 23

3.2.2 United States of America 24
3.2.3 Asia 24
3.3 Criteria for Lead-Free Solder Candidates 25
3.4 Lead-Free Solder Alloys 26
3.4.1 Sn 29
3.4.2 Sn-Ag 29
3.4.3 Sn-Cu 31
3.4.4 Sn-Ag-Cu 32
3.4.5 Sn-Bi and Sn-Zn 33
3.4.6 Other Lead-Free Alternatives 35
3.5 Summary 36
4 Electrodeposition of Lead-Free Solder Alloys 37
4.1 General Principles of Electrodeposition 37
4.2 Alloy Electrodeposition 39
4.3 Electrodeposition Parameters 42
4.3.1 Temperature 43
4.3.2 Agitation 43
4.3.3 Current Density 44
4.4 Electrodeposition Baths 45
4.4.1 Methanesulphonate Bath 45
4.4.2 Pyrophosphate Bath 50
4.4.3 Electrolyte Stability 54
4.5 Summary 56
5 Experimental Techniques 57
5.1 Electrodeposition and Polarisation Trials 57
5.1.1 Electrodes and Pretreatment 57
5.1.2 Agitation and Heating 58
5.1.3 Potentiodynamic Polarisation Studies 58
5.2 Bump Electrodeposition on Wafers 60
5.2.1 Test Wafer 61
5.2.2 UBM Deposition 61
5.2.3 Photoresist Patterning 62
5.2.4 Electrodeposition 65
5.2.5 Photoresist Etching 65

5.3 Material Characterisation 65
5.3.1 Surface Morphology 65
5.3.2 Composition and Phase Identification 66
5.3.3 Microstructure 67
5.4 Summary 69
6 Electrodeposition of Sn-Cu Alloys 70
6.1 Cathodic Polarisation Studies 70
6.1.1 Development of Electrolyte 70
6.1.2 Effects of Scan Rate 72
6.1.3 Effects of Copper Sulphate 73
6.1.4 Effects of Methanesulphonic Acid 74
6.1.5 Effects of Thiourea 75
6.1.6 Effects of OPPE 77
6.2 Surface Morphology of Electrodeposits 78
6.2.1 Effects of Methanesulphonic Acid 79
6.2.2 Effects of Thiourea 81
6.2.3 Effects of Thiourea and Methanesulphonic Acid 83
6.2.4 Effects of Thiourea and OPPE 85
6.2.5 Effects of Thiourea, Methanesulphonic Acid and OPPE 87
6.3 Compositional Analysis of Electrodeposits 89
6.4 Thermal Analysis of Electrodeposits 90
6.5 Microstructure of Electrodeposits 91
6.5.1 Phase Identification 91
6.5.2 Electrodeposit Cross-Sectional Analysis 93
6.5.3 TEM Analysis 94
6.6 Wafer Bumping of Sn-Cu Alloy 95
6.7 Summary 96
7 Electrodeposition of Sn-Ag Alloys 97
7.1 Cathodic Polarisation Studies 97
7.1.1 Development of Electrolyte 97
7.1.2 Electrodeposition Processes for Tin and Silver 98
7.1.3 Effects of Additives 100
7.2 Characterisation of Sn-Ag Electrodeposits 104
7.2.1 Compositional Analysis 104

7.2.2 Phase Identification ... 105
7.2.3 Thermal Analysis ... 105
7.2.4 Surface Morphology and Microstructure ... 106
7.3 Wafer Bumping of Sn-Ag Alloy ... 113
7.4 Summary ... 114
8 Electrodeposition of Sn-Ag-Cu Alloys ... 116
8.1 Cathodic Polarisation Studies ... 116
8.1.1 Development of Electrolyte ... 116
8.1.2 Effects of Agitation ... 117
8.1.3 Effects of Temperature ... 119
8.1.4 Effects of Additives ... 120
8.2 Electrodeposition of Sn-Ag-Cu Alloy ... 122
8.2.1 Surface Morphology of Electrodeposits ... 122
8.2.2 Compositional Analysis ... 124
8.3 Effects of Agitation on Sn-Ag-Cu Alloy Electrodeposition ... 126
8.3.1 Surface Morphology of Electrodeposits ... 126
8.3.2 Compositional Analysis ... 129
8.4 Effects of Temperature on Sn-Ag-Cu Alloy Electrodeposition ... 130
8.4.1 Surface Morphology of Electrodeposits ... 130
8.4.2 Compositional Analysis ... 133
8.5 Effects of Additives on Sn-Ag-Cu Alloy Electrodeposition ... 134
8.5.1 Surface Morphology of Electrodeposits ... 134
8.5.2 Compositional Analysis ... 137
8.6 Thermal Analysis of Electrodeposits ... 138
8.7 Microstructure of Electrodeposits ... 140
8.7.1 Phase Identification ... 140
8.7.2 Electrodeposits From A Bath Free of Additives ... 140
8.7.3 Electrodeposits in Bath With Additives ... 143
8.8 Wafer Bumping of Sn-Ag-Cu Alloy ... 147
8.9 Summary ... 148
9 Conclusions and Future Work ... 150
9.1 Conclusions ... 150
9.1.1 Electrodeposition of Sn-Cu System ... 150
9.1.2 Electrodeposition of Sn-Ag and Sn-Ag-Cu System ... 151

9.1.3 Lead-Free Wafer Level Solder Bumping 154
9.2 Recommendations for Future Work 155
References 157
Publications 168

List of Figures

Figure I Thesis structure XXIV
Figure 1-1 Moore's Law predicts the IC integration to double every 18 months [4]. .. 2
Figure 1-2 Schematic of microelectronic packaging hierarchy with first-, second- and third-level packages [7]. 3
Figure 1-3 Overview of common single-chip package types used for integrated circuit packaging [9]. 4
Figure 2-1 Illustration of chip to package or substrate interconnection techniques [12]. 7
Figure 2-2 Chip to package or substrate interconnection technique: illustration of wire bonding. 8
Figure 2-3 Chip to package or substrate interconnection technique: illustration of tape automated bonding [20]. 10
Figure 2-4 Chip to package or substrate interconnection technique: flip chip interconnection. Schematic of a typical process sequence for flip chip interconnection using solder bumps. 11
Figure 2-5 Size comparisons of wafer level flip chip packaging with alternative packaging styles (l_c = length of chip side). For small chips, the package-to-chip area ratios may be even larger for chip-on-board, TAB and QFPs [25]. 12
Figure 2-6 Predicted chronological trend of first level interconnection in transition in electronics packaging by ITRS 2007 [27]. 13
Figure 2-7 Schematic of various flip chip technologies [28]. 14
Figure 2-8 Schematic of flip chip on board using solder bumps: (a) cross-sectional view; (b) enlarged view of chip/solder and solder/PCB interface. 15
Figure 2-9 Schematic of the stencil printing process for wafer bumping. 17
Figure 2-10 Schematic key processes of wafer bumping through evaporation. 19
Figure 2-11 Schematic of the process sequence for wafer bumping through electrodeposition. 20
Figure 3-1 An illustration depicting the sequence of events that results in the ingestion of lead leached from electronic wastes in landfills. 23

Figure 3-2 Melting temperature of lead-free solders and technology [53]. 27
Figure 3-3 Sn-Ag equilibrium thermal phase diagram [57]. 30
Figure 3-4 Sn-Cu equilibrium thermal phase diagram [57]. 32
Figure 3-5 Sn-Ag-Cu equilibrium thermal phase diagram [64]. 33
Figure 3-6 Sn-Bi equilibrium thermal phase diagram [57]. 34
Figure 3-7 Sn-Zn equilibrium thermal phase diagram [57]... 35
Figure 4-1 A schematic illustration of an electrodeposition system. 38
Figure 4-2 Schematic representation of current-potential relationship during alloy deposition: E_1, the deposition potential of the more noble metal; E_2, the deposition potential of the less noble metal; i_1, the limiting current density of the more noble metal; i_2, the limiting current density of the less noble metal [73]............................. 41
Figure 4-3 General relationship between content of more noble metal in the electrodeposit and electroplating parameters: (a) current density, (b) more noble metal concentration, (c) additive concentration, (d) cathode agitation and (e) temperature [74]. 42
Figure 4-4 Idealised representation of the electrochemical double layer at the metal-solution interface [73]... 44
Figure 4-5 Schematic chemical structure of methanesulphonic acid (left) and tin methanesulphonate (right). 45
Figure 4-6 Sn-Cu electrodeposit characterisation from methanesulphonic acid electrolyte in terms of surface microstructure. The deposit structural phases: (1) 100wt.% Sn: tetragonal; (2) 100wt.% Cu: cubic; (3) Sn-65wt.%Cu: orthorhombic Cu-Sn and (4) Sn-4wt.%Cu contains two phases: tetragonal Sn and hexagonal Cu_6Sn_5 [85]. 46
Figure 4-7 Cathodic potentiodynamic polarisation curves showing the effects of additives. (a) the suppression of the cathodic current; (b) inhibition effects for stannous reduction [87]. 47
Figure 4-8 The morphologies of tin electrodeposits produced at two different current densities under the effect of additives. (a) no additives; (b) morphology of deposits under the effect of PEG; (c) grain refining effects through the addition of PPG; (d) smooth surface from the addition of all the three additives [87]................................ 48
Figure 4-9 Micrographs of Sn-3.5wt.% Ag alloys electrodeposited at different current densities: (A) 0.1 A/dm^2, (B) 0.2 A/dm^2, (C) 0.5 A/dm^2, (D) 1.0 A/dm^2, (E) 1.2 A/dm^2 and (F) 1.5 A/dm^2 [92]. 52

Figure 4-10 SEM images of fabricated near-eutectic Sn-Ag solder bumps under potentiostatic (a) galvanostatic and (b) conditions from a pyrophosphate-iodide bath [93]. 53
Figure 4-11 EPMA cross-sectional analysis of Sn-Ag mushroom bumps obtained under galvanostatic and potentiostatic conditions from a pyrophosphate-iodide bath [93]. 54
Figure 5-1 Arrangement of the electrodeposition system: (a), general view; (b), close up of the electroplating cell. 58
Figure 5-2 General cathodic polarisation curve [71]. 59
Figure 5-3 Schematic illustration of the process for the solder bumping process on wafers. 61
Figure 5-4 Thickness measurement of the UBM layers by Talysurf CLI 2000 3D laser scanner. 62
Figure 5-5 Schematic illustration of the photomask used for photoresist patterning. (a) general view of the wafer mask; (b) close up of one single block. Pattern includes diameters=15–25 µm, pitch size=50–100 µm. 64
Figure 5-6 Measurements of patterned photoresist by Talysurf CLI 2000 3D laser scanner. (a) top scanning revealing a pattern of diameter=25 µm and pitch=50 µm (distance from cursor "1" to cursor "2"=100.22 µm) and average via depth=15.4 µm; (b) 3D image of the photoresist pattern after development. 65
Figure 5-7 Micro-machining process by SEM/FIB for cross-sectional microstructure view and TEM sample preparation. (a) Pt layer deposited on top of the region of interest; (b-c) two rectangular trenches produced on both sides of the Pt layer for cross-sectional view and to prepare the TEM sample; (d) "U" cut of the sample to be lifted up; (e) Foil attached to the Omniprobe and lifted up; (f) Sample attached to the grid holder by Pt deposition; (g) Sample further attenuated to electron transparency. 69
Figure 6-1 Schematic chemical structure of OPPE (iso-octyl phenoxy polyethoxy ethanol), with the hydrophilic portion containing nine to ten oxyethylene groups (n = 9–10). 70
Figure 6-2 Cathodic potentiodynamic polarisation curves from bath A, Table 6-1 containing $Sn(CH_3SO_3)_2$ 70 g/L, showing the effects of potential scan rate: 1 mV/s (curve 1) and 10 mV/s (curve 2). 73

Figure 6-3 SEM image of Sn dendrites formed on Cu coupon after cathodic polarisation from bath A, Table 7-1 containing $Sn(CH_3SO_3)_2$ 70 g/L. Potential scan rate 1 mV/s. 73
Figure 6-4 Cathodic potentiodynamic polarisation curves from bath B, Table 6-1 containing $Sn(CH_3SO_3)_2$ 70 g/L and various concentrations of $CuSO_4$, showing the effects of $CuSO_4$ additions: $CuSO_4$=0 mol/L (curve 1), $CuSO_4$=0.002 mol/L (curve 2) and $CuSO_4$=0.02 mol/L (curve 3). Potential scan rate: 1 mV/s.................................. 74
Figure 6-5 Cathodic potentiodynamic polarisation curves from bath C, Table 6-1 containing $Sn(CH_3SO_3)_2$ 70 g/L, $CuSO_4$ 0.002 mol/L and CH_3SO_3H 100g/L, showing the effects of MSA: without MSA (curve 1) and with MSA (curve 2). Potential scan rate: 1 mV/s. 75
Figure 6-6 Cathodic potentiodynamic polarisation curves from bath D, Table 6-1 containing $Sn(CH_3SO_3)_2$ 70 g/L, $CuSO_4$ 0.002 mol/L and thiourea 0.2 mol/L, showing the effects of thiourea: without thiourea (curve 1) and with 0.2 mol/L thiourea (curve 2). Potential scan rate: 1 mV/s... 76
Figure 6-7 Cathodic potentiodynamic polarisation curves from bath E, Table 6-1 containing $Sn(CH_3SO_3)_2$ 70 g/L, $CuSO_4$ 0.002 mol/L and varying concentrations of OPPE, showing the effects of OPPE: no OPPE (curve 1), OPPE=10 ml/L (curve 2) and OPPE=50 ml/L (curve 3). Potential scan rate: 1 mV/s. 77
Figure 6-8 SEM micrograph of Sn-Cu electrodeposit under galvanostatic condition (current density = 15 mA/cm^2) from bath B, Table 6-1 containing $Sn(CH_3SO_3)_2$ 70 g/L and $CuSO_4$ 0.002 mol/L, electrical charge passed = 1500 C/dm^2. 78
Figure 6-9 SEM micrographs of Sn-Cu films electrodeposited under galvanostatic conditions from bath C, Table 6-1 containing $Sn(CH_3SO_3)_2$ 70 g/L, $CuSO_4$ 0.002 mol/L and CH_3SO_3H 100g/L, electrical charge passed = 1500 C/dm^2. 80
Figure 6-10 Chronopotentiometry of Sn-Cu alloys electrodeposition from bath C, Table 6-1 recorded under galvanostatic conditions, electrical charge passed = 1500 C/dm^2. Curves 1, 2, 3, 4,5 6 represent 5, 10, 15, 20, 25 and 30 mA/cm^2 respectively.80
Figure 6-11 SEM micrographs of Sn-Cu films electrodeposited under galvanostatic conditions from bath D, Table 6-1 containing $Sn(CH_3SO_3)_2$ 70 g/L, $CuSO_4$ 0.002 mol/L and thiourea 0.2 mol/L, electrical charge passed = 1500 C/dm^2. 82
Figure 6-12 Chronopotentiometry of Sn-Cu alloys electrodeposition from bath D, Table 6-1 recorded under galvanostatic conditions, electrical charge passed = 1500

C/dm^2. Curves 1, 2, 3, 4, 5 and 6 represent 5, 10, 15, 20, 25 and 30 mA/cm^2 respectively. 82
Figure 6-13 SEM micrographs of Sn-Cu films electrodeposited under galvanostatic conditions from bath F, Table 6-1 containing $Sn(CH_3SO_3)_2$ 70 g/L, $CuSO_4$ 0.002 mol/L, CH_3SO_3H 100g/L and thiourea 0.2 mol/L, electrical charge passed = 1500 C/dm^2. 84
Figure 6-14 Chronopotentiometry of Sn-Cu alloys electrodeposition from bath F, Table 6-1 recorded under galvanostatic conditions, electrical charge passed = 1500 C/dm^2. Curves 1, 2, 3, 4, 5 and 6 represent 5, 10, 15, 20, 25 and 30 mA/cm^2 respectively. 85
Figure 6-15 SEM micrographs of Sn-Cu films electrodeposited under galvanostatic conditions from bath G, Table 6-1 containing $Sn(CH_3SO_3)_2$ 70 g/L, $CuSO_4$ 0.002 mol/L, thiourea 0.2 mol/L and OPPE 10 ml/L, electrical charge passed = 1500 C/dm^2. 86
Figure 6-16 Chronopotentiometry of Sn-Cu alloys electrodeposition from bath G, Table 6-1 recorded under galvanostatic conditions, electrical charge passed = 1500 C/dm^2. Curves 1, 2, 3, 4, 5 and 6 represent 5, 10, 15, 20, 30 and 40 mA/cm^2 respectively. 87
Figure 6-17 SEM micrographs of Sn-Cu films electrodeposited under galvanostatic conditions from bath H, Table 6-1 containing $Sn(CH_3SO_3)_2$ 70 g/L, $CuSO_4$ 0.002 mol/L, CH_3SO_3H 100g/L, thiourea 0.2 mol/L and OPPE 10 ml/L, electrical charge passed = 1500 C/dm^2. 88
Figure 6-18 Chronopotentiometry of Sn-Cu alloys electrodeposition from bath H, Table 6-1 recorded under galvanostatic conditions, electrical charge passed = 1500 C/dm^2. Curves 1, 2, 3, 4, 5 and 6 represent 5, 10, 15, 20, 25 and 30 mA/cm^2 respectively. 89
Figure 6-19 Cu content (wt.%) of the electrodeposited Sn-Cu films vs. galvanostatic current density utilising bath H from Table 6-1 but with varying concentration of $CuSO_4$. Measurements carried out by WDX. $CuSO_4$=0.002 mol/L (curve 1), 0.005 mol/L (curve 2), 0.007 mol/L (curve 3) and 0.02 mol/L (curve 4) respectively. Broken line represents the objective Cu content, 0.7wt.%. 90
Figure 6-20 DSC measurements for Sn-Cu electrodeposits from bath H, Table 6-1. Scan rate at 10 K/min. Pure Sn presented as a reference. 91

Figure 6-21 XRD spectra of Sn-Cu films galvanostatically electrodeposited in bath D (image 1, with thiourea), bath G (image 2, with thiourea and OPPE) and bath H (image 3, with thiourea, OPPE and MSA) from Table 6-1 at a current density of 15 mA/cm^2, electrical charge passed = 1500 C/dm^2. 92
Figure 6-22 SEM/FIB processed cross-sectional images of the electrodeposited Sn-Cu film under galvanostatic conditions from bath G, Table 6-1 (15 mA/cm^2, electrical charge passed = 1500 C/dm^2). (a) secondary electron (SE) image; (b) ion-induced secondary electron (ISE) micrograph. 93
Figure 6-23 SEM/FIB processed cross-sectional ISE images of the electrodeposited Sn-Cu film under galvanostatic conditions from bath H, Table 6-1 (15 mA/cm^2, electrical charge passed = 1500 C/dm^2). (a) general view; (b) central area magnified. 94
Figure 6-24 TEM micrographs (images (a) and (b)) and EDX spectra (patterns (c) and (d)) of the Sn-Cu film electrodeposited under galvanostatic conditions (15 mA/cm^2, electrical charge passed = 1500 C/dm^2) from bath H, Table 6-1. EDX analyses were carried out at points 1 and 2, with resultant spectra shown in images (b) and (d) respectively. 95
Figure 6-25 Wafer bumping: (a) SEM micrograph of the as-electrodeposited Sn-Cu solder bumps formed under potentiostatic conditions from bath H, Table 6-1, at a potential of -0.55 V; (b) SEM/FIB processed cross-sectional ISE image of the bump at the centre of image (a). 96
Figure 7-1 Schematic chemical structure of polyethylene glycol 600 (PEG 600), n = 12. 98
Figure 7-2 Cathodic potentiodynamic polarisation curves in baths A (curve 1), B (curve 2) and C (curve 3) from Table 7-1, showing the processes of Sn and Ag deposition individually. Potential scan rate: 1 mV/s. 100
Figure 7-3 Cathodic potentiodynamic polarisation curves in baths D (curve 1), E (curve 2) and F (curve 3) from Table 7-1, showing the effects of PEG and formaldehyde. Potential scan rate: 1 mV/s. 101
Figure 7-4 Cathodic potentiodynamic polarisation curves from baths E, Table 7-1 with different concentrations of PEG and formaldehyde. Potential scan rate: 1 mV/s. 102
Figure 7-5 Cathodic potentiodynamic polarisation curves investigating the effects of formaldehyde in baths of $K_4P_2O_7$ 1 mol/L and different formaldehyde concentrations:

0 mol/L (curve 1), 0.05 mol/L (curve 2) and 0.5 mol/L (curve 3). Potential scan rate: 1 mV/s. 103
Figure 7-6 Ag content (wt.%) in the electrodeposited Sn-Ag films vs. galvanostatic current density utilising baths D, E and F from Table 7-1. Measurements carried out by WDX. Broken line represents the objective Ag content, 3.5wt.%. 104
Figure 7-7 XRD spectrum of the as-electrodeposited Sn-Ag film galvanostatically produced from bath F, Table 7-1 at a current density of 15 mA/cm^2, electrical charge passed = 1500 C/dm^2. 105
Figure 7-8 DSC measurements of Sn-Ag electrodeposits from bath D, Table 7-1. Scan rate at 10 K/min. Pure Sn presented as a reference. 106
Figure 7-9 SEM micrographs of Sn-Ag films electrodeposited under galvanostatic conditions from bath D, Table 7-1, electrical charge passed = 1500 C/dm^2. 107
Figure 7-10 SEM/FIB processed cross-sectional ISE image of the electrodeposited Sn-Ag film (Figure 7-9, image (b)) under galvanostatic conditions from bath D, Table 7-1 (10 mA/cm^2, electrical charge passed = 1500 C/dm^2). 108
Figure 7-11 SEM/FIB processed cross-sectional image of the electrodeposited Sn-Ag film (Figure 7-9, image (c)) under galvanostatic conditions from bath D, Table 7-1 (15 mA/cm^2, electrical charge passed = 1500 C/dm^2). 109
Figure 7-12 SEM/FIB processed cross-sectional image of the electrodeposited Sn-Ag film (Figure 7-9, image (d)) under galvanostatic conditions from bath D, Table 7-1 (20 mA/cm^2, electrical charge passed = 1500 C/dm^2). 109
Figure 7-13 SEM micrographs of Sn-Ag films electrodeposited under galvanostatic conditions from bath E, Table 7-1, electrical charge passed = 1500 C/dm^2. 111
Figure 7-14 SEM/FIB processed cross-sectional ISE images and EDX spectrum of the Sn-Ag electrodeposits (Figure 7-13, image (a)) under galvanostatic conditions from bath E, Table 7-1 (2 mA/cm^2, electrical charge passed = 1500 C/dm^2). (a) general view of the cross-sectioned feature and EDX spot test spectrum; (b) magnified micrograph of the deposition layer on copper substrate and underneath the “flower”. 112
Figure 7-15 SEM micrographs of Sn-Ag films electrodeposited under galvanostatic conditions from bath F, Table 7-1, electrical charge passed = 1500 C/dm^2. 113
Figure 7-16 Wafer bumping: (a) SEM micrograph of the as-electrodeposited Sn-Ag solder bumps formed under potentiostatic conditions from bath F, Table 7-1, at a potential of -1.37 V; (b) SEM/FIB processed cross-sectional image of a bump. 114

Figure 8-1 Cathodic potentiodynamic polarisation curves for the deposition of Sn-Ag-Cu alloys under the effects of agitation: (a) overall range of scans; (b) magnified initial part of scans from "A" to "B". Curve 1 is from bath A in Table 8-1; Curve 2 from bath B; Curve 3 from bath B plus agitation supplied by magnetic stirring at 300 rpm. Potential scan rate: 1 mV/s. 118
Figure 8-2 Cathodic potentiodynamic polarisation curves for the deposition of Sn-Ag-Cu alloys under varying bath temperature using bath B from Table 8-1: (a) overall range of scans; (b) magnified initial part of scans from "A" to "B". Bath temperatures: curves 1, 2 and 3 represent 20, 40 and 60°C respectively. Potential scan rate: 1 mV/s. 120
Figure 8-3 Cathodic potentiodynamic polarisation curves for the deposition of Sn-Ag-Cu alloys using bath C from Table 8-1. Potential scan rate: 1 mV/s. Curve 1: free of additives; Curve 2: with additives (PEG 600 and HCHO). 121
Figure 8-4 SEM/FIB processed cross-sectional ISE images of the sample produced after the cathodic polarisation test (Figure 8-3, curve 2) from bath C, Table 8-1. 122
Figure 8-5 SEM micrographs of Sn-Ag-Cu films electrodeposited under galvanostatic conditions from bath B, Table 8-1, electrical charge passed = 1500 C/dm^2. 124
Figure 8-6 Chronopotentiometry of Sn-Ag-Cu alloys electrodeposition from bath B, Table 8-1 recorded under galvanostatic conditions, electrical charge passed = 1500 C/dm^2. Curves (a), (b), (c), (d) and (e) represent 5, 10, 15, 20 and 25 mA/cm^2 respectively. 124
Figure 8-7 Ag and Cu contents (wt.%) in the electrodeposited Sn-Ag-Cu films vs. galvanostatic current density utilising bath B from Table 8-1. Measurements carried out by WDX. 125
Figure 8-8 SEM micrographs of Sn-Ag-Cu films electrodeposited under galvanostatic conditions from bath B, Table 8-1, electrical charge passed = 1500 C/dm^2, with agitation by magnetic stirring at 300 rpm. 128
Figure 8-9 Chronopotentiometry of Sn-Ag-Cu alloys electrodeposition recorded under galvanostatic conditions from bath B, Table 8-1 with agitation by magnetic stirring at 300 rpm, electrical charge passed = 1500 C/dm^2. Curves (a), (b), (c), (d), (e), (f), (g), (h) and (i) represent 5, 10, 15, 20, 25 30, 50, 70 and 80 mA/cm^2 respectively. 129
Figure 8-10 Ag and Cu contents (wt.%) in the electrodeposited Sn-Ag-Cu films vs. galvanostatic current density utilising baths B from Table 8-1 with agitation by magnetic stirring at 300 rpm. Measurements carried out by WDX. 130

Figure 8-11 SEM micrographs of Sn-Ag-Cu films electrodeposited under galvanostatic conditions from bath B, Table 8-1, electrical charge passed = 1500 C/dm^2. Bath temperatures of 20, 40 and 60°C, at current densities of 5, 15 and 25 mA/cm^2, respectively. 132

Figure 8-12 Chronopotentiometry of Sn-Ag-Cu alloys electrodeposition from bath B, Table 8-1 recorded under galvanostatic conditions, electrical charge passed = 1500 C/dm^2. Bath temperature=40°C (diagram (a)) and 60°C (diagram (b)). Curves (a), (b), (c), (d) and (e) represent 5, 10, 15, 20 and 25 mA/cm^2 respectively. 133

Figure 8-13 Ag (diagram (a)) and Cu (diagram (b)) contents (wt.%) in the electrodeposited Sn-Ag-Cu films vs. galvanostatic current density at varying bath temperature utilising bath B from Table 8-1. Measurements carried out by WDX. Curve 1, 2 and 3 represent 20, 40 and 60°C respectively. 134

Figure 8-14 SEM micrographs of Sn-Ag-Cu films electrodeposited under galvanostatic conditions from bath D, Table 8-1, electrical charge passed = 1500 C/dm^2. 136

Figure 8-15 AFM image (3 μm × 3 μm) of the as-electrodeposited Sn-Ag-Cu film electrodeposited under galvanostatic conditions (15 mA/cm^2, electrical charge passed = 1500 C/dm^2, Figure 8-14, image (c)) from bath D, Table 8-1. 137

Figure 8-16 Chronopotentiometry of Sn-Ag-Cu alloys electrodeposition from bath D, Table 8-1 recorded under galvanostatic conditions, electrical charge passed = 1500 C/dm^2. Curves (a), (b), (c), (d) and (e) represent 5, 10, 15, 20 and 25 mA/cm^2 respectively. 137

Figure 8-17 Ag and Cu contents (wt.%) in the electrodeposited Sn-Ag-Cu films vs. galvanostatic current density utilising bath D from Table 8-1. Measurements carried out by WDX. 138

Figure 8-18 DSC measurements of Sn-Ag-Cu electrodeposits from bath F, Table 8-1. Scan rate at 10 K/min. Pure Sn presented as a reference. 139

Figure 8-19 XRD spectrum of the Sn-Ag-Cu film galvanostatically electrodeposited from bath D (image (c)) from Table 8-1 at a current density of 15 mA/cm^2, electrical charge passed = 1500 C/dm^2. 140

Figure 8-20 SEM/FIB processed cross-sectional ISE images of the as-electrodeposited Sn-Ag-Cu film produced under galvanostatic conditions from bath B, Table 8-1. Image (a) 10 mA/cm^2; Image (b) 70 mA/cm^2. Electrical charge passed = 1500 C/dm^2, with agitation by magnetic stirring at 300 rpm. 141

Figure 8-21 TEM micrographs and EDX spectra of Ag_3Sn (images (a) and (b)) and Cu_6Sn_5 (images (c) and (d)) in the Sn-Ag-Cu film electrodeposited under galvanostatic conditions (10 mA/cm^2, electrical charge pass = 1500 C/dm^2) from bath B, Table 8-1. Image (1) shows the general review. EDX analyses carried out at points "1", "2", "3" and "4", with resultant spectra for points "1" and "3" shown in images (b) and (d). 142
Figure 8-22 SEM/FIB processed cross-sectional ISE images of the as-electrodeposited Sn-Ag-Cu film produced under galvanostatic conditions from bath D, Table 8-1 (15 mA/cm^2, electrical charge pass = 1500 C/dm^2). 143
Figure 8-23 TEM micrographs of the Sn-Ag-Cu film electrodeposited under galvanostatic conditions (10 mA/cm^2, electrical charge pass = 1500 C/dm^2) from bath D, Table 8-1. Image (a) general view of Sn gains and Ag_3Sn, Cu_6Sn_5 particle; Image (b) magnified view of Ag_3Sn particle in-between Sn grains; Image (c) magnified view of Cu_6Sn_5 particles in-between Sn grains. EDX quantitative measurements of points "1" to "7" summarised in Table 8-2. 145
Figure 8-24 TEM micrographs of dislocations in the Sn-Ag-Cu film electrodeposited under galvanostatic conditions (10 mA/cm^2, electrical charge pass = 1500 C/dm^2) from bath D, Table 8-1 with the presence of additives. 146
Figure 8-25 SEM micrographs of the as-electrodeposited Sn-Ag-Cu solder bumps formed under potentiostatic conditions at a potential of -1.1 V from bath B, Table 8-1, pitch size = 50 μm (25 μm bump diameter): (a) plan view; (b) magnified side view. 147
Figure 8-26 SEM micrographs of the as-electrodeposited Sn-Ag-Cu solder bumps formed under potentiostatic conditions at a potential of -1.45 V from bath D, Table 8-1 with the presence of additives, pitch size = 50 μm (25 μm bump diameter): (a) plan view; (b) magnified side view. 148
Figure 9-1 Illustration of a copper pillar on a wafer with a lead-free solder cap for flip chip interconnection 156

List of Tables

Table 2-1 Comparison of chip interconnection techniques (2000) [13]........................ 7
Table 3-1 Criteria used by NCMS for lead-free solder alloys [52]............................ 25
Table 3-2 Major lead-free solder system candidates to replace eutectic Sn-Pb solder [55] 28
Table 4-1 Electrochemical potentials of common metals found in solder alloys at unit molal activity versus SHE, summarised from [72] 39
Table 4-2 Electrolyte composition for the electrodeposition of Sn-Ag-Cu alloys from a methanesulphonate based bath [88]... 49
Table 4-3 Electrolyte constituents for the electrodeposition of Sn-Ag alloys from pyrophosphate-iodide based baths [92] 51
Table 6-1 Methanesulphonate-based bath constituents for near-eutectic Sn-Cu alloy electrodeposition.. 71
Table 7-1 Pyrophosphate-based bath constituents for near-eutectic Sn-Ag alloy electrodeposition.. 98
Table 8-1 Bath constituents for near-eutectic Sn-Ag-Cu alloy electrodeposition..... 116
Table 8-2 TEM-EDX quantitative compositional measurements of points shown in Figure 8-23 144

Glossary of Symbols

AFM	Atomic Force Microscope
ASIC	Application-Specific Integrated Circuit
at.%	Atomic Percentage
BGA	Ball Grid Array
C4	Controlled Collapse Chip Connection
CCD	Charge-Coupled Device
CSP	Chip Scale Package
CTE	Coefficient of Thermal Expansion
CVD	Chemical Vapour Deposition
DRAM	Dynamic Random Access Memory
DSC	Differential Scanning Calorimetry
EDX	Energy Dispersive X-Ray Spectroscopy
EPMA	Electron Probe Micro-Analyser
FCOB	Flip Chip on Board
FIB	Focused Ion Beam
IC	Integrated Circuit
IMC	Intermetallic Compound
I/O	Input/Output
ISE	Ion-induced Secondary Electron
MCM	Multi-Chip Modules
MSA	Methanesulphonic Acid
OPPE	Iso-Octyl Phenoxy Polyethoxy Ethanol

PCB	Printed Circuit Board
PEG	Polyethylene Glycol
POELE	Polyoxyethylene Lauryl Ether
PPG	Polypropylene Glycol
PTH	Pin Through Hole
QFP	Quad Flat Package
RAM	Random Access Memory
RCE	Rotating Cylinder Electrode
RDE	Rotating Disk Electrode
SCE	Saturated Calomel Electrode
SEM	Scanning Electron Microscope
SHE	Standard Hydrogen Electrode
SIP	Systems In Package
SMT	Surface Mount Technology
SOC	Systems On Chip
TAB	Tape Automatic Bonding
TEM	Transmission Electron Microscopy
XRD	X-Ray Diffraction
UBM	Under Bump Metallisation
WDX	Wavelength Dispersive X-Ray Spectroscopy
WLP	Wafer Level Packaging
wt.%	Weight Percentage

Context of the Research

One of the significant trends in electronic products today include making them lighter, smaller and faster, as well as being more functional, reliable, environmentally friendly. On one hand, to comply with the environmental restrictions introduced by worldwide legislation, such as the Directive on Treatment of Waste from Electrical and Electronic Equipment (WEEE) and the Directive on the Restriction of Hazardous Substances in Electrical and Electronic Equipment (RoHS) issued by the European Council, removal of lead from electronic products been in progress, addressing the toxicity concerns of lead over the extensive usage of conventional tin-lead solder alloys. On the other hand, compared to wire bonding which is currently the dominant chip interconnection technique, flip chip interconnection has seen fast growth in recent years, as it enables higher density of interconnect, the shortest possible leads, as well as the smallest device footprint and the lowest profile after packaging. However, efficient wafer level solder bumping is one of the critical processes in achieving this chip interconnection approach while having such merits as above.

Research Aims and Objectives

This thesis is focused on the investigation of lead-free solder bumping at wafer level for flip chip interconnection through electrodeposition, as well as applying the developed electrochemical process for lead-free solderable finishes on electronic components. The existing knowledge gap in the electrolytic systems studied as well as the fundamental understanding of the resultant tin-based lead-free alloys electrodeposits are also addressed. The objectives and tasks are therefore formulated:

1. To develop and characterise the electrochemical deposition process for the electrodeposition of near-eutectic Sn-Ag, Sn-Cu and Sn-Ag-Cu solder alloys.
2. To fully characterise the electrodeposits from different bath systems under varying process conditions.

3. To apply the developed electrochemical processes to fabricate fine pitch lead-free solder bumps at wafer level.

Contributions to the Body of Knowledge

1. Two electrolytic systems, one based on methanesulphonate and the other on pyrophosphate, were developed for the electrodeposition of near-eutectic Sn-Cu and Sn-Ag/Sn-Ag-Cu solder alloys respectively. Comprehensive electrochemical study by cathodic potentiodynamic polarisation illustrated the electrochemical behaviours of the electrolytes under varying process parameters, as well as the effects of additives in individual systems.
2. The electrodeposits were fully characterised through material analytical techniques, while achieving near-eutectic compositions for individual systems. These analyses not only enabled an in-depth view into the microstructure of the electrodeposits, revealed the specific effects of process conditions and additives on the resultant products, but also helped to fundamentally understand the electrochemical process which made improvements and optimisations possible.
3. The developed processes proved feasible of producing fine pitch lead-free (Sn-Ag, Sn-Cu and Sn-Ag-Cu) solder bumps on wafers, demonstrate the potentials of applying the current contribution to wafer-level lead-free solder bumping for flip chip interconnection.

Structure of the Thesis

The structure of the thesis is illustrated in the figure below. Chapter 1 briefly describes the background of electronics packaging. Chapter 2 first introduces chip interconnection approaches with a focus on flip chip technology, then compares different techniques for wafer bumping while highlighting the advantages of bumping by electrodeposition. Chapter 3 gives the worldwide trend of removing lead from electronic products and details the properties of popular tin-based lead-free alternative solder alloys. Chapter 4 reviews the electrodeposition of lead-free solder alloys in the different electrolyte systems. Chapter 5 presents the experimental preparations, including the photoresist-patterned wafer sample preparation and the material analytical techniques utilises in the study. Chapters 6, 7 and 8 present and discuss the

electrodeposition and characterisation of Sn-Cu, Sn-Ag and Sn-Ag-Cu solder alloys respectively. Finally, the thesis ends with conclusions and further works presented in Chapter 9.

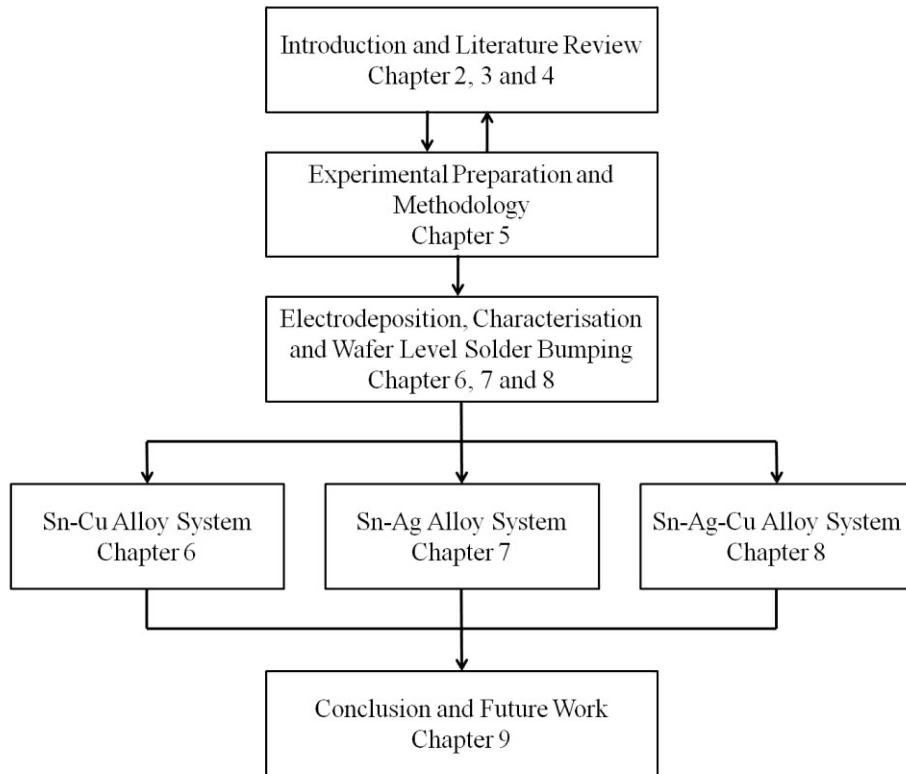

Figure I Thesis structure

Chapter 1

Electronics Packaging

This chapter introduces the subject of electronics packaging. It begins by briefly outlining the history and development trend of the integrated circuit (IC), as well as the role and function of electronics packaging in the fast growing electronics manufacturing industry. Next, the typical three-level hierarchy of electronics packaging is demonstrated. Finally, some standard IC packages are illustrated.

1.1 Introduction

The electronics industry is one the most dynamic and important areas of manufacturing. In a relatively short period of time, it has become large and pervasive all over the world.

Microelectronics, the branch of electronics that deals with miniaturising components, initiated the modern electronic evolution through the invention of the bipolar transistor in 1949 by John Bardeen, Walter Brattain and William Shockley at Bell Laboratories [1]. The transistor becomes the most important fundamental building block of all modern electronics later. To be able to achieve high functionality, the integration of transistors onto a single semiconductor chip was developed by Robert Noyce and Gordon Moore of Fairchild Semiconductor and Jack Kilby of Texas Instruments in 1959. This subsequently revolutionised the microelectronics industry because it produced the fundamental building blocks for the IC and stimulated the development of generations of ever increasing scale integration [2]. According to Moore's Law [3], it has been predicted that the number of transistors that can be integrated onto a silicon wafers would keep doubling every approximately 18 months, as shown in Figure 1-1 [4]. This has led to the basis of all modern electronic products seen today.

Figure 1-1 Moore's Law predicts the IC integration to double every 18 months [4][1].

Electronic packaging has been typically defined as the science and art of establishing interconnects and a suitable operational environment for an electronic circuit to process or store information [5]. A package generally contains a number of circuit components combined into a functional unit. The major function of electronic packaging is to protect, power and cool the microelectronic chips or components and provide electrical and mechanical connections between the microelectronic parts and the outside world. The detailed functions of the electronic packaging are: (1) to provide a electrical path that powers the circuits in the IC; (2) to distribute the signals on and off of the IC chip; (3) to remove the heat generated by circuits on the IC and (4) to support and protect the IC chip from outside hostile environments [6].

1.2 Packaging Hierarchy

As in complex electronic systems, several levels of packaging are typically involved, often referred to as a packaging hierarchy, as Figure 1-2 shows. The whole system can be divided into three levels of packaging, from the bare chip fabricated from the silicon wafer, to the final product ready for use. The first level of packaging provides the interconnection between an IC chip and a module. It should be noted that modern first-level packages might contain more than one IC chips and are then referred to as

[1] Reprinted with permission from McGraw-Hill. R. R. Tummala, Introduction to Microsystems Packaging, in Fundamentals of Microsystems Packaging, p. 8. Copyright (2004), The McGraw-Hill Companies.

multichip modules (MCM). Commonly, there are three methods for interconnecting the chips on the substrates (either to the module or the board): 1) wire bonding, 2) tape-automated bonding (TAB), 3) flip chip bonding [4].

Figure 1-2 Schematic of microelectronic packaging hierarchy with first-, second- and third-level packages [7][1].

Second level packaging finishes the interconnection between the module, as well as other components such as resistors and capacitors, to normally the printed circuit board (PCB). This interconnection is typically realised by pin through hole (PTH) technology, or surface mount technology (SMT). Take a personal computer as an example of an electronic system, second-level packages include the processor card (if not directly mounted onto the motherboard), random access memory (RAM) modules, or a graphics card. Putting second-level packages onto a motherboard is normally completed at the third-level packaging. Cards of various functionalities can be plugged in the sockets provided on the motherboard, where single-chip package and other electronic components can also be incorporated [4].

Along with the development of electronic packaging technology, to accommodate the needs from ever demanding electronic systems, plenty of variations can be found in packages nowadays on a basis of the previously discussed three-level packaging

[1] Reprinted with permission from McGraw-Hill. R. R. Tummala, Introduction to Microsystems Packaging, in Fundamentals of Microsystems Packaging, p. 18. Copyright (2004), The McGraw-Hill Companies.

hierarchy. For example, in some low-cost consumer applications, bare silicon chips are directly mounted onto PCBs, skipping the first-level package to cut down the cost. On the other hand, systems on a chip (SOC) or systems in a package (SIP) are becoming popular designs. In SOC, all the components are integrated into one single chip, while it is referred to SIP when they are all incorporated into one single package to meet the demands in specific applications. However, either in SOC or SIP, all the conventional three-level packages are combined into a first-level for purposes such as a small footprint [8].

1.3 Standard IC Packages

Different packaging technologies have been developed to satisfy the requirements for various electronic components. Electronic packages can be categorised by a number of criteria, such as package material (polymer, ceramic, or metal), interconnect configuration (peripheral or area array interconnects), assembly technology (PTH or SMT), or package types with Figure 1-3 showing the basic single-chip package types [9].

Figure 1-3 Overview of common single-chip package types used for integrated circuit packaging [9][1].

[1] Reprinted with permission from Elsevier. O. Brand, Packaging, in Comprehensive Microsystems, G. Yogesh, T. Osamu and Z. Hans, Editors. 2008, p. 437. Copyright (2004), Elsevier.

Generally, from the perspective of recent development in IC package types as shown in Figure 1-3, ball grid array (BGA) packaging is becoming increasingly popular driven by the higher and higher I/O demands in electronic products. On the other hand, the ever increasing requirement for smaller size packages has witnessed the fast development of chip scale package (CSP), which typically has a footprint maximum of 50% larger than the chip. As packaging techniques continuously develop, the ultimate CSP will have the size of the actual chip it protects and more novel types of single-chip packages will emerge in electronics packaging, however, commonly involving the technique of flip chip interconnection as discussed in Chapter 2 [10, 11].

Chapter 2

Chip Interconnection and Solder Bumping

Various studies have been conducted on the methodologies of first level chip to package interconnection, such as wire bonding, tape automated bonding and flip chip interconnection. This chapter begins with a summary of such studies. This is then followed by details of wafer bumping techniques for flip chip interconnection, including pick-and-place transfer process, stencil printing, evaporation and electrodeposition.

2.1 Chip Interconnection Techniques

Chip to package interconnection (assembly) is the first processing step after wafer fabrication and singulation. This process enables individual ICs to be packaged for system use and plays an important role in deciding the cost and performance of an electronic system. Chip to package interconnection can be defined as the process of connecting I/O bond pads on the IC to the corresponding bond pads on the package, providing electrical paths between the IC and the substrate for power and signal distribution. The package can be a single chip package, a multichip package, or a system level board [12].

There are three dominant chip interconnection methods currently in use: wire bonding, tape automated bonding (TAB) and flip chip bonding, as illustrated in Figure 2-1 and with key attributes summarised in Table 2-1. In this table, parameters of wire bonding, TAB and flip chip bonding (using solder and adhesive) are compared as practiced in the year 2000.

Figure 2-1 Illustration of chip to package or substrate interconnection techniques [12][1].

Table 2-1 Comparison of chip interconnection techniques (2000) [13][2].

[1] Reprinted with permission from McGraw-Hill. R. R. Tummala, Fundamentals of IC Assembly, in Fundamentals of Microsystems Packaging, p. 344. Copyright (2004), The McGraw-Hill Companies.
[2] Table summarised from the reference.

As can be seen from Table 2-1, although wire bonding is still the most widely utilised technology today (at least up to 700 I/Os on a single IC) and will remain so in the foreseeable future, for higher I/Os applications, flip chip bonding or TAB are the dominant technologies. Moreover, for very high I/Os beyond 2000, very high electrical performance and very high reliability that demanding wafer level packaging is required, flip chip bonding becomes virtually the only viable IC interconnection technique.

2.1.1 Wire Bonding

As currently the most popular chip-to-package interconnection technique, wire bonding typically utilises a fine metal wire for the attachment between each of the I/O pads on the chip to its associated package pad, one at each time. This technology was developed from AT&T's beam lead bonding in the 1950s. In their technology, a fine wire (typically gold wire 25 μm in thickness) is bonded using ultrasonic bonding between the IC bond pad and the matching package or substrate bond pad. Compared to other chip interconnection technologies, this point-to-point process has a major advantage of flexibility, which is also referred to as compliancy. Wire bonding also enables high yield (low defect rates) production. Meanwhile, the process of changing wires are simply modifications to a digital machine programme requiring no hard tooling or package design changes. However, new tapes for TAB packages normally requires a new process and design, increasing cost and time [14].

Figure 2-2 Chip to package or substrate interconnection technique: illustration of wire bonding.

In the year 1999, wire bonding accounted for well over 90% of all the chip-to-package interconnections practiced. Figure 2-2 shows a schematic wire bond interconnection structure for polymeric packaging, which is the dominant packaging configuration. There are two major types of wire bonds used in high volume production: gold ball bonding, which comprises over 95% of all wire bonds formed and gold or aluminum wedge bonding depending on applications [15].

Wire bonding also comprises some disadvantages including slower interconnection rates owing to the point-to-point processing of each wire bond, long chip-to-package interconnection lengths (therefore degrading the electrical performance), plus larger footprint required (low interconnection density) which is unsatisfactory for the trend of continuous miniaturising of packages [16].

2.1.2 Tape Automated Bonding

Tape automated bonding, as shows in Figure 2-3, is another common chip interconnection technique. Using this technology, ICs are mounted and interconnected on metallised flexible polymer tapes, either a single-layer metallic tape or a multilayer polymer/metal sandwich. This is based on the fully automated bonding of one end of an etched copper lead to an IC and the other end of the lead to a conventional package or PCB [17].

Tape automated bonding was invented by Frances Hugle in Silicon Valley (USA) and commercialised in 1966 by General Electric Research Laboratories (New York), who used it to fabricate small-scale integration (SSI) devices. This technology offered a lower cost replacement of wire bonding technology by providing a highly automated bonding technique (all interconnects are formed at the same time) to package high-volume and low I/O devices. During the 1970s, TAB attracted strong attentions but received relatively low industrial acceptance, except in Japan. TAB saw its most widespread application in the 1980s as SMT thrived. TAB has been applied to a variety of consumer, medical, security, computer, telecommunication, automotive and aerospace products [18, 19].

Figure 2-3 Chip to package or substrate interconnection technique: illustration of tape automated bonding [20].

Compared to wire bonding, the advantages of TAB include the ability to handle bond pads of smaller sizes and finer pitches on the IC, elimination of lengthy wire loops and improved heat transfer and electrical performance. However, similar to wire bonding, it is only a peripheral interconnection technique and the package size tends to increase with larger I/O counts. This makes it undesirable for future high density and small footprint packaging. In addition, it also requires relatively large capital equipment investment.

2.1.3 Flip Chip Bonding

Compared to wire bonding and TAB, the advancement of flip chip technology has been one of the significant developments in the electronic packaging industry to reduce cost and improve reliability and productivity. The process of flip chip interconnection was first introduced for ceramic substrates as Solid Logic Technology by IBM in 1962. Later in 1970, IBM converted this technology to the Controlled Collapse Chip Connection (C4) for IC packaging [21]. Flip chip technology is an advanced form of surface mount technology. During the flip chip bonding process, IC

chips are turned upside down, thus called flip chip (i.e. active face down) and then bonded directly to a PCB or other chip carrier substrates, as Figure 2-4 demonstrates.

Figure 2-4 Chip to package or substrate interconnection technique: flip chip interconnection. Schematic of a typical process sequence for flip chip interconnection using solder bumps.

For flip chip interconnection, the wafer is first coated with patterned under bump metallisation (UBM) layers. These metallisation layers have functions such as wetting, barrier and adhesion. After the bump fabrication step through techniques such as evaporation and electrodeposition (details discussed in Section 2.3), the wafer is reflowed, i.e. subjected to a thermal process to melt the solder bumps and form truncated spherical balls. It is then placed face down, aligned to the substrate and joined to the package in another reflow process [22].

The development of flip chip interconnection was initiated in an attempt to cut down the expense, improve the reliability and low productivity of manual wire bonding of the era. In contrast to wire bonding, which is a peripheral and time consuming bond technique, the flip chip allows all I/Os to be connected simultaneously [23]. Seeing promising applications to meet requirements for future chip interconnection technology, flip chip bonding is discussed in more details in Section 2.2.

2.2 Flip Chip Interconnection

2.2.1 Wafer Level Packaging

Currently, there is a trend of continuous miniaturisation particularly for consumer electronics, such as smart cell phones and personal computers. This has resulted in the need for much smaller IC and system level packages with low cost. While all these developments are progressing fast, an entirely new paradigm is taking place as required towards all these directions. This is referred to as wafer level packaging (WLP), addressing these needs in terms of IC packaging related stages [24].

Wafer level packaging is IC packaging completed at the wafer level in the wafer foundry. This is in contrast to conventional packaging that is carried out in sequential steps: wafer and singulation of the wafer into ICs and then the subsequent packaging of individual ICs into QFP, BGA, CSP or other packages types as previously discussed in Section 1.3. In contrast, wafer level packaging methodologies assemble functional CSPs at the smallest footprint while keeping all components of the process, including the ICs, in the wafer form. In this way, both front-end IC fabrication and back-end IC assembly are performed in the wafer foundry.

Figure 2-5 Size comparisons of wafer level flip chip packaging with alternative packaging styles (l_c = length of chip side). For small chips, the package-to-chip area ratios may be even larger for chip-on-board, TAB and QFPs [25][1].

Wafer level packaging provides many benefits, with the most important two being the lowest cost and smallest size. In general, cost reduction can possibly be realised in the IC industry by two methodologies: (a), increasing wafer size which results in more ICs per wafer; (b), decreasing feature size on the IC which results in "die shrinks" and consequently more ICs for a given wafer size. Cost reduction by wafer level packaging is achieved by the second method. Not only does wafer level packaging offer lower cost than traditional methods of IC packaging, but minimum size is also achieved which is very important. The area that a wafer level package occupies when

[1] Reprinted with permission from McGraw-Hill. R. R. Tummala, Fundamentals of Multichip Packaging, in Fundamentals of Microsystems Packaging, p. 302. Copyright (2004), The McGraw-Hill Companies.

mounted onto a system level substrate can be as small as the size of the IC itself depending on the design and processes (Figure 2-5) and this is different from all the other types of package. With this in mind, wafer level packaging can be considered the ultimate IC packaging option [5, 26]. However, it is worth mentioning that so far flip chip interconnection has been the most effective way to realise all the merits wafer level packaging enables, including the smallest feature size as Figure 2-5 demonstrates.

2.2.2 Flip Chip Interconnection Trend

Figure 2-6 Predicted chronological trend of first level interconnection in transition in electronics packaging by ITRS 2007 [27][1].

Significant advancements in flip chip interconnection technology have been made in recent years driven by its fast growing applications. Figure 2-6 plots the ITRS (International Technology Roadmap for Semiconductors) trends projected in 2007 for first level chip interconnections using wire bonding and flip chip technologies, in terms of pitch size shrinkage. As can be seen, ever finer pitch sizes and increasing I/O counts are demanded for future first level interconnection in electronics packaging. For wire bonding technology, whether it be single-in-line, two-row-staggered, three tier or wedge bond, the pitch sizes projected are all nearly approaching their limitations, particularly after the year of 2013. However, for the promising methodology of flip chip area array bonding, there are still improvements to be made

[1] Figure drawn from the data in Assembly and Packaging, International Technology Roadmap for Semiconductors, 2007.

as the pitch is projected to be continuously getting smaller in the next decade [27]. The achievement in finer pitch flip chip interconnection will enable a promising future for this technology. However, facing up to all the technical challenges, significantly more work has to be carried out to move the boundary of this technique forward as the projection forecasts.

2.2.3 Flip Chip Interconnection Configuration

As mentioned earlier in this chapter (Section 2.1.3), flip chip interconnection is defined as a chip, with the active surface or the I/O side facing down, mounted on the substrate with various interconnection materials, such as solder bumps, isotropic and anisotropic conductive adhesives, other metal bumps such as copper pillar and pressure contacts. Figure 2-7 illustrates various flip chip interconnection types, using different materials (and processes) mentioned above [28].

Figure 2-7 Schematic of various flip chip technologies [28][1].

Like its preceding chip interconnection techniques such as wire bonding, flip chip technology was initially applied to the peripheral area of the chip only. However, owing to the unique attributes of this technique, it was then quickly progressed to applications in area arrays interconnection. Compared to wire bonding using only the

[1] Reprinted with permission from McGraw-Hill. J. H. Lau, A Brief Introduction to Flip Chip Technologies for Multichip Module Applications, in Flip Chip Technologies, p.25. Copyright (1995), The McGraw-Hill Companies.

peripheral area, this allowed for much more I/O contacts and reduced the package size as the interconnection materials can be placed over the whole surface area.

For flip chip interconnection using solder as the interconnection materials (most widely used type), solder bumps are first deposited on the solder wettable bonding pads on the active surface of the chip by various techniques such as evaporation and electrodeposition. This process is also referred to as wafer level solder bumping as discussed in Section 2.3. Then, the solder bumped chip is aligned to the substrate, matching the corresponding bonding pads and then reflowed through thermal profiles optimised for the bumping solder materials. During this thermal process, both electrical and mechanical interconnections between the chip and substrate are achieved and the wetting action of the solder driven by surface tension forces will help align the bump pattern on the chip to the corresponding substrate pads [29]. A typical flip chip on board (FCOB) using solder bumps is shown in Figure 2-8.

Figure 2-8 Schematic of flip chip on board using solder bumps: (a) cross-sectional view; (b) enlarged view of chip/solder and solder/PCB interface.

As illustrated in Figure 2-8, the configuration of flip chip interconnection can be divided into four functional components: UBM, encapsulation (underfill), solder balls and the substrate pads. Typical functions of UBM layers include adhesion between the silicon chip and other top UBM layers, barrier to diffusion between the solder bump

materials and the conductive bonding pad on the chip (commonly Al or Cu) and the top wettable layer for solder wetting during the reflow process. Achieving such functions requires UBM layers normally consisting of 3–4 different metallic ones, such as Ti/Cr or TiW/Cr as the adhesion layer, Ni as the barrier and Cu or Au as the top wetting layer.

As widely used in wire bonding, underfill is also commonly seen in flip chip technology which protects the interconnection from the environment. The underfill also provides a heat bridge between the substrate and the chip. This minimises and distributes the stress loaded in the solder joints, which is generated during thermal loading due to differential heating of the chip and the rest of the system [30].

The solder bump functions as the mechanical and electrical connection from the chip to the connecting PCB substrate patterned with bonding pads (typically Cu with top layers protecting the solderability). During the subsequent reflow process in assembly, the solder melts and forms an intermetallic layer at the two interfaces: chip/solder ball, due to the dissolution of the UBM wetting layer into the molten solder during the high temperature reflow; substrate/solder ball, due to the dissolution of the protective layer and the exposed solderable finish on the bonding pads. Such intermetallic layers at both the interfaces are critical to realise a metallurgical interconnection and also important for the overall reliability of the flip chip [31, 32].

2.3 Solder Bumping Process

As shown in Figure 2-4, following the under bump metallisation step, the wafer is coated with the desired bumping material, generally a solder. This process is usually referred to as wafer bumping. Evaporation and electrodeposition are the two most commonly used bumping methods for high-end applications. Other methods include screen printing, solder jetting and pick and place solder transfer process.

2.3.1 Stencil Printing

Wafer bumping via the stencil printing method is very popular in electronics packaging. Stencil printing evolves from the screen printing process, but enables more precise control of the solder paste volume deposited, therefore allowing a relatively

finer pitch application. The stencil printing process is schematically illustrated in Figure 2-9. A stencil is typically formed of metal foil with a pattern of aperture matching the footprint on the wafer (or PCB) where deposition of solder paste is desired. This stencil is placed on top of the wafer with patterns aligned properly. The solder paste is then deposited onto one side of the stencil, followed by being wiped across the stencil with the use of a squeegee. The wafer is then detached from the stencil, with solder paste deposited on top of the corresponding pads, which is later turned into solder balls through the high temperature reflow process [33, 34].

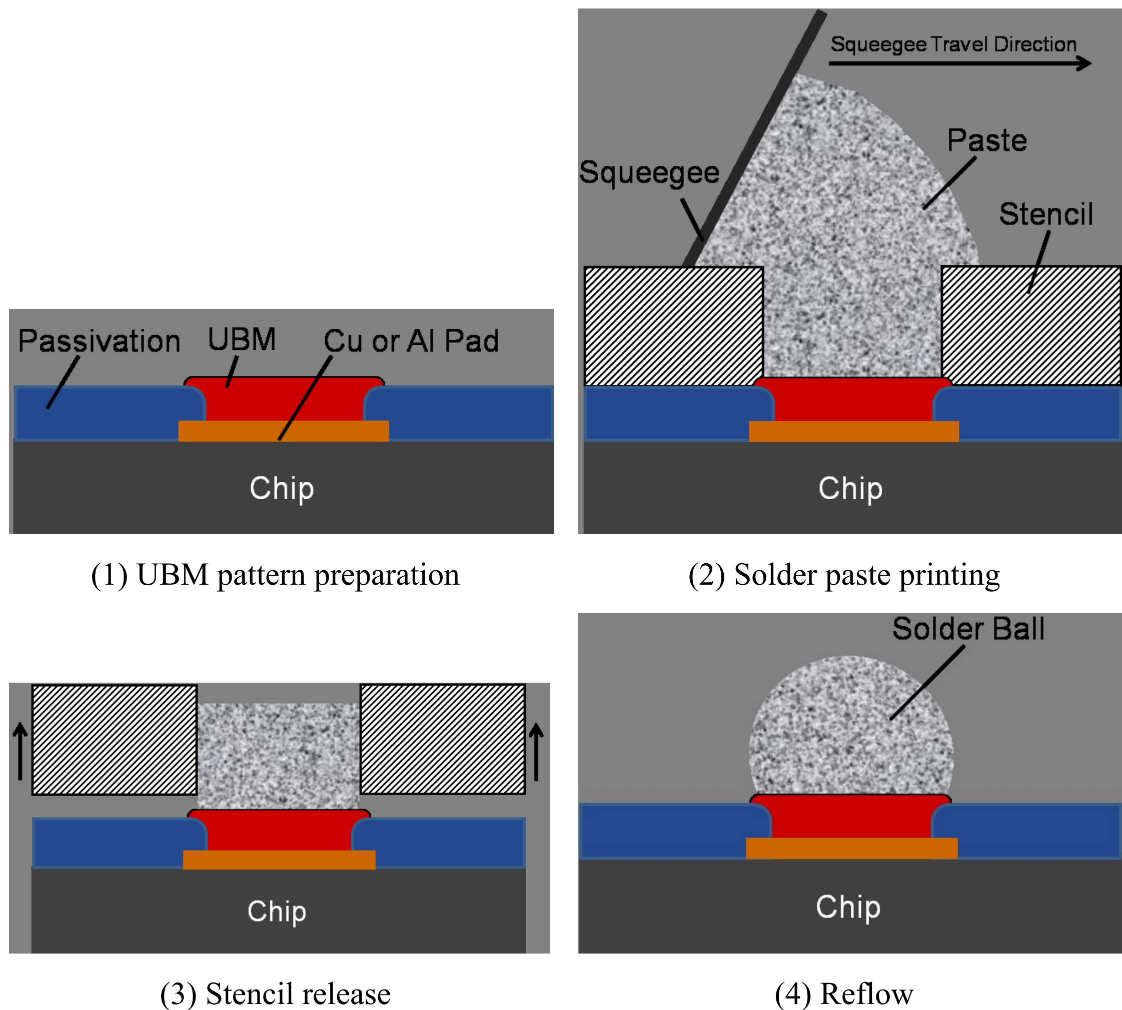

Figure 2-9 Schematic of the stencil printing process for wafer bumping.

Compared with other technologies, the stencil printing process promises a higher speed, higher throughput, better pattern registration and better solder paste volume control. The constraint of using the stencil printing process is the requirement of a flat substrate surface for the stencil to be laid on. This limits the potential of using the

printing process for rework purpose or for a soldering on a non-flat surface. For fine pitch wafer bumping, the stencil printing technology is to some extent constrained due to the required continuous reduction of pitch size. Besides, there are also concerns about quality and production yields, due to stencil manufacturing limitations and solder particle size. This means that existing printing methods are not likely to move significantly below a typical pitch of 150–200 µm, whilst even finer pitch sizes would be desirable for high density flip chip packaging [35-37].

2.3.2 Evaporation

The most mature wafer-bumping method is by evaporation, which was developed by IBM more than 30 years ago. This is a dry solder bumping process, with a schematic diagram of the process shown in Figure 2-10.

At first, a molybdenum (coefficient of thermal expansion close to that of silicon) metal mask is aligned to the bond pads on the wafer and fixed. The UBM layers are deposited through evaporation onto Al (or Cu) pads. The solder material with a known composition and volume is then also deposited through evaporation onto the UBM surface. The molybdenum metal mask is then removed and the solder bump formed is subsequently reflowed in order to form truncated spherical solder bumps.

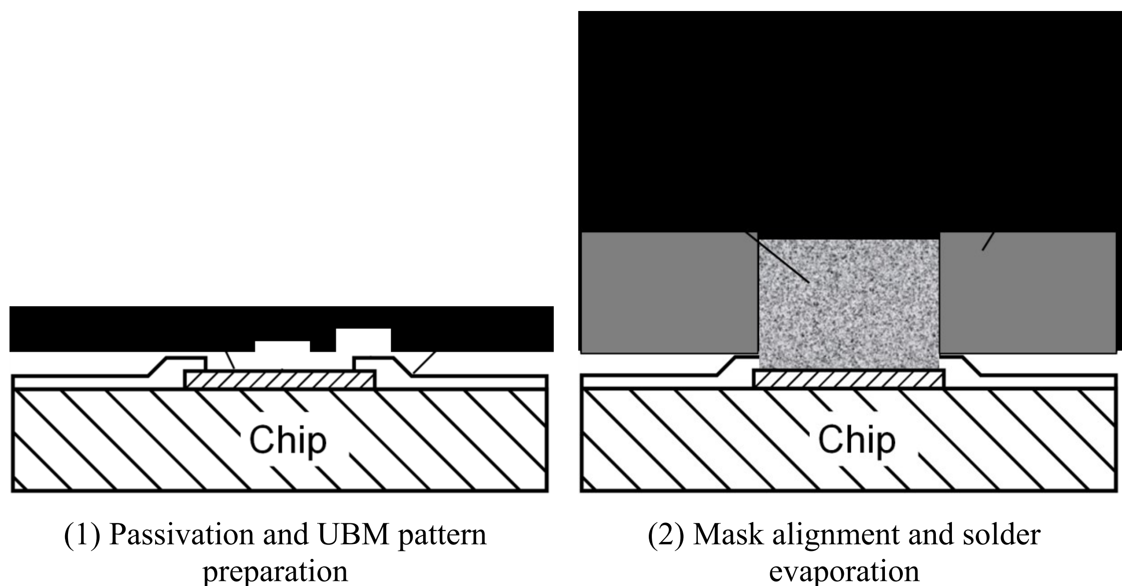

(1) Passivation and UBM pattern preparation

(2) Mask alignment and solder evaporation

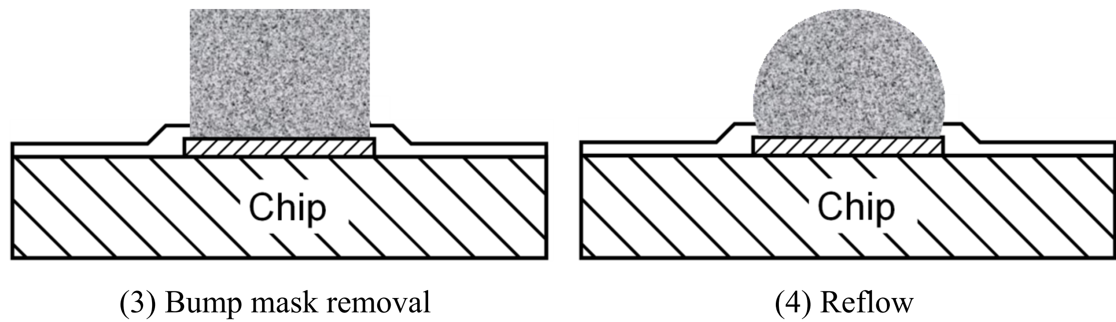

(3) Bump mask removal (4) Reflow

Figure 2-10 Schematic key processes of wafer bumping through evaporation.

In general, the evaporation process achieves a high quality solder composition and volume. It is adequate for coarse pitch and low I/O devices, but not extendible to finer bump pitches and larger (>200 mm) wafers, due to the constraints of metal mask technology, although 100 μm diameter bumps at a 250 μm pitch have been demonstrated [38].

However, the cost of the evaporation process is of concerns, such as expensive infrastructure, low-life metal mask, waste disposal. Evaporation is typically less than 5% efficient, with more than 95% of the evaporated material ending up on the evaporator wall and on the metal mask, which need to be cleaned and the lead containing waste has to be disposed by an expensive, regulated procedure. Finally and possibly most importantly, lower melting temperature Sn-rich solders, such as the eutectic Sn-Ag, Sn-Cu and Sn-Ag-Cu solder alloys in the current study, cannot be evaporated due to the lower vapour pressure of Sn. This has constrained its application for high-Sn lead-free solder alloys, which are promising alternatives to Sn-Pb solders, since legislation all over the world have confined the usage of lead in electronic products (more details will be discussed in Chapter 3) [39].

2.3.3 Electrodeposition

Developed as a more cost effective approach to bumping by evaporation, electrodeposition may be the most commonly used process for wafer bumping currently. Bumping through electrodeposition can be regarded as a wet solder build-up process. Figure 2-11 shows the process for electroplated wafer bumping. First, the whole wafer with patterned passivation is metallised with seed metals, e.g. Ti/Cu or TiW/Cu, as UBM. It is then patterned with a layer of photoresist with the desired

bumping locations exposed. A mask is then used to define the bumping pattern, with the opening in the resist a little wider than the pad openings in the passivation layer. A direct or pulsed current is then applied through the electroplating bath with the wafer as the cathode, with the application of agitation as needed. In order to deposit enough solder to achieve the final solder height, the solder is normally deposited over the photoresist top level to form a mushroom shape. After electroplating, the photoresist is stripped off and the seed metal layers (UBM) outside the bump etched away. The solder bumps deposited are then reflowed with the use of flux to form smooth solder bumps [40].

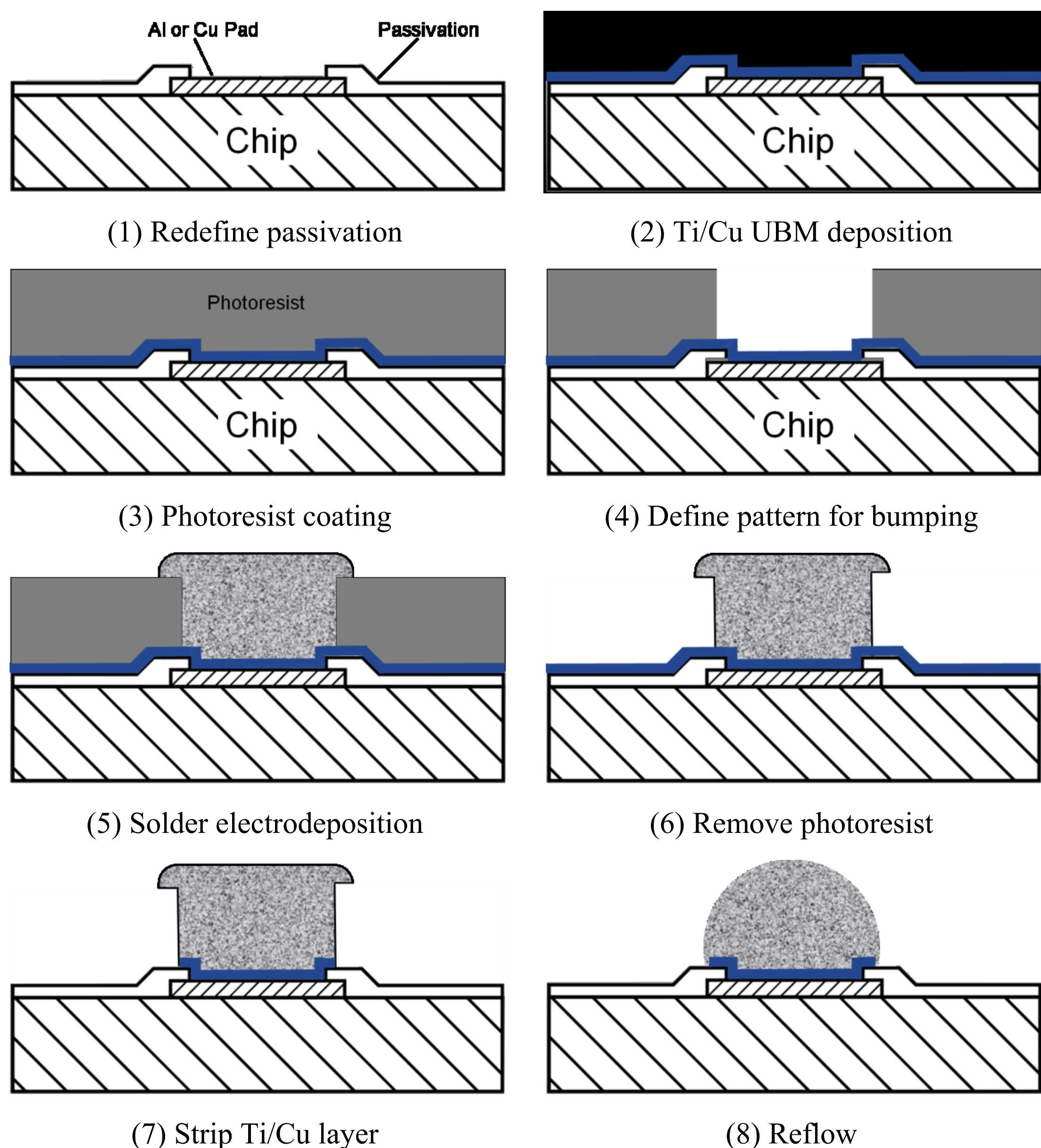

Figure 2-11 Schematic of the process sequence for wafer bumping through electrodeposition.

This electrodeposition method is very popular today because it can electroplate solders in various combinations (e.g. lead-free solder alloys). One of the drawbacks is bump height non-uniformity. Usually, due to the boundary effect, i.e. current density near the edge of the wafer is higher than the centre during the electrodeposition process, the solder bumps near the edge of the wafer are taller than those near the centre of the wafer. This therefore needs to be addressed in the electrodeposition process. However, compared to evaporation and other solder bumping techniques previously discussed, electrodeposition is becoming more and more attractive, owing to its capability of achieving all such merits at the same time as high volume and production yield, as well as its ability to produce finer pitch bumping at an acceptable cost [29].

2.4 Summary

A literature review of the chip interconnection techniques and wafer level solder bumping approaches is given. Technologies commonly used for interconnecting chip to the substrate, including wire bonding, tape automated bonding and flip chip bonding, are discussed and compared, with a focus on the advantageous of flip chip interconnection. Wafer level solder bumping are normally employed by stencil printing, evaporation and electrodeposition. By comparing these three popular techniques, it is concluded that electrodeposition is the effective method to fabricate tin-rich, fine pitch, lead-free solder bumps at wafer level for flip chip interconnection, which meets the requirements for future electronic interconnection.

Chapter 3

Lead-Free Solder Alloys

This chapter contains the background relating to the development of lead-free soldering in the electronics industry, including worldwide lead-free legislation, criteria for selecting lead-free solder alternatives and elaboration of promising binary and ternary lead-free alloy candidates.

3.1 Introduction

Sn-Pb solders have been used in electronic applications for more than 50 years on account of their low melting temperature, good reliability, low cost and compatibility with printed circuit board assemblies. However, lead in electrical and electronic waste is of a major concern to the public due the possibility of its leaching from landfills and therefore contaminate the human food chain, such as the groundwater system, causing serious health hazards. Figure 3-1 schematically represents the path of lead from electronic scrap, such as PCB, to the human body through drinking water. Lead toxicity in humans could result in cancer and also could adversely affect the liver and thyroid functions. The main effect, however, is on the central nervous system [41].

In addition to the environmental and toxicity issues, lead also poses a radioactivity problem to ICs. Conventional lead-containing solder contains a certain amount of radioisotopes such as ^{210}Pb and other radioactive elements, such as U and Th, as impurities. Since radioactive lead has a relatively long half-life, it produces α-particles during decay, which generate electron-hole pairs through elastic collisions during their penetration into silicon. If the charge density in the capacitor of a memory cell changes, it will result in a functional failure, often referred to as soft errors in dynamic random access memory (DRAM) and charge-coupled devices (CCDs).

Therefore, strict control of the amount of radioactive lead or complete lead removal is necessary especially for the application in high density memory chips [42-44].

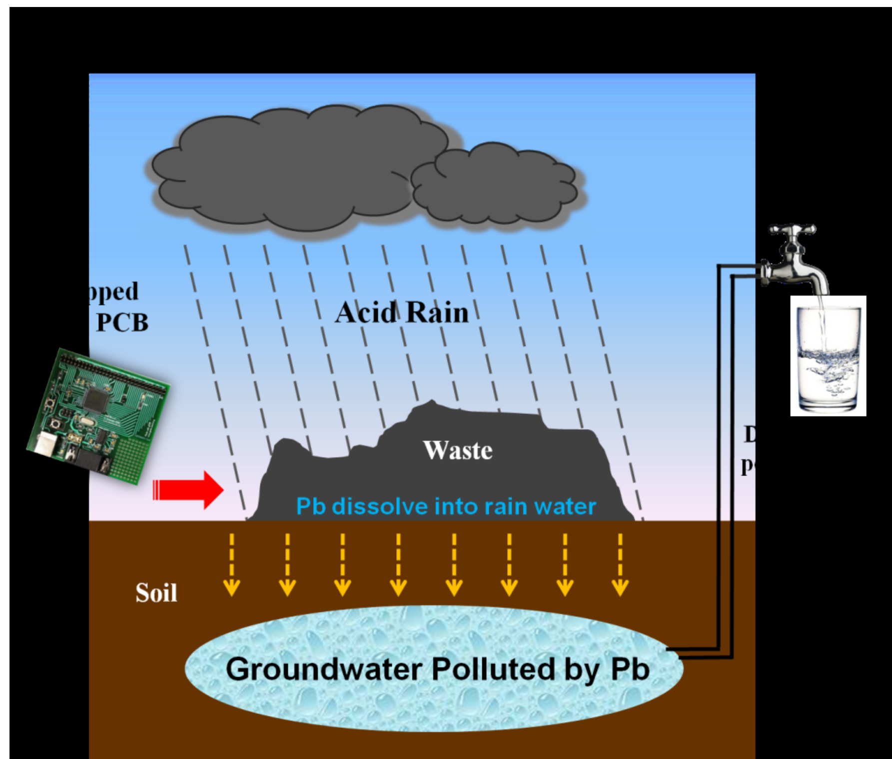

Figure 3-1 An illustration depicting the sequence of events that results in the ingestion of lead leached from electronic wastes in landfills.

3.2 Global Legislation

Since environmental regulation of electronic products was first introduced in the European Union, other governments have begun to initiate similar efforts. The US, Japan and other countries have all made efforts to reduce or limit the use of lead and other hazardous chemicals in electrical and electronic products [45].

3.2.1 European Union

The European Union has been setting trends and indicating about the future of environmental regulation of electronic products through different initiatives. On 27 January 2003, the European Council issued the Directive on Treatment of Waste from Electrical and Electronic Equipment (WEEE) and the Directive on the Limitation of Hazardous Substances in Electrical and Electronic Equipment (RoHS). Under the

RoHS, as from 1 July 2006, any new electrical and electronic equipment must not contain certain hazardous substances, including lead, cadmium, mercury and hexavalent chromium [46, 47].

The WEEE, which came into force on 13 August 2005, contains ten categories of equipment covered by the directive. The products concerned are mostly "consumer" goods such as domestic electrical appliances. Other initiatives affecting the usage of lead in electronic products in the European Union include The Energy-using Products (EuP) Directive and The Regulation on Registration, Evaluation, Authorisation and Restriction of Chemicals, also known as REACH [48].

3.2.2 United States of America

In the 1990s, US non-governmental associations started to develop lead-free initiatives. The International Electronics Manufacturing Initiative (iNEMI) worked in cooperation with major manufacturers to support lead-free manufacturing initiatives. They adopted a pro-active approach by initiating a “lead-free” committee [49].

In December 2001, the United States Environmental Protection Agency took a major step by issuing "Guidance for Reporting Releases and Other Waste Management Quantities of Toxic Chemicals: Lead and Lead Compounds" [50]. This document provides guidance on the specific details, regulating that facilities must file release reports for lead and lead compounds and methods to estimate releases of lead and lead compounds into the environment.

3.2.3 Asia

In Asia, extensive efforts have also been made to build extended producer responsibility to the electronics industry regarding environmental issues. Back to the early 1990s, the Japanese community started to implement control of the lead released out of landfills and waste disposal. The Japan Electronics and Information Technology Industries Association (JEITA) supports lead-free investigations and consolidates independent test results. The Chinese market is of growing importance for most electronics producers. A version of RoHS in China, promulgated in February of 2006 by the Ministry of Information Industry, has been in effective implementation

since March 1, 2007. Other Asian countries and districts such as South Korea and Taiwan, have also announced similar initiatives concerning environmental issues [51].

3.3 Criteria for Lead-Free Solder Candidates

Extensive investigations of alternative lead-free solder alloys have been carried out. The primary alloy design criteria have been developed using Sn-Pb eutectic as a baseline. This is because for more than 50 years, PCBs and components have been designed and utilised on a basis of the behaviour of Sn-Pb eutectic solder during circuit board assembly.

In the National Centre for Manufacturing Science (NCMS) Lead-Free Solder Project completed in 1997 in the US, the pass-fail criteria for candidate alloys were created to represent practical restrictions on the properties of lead-free solders, as seen in Table 3-1.

Table 3-1 Criteria used by NCMS for lead-free solder alloys [52][1]

[1] Table summarised from the reference.

According to this project, the desirable lead-free solder candidates should in general: 1), have a melting point as close to Sn-Pb eutectic as possible; 2), be eutectic or very close to eutectic in composition to enable low melting point; 3), contain no more than three elements (ternary composition); 4), avoid using existing patents, if possible (for ease of implementation); 5), have the potential for reliability equal to or better than Sn-Pb eutectic.

Other important properties from a manufacturing and long-term reliability standpoint include cost, electrical and thermal conductivities, corrosion and oxidation resistance, depending on the applications.

3.4 Lead-Free Solder Alloys

There are no “drop-in” replacement alloys for Sn-Pb eutectic as generally agreed by most research groups. The lead-free solder alloys currently being studied and used in

industry are mostly eutectic or near-eutectic alloys, because a eutectic alloy has a single and relatively low melting point. Formed from eutectic alloys, the entire solder joint will melt or solidify at a fixed temperature, i.e. avoiding partial melting or partial solidification, as this is detrimental for soldering and the reliability [48]. Figure 3-2 compares the typical lead-free solders in term of melting temperature. As can be seen from this figure, though it is desirable to have mounting temperature at the range of the same level or even lower than that of the conventional Sn-Pb eutectic solder, most lead-free candidates show higher melting temperature.

Figure 3-2 Melting temperature of lead-free solders and technology [53][1].

As also seen from Figure 3-2, a relatively large number of binary, ternary, or even quaternary solder alloys have been proposed so far, with some popular candidates summarised in Table 3-2. The lead-free solder alloys attracting the greatest attention are Sn based (Sn being the primary or major constituent), such as Sn-Ag, Sn-Cu, Sn-Bi, Sn-Zn, Sn-Ag-Cu and Sn-Ag-Zn. Amongst them and applying the criteria listed in Table 3-1, the Sn-Ag-Cu family of alloys seem to be the most promising alternatives for eutectic Sn-Pb solder [51, 54].

---

[1] Reprinted with permission from Marcel Dekker. K. Suganuma, Future of Lead-Free Soldering, in Lead-Free Soldering in Electronics: Science, p. 330. Copyright (2004), The Marcel Dekker, Inc.

Table 3-2 Major lead-free solder system candidates to replace eutectic Sn-Pb solder [55][1]

[1] Table summarised from the reference.

3.4.1 Sn

The ability of Sn to wet and spread on a wide range of substrates, using mild fluxes, has allowed it to become the principal component of most lead-free solder alloys used for electronic applications. Elemental Sn melts at 231°C. Tin exists in two different forms with two different crystal structures in the solid state: white or β-tin and grey tin or α-tin which is thermodynamically stable below 13°C. The Sn rich lead-free solders are relatively reactive. This should be considered in the solder interconnections during assembly in terms of forming a stable interface in the joints.

The transformation of β-tin to α-tin, also referred as “tin pest”, takes place when the temperature falls below 13.2°C and results in a large increase in volume, which can induce cracking in the tin structure. Consequently, tin pest can be a problem for applications that operate at extremely low temperature and can be particularly problematic for devices that cycle across the 13.2°C temperature point. Due to its body centred tetragonal crystal structure that is anisotropic, the thermal expansion of tin is also anisotropic. Tin whiskers, which may cause electrical shorts, are another problem that Sn (and some Sn alloy) solders may encounter [56].

3.4.2 Sn-Ag

The eutectic composition for the Sn-Ag binary system occurs at Sn-3.5wt.%Ag, with a eutectic temperature of 221°C as seen from the Sn-Ag equilibrium phase diagram in Figure 3-3.

Figure 3-3 Sn-Ag equilibrium thermal phase diagram [57][1].

The as-solidified (e.g. after the reflow process) microstructure of eutectic Sn-Ag is relatively coarse and non-uniform. It consists of two phases, an essentially pure Sn phase (β-Sn with less than 0.04% Ag in solution) with large dendritic globules and inter-dendritic regions with a eutectic dispersion of intermetallic compound, Ag_3Sn (less than a 5% volume fraction, referred to as ε-phase in Figure 3-3), within the β-Sn matrix. Such a microstructure has made it more resistant to coarsening, whilst the lamellar morphology is not routinely observed for eutectic Sn-Ag compared to eutectic Sn-Pb [58]. The presence of the Sn dendrites is indicative of a non-equilibrium cooling rate. However, the structure is noted to be stable as the Sn dendrites were observed to be present after months of room temperature aging. In non-equilibrium cooling, characteristic of solder joints, the rod-like ε-phase which typically forms, tends to minimize the surface free energy. The size and morphology of the ε-phase depends on the cooling rate during solder solidification [59].

As one of the most popular choices, Sn-Ag alloys have excellent mechanical properties. They exhibit good wetting behaviour on copper and copper alloys. However, they also exhibit a relatively high melting temperature and cost due to the

[1] Reprinted with permission from ASM International. T. B. Massalski, H. Okamoto, P. R. Subramanian and L. Kacprzak, ASM Binary Alloy Phase Diagrams. Copyright (1996), ASM International.

Ag. Considering the eutectic temperature of 221°C, assemblies must be exposed to temperatures as high as 240°C to achieve adequate wetting.

3.4.3 Sn-Cu

One example of the use of eutectic Sn-Cu alloy was reported with the world's first virtually lead-free telephone, where eutectic Sn-Cu was chosen for both solder joints and surface finish layers on PCB and component termination pads [60]. The Sn-Cu binary alloy has a eutectic composition of Sn-0.7wt.%Cu and a eutectic temperature of 227°C, as seen from the Sn-Cu equilibrium phase diagram in Figure 3-4. A typical microstructure of as-cast eutectic Sn-Cu solder consists of large dendritic β-Sn grains surrounded by a network of the eutectic microstructure containing a fine intermetallic compound, Cu_6Sn_5. It has been demonstrated that the microstructure of Sn-0.7wt.%Cu solder bumps, used in flip-chip interconnections, is composed of large, tin-rich grains with a fine dispersion of Cu_6Sn_5 intermetallics [61].

The tensile strength of eutectic Sn-Cu solder is lower than eutectic Sn-Pb solder, but the hardness is similar. To further improve its mechanical properties and control the interfacial reactions during soldering or thermal aging, several modifications of Sn-Cu-based solders have been disclosed. For example, the addition of a small amount of Ag (up to 1wt.%) refines the Sn-Cu eutectic microstructure by introducing another fine intermetallic compound, Ag_3Sn [62].

Because of its relatively high melting point, eutectic Sn-Cu solder is not the most widely recommended for surface mount technology. However, because of its relatively low material cost, it is considered as a good candidate for lead-free, wave-soldering processes in the mass production of commercial electronics. Also, the use of a Sn-Cu coating is preferred over pure Sn to avoid the growth of Sn whiskers [56].

Figure 3-4 Sn-Cu equilibrium thermal phase diagram [57][1].

3.4.4 Sn-Ag-Cu

The main benefits of the Sn-Ag-Cu alloy system are its relatively low melting temperature (217°C) compared to binary eutectic Sn-Ag and Sn-Cu alloys and its generally superior mechanical properties, as well as relatively good solderability. In addition, Sn-Ag-Cu solders have also shown good compatibility with current components [54].

With regard to the best composition, there is still disagreement, because significant variations in microstructure can occur as a result of cooling rate, complicating the determination of the eutectic Sn-Ag-Cu composition and temperature. In terms of the recommendations, Japan favours Sn-3.0wt.%Ag-0.5wt.%Cu (Japan Electronics and Information Technology Industries Association, JEITA), Europe Sn-3.8wt.%Ag-0.7wt.%Cu (European Consortium BRITE-EURAM) and America Sn-3.9wt.%Ag-0.6wt.%Cu (International National Electronics Manufacturing Initiative, iNEMI) [63].

---

[1] Reprinted with permission from ASM International. T. B. Massalski, H. Okamoto, P. R. Subramanian and L. Kacprzak, ASM Binary Alloy Phase Diagrams. Copyright (1996), ASM International.

The near-eutectic ternary Sn-Ag-Cu solidifies into three phases: β-Sn, Ag_3Sn and Cu_6Sn_5, as reported by several investigators, e.g. [64, 65]. It was demonstrated with Sn-3.5wt.%Ag-0.7wt.%Cu that a small quantity of primary Ag_3Sn was present, but almost completely ternary eutectic, indicating the composition to be only slightly deficient in copper. The solubility of the solute atoms in the intermetallic phases (i.e., Ag in Cu_6Sn_5 and Cu in Ag_3Sn) is quite limited. The strength of Sn-Ag-Cu alloys to some extent depends upon the area fraction of the eutectic network and the dispersion morphology of the fine Ag_3Sn within the network. The lower ductility of slow-cooled, higher Ag content alloys is explained on the basis that under these conditions large primary Ag_3Sn phase are formed, which are brittle and likely to result in cracks, thus reducing elongation [51, 54].

Figure 3-5 Sn-Ag-Cu equilibrium thermal phase diagram [64][1].

3.4.5 Sn-Bi and Sn-Zn

The Sn-Bi alloy has a eutectic composition of Sn-58wt.%Bi and a relatively low eutectic temperature of 139°C, making it most suitable for soldering at low

[1] Reprinted with permission from Springer Science + Business Media. K. Moon, W. Boettinger, U. Kattner, F. Biancaniello and C. Handwerker, Experimental and thermodynamic assessment of Sn-Ag-Cu solder alloys. Journal of Electronic Materials, 2000. 29 (10): p. 1122-1136. Copyright (2000), Springer.

temperature when electronic devices are prone to thermal damage. Besides the low melting temperatures, the eutectic Sn-Bi alloy has the merits of good joint strength, low surface tension, excellent creep resistance, high shear strength and good anticorrosive properties. As the equilibrium phase diagram shows in Figure 3-6, since tin has very low solubility in Bi at the eutectic solidification temperature of 139°C, the Bi phase is essentially pure Bi. As the alloy cools, Bi precipitates in the Sn phase [66].

Figure 3-6 Sn-Bi equilibrium thermal phase diagram [57][1].

The Sn9-wt.%Zn alloy, though its wettability and joint strength are relatively poor, appears to be an attractive alternative, with a melting temperature of 198°C that is relatively close to the eutectic Sn-Pb alloy. This indicates the possibility of using the conventional production infrastructures and electronic components with minor, or even no, modifications [51].

The eutectic Sn-Zn microstructure consists of two phases: β-Sn matrix phase and a secondary phase of hexagonal Zn containing less than 1% Sn in solid solution (see equilibrium phase diagram, Figure 3-7). The solidified microstructure exhibits large

[1] Reprinted with permission from ASM International. T. B. Massalski, H. Okamoto, P. R. Subramanian and L. Kacprzak, ASM Binary Alloy Phase Diagrams. Copyright (1996), ASM International.

grains with a fine uniform two-phase eutectic constituent. Compared to the Pb-Zn system, in the Sn-Zn system, both Sn and Zn interact with Cu to form intermetallic phases. However, in spite of the attractive features of Sn-Zn alloys, their poor oxidation resistance and poor compatibility with Cu substrate under high-temperature conditions are two major problems [67].

Figure 3-7 Sn-Zn equilibrium thermal phase diagram [57][1].

3.4.6 Other Lead-Free Alternatives

Amongst the studies of other lead-free solder alloys, one main category includes the doping with rare earth metals (REs) into Sn-based alloys. REs are well recognised as surface-active agents. From the available research results, the benefit of rare earth elements has many forms. Rare earth elements were found to dramatically increase the wetting property of solder, even expanding the usability of solder to ceramic surfaces. This ability is critical to lead-free solder materials because it is commonly recognised that lead-free solder has poor wetting ability compared to Sn-Pb solders. Another benefit of doping REs is to reduce the intermetallic compound growth on solder/pad interfaces. More benefits include refining the microstructure of solders and

[1] Reprinted with permission from ASM International. T. B. Massalski, H. Okamoto, P. R. Subramanian and L. Kacprzak, ASM Binary Alloy Phase Diagrams. Copyright (1996), ASM International.

thus improving the mechanical properties of the solder material and the reliability of solder joints [68, 69].

3.5 Summary

In this chapter, worldwide legislation restricting the usage of conventional Sn-Pb solders in electronic and electrical products is firstly introduced. The criteria for the development of lead-free alternative solder alloys are also outlined. As promising candidates for different applications, binary lead-free alloys such as Sn-Ag, Sn-Cu, Sn-Bi, Sn-Zn and ternary alloys such as the most promising Sn-Ag-Cu alloy family are elaborated using equilibrium phase diagrams. Information on other lead-free alloys, such as rare earth elements containing ones, are also briefly outlined.

Chapter 4

Electrodeposition of Lead-Free Solder Alloys

As electrochemical process technologies have been increasingly making an impact on different areas in electronic packaging, the electrodeposition of lead-free solder alloys, such as Sn-Ag, Sn-Cu and Sn-Ag-Cu has seen significant developments in recent years. In this chapter, the electrodeposition technology is briefly introduced. Critical parameters in this technology are discussed as to their effects on the electrodeposition process. Recent developments regarding the electrodeposition of tin based lead-free solder alloys are summarised and compared.

4.1 General Principles of Electrodeposition

Through the application of electric current, electrodeposition is an electrochemical process of producing metallic coatings or films on a conductive surface. There are four main components consisting an electrodeposition system: cathode, anode, power source and electroplating solution. A typical electroplating bath arrangement is shown in Figure 4-1. In electronics applications, various kinds of metal (e.g. Cu, Ni, Sn, Ag) are deposited on substrates (e.g. Si wafer, metal plate and PCB) with an electrical power source and electrochemical reactions occurring in the electrolyte and at the cathode surface. It is such a versatile technique that there has been an upsurge of interests in this area with the sharp growth of the microelectronics industry.

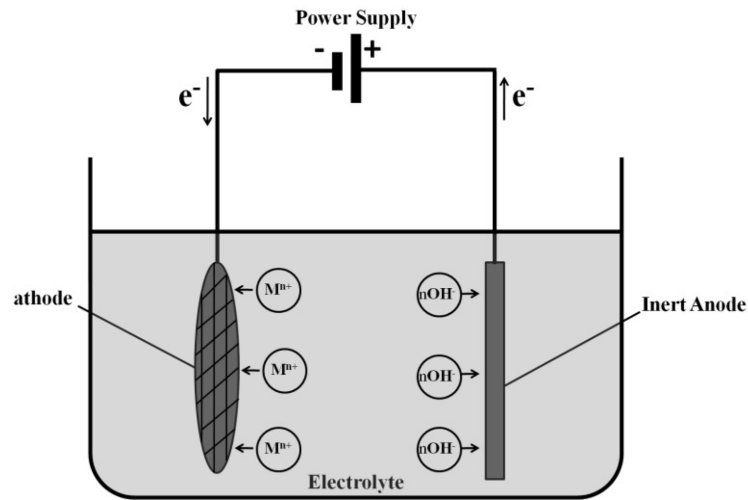

Figure 4-1 A schematic illustration of an electrodeposition system.

Electrodeposition onto the substrate, e.g. a wafer, is employed by immersing a normally inert metal, such as platinised titanium, as the non-consumable anode (consumable anodes are also commonly seen in other applications) and a wafer as the cathode in the bath with electrolyte, which contains ions of the metal to be deposited, e.g. tin and silver ions for the electrodeposition of Sn-Ag solder alloys. The electrical power is then connected to the anode and cathode and the electrical path is formed in the aqueous-metal system. This electrical path and the electrochemical reactions in the solution cause the deposits to grow on the cathode surface. On the cathodic side, metal ions (M^{n+}) are supplied by the bath solution and these ions are driven toward the cathode where the electric current supplies electrons (ne^-), the metal ions are reduced to the metallic form [70]. The reaction is sustained by a continuous supply of electrons and M^{n+} ions at the electrode surface and can be visualised in Equation 4-1. M^{n+} ions are transported to the electrode through mechanisms of diffusion, convection of the electrolyte and electro-migration. Anodic reactions for non-consumable anodes are shown in Equations 4-2 and 4-3.

Cathodic reaction:

$$M^{n+} + ne^- \leftrightarrow M \qquad \text{Equation 4-1}$$

Anodic reaction:

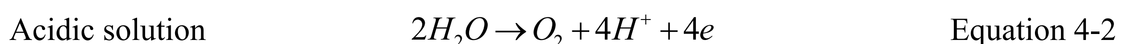

Acidic solution $$2H_2O \rightarrow O_2 + 4H^+ + 4e \qquad \text{Equation 4-2}$$

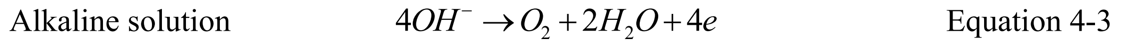

Alkaline solution $4OH^- \rightarrow O_2 + 2H_2O + 4e$ Equation 4-3

As shown in Equations 4-2 and 4-3, on the anodic side, an oxidation reaction occurs that balances the current flow, thus maintaining electrical neutrality in the solution. In the absence of any secondary reactions, the current delivered to a conductive surface during electrodeposition is directly proportional to the quantity of metal deposited (according to Faraday's law). Using this relationship, the mass (therefore the thickness of coating) deposited can be readily controlled through variations of deposition current and time.

4.2 Alloy Electrodeposition

It is known that a metallic electrode can only have one single metal-solution potential at any one time. By definition, the electrodeposition of an alloy requires the co-deposition of two or more metals. In other words, their ions must be present in an electrolyte that provides a “cathode film” where the individual deposition potential can be made to be close or even the same [71]. Table 4-1 shows the electrochemical potentials of common metals in solder alloys versus the Standard Hydrogen Electrode (SHE).

Table 4-1 Electrochemical potentials of common metals found in solder alloys at unit molal activity versus SHE, summarised from [72][1]

Metal / Ion Couple	Standard Electrode Potential versus SHE, E^{θ} (V), 25 °C
Zn/Zn^{2+}	-0.763
Cr/Cr^{3+}	-0.740
In/In^{3+}	-0.342
Ni/Ni^{2+}	-0.250
Sn/Sn^{2+}	-0.136
Pb/ Pb^{2+}	-0.126

[1] Data in the table is summarised from the reference.

$H_2/2H^+$	0.000
Bi/Bi^{3+}	+0.308
Cu/Cu^{2+}	+0.337
Ag/Ag^+	+0.799

As shown in Table 4-1, for the metals of Sn, Ag and Cu extensively used in lead-free solders, the standard potentials of Sn and Cu are widely separated, as large as 0.473V. This gap between Sn and Ag (0.935V) is almost twice as that of Sn and Cu. To electrodeposit the conventional Sn-Pb solder alloy, the potentials of Sn (-0.136V) and Pb (-0.126V) are very close. However, such a potential difference between Sn, Ag and Cu has made it difficult to co-deposit binary Sn-Ag and Sn-Cu alloys, as well as the ternary Sn-Ag-Cu alloy. Nevertheless, one of the prerequisites for alloy electrodeposition is that the deposition potentials of the metal components of the alloy lie close together. It is therefore important to use an electrolyte formulation such that the deposition potentials are as close together as possible. Otherwise, deposition of the most positive metal occurs first, e.g. Ag in a Sn-Ag electrodeposition bath and Cu in Sn-Cu. As the potential becomes more cathodic, the second metal, e.g. Sn, would then begin to deposit, as Figure 4-2 shows [73].

However, this more cathodic potential can only be reached after exceeding the diffusion limiting current density of the first. Under such conditions, an alloy will be deposited with the amount of the more noble component (Ag or Cu) determined by the level of its limiting current density. In situations where the more noble components are constituting a significant part of the deposit, it is of little practical importance since metal deposition at or close to limiting current density is normally characterised by rather rough, powdery or dendritic morphologies. However, if under precise control, this can be acceptable for the electrodeposition of eutectic/near-eutectic lead-free solder alloys, such as Sn-Ag, Sn-Cu and Sn-Ag-Cu, where the more noble components (Ag or Cu) are typically less than 5wt.%.

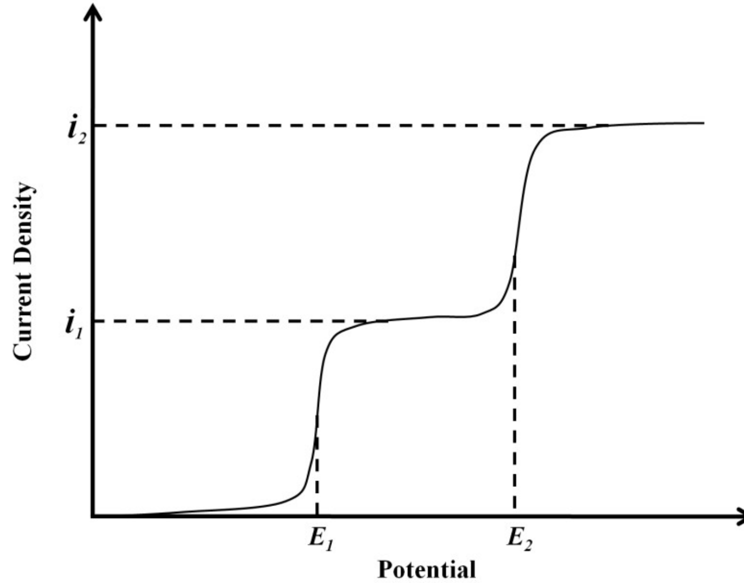

Figure 4-2 Schematic representation of current-potential relationship during alloy deposition: E_1, the deposition potential of the more noble metal; E_2, the deposition potential of the less noble metal; i_1, the limiting current density of the more noble metal; i_2, the limiting current density of the less noble metal [73][1].

In order to bring the deposition potentials of component metals closer, complexing agents are commonly introduced for alloy co-deposition to reduce the activity of the more noble metal, as given by the Nernst equation:

$$E = E^{\theta} + \frac{RT}{zF} \ln a(M^{z+}) \qquad \text{Equation 4-4}$$

Where, E is the deposition potential of the M^{z+}/M electrode in the electroplating bath (V); E^{θ} is the standard potential of the M^{z+}/M electrode (V); R is the gas constant (8.314 J mol^{-1} K^{-1}); T is the absolute temperature; z is the number of electrons involved in the deposition reaction; F is Faraday's constant (96485 C mol^{-1}). The activity of the ion, $a(M^{z+})$, is defined by

$$\alpha(M^{z+}) = \gamma c(M^{z+}) \qquad \text{Equation 4-5}$$

Where, $c(M^{z+})$ is the concentration of M^{z+} (mol/L); γ is the activity coefficient of M^{z+}.

[1] Diagram redrawn from the reference.

In simple (non-complexed) solutions, it can be assumed that the activity of a metal ion, $a(M^{z+})$, is approximately equal to its concentration, $c(M^{z+})$. However, when the complexing takes place, the activity of the metal ion may be decreased by several orders of magnitude, depending on the strength of the bonding in the complex. Therefore, the deposition potentials of the targeted alloy components can be changed and consequently brought closer together [73].

4.3 Electrodeposition Parameters

In an electrodeposition system, apart from the four main components previously discussed (cathode, anode, power source and electrolyte), there are other key parameters that might also be major factors during the electrodeposition process in achieving high-quality electrodeposits. As the electrodeposition bath is readily prepared, modifications to such process parameters as bath temperature, agitation and current density can potentially enhance the process to achieve improved electrodeposits and have a strong influence on the composition and morphology of an alloy deposit, e.g. the contents of Ag and Cu minorities in the Sn-Ag, Sn-Cu and Sn-Ag-Cu alloys in the present study. Figure 4-3 shows the general relationships between the process variables and the content of the more noble metal in the deposits.

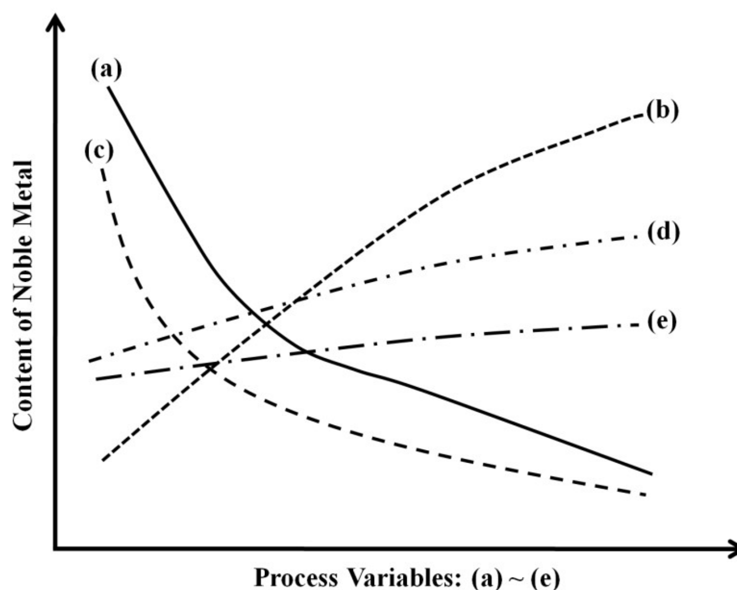

Figure 4-3 General relationship between content of more noble metal in the electrodeposit and

electroplating parameters: (a) current density, (b) more noble metal concentration, (c) additive concentration, (d) cathode agitation and (e) temperature [74][1].

4.3.1 Temperature

Bath temperature for electrodeposition can typically vary from room temperature up to approximately 80°C, depending on specific requirements. Increased electrolyte temperature results in a higher mass transportation rate in the system. This will improve ion supply to the cathode surface and as a result, higher electrodeposition rates are normally achieved. However, concurrent with the enhanced deposition rates, the microstructure of the electrodeposit could be altered in the meantime, e.g. the size of grains. Therefore, the bath temperature has to be determined by considering all the relevant parameters and requirements as a whole.

4.3.2 Agitation

To keep the electrodeposition process proceeding, mass transport must be available to continuously convey metal ions (e.g. Sn^{2+}, Ag^{+}) from the bulk of the electrolyte to the cathode surface. Figure 4-4 illustrates the double-layer metal-solution interfacial region. Three distinct mass transport processes operate in this region: diffusion, convection and electromigration, with convection of the most practical significance.

As illustrated in Figure 4-4, adjacent to the inner-layer is the diffuse double layer. Transport of reactants to the electrode through the bulk of solution is predominantly by convection. Once the species reach the outer edge of the diffuse layer, diffusion becomes the main transport process. If the electrolyte is relatively immobile, without agitation for example, convection acts little effect as a mass transport mechanism across the double layer. During the electrodeposition process, once the consuming and supplying of metal cations is balanced, the limiting current density is defined. Therefore, depending on the applications, it is important and useful to enhance the mass transport through the diffuse double layer by means of agitations [75].

---

[1] Diagram redrawn from the reference.

Figure 4-4 Idealised representation of the electrochemical double layer at the metal-solution interface [73][1].

Amongst various ways of agitation, magnetic stirring is popular for bench size process but rudimentary, because it does not provide controlled hydrodynamic conditions at the cathode surface. Ultrasonic [76, 77], even megasonic [78] agitation have been widely explored to effectively enhance mass transport during the deposition process and improve the deposition rate and properties of electrodeposits in some applications. For more precise control, proper tools and apparatus, such as rotating disk electrode (RDE) and rotating cylinder electrode (RCE) jigs, have to be designed for dedicated applications to ensure uniform current density and equalised agitation [79].

4.3.3 Current Density

Current density applied during the electrodeposition process has the direct influence on the deposition rate, as well as the composition and properties of the resultant electrodeposits. Each current density is associated with a corresponding driving potential applied at the cathode provided by the external power source. In cases of electrodeposition in features such as recesses or vias, insufficient current density could result in poor coverage of the area, whilst approaching or exceeding the limiting

[1] Reprinted with permission from Eugen G.Leuze Publishers. M. Jordan, The Electrodeposition of Tin and its Alloys, p. 22. Copyright (1995), Eugen G.Leuze Publishers.

current density, nodular or dendritic electrodeposits are typical with concurrent hydrogen evolution.

4.4 Electrodeposition Baths

The electrodeposition of tin and tin alloys has been widely explored for many years due to their extensive applications. Amongst previous investigations, fluoborate based baths have been widely explored. Tam *et al* [80] investigated the kinetics of Sn-Pb alloy electrodeposition from fluoborate baths and the use of peptone as an additive to improve the properties of the deposits. Kohl *et al* [81] examined other additives agents including lactones to improve the stability of the bath and increased the deposition rate significantly. However, as the awareness of environmental issues increased, these toxic and highly corrosive fluoborate baths have been gradually phased out by environmental regulations and initiatives. Consequently, investigations to explore environmentally friendly replacements have led to a variety of benign baths for tin and tin alloy electrodeposition. Amongst them, methanesulphonate and pyrophosphate based baths have been attractive because of their distinct characteristics.

4.4.1 Methanesulphonate Bath

Tin and tin alloy electrodeposition have been commonly conducted recently from an acidic methanesulphonate solution containing methanesulphonic acid (MSA), CH_3SO_3H (chemical structure shown in Figure 4-5). This methanesulphonate based bath has such merits as significant metal salt solubility, non-toxicity, low corrosivity and excellent biodegradability, compared to the fluoborate bath previously mentioned [82].

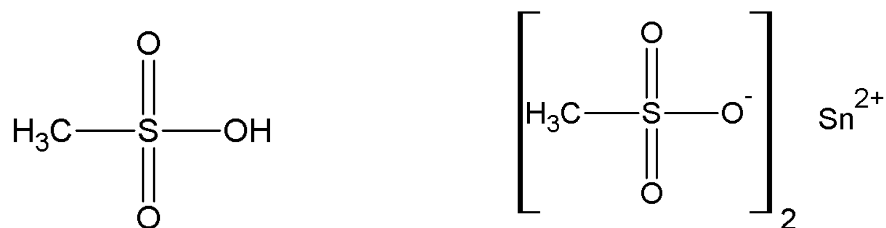

Figure 4-5 Schematic chemical structure of methanesulphonic acid (left) and tin methanesulphonate (right).

Before worldwide lead-free legislation in electronics, methanesulphonate electrolytes used to be employed for conventional Sn-Pb solder alloy electrodeposition. A general investigation was conducted by Rosenstein *et al* on several kinds of methanesulphonate based baths [83]. As the kinetics for tin and lead deposition from methanesulphonate baths is rapid, the electrodeposits tend to be needles and dendrites and therefore, additives are useful constituents in the baths to inhibit the deposition reactions and control the properties of the electrodeposits including the composition. Goodenough and Whitlaw examined the effects of typical organic additives in methanesulphonic acid and explored their roles and mechanisms in methanesulphonate baths using cathodic polarisation trials [84].

Figure 4-6 Sn-Cu electrodeposit characterisation from methanesulphonic acid electrolyte in terms of surface microstructure. The deposit structural phases: (1) 100wt.% Sn: tetragonal; (2) 100wt.% Cu: cubic; (3) Sn-65wt.%Cu: orthorhombic Cu-Sn and (4) Sn-4wt.%Cu contains two phases: tetragonal Sn

and hexagonal Cu_6Sn_5 [85][1].

Amongst other investigations for tin and tin alloy electrodeposition from methanesulphonic acid electrolytes, Low *et al* studied the electrodeposition of Sn-Cu alloys of different compositions from methanesulphonic acid electrolytes containing a perfluorinated cationic surfactant. Cu contents in the electrodeposits ranging from 3wt.% to 80wt.% was achieved in their studies. The surface morphology changes over such a wide range of copper contents in the deposits are shown in Figure 4-6 [85, 86].

Figure 4-7 Cathodic potentiodynamic polarisation curves showing the effects of additives. (a) the

[1] Reprinted with permission from Elsevier. C. T. J. Low and F. C. Walsh, Electrodeposition of tin, copper and tin-copper alloys from a methanesulfonic acid electrolyte containing a perfluorinated cationic surfactant. Surface and Coatings Technology, 2008. 202 (8): p. 1339-1349. Copyright (2000), Elsevier.

suppression of the cathodic current; (b) inhibition effects for stannous reduction [87][1].

Martyak *et al* studied the effects of additives through electrochemical characterisations, such as cathodic potentiodynamic polarisation curves with results shown in Figure 4-7. Without additives, the tin deposition process is diffusion controlled with concurrent hydrogen evolution, owing to which the deposits are normally rough [87]. It was found that the addition of polyethylene glycol (PEG) suppressed the hydrogen evolution reaction whilst showing little effect on the mechanism of the tin ion reduction process and the deposit microstructure. Polypropylene glycol (PPG) enhanced the tin deposition process and helped to achieve a smoother tin film. With further addition of phenolphthalein into the electrolyte already including the previous two glycol additives, the tin deposition process became kinetically-controlled and a smooth matte tin deposit was produced. Figure 4-8 shows the morphological features of the electrodeposits with the addition of additives at different current densities.

Figure 4-8 The morphologies of tin electrodeposits produced at two different current densities under the effect of additives. (a) no additives; (b) morphology of deposits under the effect of PEG; (c) grain

[1] Reprinted with permission from Elsevier. N. M. Martyak and R. Seefeldt, Additive-effects during plating in acid tin methanesulfonate electrolytes. Electrochimica Acta, 2004. 49 (25): p. 4303-4311. Copyright (2000), Elsevier.

refining effects through the addition of PPG; (d) smooth surface from the addition of all the three additives [87][1].

Joseph *et al* developed a methanesulphonate based electrolyte for the electrodeposition of ternary Sn-Ag-Cu solder alloy as a lead-free alternative to conventional Sn-Pb solders [88]. The constituents of the bath are outlined in Table 4-2. $Sn(CH_3SO_3)_2$, $CuSO_4$ and Ag_2SO_4 were used as the sources of cations in the electrolyte. Thiourea acted as the complexing agent mainly for Cu^{2+} and Ag^{+}. The OPPE (iso-octyl phenoxy polyethoxy ethanol), also known as Triton X-100, was used as a surfactant to improve the microstructure of the deposits. As a result, a near eutectic Sn-Ag-Cu film of grain size of 6–8 μm was produced under the effects of Triton X-100.

Table 4-2 Electrolyte composition for the electrodeposition of Sn-Ag-Cu alloys from a methanesulphonate based bath [88][2]

[1] Reprinted with permission from Elsevier. N. M. Martyak and R. Seefeldt, Additive-effects during plating in acid tin methanesulfonate electrolytes. Electrochimica Acta, 2004. 49 (25): p. 4303-4311. Copyright (2000), Elsevier.
[2] Table summarised from the reference.

4.4.2 Pyrophosphate Bath

Due to the principle advantages including the non-toxic nature, long stability and low metal ion concentration owing to complex formation, tin and tin alloy electroplating using pyrophosphate based electrolytes has also seen developments over many years. Good throwing power is another merit pyrophosphate baths exhibits as they have been widely used for "through-hole" electrodeposition. This also makes the bath particularly attractive for wafer level fine pitch solder bumping application, where small holes are filled with solder electrodeposits [89].

In Beattie *et al*'s study, binary $Cu_{1-x}Sn_x$ alloys were produced from a single bath consisting of 36 g/L $Sn_2P_2O_7$, 135 g/L $K_4P_2O_7$, 1 g/L $Cu_2P_2O_7 \cdot 3H_2O$ [90]. Although the investigations were primarily for applications in Li-ion cells, the potential application of electroplating Sn-Cu solder alloys also exists. The mechanism of nucleation and growth of Sn-Cu alloy coatings from pyrophosphate baths was studied through cyclic voltammetry and chronoamperometry by Correia *et al* [91]. In their studies, voltammetric results displayed only one oxidation peak for tin and two for Sn-Cu alloys. The reduction processes were found to be diffusion controlled from the sweep rate dependence in voltammograms.

The use of pyrophosphate electrolytes to electrodeposit lead-free solder alloys and bumps has been carried out by a few research groups. Neveu *et al* achieved near eutectic Sn-Ag alloys (Sn-3.5wt.%Ag) using pyrophosphate-iodide electroplating baths under both direct and pulsed current conditions [92]. The effects of additives, including triethanolamine, Triton X-100, sorbitol, sodium gluconate and 1,4-hydroxybenzene, have also been examined through cathodic polarisation data. To varying extents, all of them suppressed the dendritic Sn-Ag growth. Table 4-3 lists the bath compositions in the investigations.

Table 4-3 Electrolyte constituents for the electrodeposition of Sn-Ag alloys from pyrophosphate-iodide based baths [92][1]

With the absence of additives, as shown in Figure 4-9, it was found in Neveu *et al*'s studies that although of roughly the same composition, the morphology of Sn-Ag electrodeposits varied largely from a fine grained structure to well-defined crystals about 2–5 μm in size, until finally dendrites dominated as the current density increased.

[1] Table summarised from the reference.

Figure 4-9 Micrographs of Sn-3.5wt.% Ag alloys electrodeposited at different current densities: (A) 0.1 A/dm^2, (B) 0.2 A/dm^2, (C) 0.5 A/dm^2, (D) 1.0 A/dm^2, (E) 1.2 A/dm^2 and (F) 1.5 A/dm^2 [92][1].

Arai's *et al* have applied the pyrophosphate-iodide based systems to produce near-eutectic Sn-Ag solder bumps at the wafer level through photolithography [93]. Both straight-walled bumps and mushroom bumps were formed under galvanostatic and potentiostatic conditions, as shown in

Figure 4-10. It was found that under potentiostatic conditions (

[1] Reprinted with permission from Elsevier. B. Neveu, F. Lallemand, G. Poupon and Z. Mekhalif, Electrodeposition of Pb-free Sn alloys in pulsed current. Applied Surface Science, 2006. 252 (10): p. 3561-3573. Copyright (2000), Elsevier.

Figure 4-10, image (a)), even if the surface area of the cathode was changed, because the cathodic potential stayed the same, the caps of the mushroom bumps had smooth and uniform surfaces. However, rough surfaces appeared under galvanostatic conditions as the current density was changed with the varying cathode area of the caps.

Figure 4-10 SEM images of fabricated near-eutectic Sn-Ag solder bumps under potentiostatic (a) galvanostatic and (b) conditions from a pyrophosphate-iodide bath [93][1].

Figure 4-11 shows cross-sectional electron probe microanalysis (EPMA) data for mushroom Sn-Ag solder bumps under both galvanostatic and potentiostatic conditions. It is demonstrated in this figure that under galvanostatic conditions, the cap of the bump contains more Ag than the part grown within the confines of the pattern. This is owing to a decrease in the current density as the top of the mushroom bumps grow into a cap, resulting in a shift in the cathodic potential. However, under potentiostatic conditions, Ag is distributed uniformly throughout the bumps according to Figure 4-11. This is due to the fixed potential throughout the deposition process regardless of the change in cathode surface area. Therefore, it reveals that potentiostatic conditions can help to achieve a uniform compositional microstructure of the bump.

[1] Reprinted with permission from The Electrochemical Society. S. Arai, H. Akatsuka and N. Kaneko, Sn-Ag Solder Bump Formation for Flip-Chip Bonding by Electroplating. Journal of The Electrochemical Society, 2003. 150 (10): p. C730-C734. Copyright (2000), The Electrochemical Society.

Figure 4-11 EPMA cross-sectional analysis of Sn-Ag mushroom bumps obtained under galvanostatic and potentiostatic conditions from a pyrophosphate-iodide bath [93][1].

4.4.3 Electrolyte Stability

Electrolyte stability has been a universal and inevitable problem for the electrodeposition of tin and tin alloys. In aqueous systems, Sn^{2+} ions tend to be oxidised to Sn^{4+} by the atmospheric oxygen (Equations 4-6 and 4-7) to form tetravalent tin compounds which are more stable than the divalent ones. This will result in the loss of Sn^{2+} ions which are the source of tin in the electrodeposits and consequently undermine the efficiency of the electrolytes and increase the cost of chemicals. Meanwhile, owing to this undesirable oxidation reaction, insoluble products normally form and exist as a sludge in the bath and consequently deteriorate the properties of the electroplating bath.

Acidic electrolyte: $2Sn^{2+} + O_2 + 4H^+ \rightarrow 2Sn^{4+} + 2H_2O$ Equation 4-6

[1] Reprinted with permission from The Electrochemical Society. S. Arai, H. Akatsuka and N. Kaneko, Sn-Ag Solder Bump Formation for Flip-Chip Bonding by Electroplating. Journal of The Electrochemical Society, 2003. 150 (10): p. C730-C734. Copyright (2000), The Electrochemical Society.

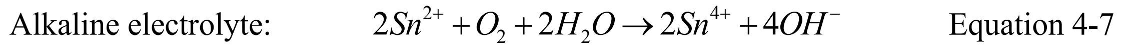

Alkaline electrolyte: $$2Sn^{2+} + O_2 + 2H_2O \rightarrow 2Sn^{4+} + 4OH^-$$ Equation 4-7

There are a few factors affecting this oxidation reaction in the electrolyte, such as the concentration of Sn^{2+} ions. From the reaction balance's point of view, it is known that the higher concentration of Sn^{2+} ions, the higher the rate of oxidation. The bath temperature also plays an important role in the reaction. Reactions are accelerated at elevated temperatures, resulting in more Sn^{2+} ions lost during the operation. Other factors affecting the oxidation include agitation and the anion types in the electrolytes.

There are even more challenges posed for the stability of electrolytes designed for tin alloy electrodeposition including copper as one of the elements, because in the presence of cupric ions, the oxidation of Sn^{2+} is catalytically accelerated, with the reaction mechanism described by Murray *et al* [94]. Cupric ions can be reduced into monovalent copper by the divalent tin, whilst the monovalent copper is re-oxidised to the divalent form by the atmospheric oxygen, with hydrogen peroxide produced as an intermediate product. Equations 4-8 and 4-9 show the mechanism in detail:

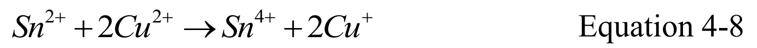

$$Sn^{2+} + 2Cu^{2+} \rightarrow Sn^{4+} + 2Cu^+$$ Equation 4-8

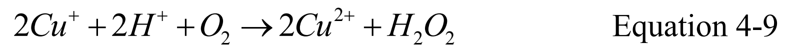

$$2Cu^+ + 2H^+ + O_2 \rightarrow 2Cu^{2+} + H_2O_2$$ Equation 4-9

With respect to the stability of methanesulphonate based electrolyte, for tin alloy electrodeposition, although the methanesulphonic acid is a reducing agent, there are still stability concerns. Joseph *et al* found that without any additives, the bath stability of methanesulphonate based electrolyte for Sn-Ag-Cu alloy electrodeposition did not extend beyond 2 hours, whilst the addition of Triton X-100 only held the bath clear for about a week as investigated [88].

Other studies have explored using hydroquinone as an antioxidant to slow down the oxidation from Sn^{2+} to Sn^{4+} and enhance the electrolyte stability, because hydroquinone can consume the oxygen dissolved in the solution as Equation 4-10 below shows [87, 95]. However, the results are still not promising.

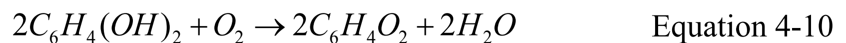

$$2C_6H_4(OH)_2 + O_2 \rightarrow 2C_6H_4O_2 + 2H_2O$$ Equation 4-10

Nevertheless, the pyrophosphate based electrolyte has been found to be of better stability than most other tin alloy electroplating electrolytes [96]. In 1984, Kubota *et al* explored tin electroplating from a bath developed by dissolving $SnCl_2$ into a solution of $K_4P_2O_7$ [97]. Potentiometric and conductimetric titration studies showed that in the complex formed, the ratio of pyrophosphate to tin was 2:1, as Equation 4-11 shows. As a result, the tin ion concentration in the electrolyte was of the order of 10^{-14} g/L. With such a low concentration, tin ions available for the oxidation reaction become very limited and owing to that, the bath stability is significantly improved.

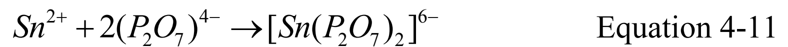

$$Sn^{2+} + 2(P_2O_7)^{4-} \rightarrow [Sn(P_2O_7)_2]^{6-} \qquad \text{Equation 4-11}$$

4.5 Summary

In summary, the general principles of electrodeposition technology, including the challenges that lie in the co-deposition of Sn, Ag and Cu as alloys, are introduced in this chapter. Due to the relatively large potential gaps between Sn/Ag and Sn/Cu, an effective complexing agent is desirable in the bath systems to achieve the co-deposition of alloys, whilst avoiding undesirable microstructures such as nodules and dendrites. Three significant parameters during the electrodeposition process, including temperature, agitation and current density, are discussed with respect to their effects on the electrodeposits. Recent advancement using methanesulphonate and pyrophosphate based bath systems to electroplate Sn-Cu, Sn-Ag and Sn-Ag-Cu alloys is summarised. With respect to the universal stability issue for tin alloy electrodeposition, pyrophosphate exceeds methanesulphonate due to its strong complexing ability, although studies have shown that the addition of antioxidants could improve the latter to some extent.

Chapter 5

Experimental Techniques

In this chapter, details of the experimental arrangements and analytical techniques utilised in this investigation are introduced.

5.1 Electrodeposition and Polarisation Trials

5.1.1 Electrodes and Pretreatment

All the electrodeposition investigations were carried out in a 500 mL beaker cell, with potential and current control via a potentiostat (PARSTAT 263(A) or 2273, Princeton Applied Research, AMETEK) and a computer. A conventional three-electrode cell configuration was used throughout. A photograph of the electroplating system arrangement is shown in Figure 5-1.

For initial investigations, copper coupons of 1 cm^2 working area, defined by chemically inert tape (3M Scotch), were used as the working electrode (cathode). During wafer bumping processes, glass or silicon wafers with surface metallisation layers were used as the cathode, more details are outlined in Section 5.3. A Pt plate (4 cm × 4 cm) was used as the counter electrode (anode). To measure the working electrode potentials, a saturated calomel electrode (SCE, +0.241 V vs. SHE at 25 °C) was used as the reference electrode, against which all electrode potentials were reported. The probe with ceramic frit, connected to the reference electrode through salt bridge, was positioned approximately 2 cm form the working electrode each time.

Prior to experimentation, copper coupon working electrodes were immersed in a 20wt.% potassium hydroxide solution for 5 min and then 30 s in a 50vol.% nitric acid (S.G. 1.51) solution. They were then rinsed thoroughly with deionised water and quickly immersed into the electroplating bath.

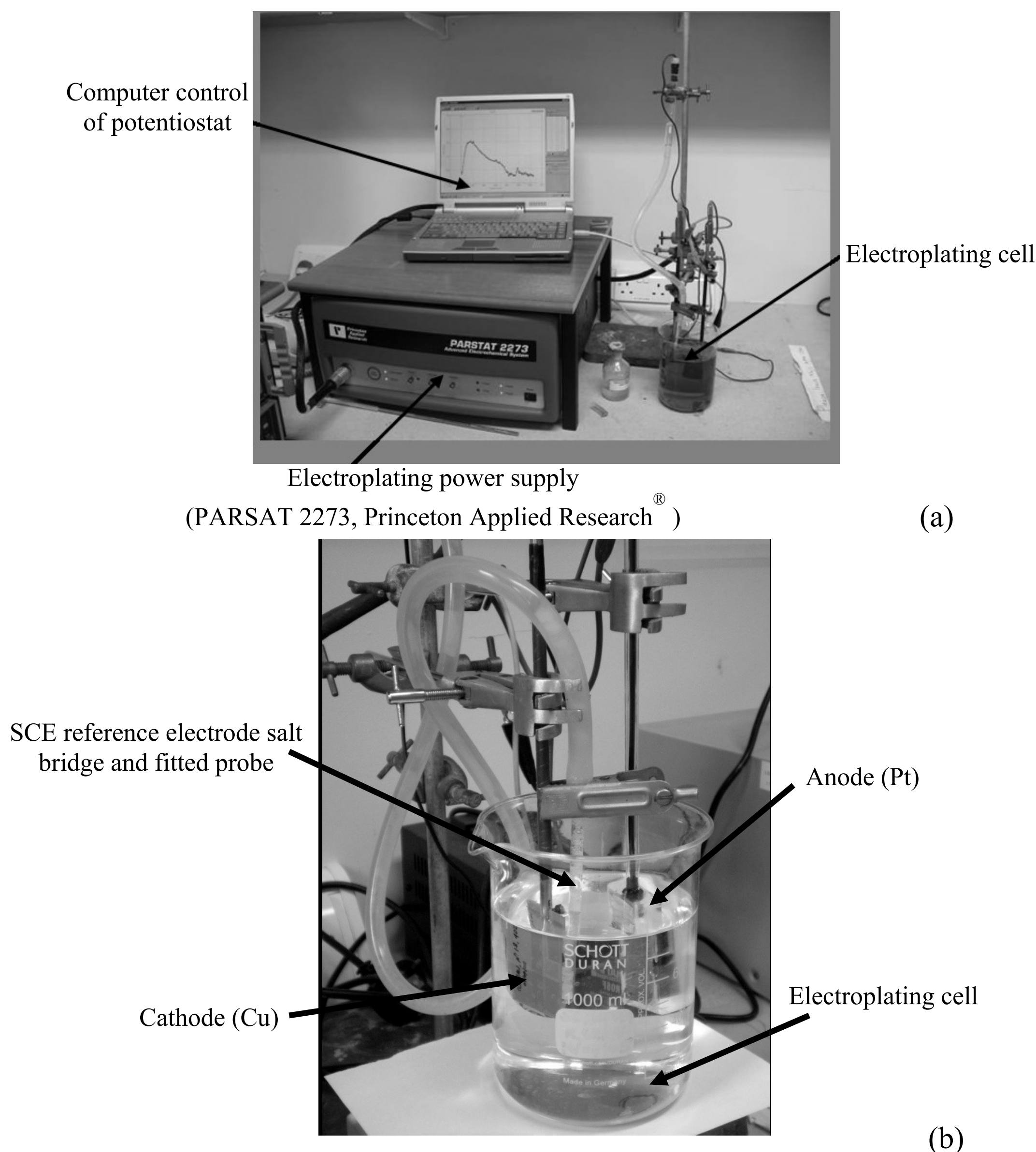

Figure 5-1 Arrangement of the electrodeposition system: (a), general view; (b), close up of the electroplating cell.

5.1.2 Agitation and Heating

Magnetic stirring was used as the method of agitation in the current study. A stirring hotplate (Fisher Scientific) with a control of agitation level (rotation rate by rpm) was utilised.

When an elevated bath temperature was required, a ~25 L water bath was used to heat up the electrolyte, maintaining a stable temperature control (±1°C).

5.1.3 Potentiodynamic Polarisation Studies

In order to elucidate the electrodeposition processes, such as the distinctive roles of chemicals and electrode reactions (indicated by the current), potentiodynamic cathodic polarisation measurements were conducted using an electrochemical system under computer control. PARSTAT 263(A) or 2273 (Princeton Applied Research, AMETEK) and Auto Tafel HP (ACM Instruments) were used for the polarisation tests.

A general cathodic potentiodynamic polarisation curve (current-potential relationship) is shown in Figure 5-2. The curve is defined by four regions: 1, linear region; 2, exponential region (Butler-Volmer exponential relationship); 3, mixed control (activation and mass transport) region; 4. limiting current density region [71]. Such a polarisation curve can be instructive for the electrodeposition process. Factors, such as temperature and agitation, also affects on the curves. The curves can, therefore, facilitate setting up the parameters required. An indication of the impact of additives on the limiting current density can also be recognised through polarisation curves.

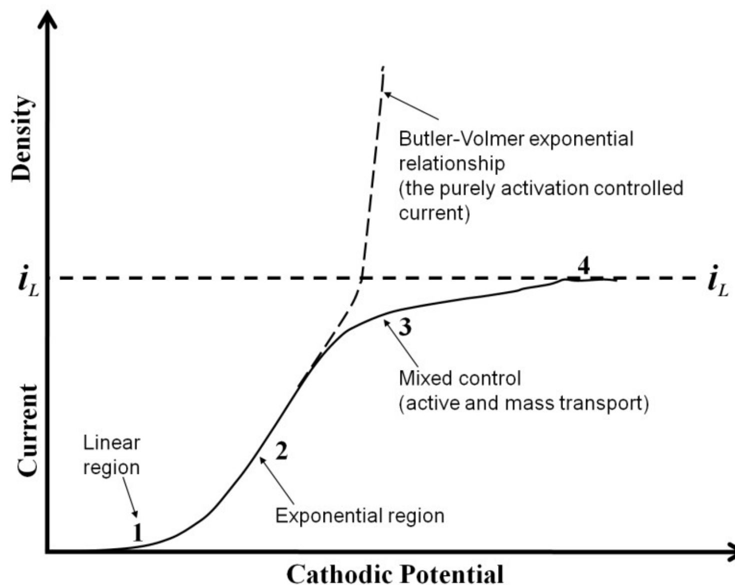

Figure 5-2 General cathodic polarisation curve [71][1].

Copper coupons used for cathodic polarisation measurements as the working electrode were prepared and pre-treated in the same manner as those for electrodeposition trials (see Section 5.1.1). Prior to each polarisation test, the copper

[1] Figure redrawn from the reference.

coupon after pretreatment, was left in the electrodeposition bath for approximately 15 minutes to stabilise. The open-circuit potential between the cathode and the reference electrode (SCE) at open circuit was recorded each time. Different sweep rates, of 1, 5 and 10 mV/s, were applied depending on the specific requirement. Scanning was conducted cathodically from the open-circuit potential until the hydrogen evolution heavily occurred. Three independent curves were recorded for each electrolyte variation and one typical curve was reported in each case. Again, all potentials are quoted versus SCE.

5.2 Bump Electrodeposition on Wafers

Figure 5-3 demonstrates the process of solder bumping process on wafers through electrodeposition, with details discussed in the following sections.

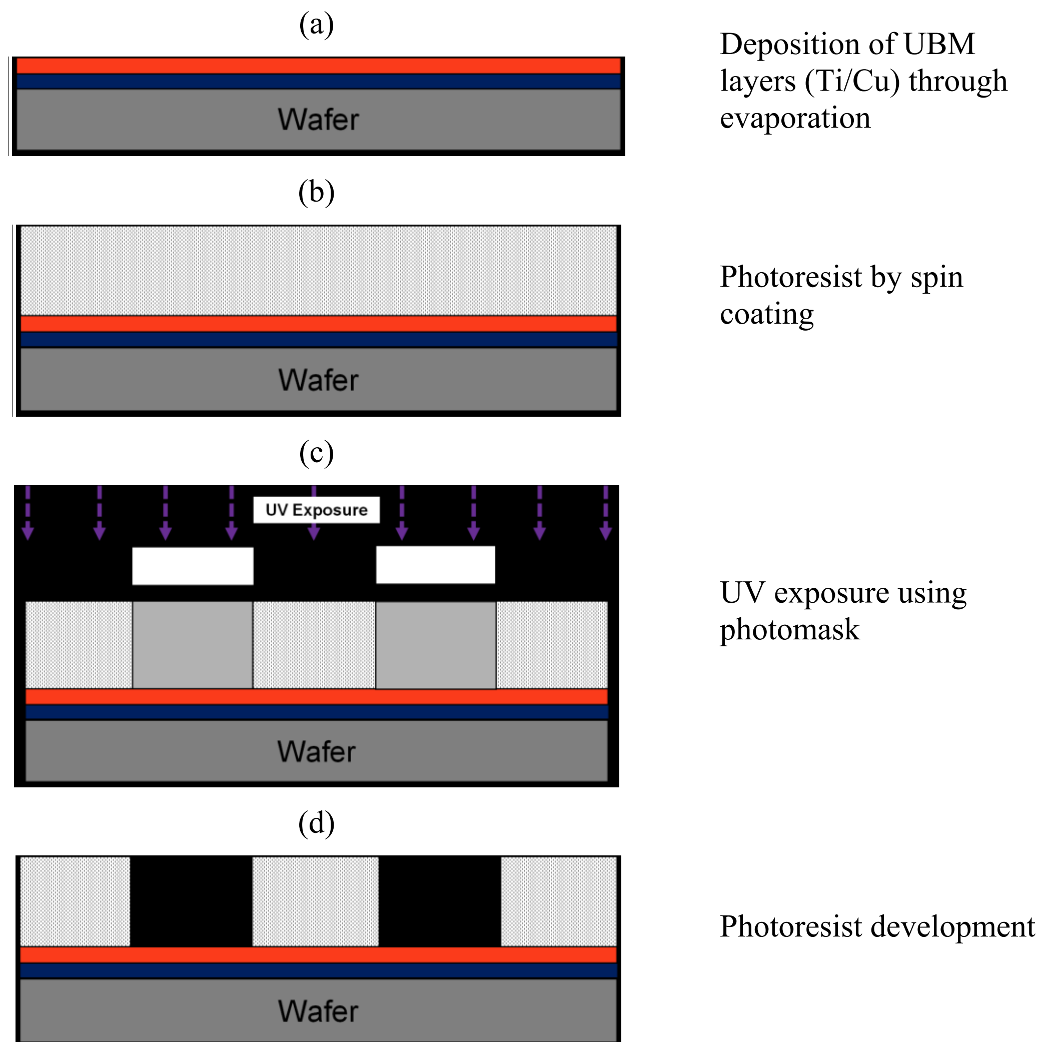

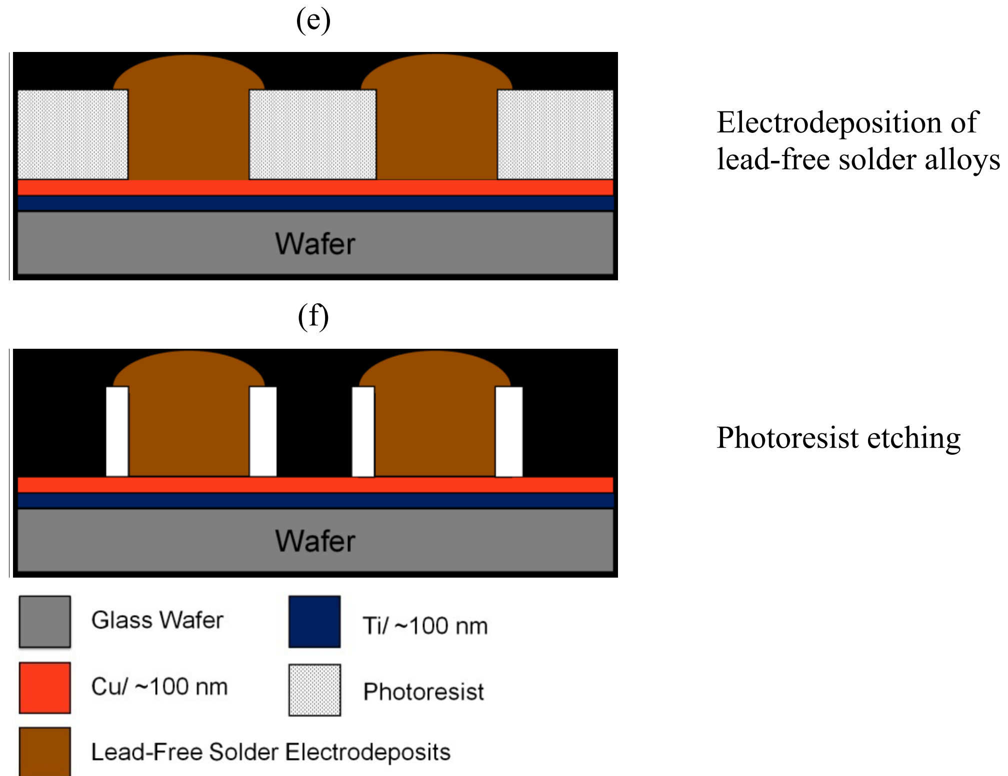

Figure 5-3 Schematic illustration of the process for the solder bumping process on wafers.

5.2.1 Test Wafer

3 inch (76.2 mm) single-crystal silicon wafers from Compart Technology Ltd and glass wafers from Chance Glass Ltd in the UK were used for the electrodeposition tests. As the current study has been focused on the bumping process at wafer level, the nature of wafer material therefore plays an less important role in the investigations as the process schematic in Figure 5-3 illustrates.

5.2.2 UBM Deposition

UBM layers were firstly deposited on the wafer as Figure 5-3 (a) shows. The main role of UBM in a solder joint has been discussed in Section 2.2.3. With respect to the solder bumping process by electrodeposition, UBM layers also serve as a conductive seed layer to enable the electrochemical reactions at the cathode surface.

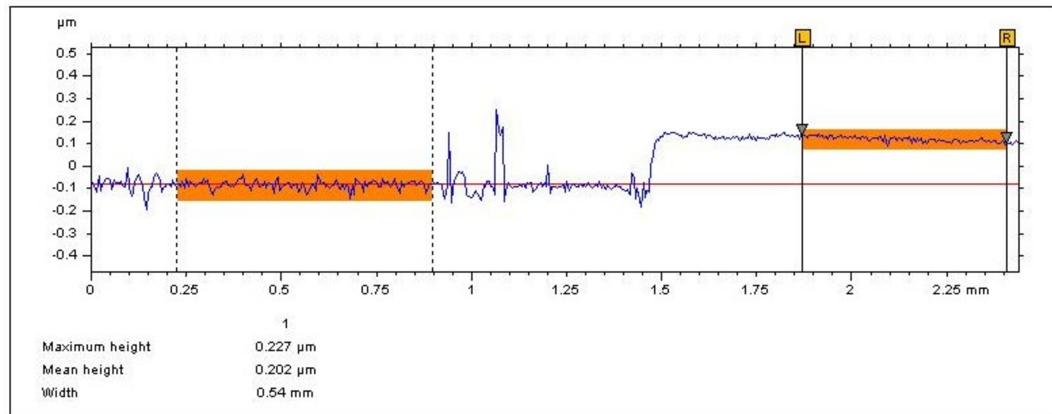

Figure 5-4 Thickness measurement of the UBM layers by Talysurf CLI 2000 3D laser scanner.

In the present study, e-beam (electron beam) evaporation technology was applied to deposit Ti and Cu sequentially, with Ti being the adhesion layer to improve the relatively poor adhesion between the seed layer (Cu) and the wafer. After placing the 3 inch wafers onto the wafer holder in the e-beam chamber, a rotary pump was firstly used and then a diffusion pump to produce a high level vacuum. When the vacuum level was down to around 2.0×10^{-5} mbar, the electron beam evaporation was performed. By focusing the electron beam on target materials (Ti or Cu), the metals evaporated into the chamber and deposited onto the glass wafers. The process was performed wafer by wafer by using a protecting wafer holder. After deposition, the chamber was left to cool and the wafers with Ti/Cu metal layers were then removed for the next processing step. Through the deposition process, Ti/Cu layers (~100 nm thick each) were produced on the wafers, with the total thickness measured at approximately 200 nm by Talysurf CLI 2000 3D laser scanner from Taylor Hobson (Figure 5-4).

5.2.3 Photoresist Patterning

As images (b)–(d) in Figure 5-3 show, photoresist patterns were produced through photolithography, which is the most widely used form of lithography to transfer patterns from masks onto the photoresist.

5.2.3.1 Photoresist Spin-Coating

Once the wafer was stabilised on the spin coater by vacuum suction, a positive AZ9260 photoresist from Clariant was dispersed smoothly onto the wafer by spinning

at: 1), 70 rpm for 20s; 2), 400 rpm for 20s; 3), 1000 rpm for 40s. After all the steps, a AZ9260 layer of ~15 μm was left on the wafer. The wafer with photoresist was then transferred onto a hotplate of 80°C for 5 minutes soft baking to remove the solvent in the photoresist film. AZ9260 photoresist was used because it was suitable for high aspect ratio structures and was easily strippable in acetone solution compared to SU-8 and other common photoresists [98].

5.2.3.2 Exposure and Development

After soft baking on the hotplate, the photoresist was exposed to UV light (hard bake) through a photomask to produce via structures. For a positive photoresist like AZ9260, the exposed area under the mask was weakened by UV light and could be etched away by developer solvent. Figure 5-5 shows the photomask pattern used in the current study. The photomask was made of soda-lime glass with chromium coating. The designed patterns included diameters of 15–25 μm and pitch sizes of 50–100 μm. A broadband mask aligner (Tamarack) was used as the UV-exposure source (365 nm wavelength UV radiation) for exposure.

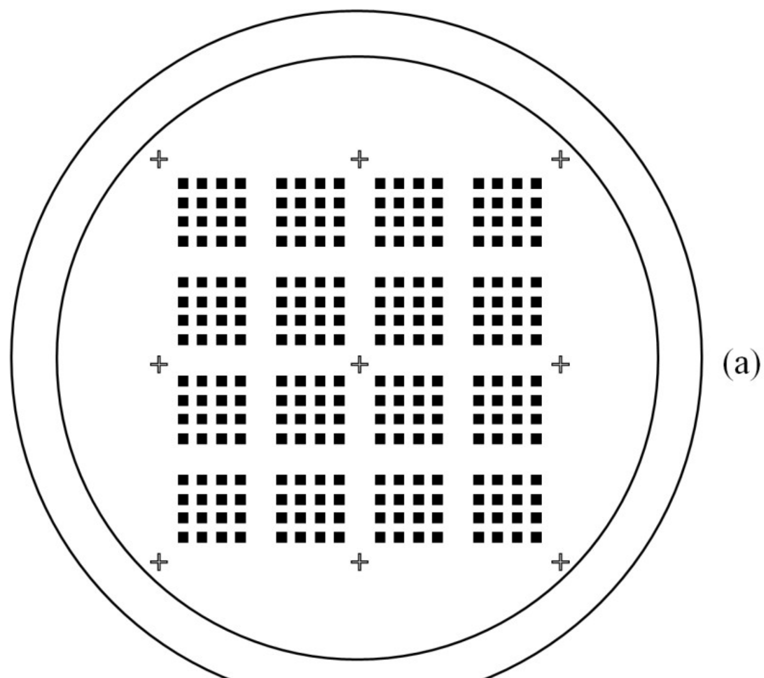

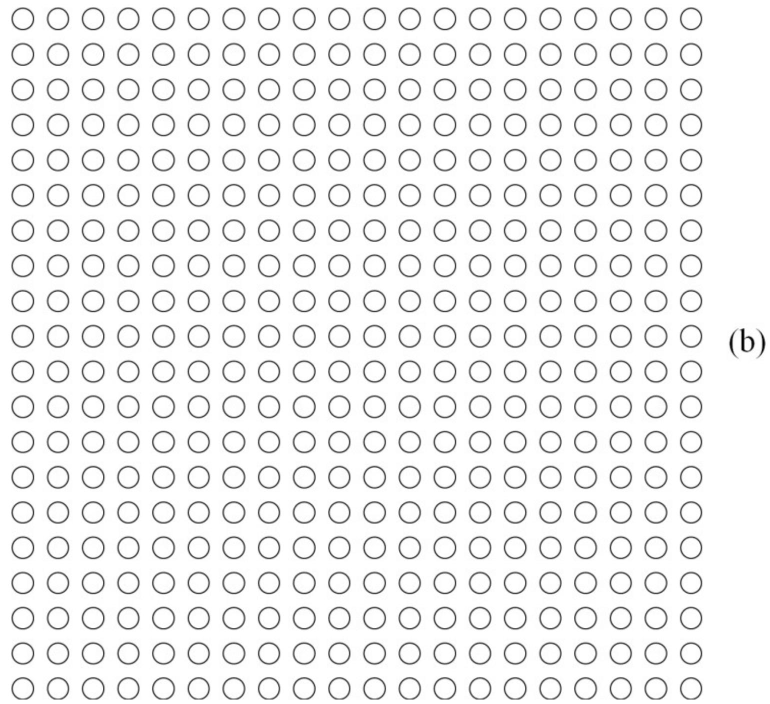

Figure 5-5 Schematic illustration of the photomask used for photoresist patterning. (a) general view of the wafer mask; (b) close up of one single block. Pattern includes diameters=15–25 µm, pitch size=50–100 µm.

After exposure the wafers were immersed into the developing solvent (AZ400K), rinsed with deionised water and blown dry with nitrogen. Figure 5-6 illustrates one wafer sample measured by Talysurf CLI 2000 3D laser scanner (Taylor Hobson), revealing the via features fabricated in the photoresist.

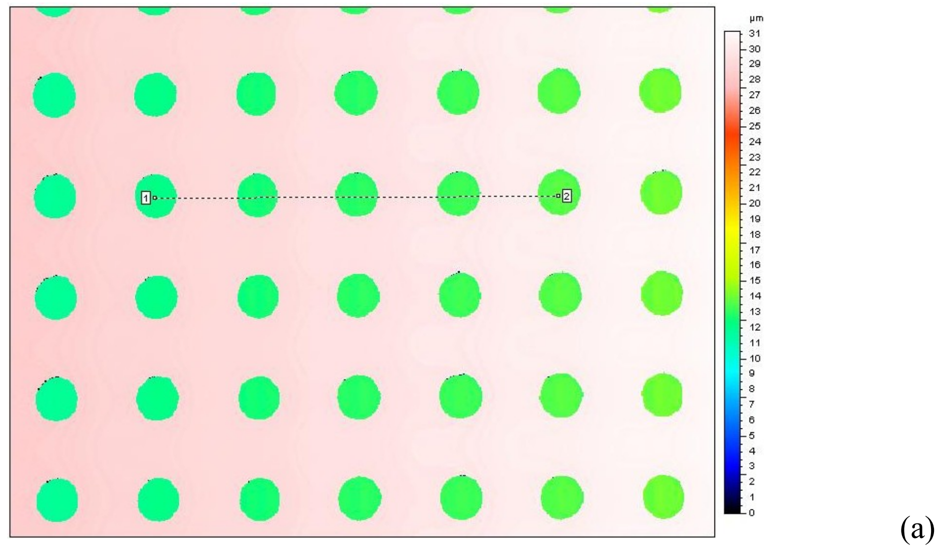

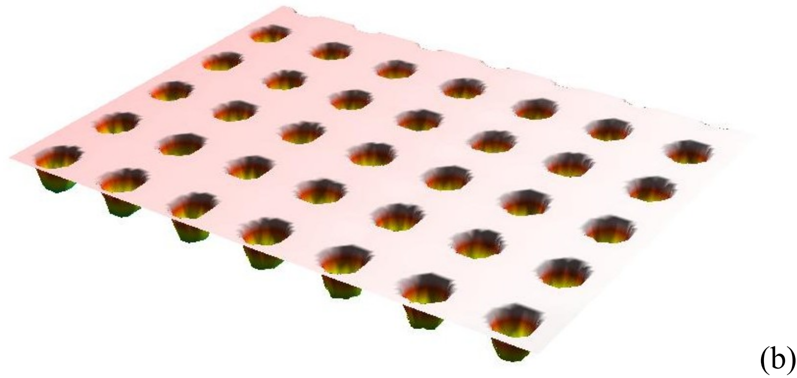

(b)

Figure 5-6 Measurements of patterned photoresist by Talysurf CLI 2000 3D laser scanner. (a) top scanning revealing a pattern of diameter=25 μm and pitch=50 μm (distance from cursor "1" to cursor "2"=100.22 μm) and average via depth=15.4 μm; (b) 3D image of the photoresist pattern after development.

5.2.4 Electrodeposition

Upon completion of the photoresist pattern on the wafer, the solder electrodeposition process was readily carried out, as Figure 5-3 (e) shows. Lead-free solder alloys, such as Sn-Ag, Sn-Cu and Sn-Ag-Cu, were electrodeposited in the via structures from specifically formulated baths. Both straight-walled and mushroom bumps could be fabricated. More details regarding this process and the resultant lead-free solder bumps are discussed in the following chapters.

5.2.5 Photoresist Etching

After the electrodeposition process, the AZ9260 photoresist was stripped off in acetone. Solder bumps were then exposed as shown in Figure 5-3 (f).

5.3 Material Characterisation

The electrodeposited lead-free solder alloys were characterised in terms of surface morphology, alloy deposit composition and microstructure respectively.

5.3.1 Surface Morphology

The surface morphology of the electrodeposits was observed using Cambridge 360 Scanning Electron Microscope (SEM), or Leo 1530VP Field Emission Gun Scanning

Electron Microscope (FEG-SEM), typically at a voltage of 10 kV. Atomic Force Microscope (AFM) was also utilised in some situations such as assessing the roughness of electrodeposits under the effects of additives, characterising not only surface morphology. AFM images were recorded in tapping mode on a Nanoscope III multimode microscope (Digital Instruments, Veeco). Measurements were performed in air using etched silicon tip cantilevers of 5–10 nm nominal curvature (RTESP, Veeco) with a resonance frequency of 247–298 kHz.

5.3.2 Composition and Phase Identification

Both Energy Dispersive X-ray spectroscopy (EDX) and Wavelength Dispersive X-ray spectroscopy (WDX) were used to measure the compositional constituents of the electrodeposits. Though EDX is more commonly applied due to its simplicity and speed and gives sensible results in most occasions, WDX is complementary to EDX in that WDX spectrometers have significantly higher spectral resolution and enhanced quantitative potential (down to parts per million levels) [99]. This is particularly useful for the current study as only small amounts of Ag or Cu are included in the lead-free solder alloys. The advantage of WDX in resolving elements with overlapping peaks in an X-ray energy dispersive spectrum also applies to the situation for Sn and Ag (characteristic X-ray lines Ag: Ag L =3.151 keV and Sn: Sn L=3.045 keV) [100].

As the melting points of an electrodeposit is closely related to its composition, thermal measurements were carried out using Differential Scanning Calorimetry (DSC 2010 TA Instruments). Samples (1–1.1 mg each time) were prepared by scraping the deposits off the copper coupons. A heating rate of 10 K/min was used throughout. Tests were carried out in a nitrogen atmosphere from room temperature to well above the melting points.

The alloy phase information for the electrodeposits was obtained by X-Ray Diffraction (XRD) from a Bruker D8 X-ray diffractometer. Sample were scanned through a 2θ angle from 20° to 100° with a step of 0.02°/s, using an X-ray source of Cu Kα radiation (λ=0.15406 nm). The spectra were analysed on the basis of a powder diffraction database from JCPDS-ICDD 2002©.

5.3.3 Microstructure

The microstructural analysis of the electrodeposits was conducted by Focused Ion Beam (FIB) micro-machining and Transmission Electron Microscopy (TEM). An FEI Nova 600 NanoLab dual beam FIB (SEM/FIB) and JEOL 2000FX TEM with EDX were used. The combination of micro-processing and the lift-out technique using the micro pickup system in the dual-beam FIB served as a powerful tool for the preparation of TEM specimens in the current study.

For cross-sectional microstructural views of the electrodeposits, samples were micro-processed using SEM/FIB to produce rectangular trenches at both sides, with a Pt protective layer deposited above (1 μm thick × 1 μm wide approximately) by chemical vapour deposition (CVD), as Figure 5-7 (a) and (b) show. This enabled the cross-sectional planes to be observed and micrographs taken. Both Secondary Electron (SE) images and Ion-Induced Secondary Electron (ISE) images were available from the SEM/FIB system. However, owing to factors including the crystal orientation, ISE images tended to deliver stronger channelling contrast in crystal structures and therefore more details could be generated in crystalline electrodeposits through ISE images [101].

To proceed the TEM sample preparation, the centre “wall” was further thinned, followed by a “U” cut, as Figure 5-7 (d) illustrates. Then the TEM sample was finally cut off the bulk electrodeposit when approached by the Omniprobe, which was used to transfer the sample to the TEM mounting grid by attaching the sample to the tip through Pt deposition, as image (e) shows. The TEM sample was then mounted on the Mo grid by repeating the steps of micro-cutting and attachment (image (f)). In the current study, instead of the commonly used Cu grid, a Mo grid was used to rule out the potential compositional interference by X-ray energy overlapping during the EDX measurements in the TEM. The scanning ion beam with low current was the final process to finally attenuate the foil down to no more than ~100 nm for electron transparency purposes (image (g)). The sample was then ready for TEM analysis.

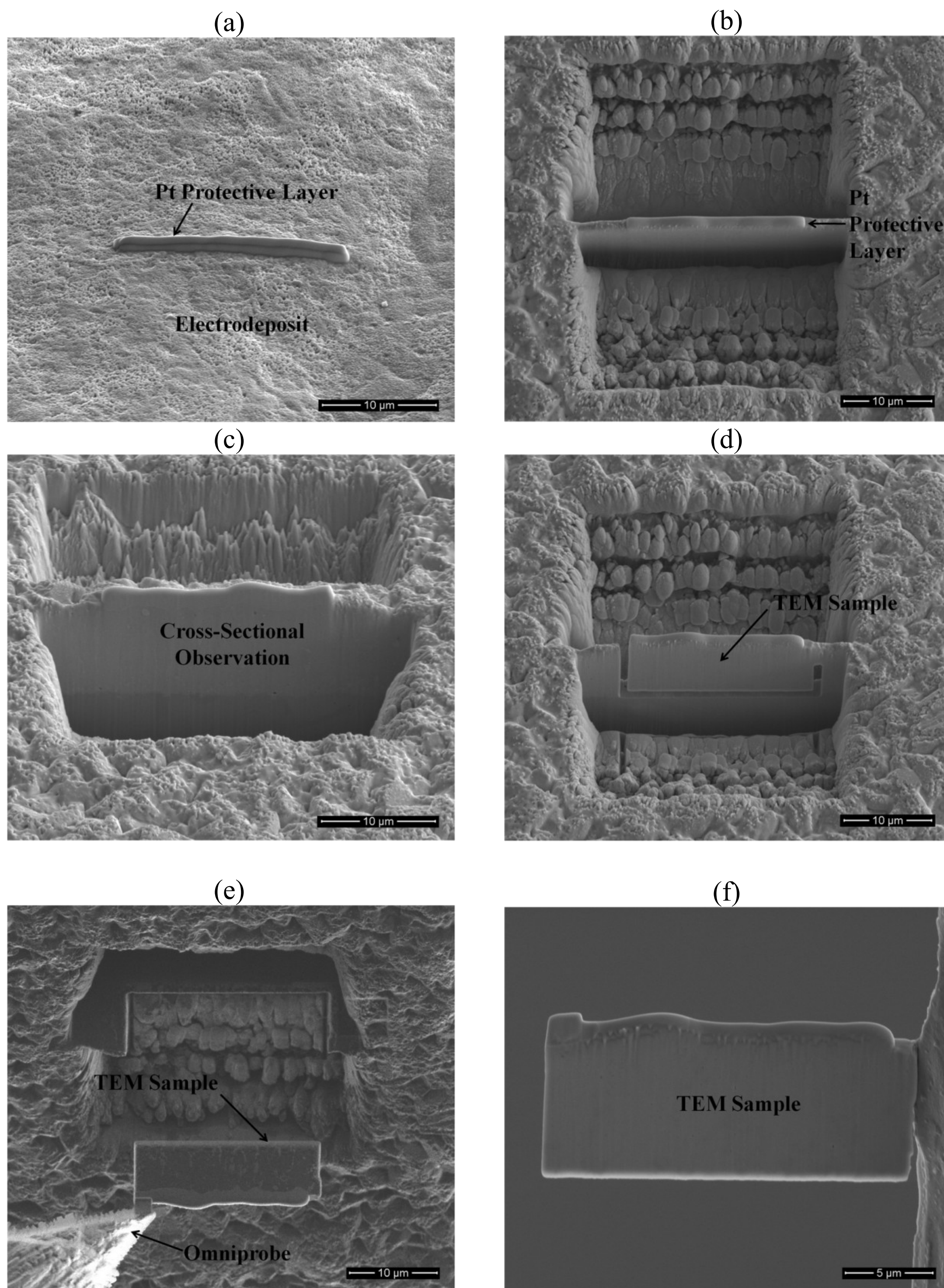
(a)
Pt Protective Layer
Electrodeposit
10 µm
(b)
Pt
Protective
Layer
10 µm
(c)
Cross-Sectional
Observation
10 µm
(d)
TEM Sample
10 µm
(e)
TEM Sample
Omniprobe
10 µm
(f)
TEM Sample
5 µm

(g)

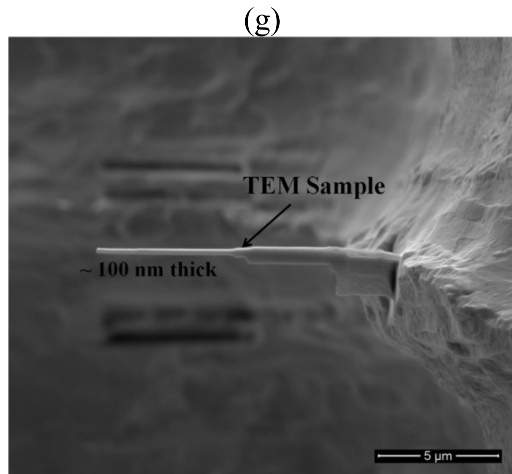

Figure 5-7 Micro-machining process by SEM/FIB for cross-sectional microstructure view and TEM sample preparation. (a) Pt layer deposited on top of the region of interest; (b-c) two rectangular trenches produced on both sides of the Pt layer for cross-sectional view and to prepare the TEM sample; (d) "U" cut of the sample to be lifted up; (e) Foil attached to the Omniprobe and lifted up; (f) Sample attached to the grid holder by Pt deposition; (g) Sample further attenuated to electron transparency.

5.4 Summary

In this chapter, the experimental arrangement of the electrodeposition system is first introduced, with details of agitation and bath heating provided. Potentiodynamic polarisation studies were employed to characterise the electrochemical behaviour of the electroplating baths under different process parameters and bath constituents. Details regarding the preparation of photoresist patterned wafers are elaborated step by step. Finally, characterisation techniques utilised in the study of the electrodeposits are summarised. SEM and AFM were used to observe the surface morphologies of electrodeposits. The compositional information were gathered from EDX and WDX. These results were combined with DSC measurements to test the alloy thermal properties such as melting point. XRD spectra identified the phase constituents of the electrodeposits and the microstructure was analysed in-depth by dual-beam FIB (SEM/FIB) and TEM.

Chapter 6

Electrodeposition of Sn-Cu Alloys

In this chapter, the electrodeposition of near-eutectic Sn-Cu alloys from methanesulphonate based baths developed was investigated. Sn-Cu electrodeposits were characterised by different techniques to monitor the process and finally achieve near-eutectic Sn-Cu solder bumps on silicon or glass wafers.

6.1 Cathodic Polarisation Studies

6.1.1 Development of Electrolyte

In the current study, methanesulphonate based electrolytes were developed for the electrodeposition of near-eutectic Sn-Cu alloys. Tin methanesulphonate and copper sulphate were used as Sn^{2+} and Cu^{2+} sources. Thiourea was added as the complexing agent for Cu^{2+} ions and iso-octyl phenoxy polyethoxy ethanol (OPPE) as the organic additive (chemical structure shown in Figure 6-1: $(CH_3)_3C\text{-}CH_2\text{-}C(CH_3)_2\text{-}\Phi\text{-}(OCH_2CH_2)_n\text{-}OH$, where Φ is a benzyl ring). As a reducing agent, methanesulphonic acid (MSA) was used to provide the conductivity in the bath while prohibiting the oxidation of Sn^{2+} ions. The role of each constituent was characterised by cathodic potentiodynamic polarisation at room temperature, with different bath formulations (summarised in Table 6-1), with results discussed in the following sections.

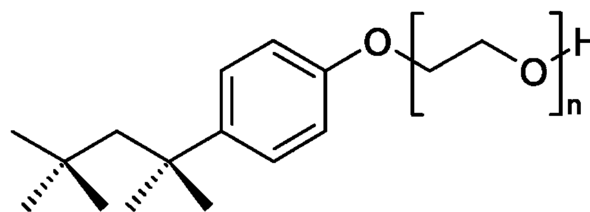

Figure 6-1 Schematic chemical structure of OPPE (iso-octyl phenoxy polyethoxy ethanol), with the hydrophilic portion containing nine to ten oxyethylene groups (n = 9–10).

Table 6-1 Methanesulphonate-based bath constituents for near-eutectic Sn-Cu alloy electrodeposition

Chemicals	Baths constituents and concentrations							
	A	B	C	D	E	F	G	H
$Sn(CH_3SO_3)_2$	70 g/L	70 g/L	70 g/L	70 g/L	70 g/L	70 g/L	70 g/L	70 g/L
$CuSO_4 \cdot 5H_2O$	–	0.002–0.02 mol/L	0.002 mol/L	0.002 mol/L	0.002 mol/L	0.002 mol/L	0.002 mol/L	0.002 mol/L
CH_3SO_3H	–	–	100 g/L	–	–	100 g/L	–	100 g/L
Thiourea	–	–	–	0.2 mol/L	–	0.2 mol/L	0.2 mol/L	0.2 mol/L
OPPE	–	–	–	–	10–50 ml/L	–	10 ml/L	10 ml/L

6.1.2 Effects of Scan Rate

Two scan rates, 1 mV/s and 10 mV/s, were investigated for bath A (Table 6-1) as shown in Figure 6-2. The open-circuit potentials of Cu coupons in both curves were recorded at around -0.05 V (versus SCE). No appreciable current is observed until the potential is swept to about -0.44 V, where the deposition of Sn commences. As the scan proceeds, the two curves exhibit two different formats.

At the scan rate of 1 mV/s (curve 1), the current density exponentially increases after the commencement of Sn deposition, whilst for 10 mV/s (curve 2) the current density increases more gently to a similar current density value (~320 mA/cm^2). However, although this has illustrated such a methanesulphonate based electrolyte is capable of achieving a relatively high current density, under such conditions only undesirable rough Sn dendrites (Figure 6-3) are produced. This also indicates that modifications to the bath formulation are required to improve the microstructure of electrodeposits.

The American Society for Testing and Materials (ASTM) recommends a scan rate of 0.1667 mV/s, particularly for corrosion studies [102], as such a low rate more faithfully reveals balanced cathodic reactions at a specific driving force. By comparing the two curves in Figure 6-2, a scan rate of 1 mV/s was therefore used in the following studies, as it finished measurements in a reasonable time duration while still illustrating the cathodic electrochemical trends.

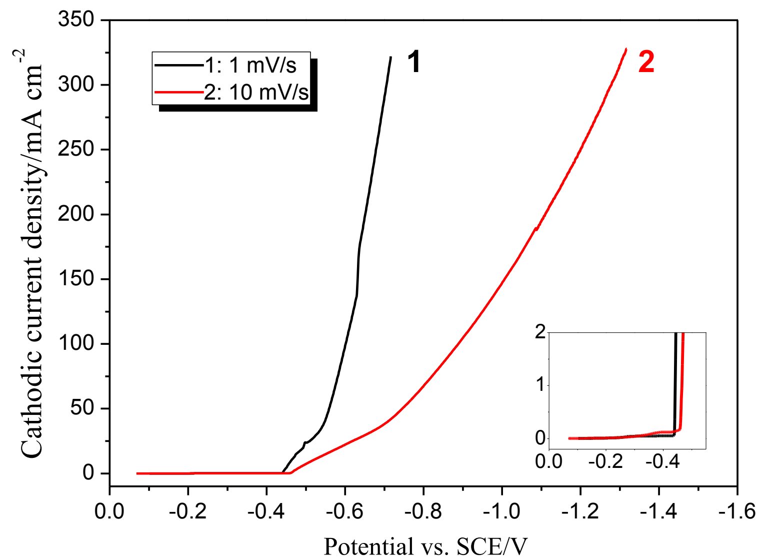

Figure 6-2 Cathodic potentiodynamic polarisation curves from bath A, Table 6-1 containing $Sn(CH_3SO_3)_2$ 70 g/L, showing the effects of potential scan rate: 1 mV/s (curve 1) and 10 mV/s (curve 2).

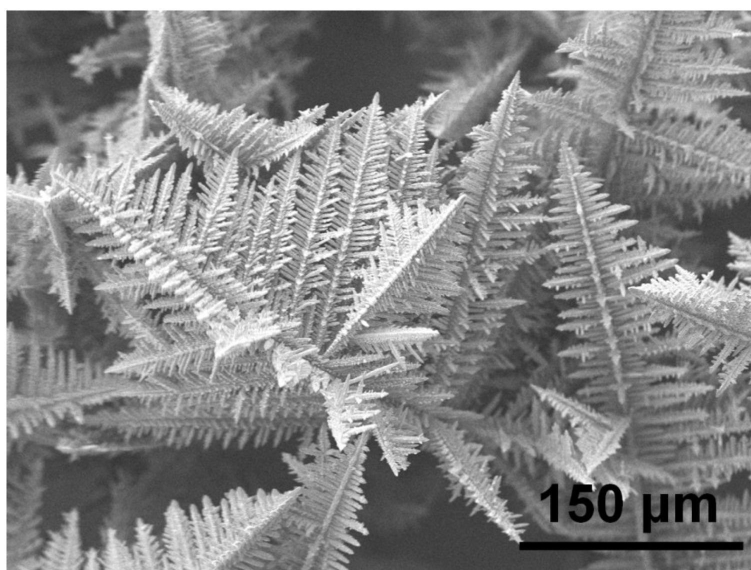

Figure 6-3 SEM image of Sn dendrites formed on Cu coupon after cathodic polarisation from bath A, Table 6-1 containing $Sn(CH_3SO_3)_2$ 70 g/L. Potential scan rate 1 mV/s.

6.1.3 Effects of Copper Sulphate

The cathodic polarisation curves for the electrodeposition of Sn-Cu alloys in bath B from Table 6-1 are given in Figure 6-4. Solutions were made by adding $CuSO_4$ (concentrations of 0 mol/L, 0.002 mol/L and 0.02 mol/L respectively) into a 70 g/L $Sn(CH_3SO_3)_2$ electrolyte. As the objective Sn-Cu electrodeposit contains only 0.7wt.% of Cu, it is expected that the appropriate $CuSO_4$ concentration should be maintained in the range from 0.002 mol/L to 0.02 mol/L after consideration of the results from other studies [103, 104].

As can be observed in Figure 6-4, the deposition of Sn commences at the potential of -0.44 V in all curves, the same as that in Figure 6-2. Before this potential, current density plateaux appear in the curves, which should be attributed to the deposition of Cu at their limiting current densities when Cu ions are present (curves 2 and 3). The higher limiting current density (approximately 2 mA/cm^2, curve 3) relates to a higher $CuSO_4$ concentration (0.02 M), whilst the lower (curve 2) shows a much lower value (less than 0.1 mA/cm^2). Therefore, under such conditions free of complexing agents

or additives, the deposition of Cu occurs before Sn and the co-deposition of Sn-Cu alloy follows thereafter.

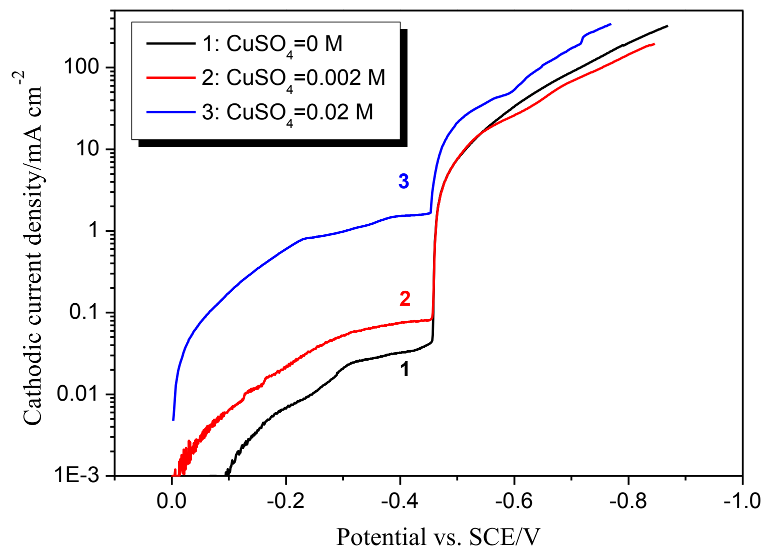

Figure 6-4 Cathodic potentiodynamic polarisation curves from bath B, Table 6-1 containing $Sn(CH_3SO_3)_2$ 70 g/L and various concentrations of $CuSO_4$, showing the effects of $CuSO_4$ additions: $CuSO_4$=0 mol/L (curve 1), $CuSO_4$=0.002 mol/L (curve 2) and $CuSO_4$=0.02 mol/L (curve 3). Potential scan rate: 1 mV/s.

6.1.4 Effects of Methanesulphonic Acid

The effects MSA on the electrodeposition of Sn-Cu alloys were studied with bath C (Table 6-1). From the cathodic potentiodynamic polarisation measurements (Figure 6-5), little effect is shown with the addition of MSA. Open-circuit potentials of Cu coupons kept constant at -0.1 V, followed by Cu deposition plateaux and Sn-Cu alloy deposition from approximately -0.44 V.

MSA is initially added for improvement of the stability of electrolyte as it is able to produce a reducing medium for Sn^{2+} stability and to provide conductivity for the electrolyte. Though there is no electrochemical effect evident from Figure 6-5, it does show effects on other aspects such as electrodeposit microstructure, which will be discussed in later sections.

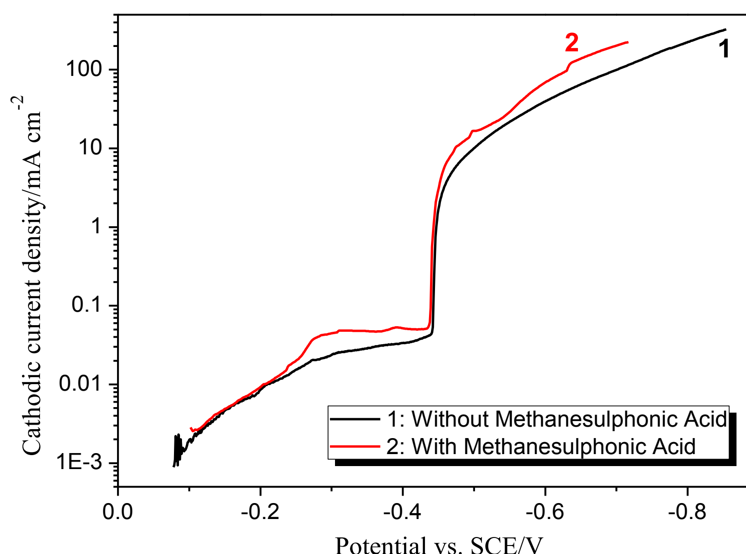

Figure 6-5 Cathodic potentiodynamic polarisation curves from bath C, Table 6-1 containing $Sn(CH_3SO_3)_2$ 70 g/L, $CuSO_4$ 0.002 mol/L and CH_3SO_3H 100g/L, showing the effects of MSA: without MSA (curve 1) and with MSA (curve 2). Potential scan rate: 1 mV/s.

6.1.5 Effects of Thiourea

The effects of thiourea on the electrodeposition of Sn-Cu alloys have also been studied by cathodic polarisation curves and are illustrated in Figure 6-6. The most noticeable difference from the presence of thiourea (curve 2) is the new open-circuit potential of the Cu coupons in the solution (-0.44 V). With the absence of thiourea, the open-circuit potential (curve 1) is close to 0 V as previously observed. Nonetheless, when 0.2 mol/L thiourea is added in the solution (curve 2), the open-circuit potential changes to approximately the same value as that for Sn deposition.

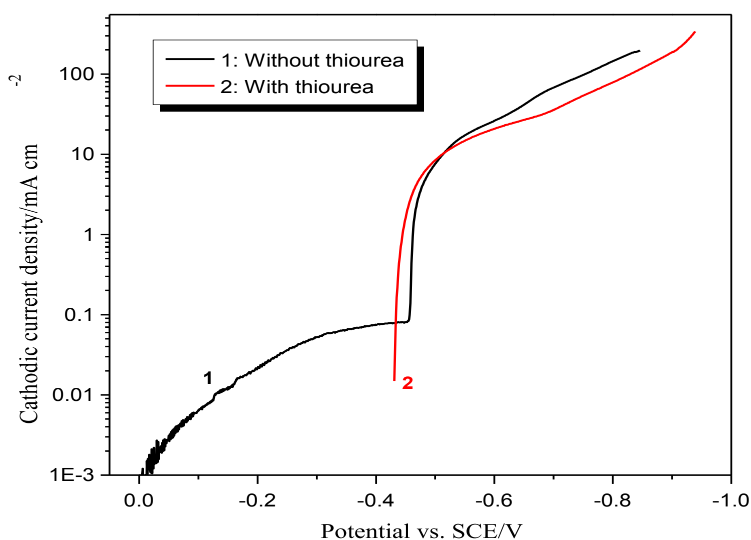

Figure 6-6 Cathodic potentiodynamic polarisation curves from bath D, Table 6-1 containing $Sn(CH_3SO_3)_2$ 70 g/L, $CuSO_4$ 0.002 mol/L and thiourea 0.2 mol/L, showing the effects of thiourea: without thiourea (curve 1) and with 0.2 mol/L thiourea (curve 2). Potential scan rate: 1 mV/s.

It was also noticed during experimentation that the newly treated Cu coupon surface was immediately covered by a silver grey layer once the Cu sample was immersed into the solution before any current passed. This is because in the presence of thiourea as a complexing agent with Cu ions, the electrode potentials of Sn and Cu markedly change from their original electrode potentials (their standard electrode potentials are Sn^{2+}: -0.136 V and Cu^{2+}: +0.337 V) that even the order in the electrochemical series is changed [105]. Thus, the electroless Sn coating on Cu is conducted without applying any external current by a displacement reaction:

$$Sn^{2+} + Cu \rightarrow Sn + Cu^{2+} \qquad \text{Equation 6-1}$$

In this manner, under the complexing effect of thiourea on Cu ions, the deposition potential of Cu is shifted closer to tin. Owing to this effect, the current density plateau for Cu deposition (shown in Figure 6-4) disappears and co-deposition of Sn-Cu alloy is realised from the Sn deposition potential of approximately -0.44 V onward. By comparing the two curves in Figure 6-6, though thiourea shows a strong chelating effect on Cu ions, its effect on the current density of Sn deposition proves to be negligible.

6.1.6 Effects of OPPE

As a widely used non-ionic surfactant to improve the microstructure of tin and tin alloy electrodeposits, OPPE was added in bath E (Table 6-1). Its effects, revealed by cathodic potentiodynamic polarisations, are shown in Figure 6-7 with varying concentrations (10 ml/L and 50 ml/L) present. In Aragon *et al*'s study in the electrodeposition of Sn(II) in a sulphate electrolyte, it was found that below 0.12 g/L, the presence of OPPE, containing longer oxyethylene groups (n=12–13) than in the current study, had little effect on the quality of the Sn deposits.

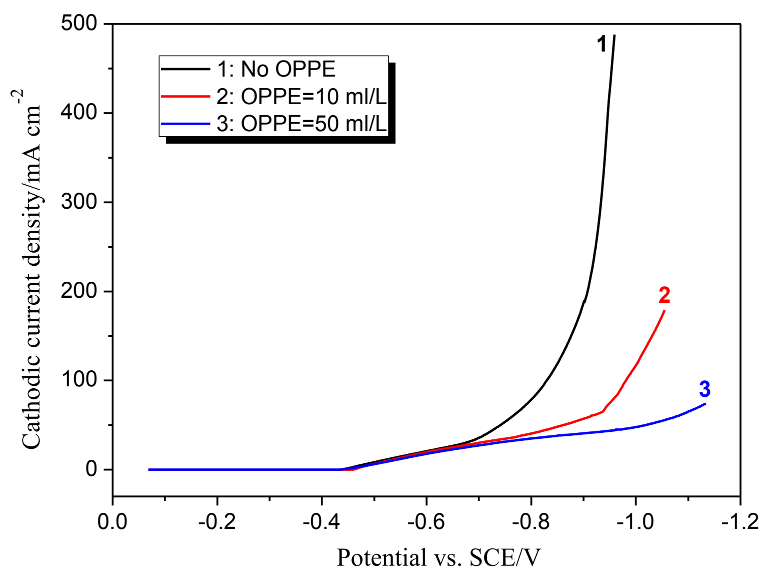

Figure 6-7 Cathodic potentiodynamic polarisation curves from bath E, Table 6-1 containing $Sn(CH_3SO_3)_2$ 70 g/L, $CuSO_4$ 0.002 mol/L and varying concentrations of OPPE, showing the effects of OPPE: no OPPE (curve 1), OPPE=10 ml/L (curve 2) and OPPE=50 ml/L (curve 3). Potential scan rate: 1 mV/s.

As can be seen from Figure 6-7, under the effects of OPPE, the overall shape of the polarisation curves is changed from curve 1 to curves 2 and 3. Compared to curve 1 (no addition), with the presence of OPPE (curves 2 and 3), the Sn electrodeposition is largely inhibited as evidenced by the marked decrease in current density. Without OPPE (curve 1), the current density reaches about 200 mA/cm^2 at a potential of -0.9 V, although Sn dendrites result as shown in Figure 6-3. This current density value is only around 40 mA/cm^2 and 15 mA/cm^2 at such a potential under the effects of 10 ml/L (curve 2) and 50 ml/L OPPE (curve 3) respectively. This inhibitive effect of OPPE has changed the undesirable dendrite microstructure of the electrodeposits and is

discussed in detail in later sections of this chapter. By comparing curves 2 and 3, 10 ml/L of OPPE is considered to be an effective concentration that does not overly restrict the Sn deposition.

6.2 Surface Morphology of Electrodeposits

Surface morphology is one of the most important features of electrodeposit microstructure, as smooth and compact electrodeposits are the rudimentary requirements for applications in electronics. In bath B from Table 6-1 where only Sn and Cu sources are present, the morphology of Sn-Cu electrodeposits is typically rough and porous. As can be seen from Figure 6-8, this bath is incapable of producing a uniform coating. Part of the Cu substrate remains uncovered by the electrodeposit.

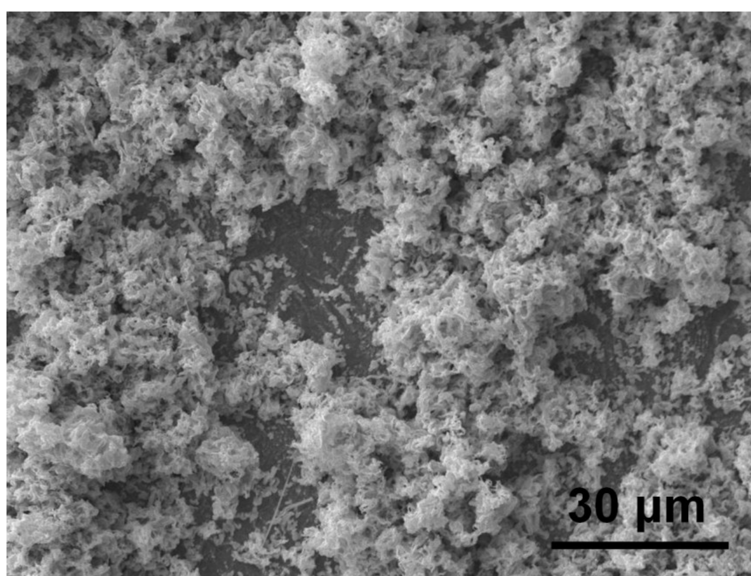

Figure 6-8 SEM micrograph of Sn-Cu electrodeposit under galvanostatic condition (current density = 15 mA/cm^2) from bath B, Table 6-1 containing $Sn(CH_3SO_3)_2$ 70 g/L and $CuSO_4$ 0.002 mol/L, electrical charge passed = 1500 C/dm^2.

In this section, SEM images of Sn-Cu electrodeposits prepared in different baths from Table 6-1 are presented to investigate the influence of each bath constituent in terms of surface morphology. To make the results comparable, the electrical charge of each trial was kept constant at 1500 C/dm^2.

6.2.1 Effects of Methanesulphonic Acid

Figure 6-9 shows the effects of MSA on surface morphology. It is known that sufficient electrolyte in the bath providing conductivity is one of the prerequisites for a relatively uniform coating [106, 107]. This is emphasised by the addition of MSA in bath C, Table 6-1. Compared with bath B where no MSA was present and a rough electrodeposit was produced (Figure 6-8), relatively uniform electrodeposits are expected and justified as shown in Figure 6-9 over a range of current densities.

In Figure 6-9, the surface morphology of electrodeposits at different current densities (5, 10, 15, 20, 25 and 30 mA/cm^2 respectively) with the presence of 100g/L CH_3SO_3H is demonstrated. It is found that all the micrographs appear similar over the whole current density range examined. The typical microstructure in these samples is that the deposits consist of closely-packed small nodules with a size of only a few microns. The cross-sectional observation of the microstructure is examined later in this chapter.

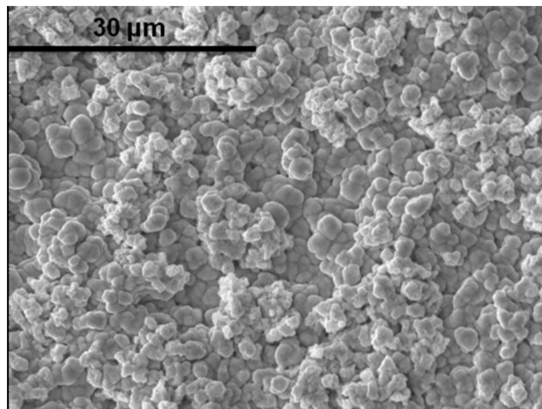

(a) current density = 5 mA/cm^2

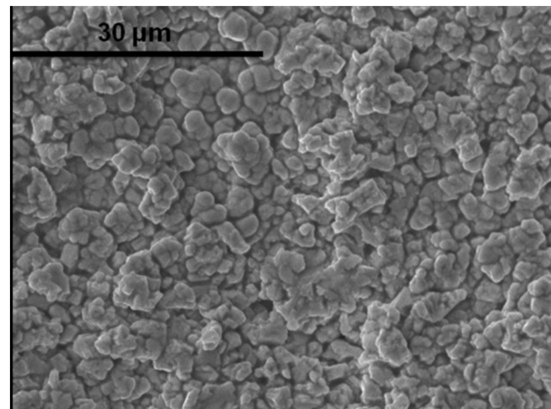

(b) current density = 10 mA/cm^2

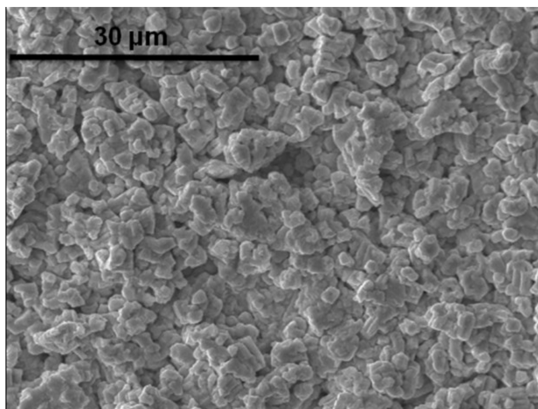

(c) current density = 15 mA/cm^2

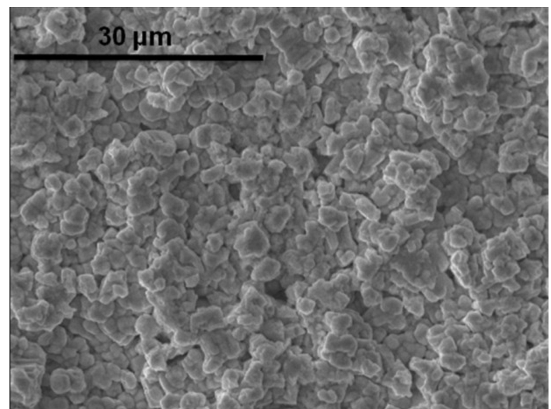

(d) current density = 20 mA/cm^2

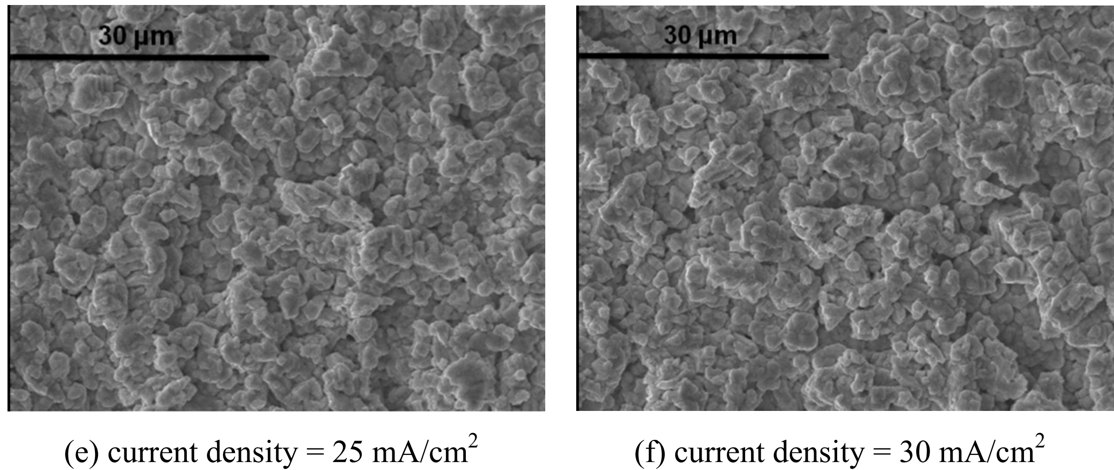

(e) current density = 25 mA/cm^2 (f) current density = 30 mA/cm^2

Figure 6-9 SEM micrographs of Sn-Cu films electrodeposited under galvanostatic conditions from bath C, Table 6-1 containing $Sn(CH_3SO_3)_2$ 70 g/L, $CuSO_4$ 0.002 mol/L and CH_3SO_3H 100g/L, electrical charge passed = 1500 C/dm^2.

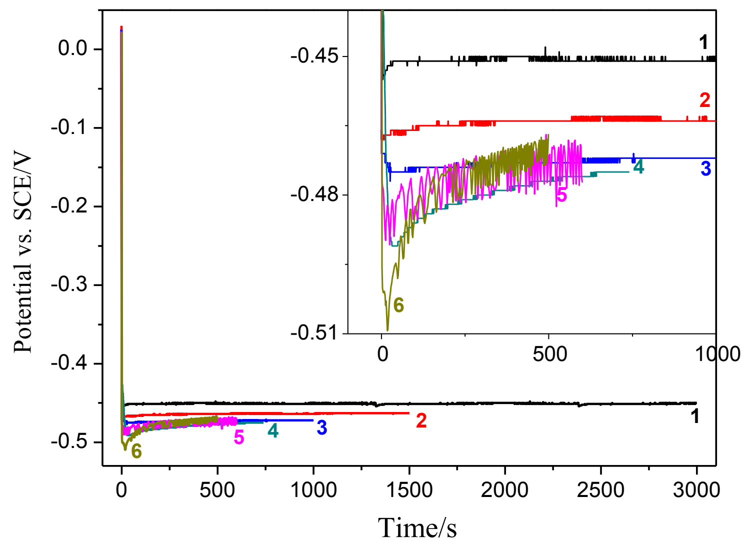

Figure 6-10 Chronopotentiometry of Sn-Cu alloys electrodeposition from bath C, Table 6-1 recorded under galvanostatic conditions, electrical charge passed = 1500 C/dm^2. Curves 1, 2, 3, 4,5 6 represent 5, 10, 15, 20, 25 and 30 mA/cm^2 respectively.

The chronopotentiometry curves responding to the galvanostatic conditions are shown in Figure 6-10. As the total electrical charge for each test was kept constant at 1500 C/dm^2, a lower current density needed a longer deposition time as the curves show. The driving force (potential) varies between -0.45 V and -0.49 V at the end of each test when the processes are relatively stabilised. The potentiodynamic cathodic polarisation curves (Figure 6-6) for bath C from Table 6-1 has indicated a potential range of -0.45 V to -0.52 V for the current densities investigated but under dynamic

conditions. The noisy curves for higher current densities (curves 5 and 6 for 25 and 30 mA/cm^2 in Figure 6-10 respectively) represent a relatively unstable cathodic process and probably might take longer to stabilise.

6.2.2 Effects of Thiourea

The complexing effect of thiourea on copper to bring its deposition potential closer to Sn has been demonstrated by cathodic polarisation studies in Figure 6-6. Figure 6-11 shows the surface morphology of electrodeposits under the effects of thiourea only.

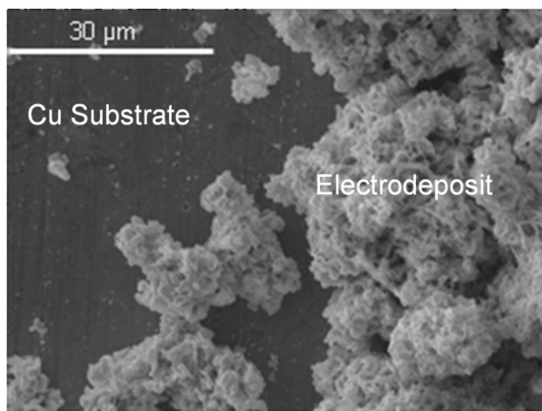

(a) current density = 5 mA/cm^2

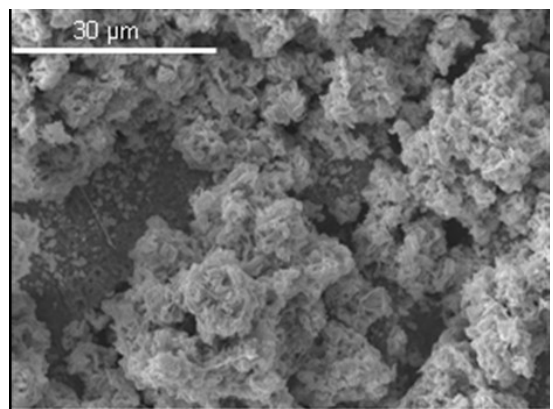

(b) current density = 10 mA/cm^2

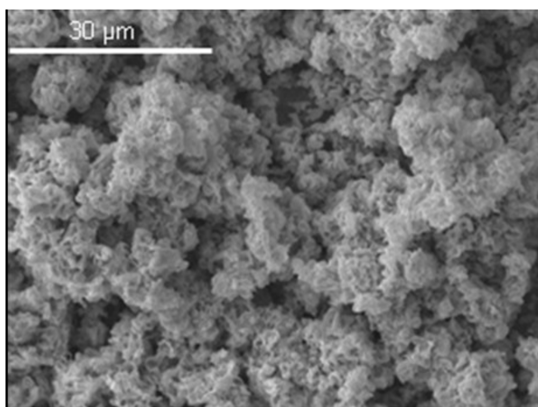

(c) current density = 15 mA/cm^2

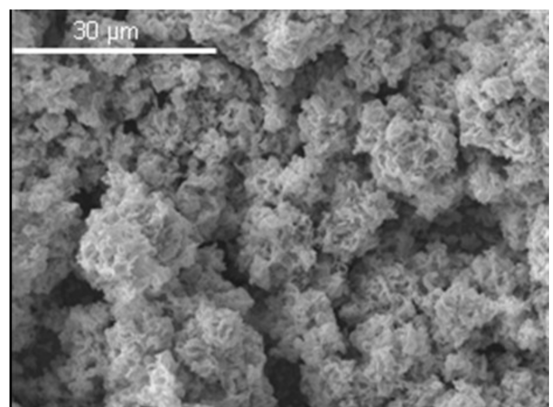

(d) current density = 20 mA/cm^2

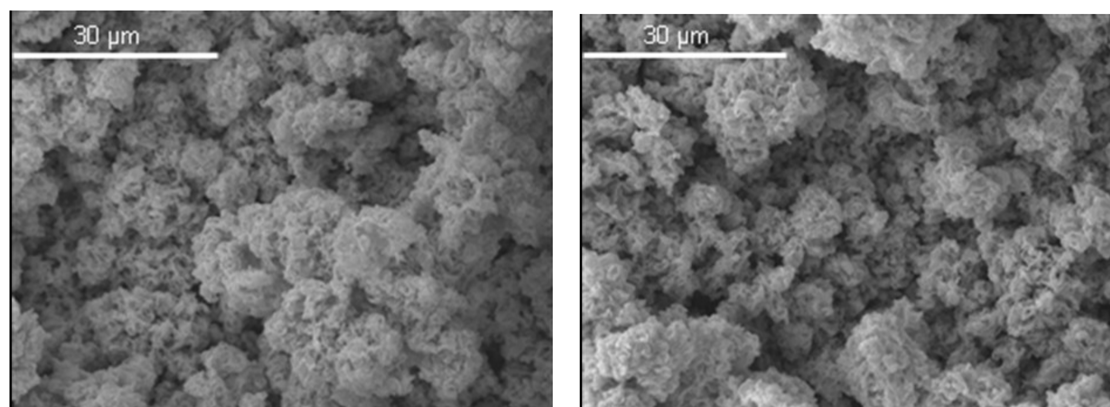

(e) current density = 25 mA/cm^2 (f) current density = 30 mA/cm^2

Figure 6-11 SEM micrographs of Sn-Cu films electrodeposited under galvanostatic conditions from bath D, Table 6-1 containing $Sn(CH_3SO_3)_2$ 70 g/L, $CuSO_4$ 0.002 mol/L and thiourea 0.2 mol/L, electrical charge passed = 1500 C/dm^2.

In bath D (Table 6-1) where the previously included 100g/L CH_3SO_3H was not added, with only the addition of thiourea, all the samples produced under various galvanostatic conditions show a completely rough and porous morphology, similar to the one shown in Figure 6-8 without any addition. At 5 mA/cm^2 (image (a)), a large part of the Cu substrate is still uncovered as revealed by EDX. This is again probably due to lack of conductivity in the electrolyte, which MSA is capable of bringing in (as results in Section 6.2.1 show) whilst thiourea not.

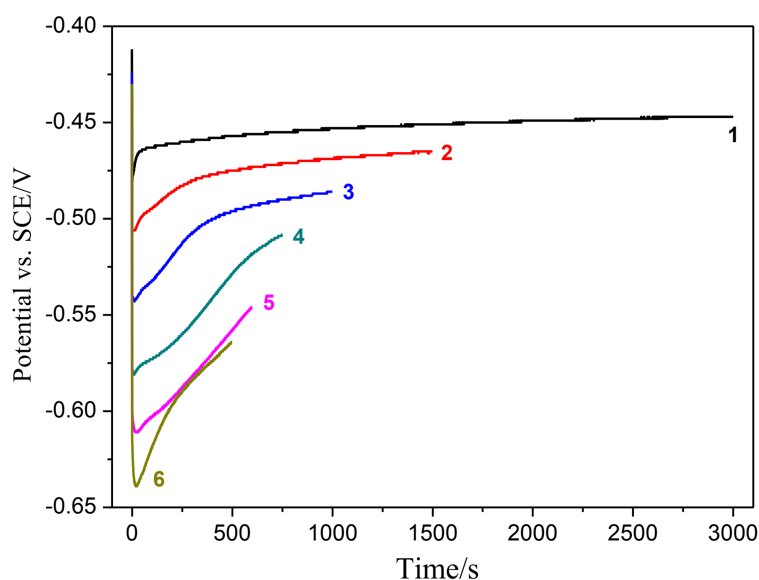

Figure 6-12 Chronopotentiometry of Sn-Cu alloys electrodeposition from bath D, Table 6-1 recorded under galvanostatic conditions, electrical charge passed = 1500 C/dm^2. Curves 1, 2, 3, 4, 5 and 6 represent 5, 10, 15, 20, 25 and 30 mA/cm^2 respectively.

Figure 6-12 shows the potential responses to the current densities utilised in the presence of thiourea. It is seen that the open-circuit potentials for all Cu coupons are recorded approximately at -0.44 V because of the immersion deposited Sn on Cu surface as previously discussed. A wider potential span from -0.45 V to -0.63 is observed, compared to Figure 6-10 under the effects of MSA. The “V” shape of the curves, particularly responding to higher current densities, is likely due to the initial unstable stage when higher driving force (more negative potential) is required for the applied current flow, which is consistent with the conclusions from Kim *et al* [108]. The levelling off tendency represents the gradually balanced process (consuming and replenishing and transport of metallic ions at the cathode) during deposition over time.

6.2.3 Effects of Thiourea and Methanesulphonic Acid

As discussed in Sections 6.2.1 and 6.2.2, both thiourea and MSA are essential constituents in the bath, their synergetic effects on the surface morphology of electrodeposits are studied and shown in Figure 6-13, with the chronopotentiometry curves for producing such samples plotted in Figure 6-14.

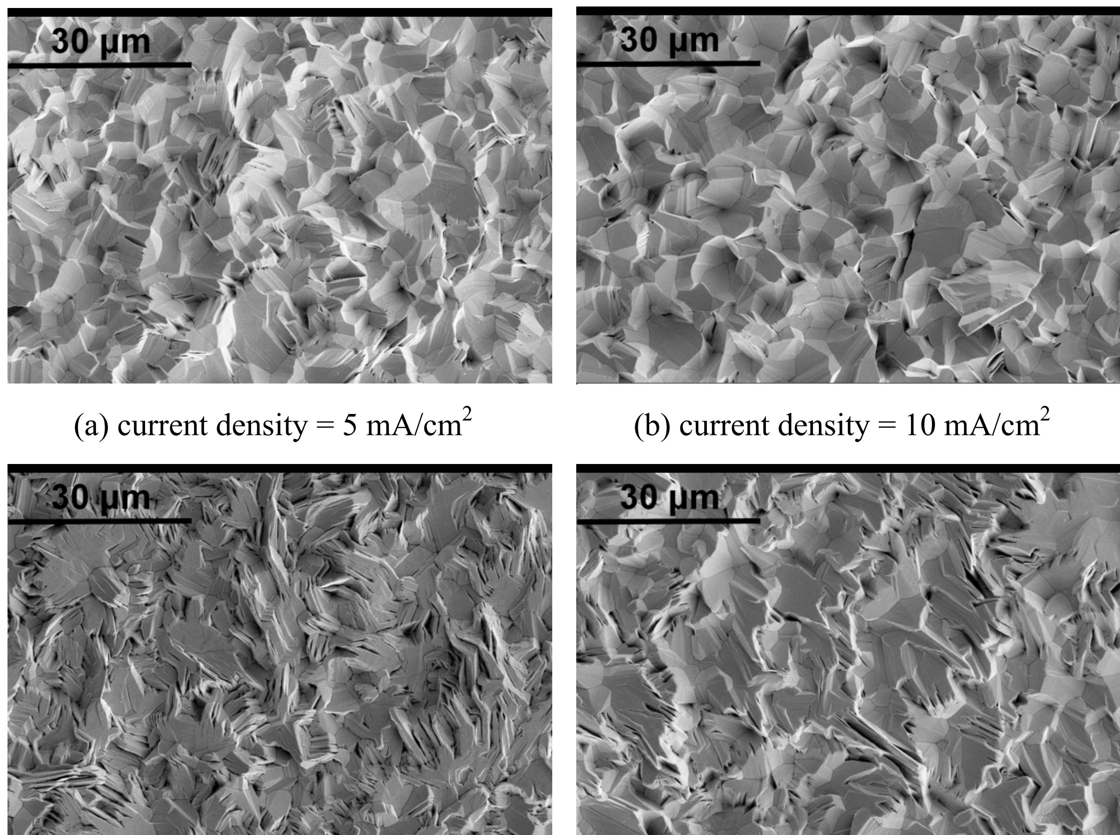

(a) current density = 5 mA/cm^2 (b) current density = 10 mA/cm^2

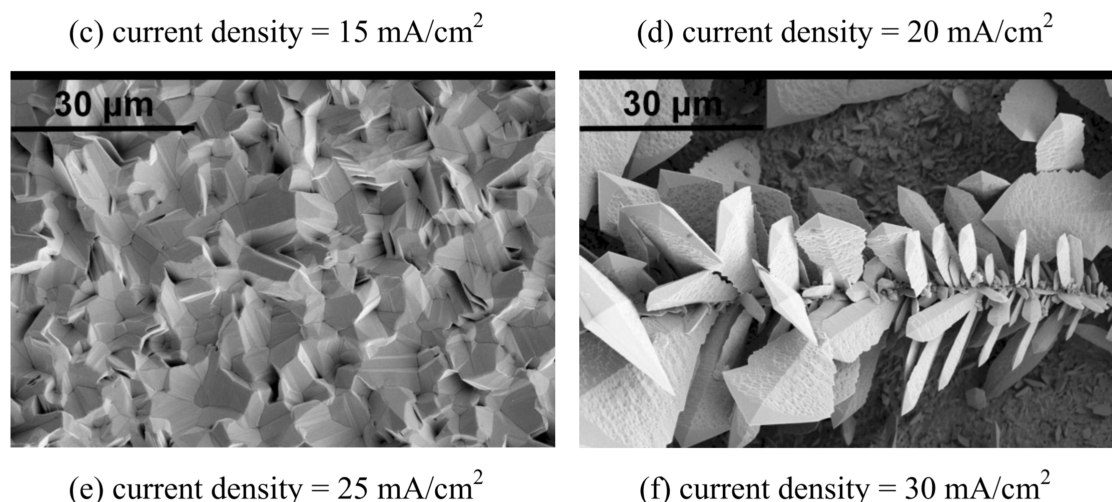

Figure 6-13 SEM micrographs of Sn-Cu films electrodeposited under galvanostatic conditions from bath F, Table 6-1 containing $Sn(CH_3SO_3)_2$ 70 g/L, $CuSO_4$ 0.002 mol/L, CH_3SO_3H 100g/L and thiourea 0.2 mol/L, electrical charge passed = 1500 C/dm^2.

Compared to Figure 6-9 and Figure 6-11, the electrodeposits in Figure 6-13 show finer crystalline structures on the surface, with well defined crystal facets clearly seen in images (a), (b) and (e), although images (c) and (d) look like closely packed platelets. The latter morphology is typical under the effects of thiourea, as similar electrodeposited Sn films were observed by Fukuda *et al* from a sulphate bath [109]. However, at the highest current density examined (30 mA/cm^2), large scale dendrites are evident as image (f) shows. This has led to the conclusion that the ability of MSA to achieve uniform deposits is to some extent weakened by the presence of thiourea. This can be seen by comparing Figure 6-13, image (f) to Figure 6-9 where no such dendrites were observed at the same current density.

The chronopotentiometry curves in Figure 6-14 help to explain the dendrite formation in Figure 6-13, image (f) at a current density of 30 mA/cm^2. The -0.75 V driving potential responsible is the highest value recorded so far with the addition of MSA, thiourea and their combinations. Under such a potential, hydrogen evolution is concurrent with the Sn-Cu alloy deposition. This indicates that the current combination of bath constituents is not capable of deposition at such a high current density and that hydrogen evolution has to contribute to the total current flow. As a result, dendrites are the typical electrodeposits, similar to observations obtained by

other investigators but from tin chloride electroplating systems [110] and under the effects of additives [111].

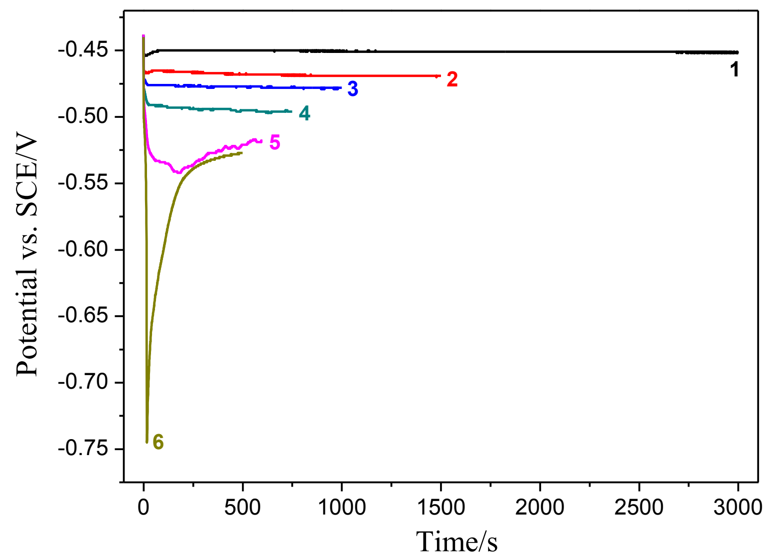

Figure 6-14 Chronopotentiometry of Sn-Cu alloys electrodeposition from bath F, Table 6-1 recorded under galvanostatic conditions, electrical charge passed = 1500 C/dm^2. Curves 1, 2, 3, 4, 5 and 6 represent 5, 10, 15, 20, 25 and 30 mA/cm^2 respectively.

6.2.4 Effects of Thiourea and OPPE

Figure 6-15 shows SEM micrographs of electrodeposits prepared with thiourea and OPPE in the electrolyte. With the addition of OPPE, crystalline features are apparent in all the micrographs. Compared to the porous electrodeposits obtained under sole thiourea in Figure 6-11, although the addition of non-ionic OPPE is not supposed to be providing any improvement in bath conductivity as MSA does, the strong inhibitive effect by OPPE (characterised in Figure 6-7) makes the electrodeposits compact and crystalline.

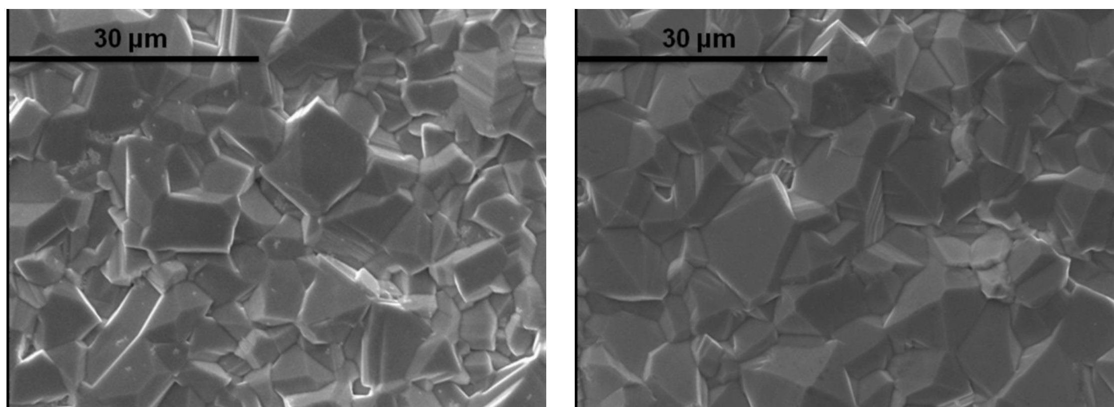

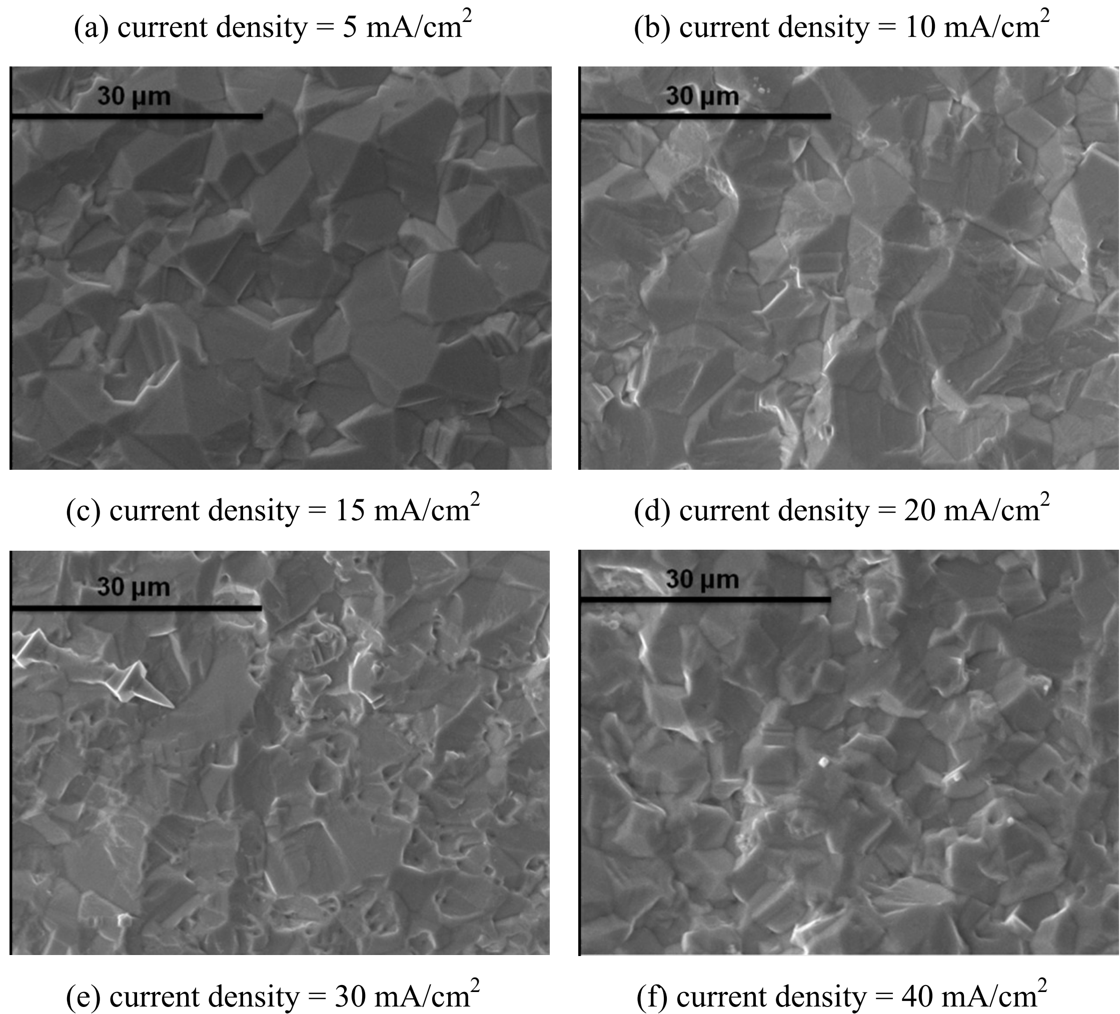

Figure 6-15 SEM micrographs of Sn-Cu films electrodeposited under galvanostatic conditions from bath G, Table 6-1 containing $Sn(CH_3SO_3)_2$ 70 g/L, $CuSO_4$ 0.002 mol/L, thiourea 0.2 mol/L and OPPE 10 ml/L, electrical charge passed = 1500 C/dm^2.

It can be clearly seen from Figure 6-16 that in order to prepare samples at galvanostatic current densities of 30–40 mA/cm^2, the potential has to be nearly -1.0 V, however, no dendrites were observed at this current density and potential combination. Neither is hydrogen evolution occurring with the electrodeposition. This is also due to the effects of OPPE, which means the addition of OPPE not only inhibits Sn deposition but also hydrogen evolution. In Barry *et al*'s studies, it was found that although the cathodic discharge mechanism for Sn^{2+} species remained that same, the nucleation mechanism of tin electrodeposition was changed by OPPE from instantaneous to progressive nucleation [112].

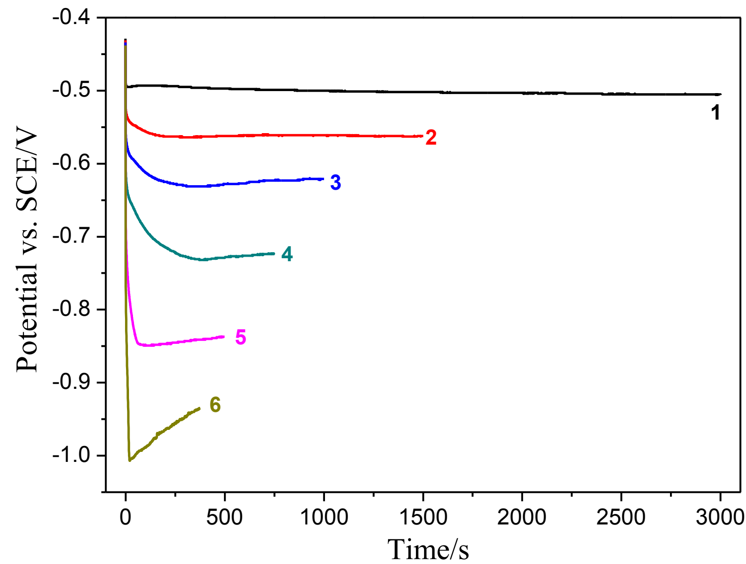

Figure 6-16 Chronopotentiometry of Sn-Cu alloys electrodeposition from bath G, Table 6-1 recorded under galvanostatic conditions, electrical charge passed = 1500 C/dm^2. Curves 1, 2, 3, 4, 5 and 6 represent 5, 10, 15, 20, 30 and 40 mA/cm^2 respectively.

6.2.5 Effects of Thiourea, Methanesulphonic Acid and OPPE

Figure 6-17 shows micrographs of the samples produced in bath H (Table 6-1) with all the additions (thiourea, MSA and OPPE). As the current density increases, electrodeposit morphology shows a change from a distinctive crystalline microstructure at low current densities (images (a) and (b)) to a relatively flat surface (images (c) and (d)), then the less compact and nodular morphology appears as the current density increases. This result implies that over a current density range of 10–20 mA/cm^2, compact electrodeposits with relatively smooth surface can be obtained.

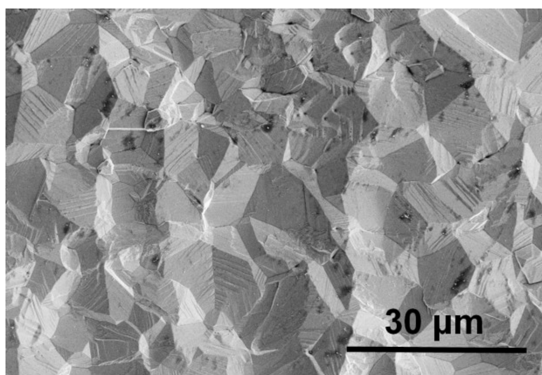

(a) current density = 5 mA/cm^2

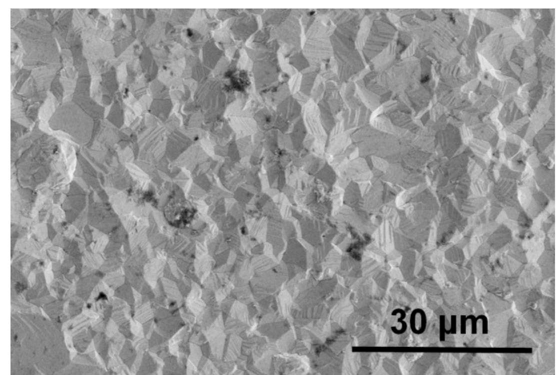

(b) current density = 10 mA/cm^2

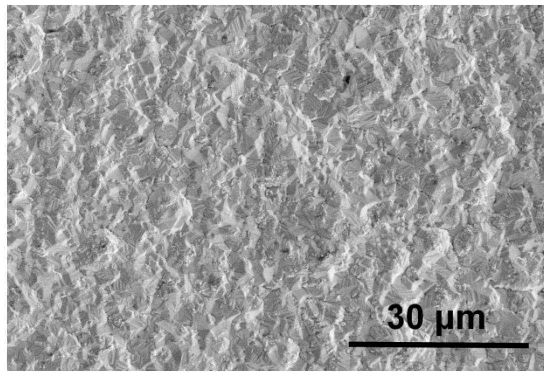

(c) current density = 15 mA/cm^2

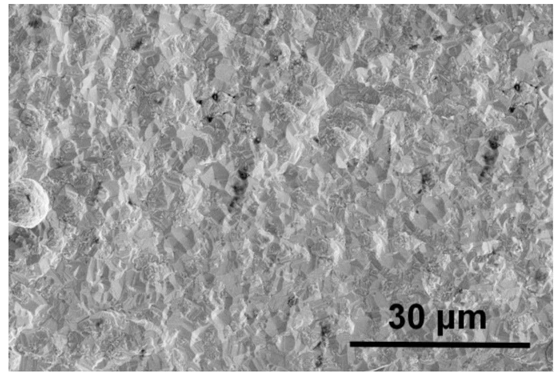

(d) current density = 20 mA/cm^2

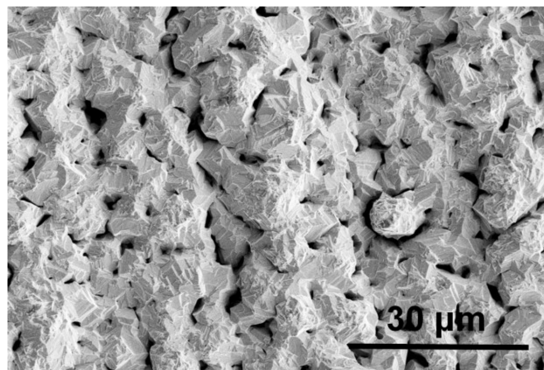

(e) current density = 25 mA/cm^2

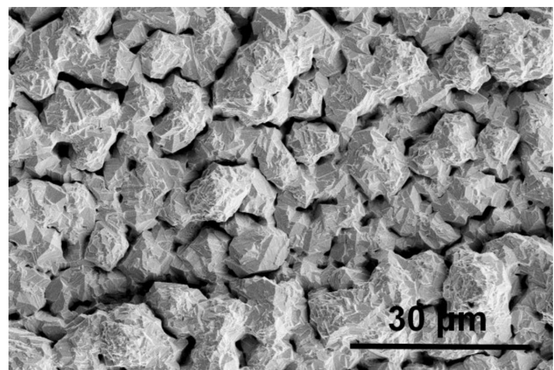

(f) current density = 30 mA/cm^2

Figure 6-17 SEM micrographs of Sn-Cu films electrodeposited under galvanostatic conditions from bath H, Table 6-1 containing $Sn(CH_3SO_3)_2$ 70 g/L, $CuSO_4$ 0.002 mol/L, CH_3SO_3H 100g/L, thiourea 0.2 mol/L and OPPE 10 ml/L, electrical charge passed = 1500 C/dm^2.

The chronopotentiometry curves in Figure 6-18 show that for a current density range of 10–20 mA/cm^2 (curves 2, 3 and 4), the potentials remain between -0.5 V and -0.6 V when stabilised. For the nodular deposits shown in Figure 6-17 images (e) and (f), the potentials undergo early stage fluctuations before stabilising.

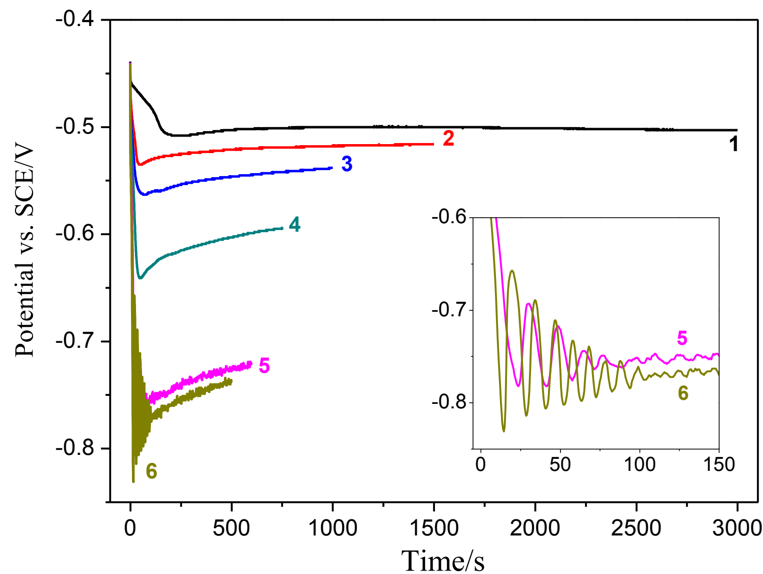

Figure 6-18 Chronopotentiometry of Sn-Cu alloys electrodeposition from bath H, Table 6-1 recorded under galvanostatic conditions, electrical charge passed = 1500 C/dm^2. Curves 1, 2, 3, 4, 5 and 6 represent 5, 10, 15, 20, 25 and 30 mA/cm^2 respectively.

6.3 Compositional Analysis of Electrodeposits

The composition of electrodeposited Sn-Cu films on Cu coupons under galvanostatic conditions is analysed by WDX. Figure 6-19 plots the Cu contents in samples prepared in bath H from Table 6-1, with different concentrations of $CuSO_4$ in the solution (curves 1, 2, 3 and 4 corresponding to 0.002 mol/L, 0.005 mol/L, 0.007 mol/L and 0.02 mol/L respectively). The horizontal broken line in this figure shows the eutectic composition of the Sn-Cu alloy (Sn-0.7wt.%Cu from the phase diagram in Figure 3-4). It can be seen from Figure 6-19 that at all current densities investigated, the Cu content grows with increasing $CuSO_4$ concentration. However, the measured alloy composition appear closest to 0.7wt.% over a relatively wide range of current densities (10–25 mA/cm^2) in curve 3 where the $CuSO_4$ concentration is 0.007 mol/L. Overall, 0.007 mol/L of $CuSO_4$ is the appropriate concentration in the bath for near-eutectic Sn-Cu alloy electrodeposition under the examined conditions.

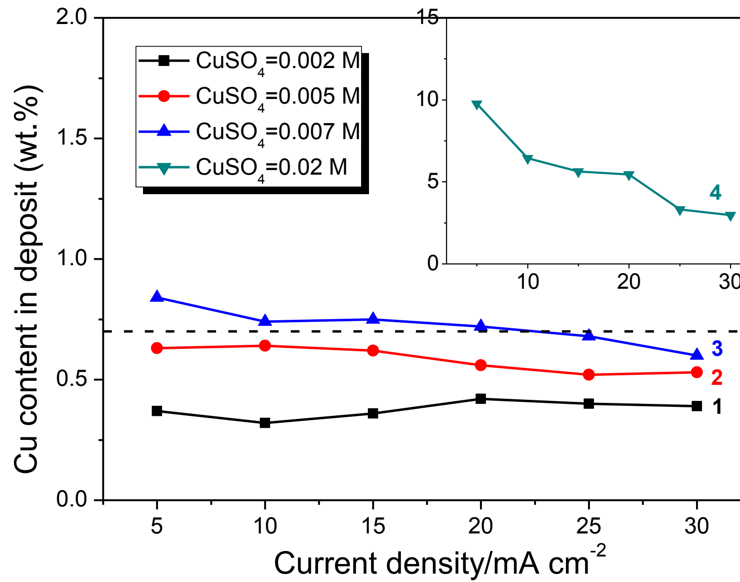

Figure 6-19 Cu content (wt.%) of the electrodeposited Sn-Cu films vs. galvanostatic current density utilising bath H from Table 6-1 but with varying concentration of $CuSO_4$. Measurements carried out by WDX. $CuSO_4$=0.002 mol/L (curve 1), 0.005 mol/L (curve 2), 0.007 mol/L (curve 3) and 0.02 mol/L (curve 4) respectively. Broken line represents the objective Cu content, 0.7wt.%.

6.4 Thermal Analysis of Electrodeposits

Differential scanning calorimetry (DSC) measurements were employed to characterise the thermal property of the Sn-Cu electrodeposits for various compositions, as shown in Figure 6-20. Nishikawa *et al* found that the shape of DSC curves was strongly dependent on the heating rate during the temperature ramping process [113] and 10 K/min was applied throughout the measurements in the current study, illustrating the trends during the endothermic process.

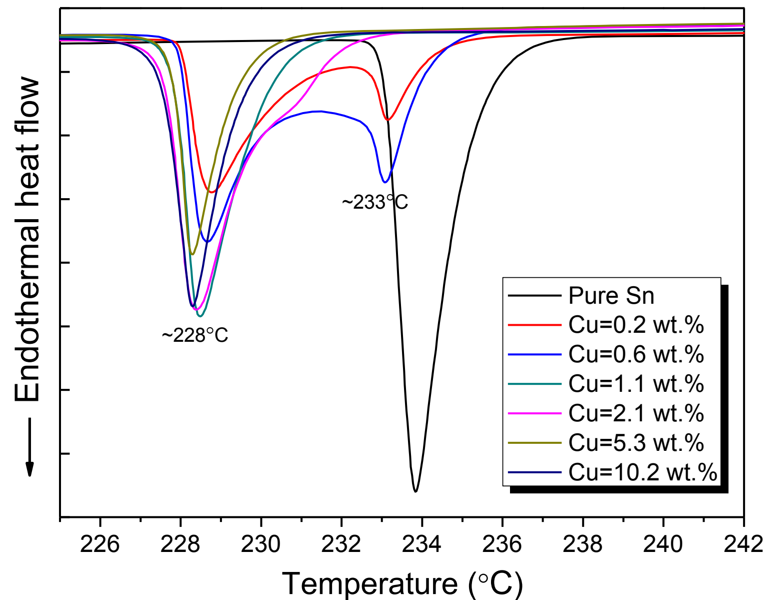

Figure 6-20 DSC measurements for Sn-Cu electrodeposits from bath H, Table 6-1. Scan rate at 10 K/min. Pure Sn presented as a reference.

As can be seen from Figure 6-20, for reference purposes, a pure Sn electrodeposit was also measured and shows a single peak with the onset point of melting at approximately 233°C and the resultant peak at 234°C, slightly higher than the theoretical melting point (232°C) probably because of the dynamic non-equilibrium scanning process. For all the Sn-Cu electrodeposits, onset points of approximately 227°C and peaks of about 228°C were recorded as Figure 6-20 shows. This melting temperature should be attributed to the eutectic Sn-Cu constituent in the deposits as the Sn-Cu equilibrium phase diagram shows (Figure 3-4). However, for the electrodeposits containing 0.2wt.% and 0.6wt.% of Cu, it is believed that pure Sn is still present and therefore the peak attributed to Sn (similar to the pure Sn curve) is also observed. Multi-peaks during the heating process in DSC measurements were also observed by Sopoušek *et al* [114] owing to different phases or phase transitions in their quaternary Sn-Ag-Cu-In solder alloys.

6.5 Microstructure of Electrodeposits

6.5.1 Phase Identification

The phases in the electrodeposited Sn-Cu alloy films in baths from Table 6-1 (baths D, G and H specifically) are identified by X-ray diffraction and shown in Figure 6-21.

Except two peaks from the Cu substrate, Cu (111) and Cu (200), all the other peaks could be attributed to two phases: β-Sn and Cu_6Sn_5. There is no fundamental difference between those three diagrams, the most noticeable being the intensity of Sn (200) orientation. It is easily seen that the additions of thiourea, OPPE and MSA do not significantly affect the phases in the Sn-Cu alloy electrodeposits.

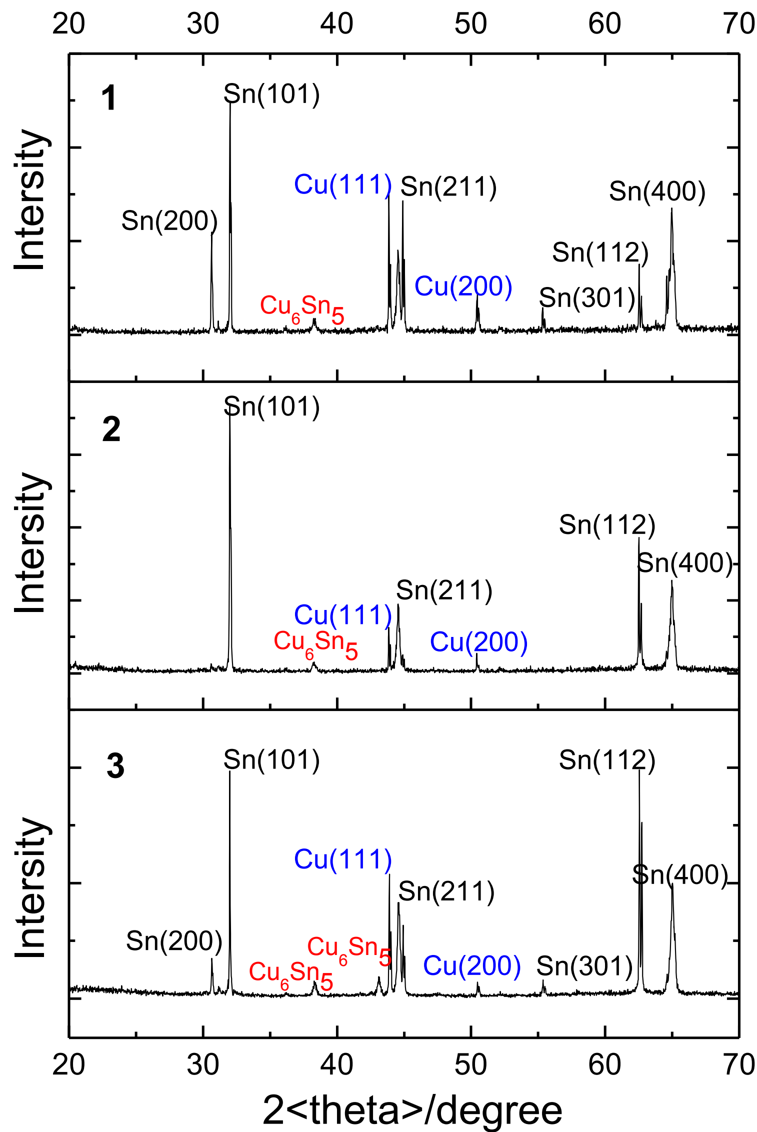

Figure 6-21 XRD spectra of Sn-Cu films galvanostatically electrodeposited in bath D (image 1, with thiourea), bath G (image 2, with thiourea and OPPE) and bath H (image 3, with thiourea, OPPE and MSA) from Table 6-1 at a current density of 15 mA/cm^2, electrical charge passed = 1500 C/dm^2.

6.5.2 Electrodeposit Cross-Sectional Analysis

An *in situ* analysis of the microstructure of Sn-Cu electrodeposits was undertaken using SEM/FIB micro-processing and imaging as discussed in Chapter 5. Figure 6-22 shows the deposits produced with thiourea and OPPE but without MSA. As can be seen in image (a), a secondary electron image, little detail is evident, with only the interface between the Sn-Cu electrodeposit (top) and the Cu substrate (bottom) visible.

However, under the ion-induced secondary electron (ISE) mode (micrograph (b)), grains are clearly seen due to different orientations indicating a varied contrast. It can be noted that the sizes of the tin grains are ranging approximately at 7–8 μm with the absence of MSA in bath G from Table 6-1.

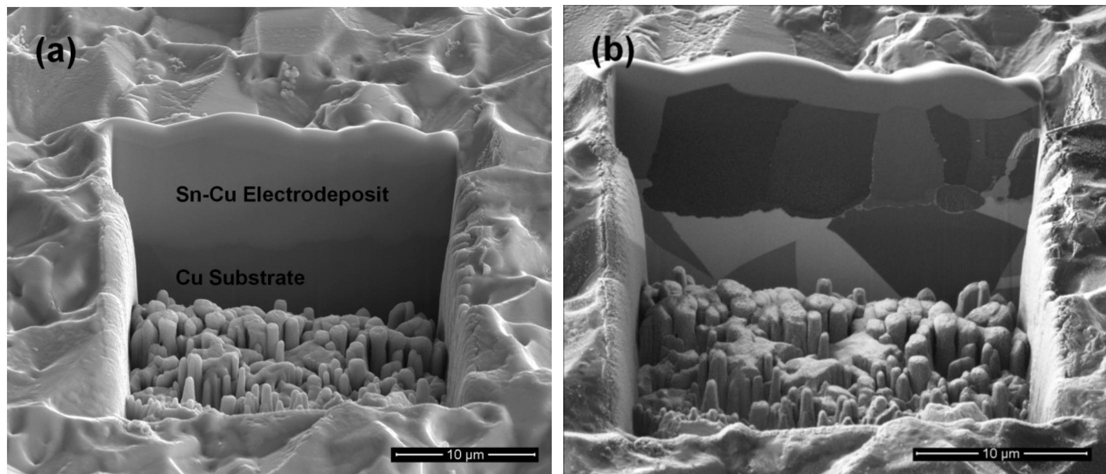

Figure 6-22 SEM/FIB processed cross-sectional images of the electrodeposited Sn-Cu film under galvanostatic conditions from bath G, Table 6-1 (15 mA/cm^2, electrical charge passed = 1500 C/dm^2). (a) secondary electron (SE) image; (b) ion-induced secondary electron (ISE) micrograph.

Figure 6-23 illustrates the cross-sectional micrographs of the sample prepared from bath H (Table 6-1) with all the additives. Sn grains are distinguishable due to their contrast. So are the intermittently curving white “lines”, predominantly spreading along Sn grain boundaries, which are believed to the Cu_6Sn_5 phase as recognised by XRD analysis in Figure 6-21. This phase is further evidenced by TEM analysis which is discussed in Session 6.5.3. However, compared to the results in Figure 6-22, it is worth mentioning that with the presence of MSA, the Sn grains are significantly refined, from 7–8 μm to approximately 1–3 μm. This allows the conclusion that the

addition of MSA not only stabilises the electrolyte, generates a uniform coating (Figure 6-9) and also refines the tin grain size.

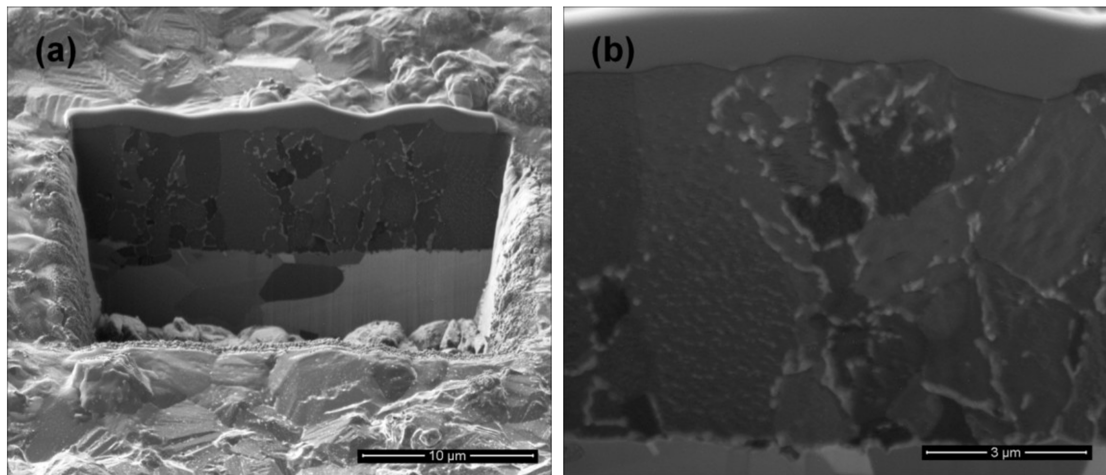

Figure 6-23 SEM/FIB processed cross-sectional ISE images of the electrodeposited Sn-Cu film under galvanostatic conditions from bath H, Table 6-1 (15 mA/cm^2, electrical charge passed = 1500 C/dm^2). (a) general view; (b) central area magnified.

6.5.3 TEM Analysis

TEM observation of the electrodeposited Sn-Cu films were carried out to indentify the microstructure of the Sn-Cu electrodeposits from bath H (Table 6-1). Figure 6-24 image (a) shows the TEM micrograph of the white "line" (width no more than 100 nm) in Figure 6-23, with a localised observation in image (b) at a higher magnification. EDX analysis shows that point "1" in image (b) is pure Sn (tin grains) as spectrum (c) shows (the Mo peak was from the sample mounting grid). Point "2" has a composition of 48.9at.% Sn and 51.1at.% of Cu after disregarding the Mo signal. These results further suggest the existence of the Cu_6Sn_5 intermetallic phase, particularly in combination with the XRD data in Figure 6-21.

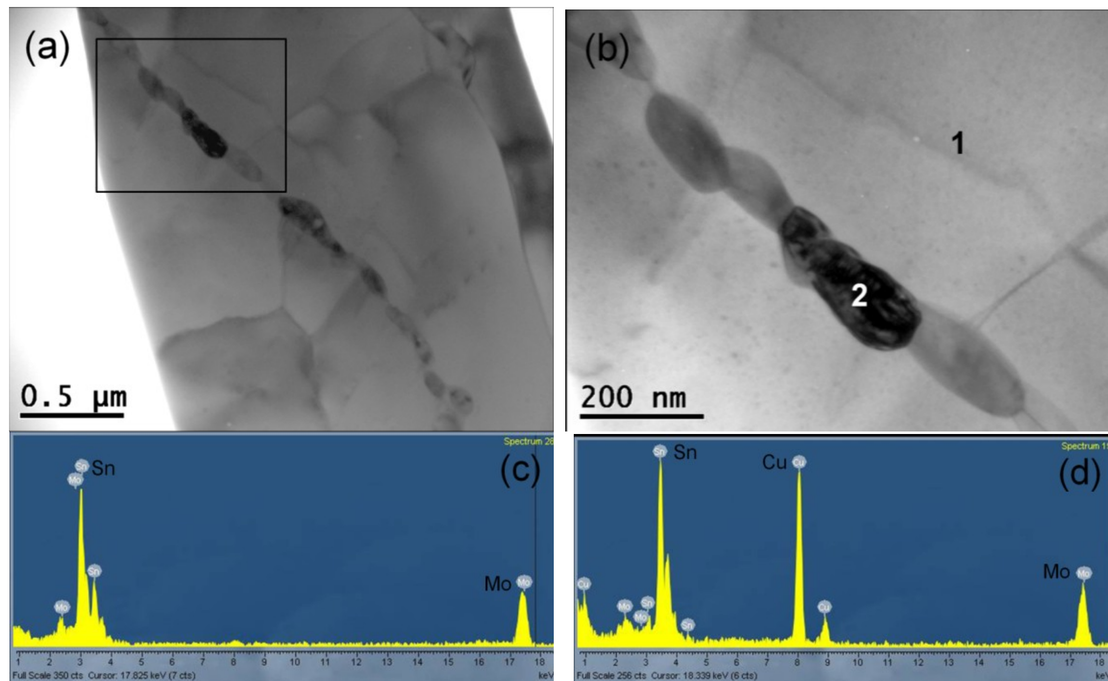

Figure 6-24 TEM micrographs (images (a) and (b)) and EDX spectra (patterns (c) and (d)) of the Sn-Cu film electrodeposited under galvanostatic conditions (15 mA/cm^2, electrical charge passed = 1500 C/dm^2) from bath H, Table 6-1. EDX analyses were carried out at points 1 and 2, with resultant spectra shown in images (b) and (d) respectively.

6.6 Wafer Bumping of Sn-Cu Alloy

Near-eutectic Sn-Cu alloy wafer bumping has been demonstrated in Figure 6-25 by utilising bath H from Table 6-1 and the developed process. Fine pitch (50 µm) near-eutectic Sn-Cu solder bumps were fabricated under potentiostatic conditions (-0.55 V, equates to approximately 15 mA/cm^2). The ISE image in Figure 6-25 micrograph (b) shows that the microstructure in the bumps reveals similar feature to the electrodeposits on Cu coupons (Figure 6-23). Cu_6Sn_5 intermetallics are uniformly spread throughout the bump, which is critical for a robust solder joint at later stages of the bump joining applications. This is because having a brittle nature, intermetallics such as Cu_6Sn_5 are popularly accepted as weak point for the failure of solder joint during service and overgrown or over-aggregated intermetallic phase in the solder joint tends to the locations where cracks typically initiate from [115].

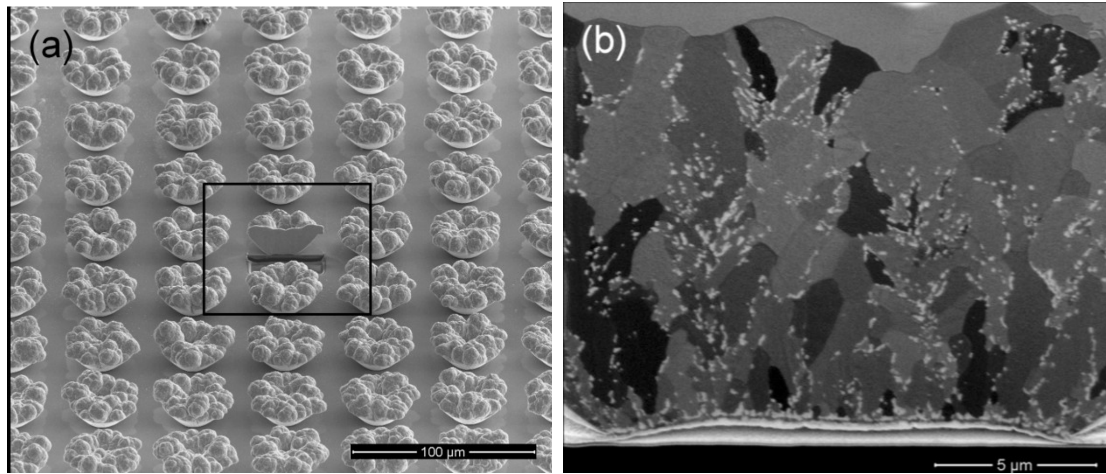

Figure 6-25 Wafer bumping: (a) SEM micrograph of the as-electrodeposited Sn-Cu solder bumps formed under potentiostatic conditions from bath H, Table 6-1, at a potential of -0.55 V; (b) SEM/FIB processed cross-sectional ISE image of the bump at the centre of image (a).

6.7 Summary

Near-eutectic Sn-Cu alloys were electrodeposited from methanesulphonate based baths with the addition of thiourea, OPPE and MSA, the roles and effects of which were analysed by cathodic potentiodynamic polarisation curves. It was found that thiourea complexed with Cu^{2+} ions, which enabled the co-deposition of a Sn-Cu alloy. OPPE showed strong inhibitive effects to Sn deposition and dendrites were eliminated by its presence. MSA not only helped to achieve uniform film deposition, but also significantly refined the Sn grains. Compositional analysis revealed that near-eutectic Sn-Cu alloys (0.6–0.8wt.%Cu) were achievable with a Cu sulphate concentration of 0.007 mol/L in the electrolyte. XRD recognised two phases, Sn and Cu_6Sn_5 in the electrodeposits. This was further confirmed by TEM observations and EDX analysis. Cross-sectional micrographs showed that Cu_6Sn_5 intermetallics were predominantly spread along Sn grain boundaries. Fine pitch near-eutectic Sn-Cu solder bumps were fabricated on wafers, with a uniform distribution of Cu_6Sn_5 throughout the bump.

Chapter 7

Electrodeposition of Sn-Ag Alloys

In this chapter, the electrodeposition of near-eutectic Sn-Ag alloys was investigated from a pyrophosphate-iodide based electrolyte system. The electroplating baths were formulated with additives to improve the microstructure of the electrodeposits. Sn-Ag electrodeposits were characterised to assist the optimisation of the process and to finally achieve near-eutectic Sn-Ag solder bumps on wafers.

7.1 Cathodic Polarisation Studies

7.1.1 Development of Electrolyte

Electrodeposition baths for near-eutectic Sn-Ag alloys were formulated based on a pyrophosphate and iodide system. The details of the electrolytes are listed in Table 7-1. Tin pyrophosphate and silver iodide were respectively used as Sn and Ag sources for the deposition. In order to bring deposition potentials of Sn and Ag closer (ΔE_{Sn-Ag}=0.937 V between Ag/Ag^+ and Sn/Sn^{2+}), $K_4P_2O_7$ was used as the complexing agent for Sn and KI for Ag. Duffield *et al* [116] studied Sn (II) pyrophosphate complexes in aqueous solution. The general dissolution equilibrium involved Sn^{2+} cations (M), Pyr^{4-} anions (L) and H^+ ions and the overall formation constant can thus be expressed:

$$pM + qL + rH \rightleftharpoons M_pL_qH_r;\ \text{Equlibrium Constant}\ \beta_{pqr} = \frac{[M_pL_qH_r]}{[M]^p[L]^q[H]^r} \quad \text{Equation 7-1}$$

Measured by precipitation and dissolution approaches, they found the solubility product of $Sn_2P_2O_7$ (pK_{sp}, K_{sp} =$[Sn^{2+}]^2[(P_2O_7)^{4-}]$) was 19.65, which meant an extremely low concentration of free Sn ions. Therefore, the universal oxidation reaction causing stability issues in Sn electrolyte (discussed in Section 4.4.3) was

effectively inhibited with limited free Sn ion sources and the bath stability was thus significantly improved.

Table 7-1 Pyrophosphate-based bath constituents for near-eutectic Sn-Ag alloy electrodeposition

Chemicals	Baths constituents and concentrations (mol/L)					
	A	B	C	D	E	F
$K_4P_2O_7$	1.00	1.00	1.00	1.00	1.00	1.00
KI	2.00	2.00	2.00	2.00	2.00	2.00
$Sn_2P_2O_7$	–	0.20	–	0.20	0.20	0.20
AgI	–	–	0.005	0.005	0.005	0.005
PEG 600 (ml/L)	–	–	–	–	2	2
HCHO	–	–	–	–	–	0.05

In some baths from Table 7-1, polyethylene glycol 600 (PEG 600, average molecular weight of 600, Figure 7-1) and formaldehyde were added for improvement in the microstructure of electrodeposits. Their effects on the electrodeposition process were studied using cathodic potentiodynamic polarisation.

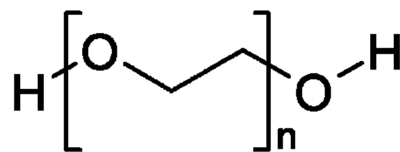

Figure 7-1 Schematic chemical structure of polyethylene glycol 600 (PEG 600), n = 12.

7.1.2 Electrodeposition Processes for Tin and Silver

The electrochemical reduction of metallic species (tin and silver) in the pyrophosphate-iodide based electrolytes and other cathodic behaviour of the baths are examined and illustrated in Figure 7-2. For curve 1 in bath A which contains neither Sn or Ag ions (complexing agents $K_4P_2O_7$ and KI are providing sufficient conductivity in the electrolyte), the initial partial of the curve stays stable and shows a

negligible current density (lower than 0.01 mA/cm^2) as the potential is swept cathodically. After a potential of approximately -1.3 V, an obvious increase of current density is observed and the value jumps quickly over 10 mA/cm^2. This current density should be attributed to the hydrogen evolution at the cathode surface, as confirmed by the bubbles observed during the experiment.

The cathodic polarisation curve for bath B (Figure 7-2, curve 2) shows the deposition process for tin. It can be noted that the open-circuit potential for the copper coupon moves from -0.6 V to approximately -0.5 V, with the addition of Sn pyrophosphate in bath B. As can be seen in curve 2, the electrodeposition of Sn commences rapidly at a potential of about -0.85 V and approaches to a limiting current density of approximately 20 mA/cm^2 after fluctuations. Earlier reports [117] proposed that the discharge of metallic pyrophosphate-based Sn complexes might occur as follows:

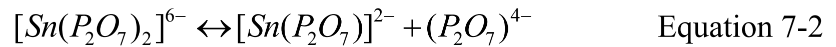

$$[Sn(P_2O_7)_2]^{6-} \leftrightarrow [Sn(P_2O_7)]^{2-} + (P_2O_7)^{4-} \qquad \text{Equation 7-2}$$

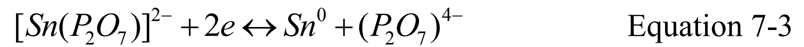

$$[Sn(P_2O_7)]^{2-} + 2e \leftrightarrow Sn^0 + (P_2O_7)^{4-} \qquad \text{Equation 7-3}$$

The further increase in the current density of curve 2 from the potential of -1.3 V onward should be attributed to the concurrent hydrogen evolution reaction, as similarly indicated in the curve 1.

A typical cathodic polarisation curve for the deposition of Ag in bath C from Table 7-1 is also included in Figure 7-2 (curve 3), which appears to present a mass-transport controlled mechanism. The electrodeposition of Ag begins at a potential of -0.55 V and then remains stable at a current density of close to 0.1 mA/cm^2 as the potential increases cathodically. This limiting rate of deposition, largely defined by the concentration of Ag ions in the solution, is achieved by the consumption and replenishment of Ag ions at the cathode. It is observed that the current density steadily increases again after -1.3 V and this cathodic current increase is also due to hydrogen evolution.

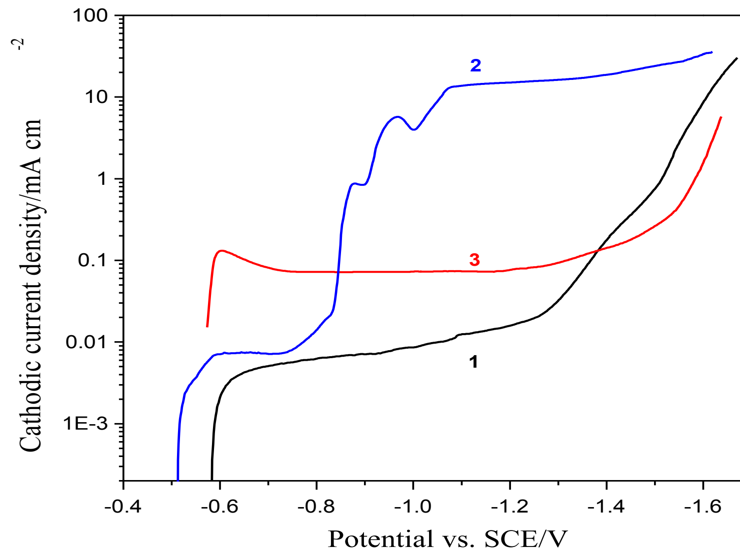

Figure 7-2 Cathodic potentiodynamic polarisation curves in baths A (curve 1), B (curve 2) and C (curve 3) from Table 7-1, showing the processes of Sn and Ag deposition individually. Potential scan rate: 1 mV/s.

The kinetics of Ag electrodeposition from a suspension of silver iodide in aqueous media were studied by Fourcade and Tzedakis [118]. In their study, the reduction of silver iodide at the silver electrode could take place through several processes such as direct reduction of solid particles, or reduction of the adsorbed silver iodide. Oliveira *et al* [119] studied the effects of KI on Ag electrodeposition and proposed a electrodeposition mechanism as below:

$$AgI_p^{(1-p)} + e \leftrightarrow Ag + pI^- \qquad \text{Equation 7-4 [119]}$$

Where p can have a value between 2 and 4.

7.1.3 Effects of Additives

The cathodic polarisation curves illustrating the co-reduction of the Sn-Ag alloy with and without the addition of PEG 600 and formaldehyde (baths D, E and F from Table 7-1) are presented in Figure 7-3. It can be seen in all the three curves that Ag deposition begins at a potential of approximately -0.5 V, almost the same as that in Figure 7-2, curve 3. For curve 1 in bath D where no additives are present, co-deposition of Sn and Ag occurs at potentials more negative than -0.88 V and again reaches a diffusion limiting current density plateau of ~20 mA/cm^2, as the potential is

cathodically scanned. After the Sn deposition potential is reached, Ag therefore is co-depositing with Sn at its limiting current density [97].

With the addition of PEG and formaldehyde, the shape of cathodic polarisation curves is significantly modified (Figure 7-3, curves 2 and 3). When only PEG 600 is introduced in bath E (curve 2), Sn deposition is highly inhibited, demonstrated by the depressed co-deposition current density in the curve. This is because glycol molecules are likely to be adsorbed on the freshly deposited Sn surface and therefore inhibit further deposition [120, 121].

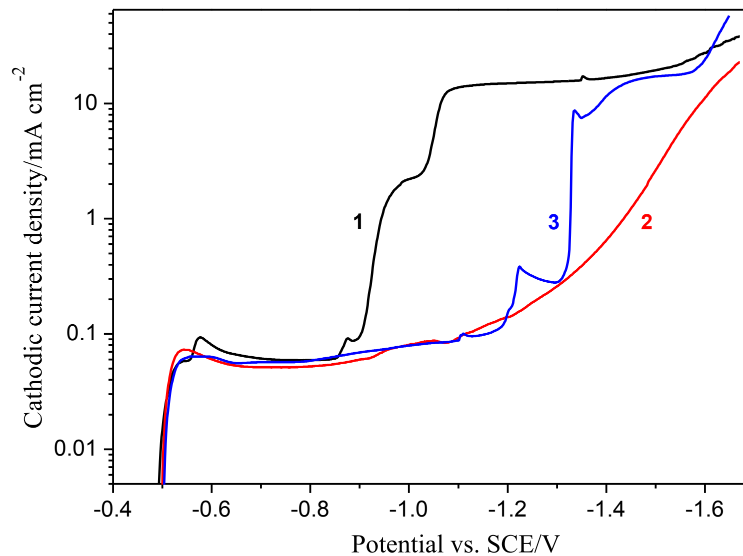

Figure 7-3 Cathodic potentiodynamic polarisation curves in baths D (curve 1), E (curve 2) and F (curve 3) from Table 7-1, showing the effects of PEG and formaldehyde. Potential scan rate: 1 mV/s.

In order to further examine the effect of PEG 600 on the deposition behaviour of Sn, different concentrations of PEG 600 (2, 4 and 10 ml/L) were added to bath E, as illustrated in Figure 7-4. At the various concentrations examined, PEG 600 shows very similar effects. Chen *et al* [120] explored the effect of PEG (molecular weights of 200, 600, 2000 and 4000) as an inhibitive agent on tin alloy deposition and concluded that a molecular weight of 200 showed the least effects. PEG with a molecular weight of 4000 exhibited the strongest inhibition because of its heavier and longer molecules. However, this would result in a very limited process window for the desirable near eutectic alloy composition, as such PEG 600 is proven to be a suitable choice.

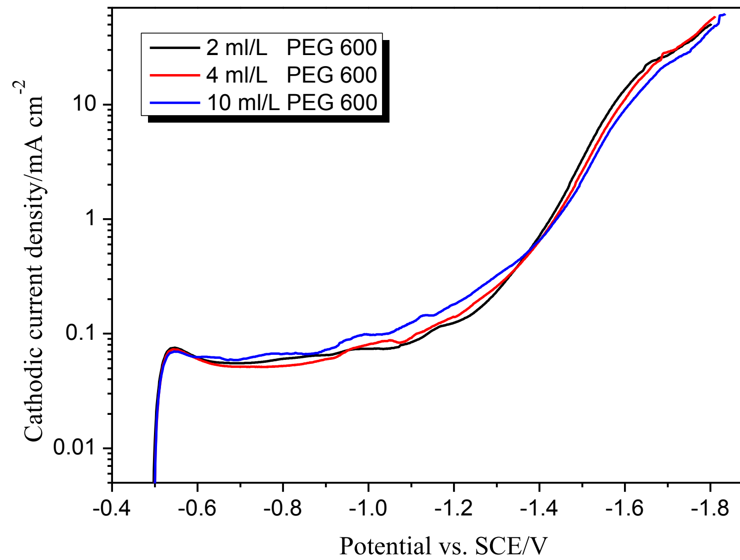

Figure 7-4 Cathodic potentiodynamic polarisation curves from baths E, Table 7-1 with different concentrations of PEG and formaldehyde. Potential scan rate: 1 mV/s.

It can also be seen that in bath F from Table 7-1, where formaldehyde is added to the solution, distinctive changes can be observed from the cathodic polarisation curve plotted (Figure 7-3, curve 3). At a potential of -1.2 V, the curve diverges from curve 2 for bath D (no formaldehyde) with a sharp but limited increase in current density. Following a current arrest at approximately 0.3 mA/cm^2, the current density rises quickly again all the way to the limiting current density (~20 mA/cm^2) and this value remains stable until hydrogen evolution becomes evident. Such changes in the cathodic polarisation curves in Figure 7-3 indicate that the introduction of formaldehyde has affected the inhibitive effect of PEG 600 on Sn deposition.

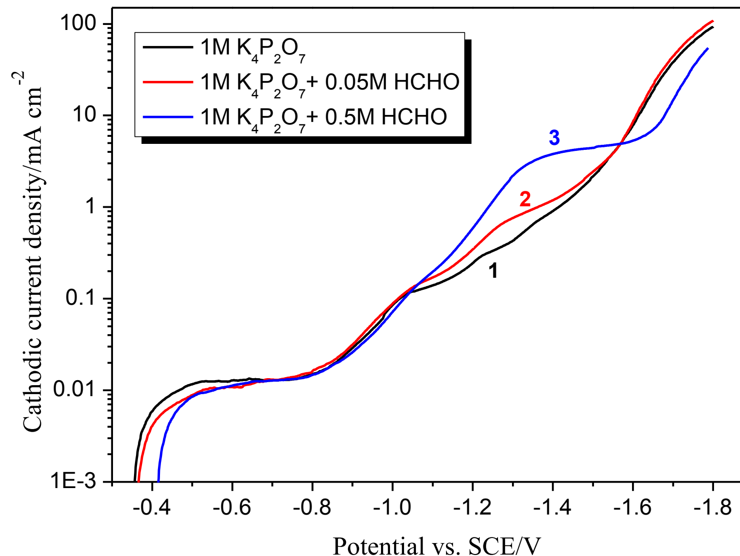

Figure 7-5 Cathodic potentiodynamic polarisation curves investigating the effects of formaldehyde in baths of $K_4P_2O_7$ 1 mol/L and different formaldehyde concentrations: 0 mol/L (curve 1), 0.05 mol/L (curve 2) and 0.5 mol/L (curve 3). Potential scan rate: 1 mV/s.

In order to further understand the effects of formaldehyde, cathodic polarisation curves were conducted in $K_4P_2O_7$ (1 mol/L) + formaldehyde (0.05 mol/L and 0.5 mol/L) solutions, with results shown in Figure 7-5. By comparing the three curves, increases in current density (curves 2 and 3) from a potential of around -1.2 V are found due to the addition of formaldehyde. When the concentration of formaldehyde is increased from 0.05 mol/L to 0.5 mol/L, a limiting current density plateau can be observed in curve 3, which demonstrates the reductive decomposition of the formaldehyde to methanol as shown in the equation below [122, 123]:

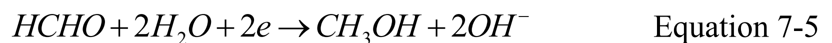

$$HCHO + 2H_2O + 2e \rightarrow CH_3OH + 2OH^- \quad \text{Equation 7-5}$$

This equation explains the current density shoulder at about -1.2 V in Figure 7-3, curve 3. The reduction of formaldehyde to methanol occurs before the potential of Sn deposition is reached with both PEG 600 and formaldehyde present. This indicates that the deposition of Sn (and silver) is accompanied by the reduction of formaldehyde and the inhibitive effects of PEG. These synergetic effects result in a smooth and bright surface as is discussed in later sections of this chapter.

7.2 Characterisation of Sn-Ag Electrodeposits

Samples of Sn-Ag electrodeposits on copper coupons were obtained in the baths listed in Table 7-1. Characterisation followed to analyse the deposits in terms of composition, phase identification and microstructural observation.

7.2.1 Compositional Analysis

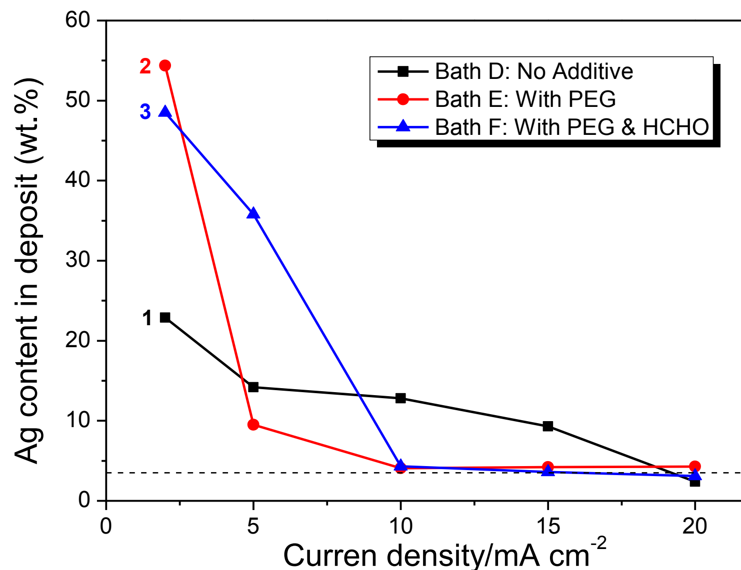

Figure 7-6 Ag content (wt.%) in the electrodeposited Sn-Ag films vs. galvanostatic current density utilising baths D, E and F from Table 7-1. Measurements carried out by WDX. Broken line represents the objective Ag content, 3.5wt.%.

The composition of the as-electrodeposited Sn-Ag films under galvanostatic conditions in baths D, E and F from Table 7-1 is analysed by WDX. Figure 7-6 shows the Ag content in Sn-Ag films produced at galvanostatic current densities of 2, 5, 10, 15 and 20 mA/cm^2 respectively. The objective eutectic Sn-Ag alloy contains 3.5wt.% of Ag (represented by broken line in Figure 7-6). It can be seen from this figure that the Ag content decreases gradually with increasing current density from all the three baths examined. In bath D (no additives), the Ag content drops relatively smoothly from 23wt.% at a current density of 2 mA/cm^2 to slightly below the eutectic content (3.5 wt.%) when the current density reaches up to 20 mA/cm^2. In baths E and F, the Ag contents are approaching or even exceeding 50wt.% at 2 mA/cm^2. This is likely to be attributed to the strong inhibitive effect of PEG on Sn electrodeposition as shown in Figure 7-3 and Figure 7-4. However, it is worth noting that the Ag content

decreases quickly to approximately the eutectic composition over a current density range from 10 to 20 mA/cm^2 in baths E and F, making the deposition of near-eutectic Sn-Ag alloys (3.1–4.3wt.%Ag) feasible.

7.2.2 Phase Identification

The phases in the electrodeposited Sn-Ag alloy film in bath F from Table 7-1 at a current density of 15 mA/cm^2 are identified by X-ray diffraction and shown in Figure 7-7. Except the Cu (200) peak from the copper substrate, all the other peaks represent two phases: β-Sn and Ag_3Sn. This means that the electrodeposited Sn-Ag alloy film from the pyrophosphate-iodide bath has a biphasic structure. This result agrees with the phase structure from the Sn-Ag thermal equilibrium phase diagram in Figure 3-3, showing phases of β-Sn and ε(Ag_3Sn) at the composition investigated.

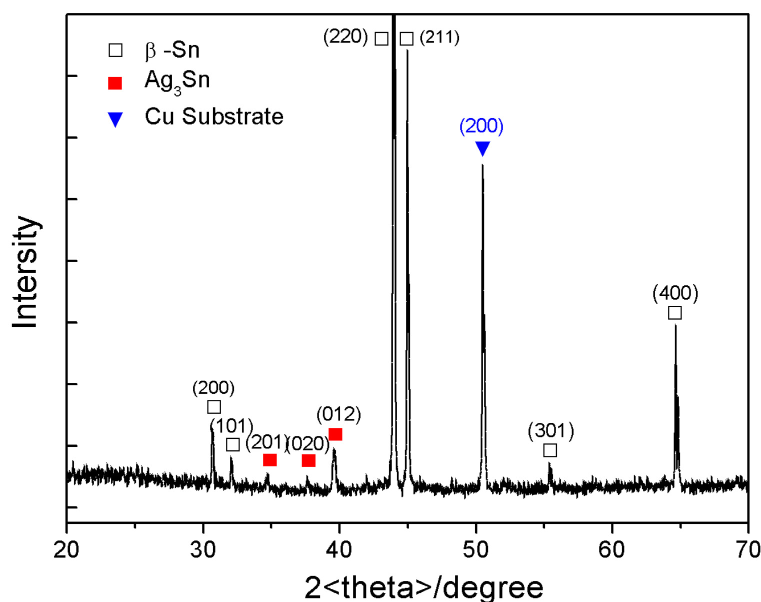

Figure 7-7 XRD spectrum of the as-electrodeposited Sn-Ag film galvanostatically produced from bath F, Table 7-1 at a current density of 15 mA/cm^2, electrical charge passed = 1500 C/dm^2.

7.2.3 Thermal Analysis

The differential scanning calorimetry (DSC) measurements were conducted to characterise the thermal properties of Sn-Ag electrodeposits, data is illustrated in Figure 7-8. Test samples were prepared in bath D from Table 7-1 by varying the galvanostatic current density applied. Again, the endothermic curve for a pure tin

electrodeposit, showing a peak value of 234°C, is provided in Figure 7-8 as a reference. In the equilibrium phase diagram for Sn-Ag alloy (Figure 3-3), the eutectic composition (Sn-3.5wt.%Ag) shows a melting point of 221°C in the equilibrium form. For the three curves measured in Figure 7-8, peaks at approximately 222°C are observed, confirming the existence of eutectic constituents in the electrodeposits. However, variations can be observed in different curves. With a similar onset temperature of about 216°C, the off-eutectic compositions, 4.3wt.% and 11.3wt.% of Ag, tend to show a widened melting interval, particularly for the latter, compared to the near-eutectic composition (3.6wt.%).

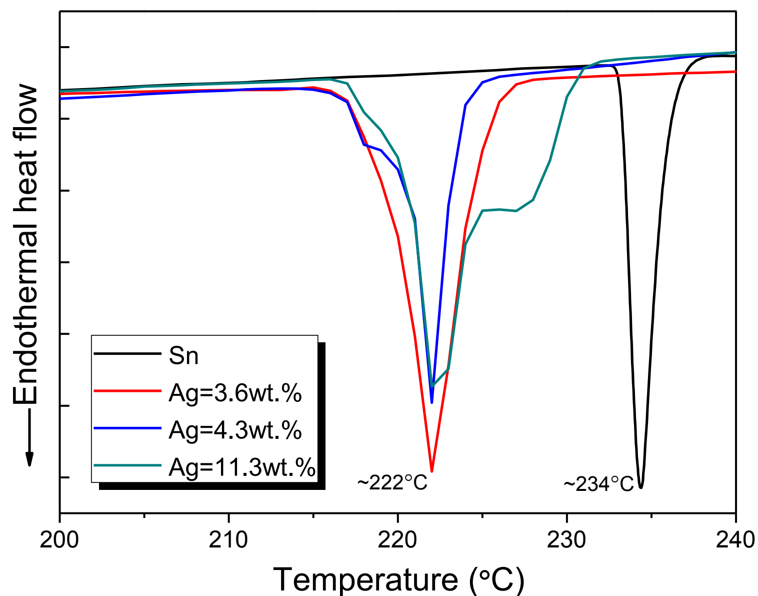

Figure 7-8 DSC measurements of Sn-Ag electrodeposits from bath D, Table 7-1. Scan rate at 10 K/min. Pure Sn presented as a reference.

7.2.4 Surface Morphology and Microstructure

The electrodeposited Sn-Ag films at galvanostatic current densities of 2, 10 15 and 20 mA/cm^2 in baths D, E and F respectively (Table 7-1) were analysed by SEM to study their surface morphologies. During each electrodeposition trial, the total electrical charge for each sample was again kept constant at 1500 C/dm^2. SEM/FIB micro-processing was applied to selected samples for cross-sectional observation.

7.2.4.1 Electrodeposits from Additive-Free Bath

The surface morphology of electrodeposits from bath D in Table 7-1, where no additive is present, is shown in Figure 7-9. A relatively flat and non-porous surface with a few protrusions is produced as shown in image (a), at a low current density of 2 mA/cm^2. Although it shows a relatively smooth morphology, the composition of the deposit (22.9wt.% Ag) is far from the eutectic composition (3.5wt.% Ag), as measurements illustrated in Figure 7-6, curve 1. As the current density is increased to 10 mA/cm^2 (Figure 7-9, image (b)), a much more porous morphology was produced as voids can be easily seen in the image. The cross-sectional image taken by SEM/FIB in Figure 7-10 reveals that the electrodeposit consists of long columnar shape (tin) grains, with sizes smaller at the bottom close to the copper substrate.

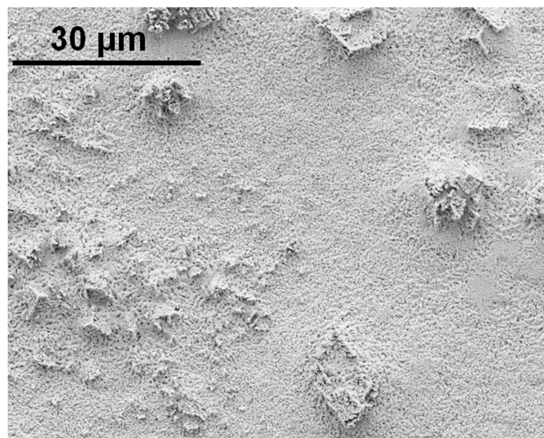

(a) current density = 2 mA/cm^2

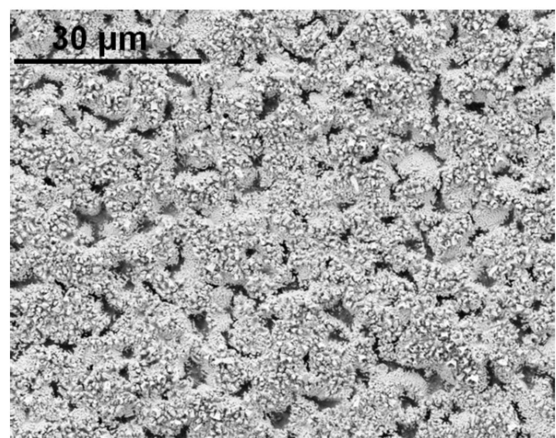

(b) current density = 10 mA/cm^2

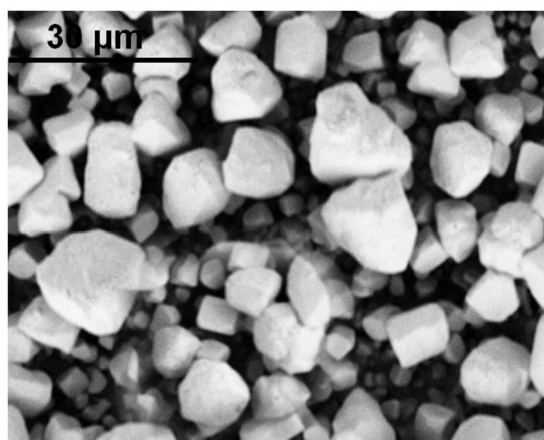

(c) current density = 15 mA/cm^2

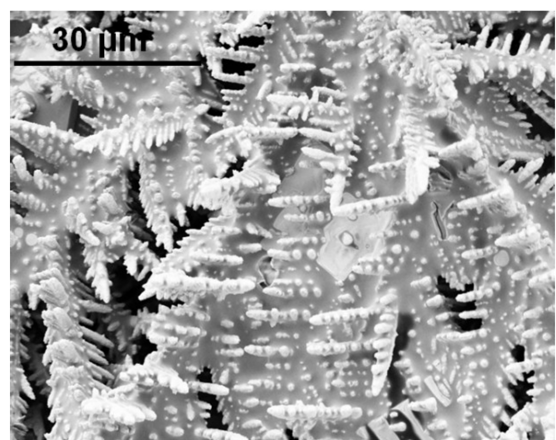

(d) current density = 20 mA/cm^2

Figure 7-9 SEM micrographs of Sn-Ag films electrodeposited under galvanostatic conditions from bath D, Table 7-1, electrical charge passed = 1500 C/dm^2.

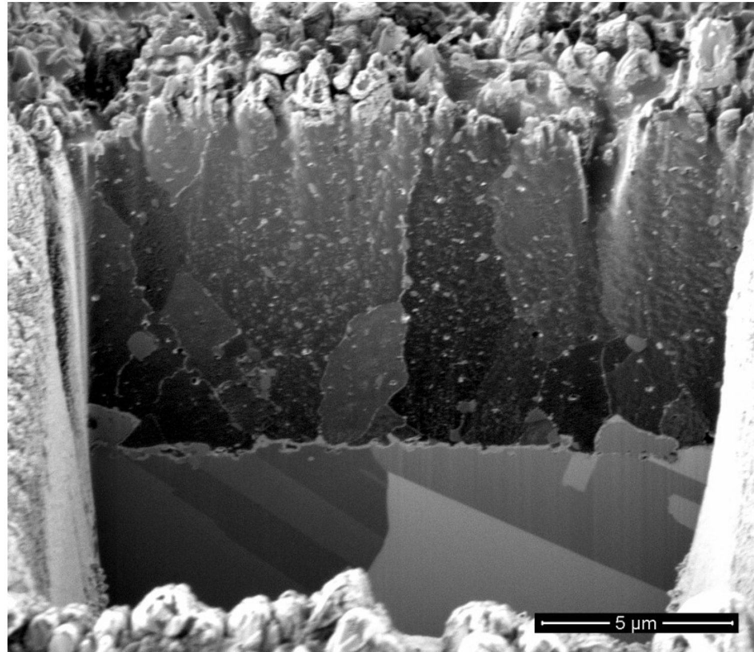

Figure 7-10 SEM/FIB processed cross-sectional ISE image of the electrodeposited Sn-Ag film (Figure 7-9, image (b)) under galvanostatic conditions from bath D, Table 7-1 (10 mA/cm^2, electrical charge passed = 1500 C/dm^2).

Figure 7-9, image (c) shows a nodular characteristic on the sample surface. Nodules are of several microns in size and they seem to consist of smaller grains as shown in the SEM/FIB cross-sectional image in Figure 7-11. These nodules loosely pile up in the electrodeposits and the outermost ones appear to be of larger size than those underneath.

Figure 7-9, image (d) shows a dendritic morphology from the highest current density examined (20 mA/cm^2). These fern-like electrodeposits contain significant porosity. The SEM/FIB cross-sectional image of one dendrite is shown in Figure 7-12. As can be seen from this figure, each fern-like structure consists of grains loosely aggregating with easily seen pores in-between. According to the composition measurement in Figure 7-6, though these dendritic deposits are close to the eutectic composition, deposits of such morphologies are not desirable for electroplating Sn-Ag solder alloy proposed for flip-chip interconnection in electronics. It is commonly seen that the current densities, at which such dendritic and nodular morphologies are formed, are approaching or exceeding the limiting current density. At such high current density conditions, there can be a strong tendency for outward growth, which eventually leads to dendritic and nodular deposits.

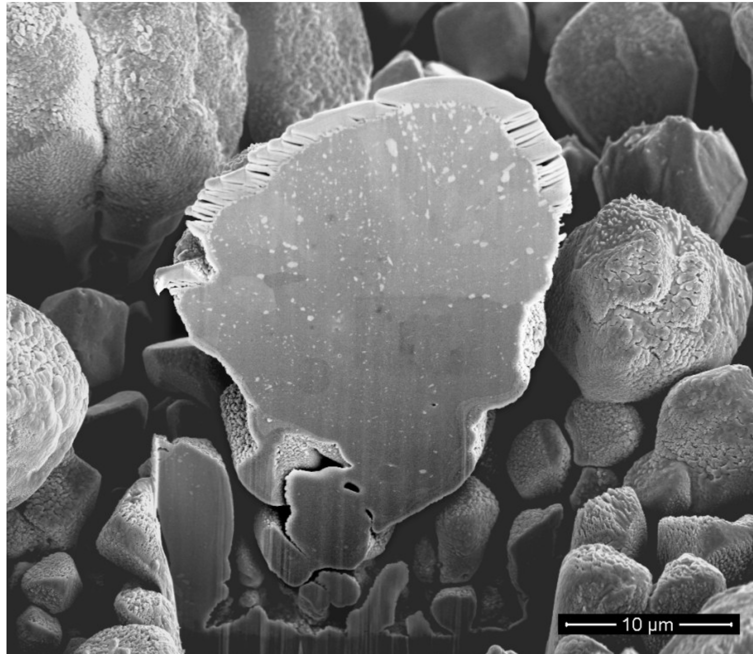

Figure 7-11 SEM/FIB processed cross-sectional image of the electrodeposited Sn-Ag film (Figure 7-9, image (c)) under galvanostatic conditions from bath D, Table 7-1 (15 mA/cm^2, electrical charge passed = 1500 C/dm^2).

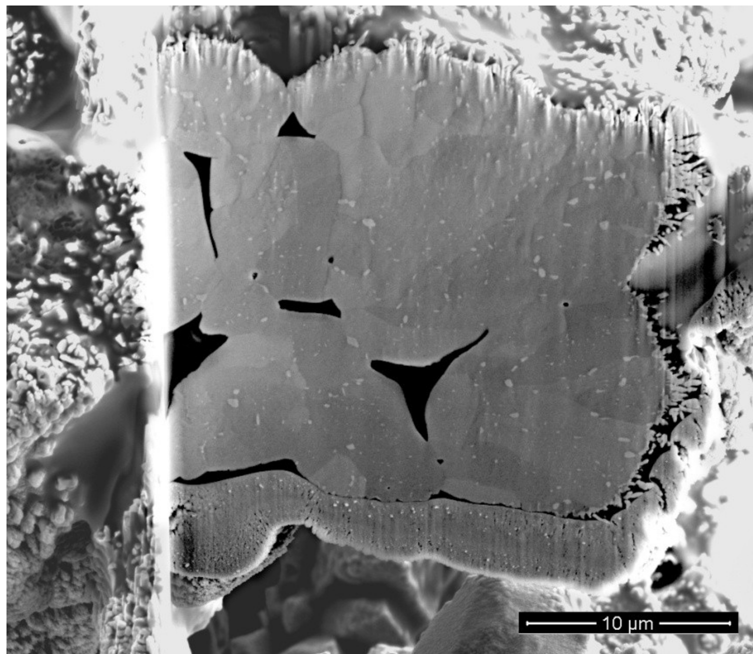

Figure 7-12 SEM/FIB processed cross-sectional image of the electrodeposited Sn-Ag film (Figure 7-9, image (d)) under galvanostatic conditions from bath D, Table 7-1 (20 mA/cm^2, electrical charge passed = 1500 C/dm^2).

There is one common feature that is worth mentioning and evident in all the three cross-sectioned images (Figures 7-10, 7-11 and 7-12). Small particles (white spots in

the images) precipitated evenly within all the deposits as can be seen in all the three images. These second phases are most likely the intermetallic phase (e.g. Ag_3Sn, as is evidenced by XRD analysis in Figure 7-7) in the electrodeposits, demonstrating the existence of silver in the electrodeposit.

7.2.4.2 Effects of PEG

The inhibitive effects of PEG 600 on Sn deposition have been demonstrated by the cathodic polarisation curves in Figure 7-3 and Figure 7-4. Under such effects, the surface morphology of electrodeposits produced in bath E, with the presence of 2 ml/L PEG 600, is shown in Figure 7-13. Compared to the electrodeposits in bath D, there are no dendritic or nodular morphologies. However, irregular shaped protrusions can be observed growing over the current density range examined, as shown in Figure 7-13. This is probably owing to the adsorptive behaviour of PEG on the newly deposited Sn surface, which has left limited locations for the proceeding of outgrowth. Nevertheless, compared to images (b), (c) and (d), the morphology shown in image (a) appears to be unique with distinct flower-like deposits with a compact layer beneath them.

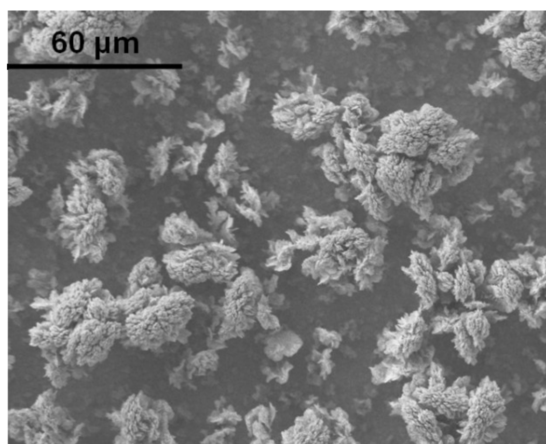

(a) current density = 2 mA/cm^2

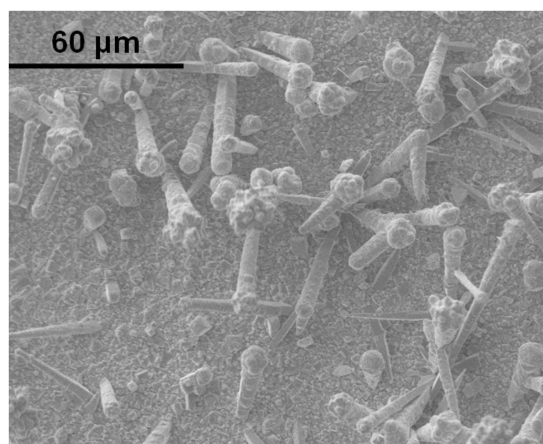

(b) current density = 10 mA/cm^2

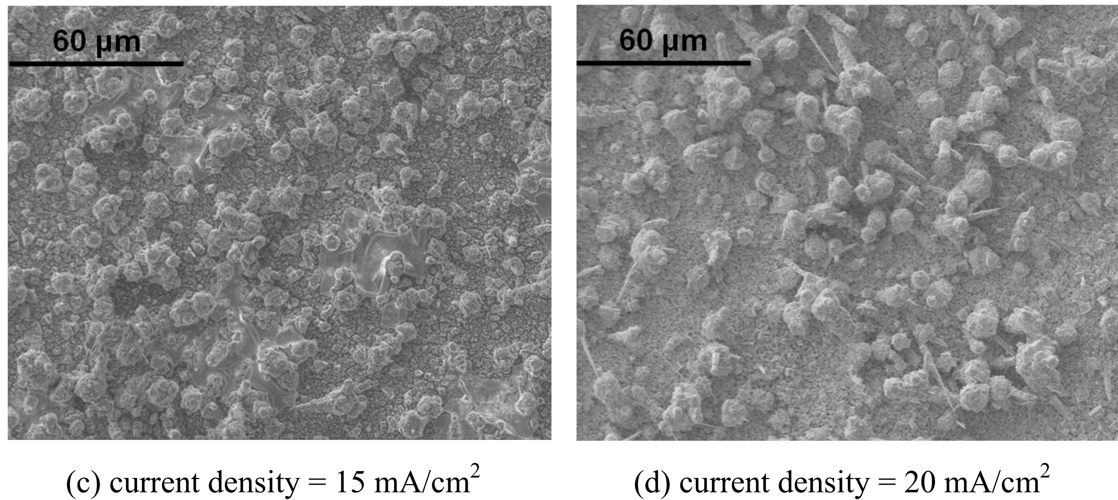

(c) current density = 15 mA/cm^2 (d) current density = 20 mA/cm^2

Figure 7-13 SEM micrographs of Sn-Ag films electrodeposited under galvanostatic conditions from bath E, Table 7-1, electrical charge passed = 1500 C/dm^2.

To understand its formation, such a flower-like feature was cross-sectioned and observed by SEM/FIB with results shown in Figure 7-14. Image (a) in this figure confirms a highly porous microstructure within the “flower”. EDX measurement shows that such a “flower” chemically consists of pure silver. The mechanism to explain this is that under the electrodeposition potential corresponding to the relatively low current density applied (2 mA/cm^2), the electrodeposition of Sn has just commenced owing to the inhibitive effect of PEG 600. Therefore, the electrodeposition current (limiting current) for Ag primarily contributes to the total current value and as such a deposit of pure Ag “flowers” is consequently observed. This porous microstructure shows some similarity with previously analysed dendritic and nodular morphologies (Figure 7-9, images (c) and (d)) in terms of the non-compact nature, when the corresponding current densities are approaching or exceeding the limiting value.

In Figure 7-14, image (b), a compact layer grown above the copper substrate but underneath the “flower” feature can be observed. This layer is believed to be deposited before the formation of the “flower” features above and probably contains significant amount of both Sn and silver. As a result the whole deposit exhibits an average Ag content of 55wt.% as indicated in Figure 7-6.

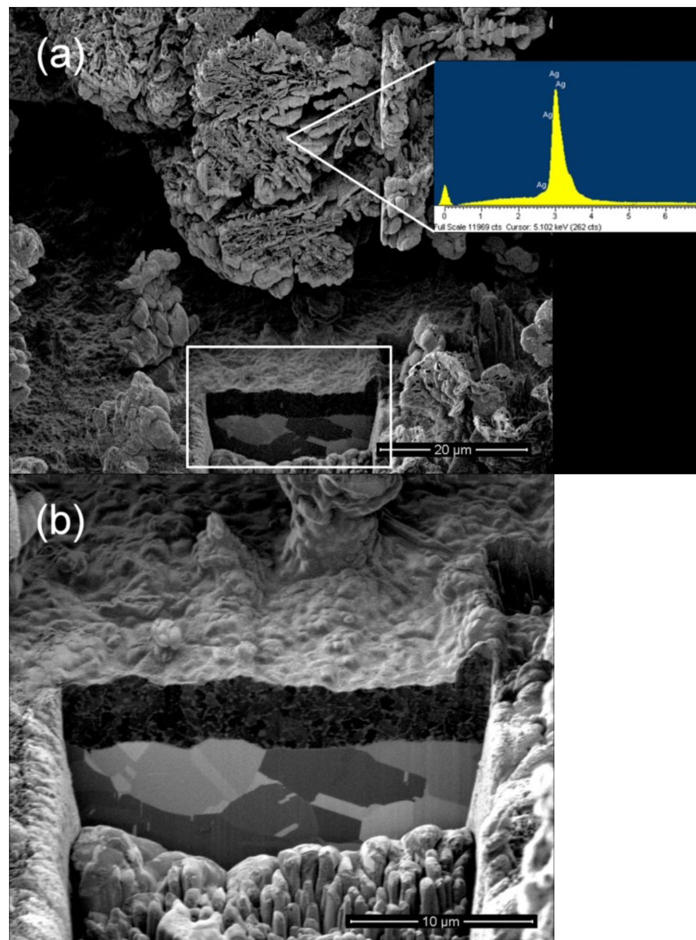

Figure 7-14 SEM/FIB processed cross-sectional ISE images and EDX spectrum of the Sn-Ag electrodeposits (Figure 7-13, image (a)) under galvanostatic conditions from bath E, Table 7-1 (2 mA/cm^2, electrical charge passed = 1500 C/dm^2). (a) general view of the cross-sectioned feature and EDX spot test spectrum; (b) magnified micrograph of the deposition layer on copper substrate and underneath the "flower".

7.2.4.3 Effects of PEG and Formaldehyde

Finally, under the synergetic effects of both PEG 600 and formaldehyde, smooth and bright surfaces are achieved in a current density range from 10 to 20 mA/cm^2 as shown in Figure 7-15. Near-eutectic composition is also achieved over this current density range as indicated in Figure 7-6 (3.1–4.3wt.%). However, when the current density is as low as 2 mA/cm^2 (Figure 7-15, image (a)), a flower-like morphology can again be observed, the reason for which is similarly analysed in Section 7.2.4.2.

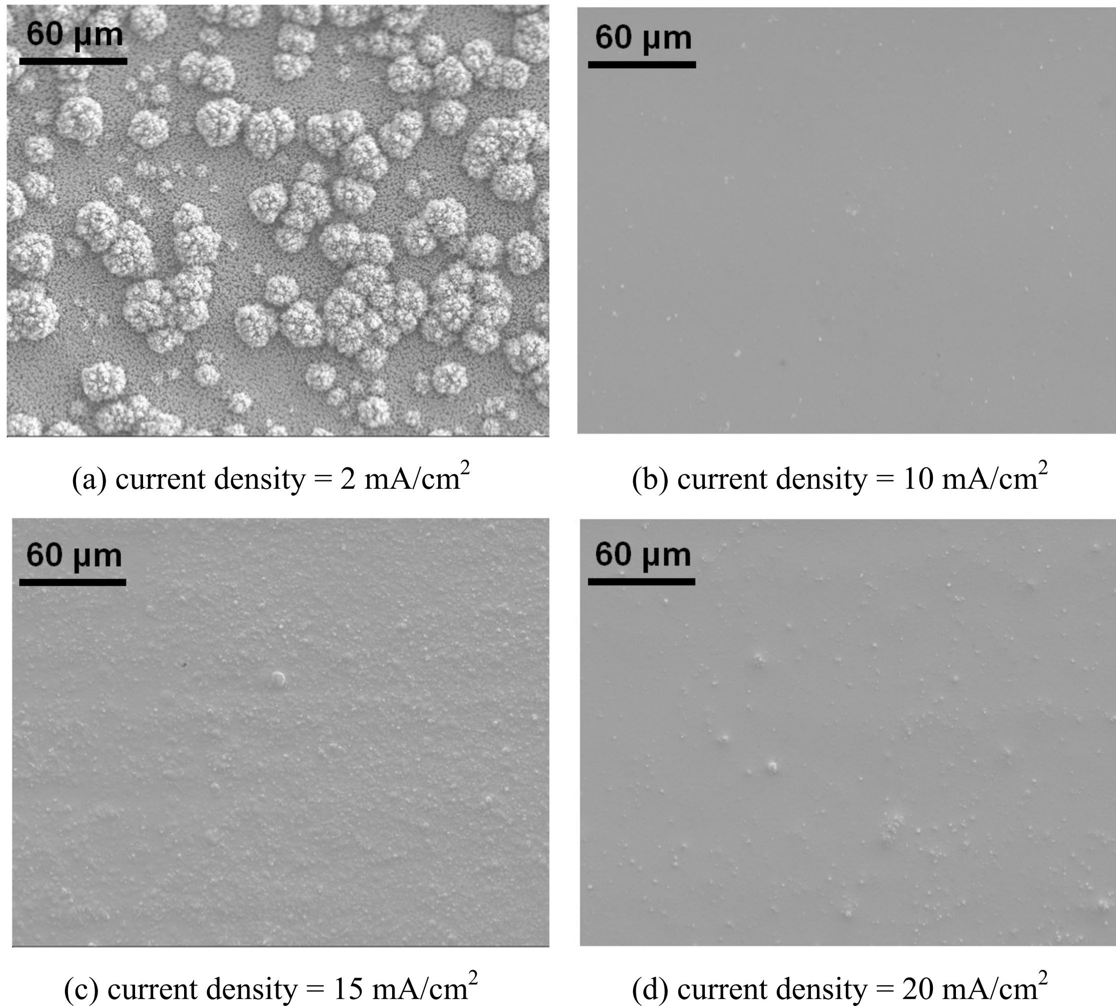

(a) current density = 2 mA/cm^2 (b) current density = 10 mA/cm^2

(c) current density = 15 mA/cm^2 (d) current density = 20 mA/cm^2

Figure 7-15 SEM micrographs of Sn-Ag films electrodeposited under galvanostatic conditions from bath F, Table 7-1, electrical charge passed = 1500 C/dm^2.

7.3 Wafer Bumping of Sn-Ag Alloy

Based on the previous study, near-eutectic Sn-Ag solder bumps were produced on wafers using the pyrophosphate-iodide system developed. Figure 6-25 shows the as-electrodeposited bumps in bath F with the presence of additives under potentiostatic conditions (-1.37 V), which corresponds to a current density of 15 mA/cm^2 according to the cathodic polarisation curve (Figure 7-3). Near-eutectic Sn-Ag alloy composition is therefore achieved under such conditions. Image (b) of Figure 6-25 shows a cross-sectioned image of a solder bump using FIB/SEM. It is clearly seen that Ag_3Sn phase homogenously disperses within the solder bump, which is critical for a robust solder joint at later stages of the bump joining applications [124].

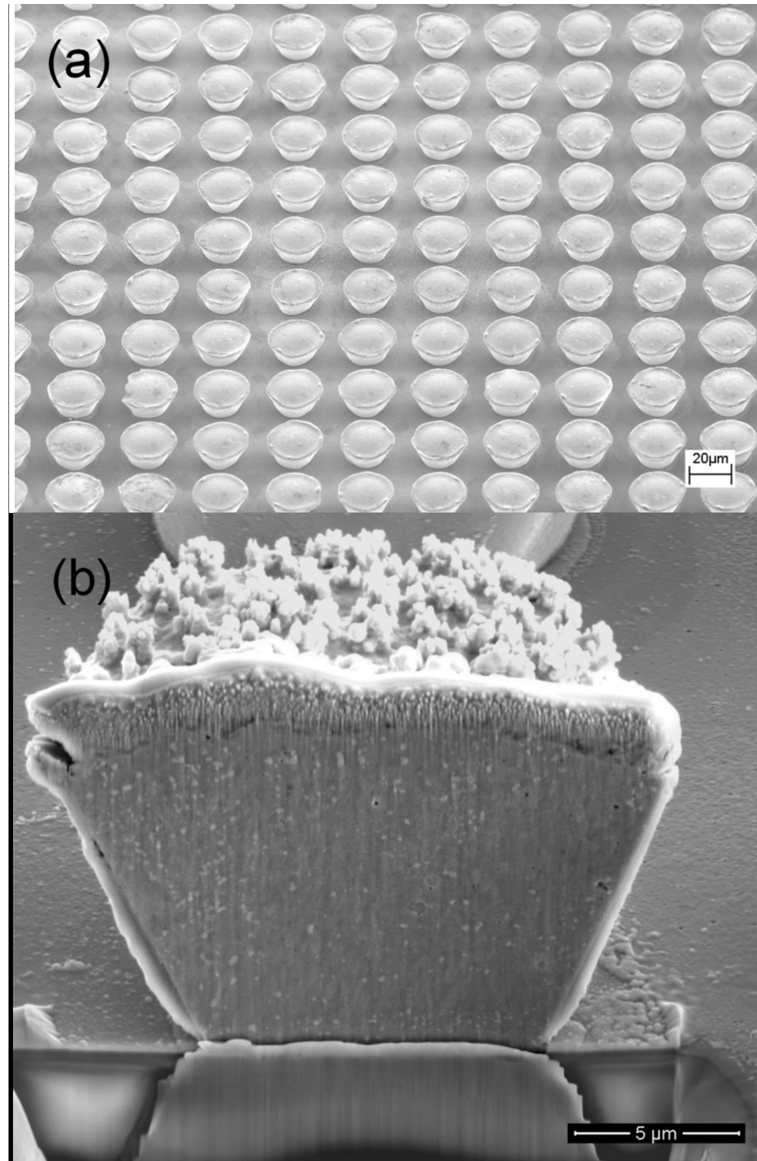

Figure 7-16 Wafer bumping: (a) SEM micrograph of the as-electrodeposited Sn-Ag solder bumps formed under potentiostatic conditions from bath F, Table 7-1, at a potential of -1.37 V; (b) SEM/FIB processed cross-sectional image of a bump.

7.4 Summary

Near-eutectic Sn-Ag alloys were electrodeposited from a pyrophosphate-iodide system with the addition of PEG 600 and formaldehyde, the roles and effects of which were analysed by cathodic potentiodynamic polarisation curves. It was demonstrated that PEG had a strong inhibitive effect on Sn deposition, as a result producing Sn deposits with protrusions on the surface, whilst the synergetic effects of both PEG and formaldehyde enabled a smooth morphology of Sn-Ag film. The microstructure of electrodeposits from different baths was observed. Without additives, surface

morphology evolved from flat to nodular and dendritic features with an increasing applied current density. Compositional analysis revealed that near-eutectic Sn-Ag alloys (3.1–4.3wt.%Ag) were achievable with the addition of PEG and formaldehyde. XRD identified two phase, β-Sn and Ag_3Sn in the electrodeposits. Near-eutectic Sn-Ag solder bumps were fabricated at a wafer scale, with a uniform distribution of Ag_3Sn throughout the bump. These bumps can be readily applied to solder interconnects through the flip chip assembly process.

Chapter 8

Electrodeposition of Sn-Ag-Cu Alloys

With knowledge from the electrodeposition of Sn-Ag alloys from a pyrophosphate-iodide based electrolyte system in Chapter 7, the electrodeposition of near-eutectic Sn-Ag-Cu ternary alloys is investigated in this chapter.

8.1 Cathodic Polarisation Studies

8.1.1 Development of Electrolyte

The pyrophosphate-iodide system has proved to be capable of producing near-eutectic Sn-Ag alloys with a smooth surface morphology under the effects of additives (PEG 600 and formaldehyde), as discussed in Chapter 7. This electrolyte system has also shown excellent stability compared to the methanesulphonate based baths formulated for Sn-Cu alloy electrodeposition (Chapter 6). Therefore, such a pyrophosphate-iodide system was further investigated for producing near-eutectic Sn-Ag-Cu ternary alloys.

The bath constituents were considered and adjusted on the basis of the binary Sn-Ag system, with Table 8-1 listing the combinations examined for the ternary Sn-Ag-Cu system. Cathodic potentiodynamic polarisation was carried out to investigate the characteristics of the baths under varying process conditions, such as agitation and operating bath temperature.

Table 8-1 Bath constituents for near-eutectic Sn-Ag-Cu alloy electrodeposition

Chemicals	Baths constituents and concentrations (mol/L)			
	A	B	C	D
$K_4P_2O_7$	1.00	1.00	1.00	1.00

KI	2.00	2.00	2.00	2.00
$Sn_2P_2O_7$	0.25	0.25	0.25	0.25
AgI	–	0.005	0.008	0.008
$Cu_2P_2O_7$	–	0.0025	0.002	0.002
PEG 600 (ml/L)	–	–	–	2
HCHO	–	–	–	0.02

8.1.2 Effects of Agitation

The electrodeposition process of Sn-Ag-Cu alloys, as well as the effects of agitation, were investigated by potentiodynamic polarisation, as shown in Figure 8-1 (a) and (b), with plot (b) showing the magnified initial scans for a close analysis. Curve 1 illustrates the electrodeposition behaviour of bath A from Table 8-1, where Sn is the only metallic species to deposit. Moreover, with the addition of Ag (AgI) and Cu ($Cu_2P_2O_7$) into the electrolyte, i.e. bath B from Table 8-1, the co-deposition behaviour of ternary Sn-Ag-Cu alloy is characterised in curve 2. The effects of agitation (magnetic stirring at 300 rpm) on the cathodic electrodeposition behaviour of Sn-Ag-Cu alloys are investigated in curve 3.

In Figure 8-1, diagram (a), curve 1, as the scan starts from the open-circuit potential (around -0.5 V), the deposition of Sn commences from -0.88 V, where the current density increases to form a lengthy plateau (~20 mA/cm^2). The mass-transport limitation of Sn ions (Sn^{2+}) from the bulk electrolyte to the cathode surface is responsible for this plateau formation [125]. It is noticeable that in the other two curves (2 and 3) in diagram (a), similar current density increases can be observed at the same potential, which are also responsible for Sn deposition. The further increase in current density in curve 1 after a potential of approximately -1.2 V is due to concurrent hydrogen evolution.

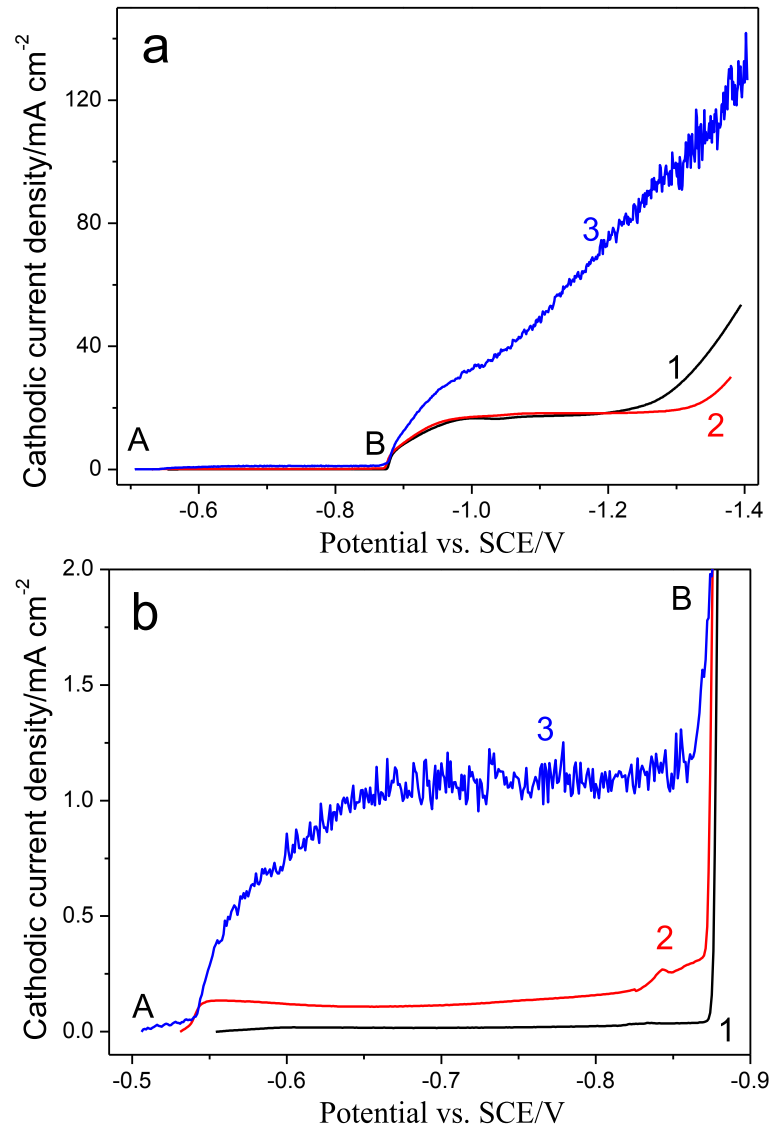

Figure 8-1 Cathodic potentiodynamic polarisation curves for the deposition of Sn-Ag-Cu alloys under the effects of agitation: (a) overall range of scans; (b) magnified initial part of scans from “A” to “B”. Curve 1 is from bath A in Table 8-1; Curve 2 from bath B; Curve 3 from bath B plus agitation supplied by magnetic stirring at 300 rpm. Potential scan rate: 1 mV/s.

After introducing Ag (AgI) and Cu ($Cu_2P_2O_7$) into the Sn solution to form bath B from Table 8-1, compared to curve 1, the plateau is prolonged in curve 2 (diagram (a)) and as a result the initiation of observed hydrogen evolution is delayed from about -1.2 V to approximately -1.3 V. This shift can be beneficial to the process, as hydrogen evolution should ideally be avoided so as to obtain a compact and dendrite-free electrodeposit. With agitation applied to the process (Figure 8-1, diagram (a), curve 3), the mass-transport dominated plateaux in both curves 1 and 2 are eliminated and replaced by an unsteady but gradually increasing current density. This increase

reaches values of more than 100 mA/cm^2 with hydrogen evolution eventually becoming dominant. It is probably because the agitation has significantly enhanced the mass supply for the deposition behaviour at the cathode surface so that a much higher current density is achievable under an identical potential.

In order to take a closer investigation of the initial stages in Figure 8-1, diagram (a), magnified details of all the three curves from points “A” to “B” are revealed in diagram (b). As curve 1 in this diagram shows, there is no noticeable current density measured until the beginning of Sn deposition at -0.88 V. For all the three curves, the deposition of Sn commences sharply once the driving potential, -0.88 V, is reached. When Ag (AgI) and Cu ($Cu_2P_2O_7$) are introduced into the Sn solution to form bath B (curve 2), a current density plateau (approximately 0.2 mA/cm^2) forms from a potential of -0.54 V, immediately after the scan commences. This plateau presumably originates from the electrodeposition of binary Ag-Cu alloys and consequently from -0.88 V onward, i.e. during the plateaux in Figure 8-1 diagram (a) after point “B”, the co-deposition of Sn-Ag-Cu alloys can be achieved, with Ag and Cu being electrodeposited at their limiting current densities. The application of agitation (diagram (b), curve 3) significantly increases the mass transport and as a result, the limiting current density plateau attributed to Ag and Cu deposition is increased fourfold to around 1 mA/cm^2 before the deposition of Sn commences.

8.1.3 Effects of Temperature

The effects of bath temperature on the electrodeposition behaviour of Sn-Ag-Cu alloys were also examined using bath B from Table 8-1 and cathodic potentiodynamic polarisation experiments are shown in Figure 8-2. Similar to the effects of agitation, increased bath temperature tends to accelerate the diffusion of metal ions (due to increased mobility) to the cathode and therefore potentially permits higher deposition rates [126]. Consequently, the current density plateaux for the deposition of both ternary Sn-Ag-Cu alloys (plateaux in Figure 8-2, diagram (a)) and binary Ag-Cu alloys (plateaux in Figure 8-2, diagram (b)) are to some extent increased, as the bath temperature is increased from 20°C to 40°C and 60°C. Specifically, the limiting current density for ternary Sn-Ag-Cu alloy deposition (Figure 8-2, diagram (a)) increases from approximately 20 mA/cm^2 at 20°C to more than 40 mA/cm^2 at 60°C

and from about 0.2 mA/cm^2 at 20°C to around 0.5 mA/cm^2 at 60°C for binary Ag-Cu alloys (Figure 8-2, diagram (b)). However, the deposition potentials, for example -0.88 V for tin, have not been affected with varying the bath temperature.

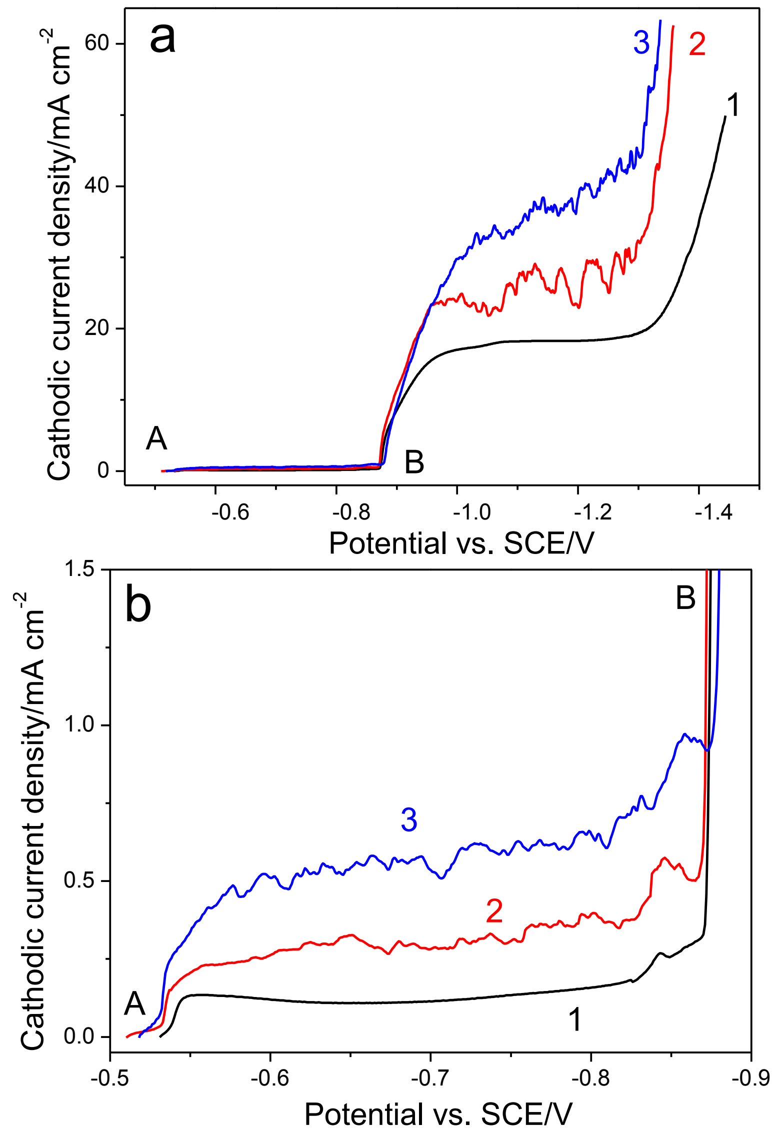

Figure 8-2 Cathodic potentiodynamic polarisation curves for the deposition of Sn-Ag-Cu alloys under varying bath temperature using bath B from Table 8-1: (a) overall range of scans; (b) magnified initial part of scans from "A" to "B". Bath temperatures: curves 1, 2 and 3 represent 20, 40 and 60°C respectively. Potential scan rate: 1 mV/s.

8.1.4 Effects of Additives

From cathodic polarisation trials in baths C and D from Table 8-1, the effects of additives (PEG 600 and formaldehyde) on the deposition of Sn-Ag-Cu ternary alloys are presented in Figure 8-3. In curve 1, free of additives, the current density increases

sharply to reach a lengthy plateau (0.1–0.2 mA/cm^2) from the beginning of the scan. This plateau is believed to be the stage where the less noble metals, i.e. Ag and Cu, start to deposit at their limiting current densities as discussed in Section 8.1.3. The co-deposition of ternary Sn-Ag-Cu alloy is then realised over the second plateau process in Figure 8-3, curve 1, with a further increase in current density after a potential of around -1.3 V owing to hydrogen evolution.

In Figure 8-3, curve 2, with the addition of PEG 600 and formaldehyde, the most noticeable change is the elongated plateau stage for Ag and Cu deposition, which is attributed to the cathodic potential shift of Sn deposition from -0.88 V to -1.22 V under the synergetic effects of both PEG and formaldehyde as discussed in Section 7.1.3. It is also noteworthy that with the additives involved, the hydrogen evolution is correspondingly delayed from -1.3 V to -1.6 V, bringing in another benefit by this additive combination and helping to obtain porosity-free deposits.

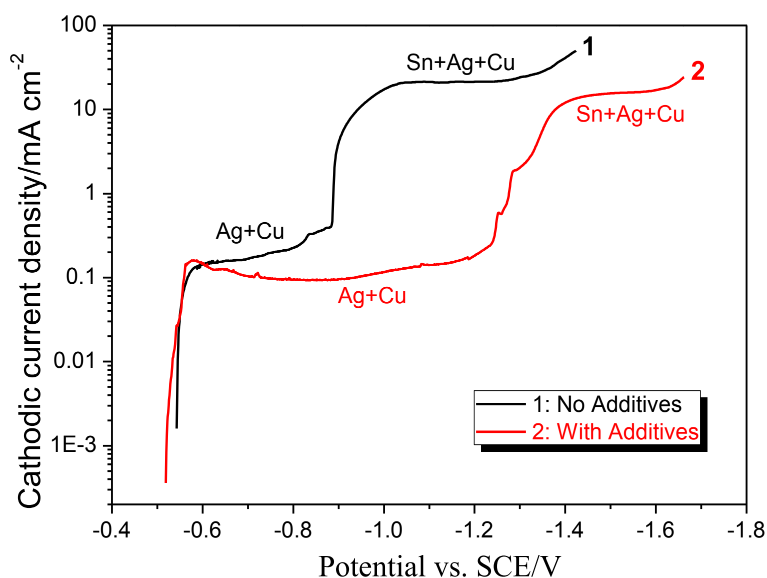

Figure 8-3 Cathodic potentiodynamic polarisation curves for the deposition of Sn-Ag-Cu alloys using bath C from Table 8-1. Potential scan rate: 1 mV/s. Curve 1: free of additives; Curve 2: with additives (PEG 600 and HCHO).

To further elaborate the cathodic polarisation process for a fundamental understanding of the reduction of metallic species in the electrolyte, the sample employed for the cathodic polarisation test (Figure 8-3, curve 2) in bath D of Table 8-1 was analysed by SEM/FIB, with the cross-sectional ISE image shown in Figure 8-4. As can be seen in this figure, the first layer above the Cu substrate is likely associated with the Ag and

Cu binary deposition layer which corresponds to the Ag+Cu electrodeposition plateau process in Figure 8-3, curve 2. At this stage, Ag and Cu are deposited at their limiting current densities and a loosely-packed particle morphology was formed as can be observed in this micrograph. After the deposition of Sn is triggered by the negatively shifting potential, Sn deposition commences from a potential of approximately -1.22 V shown in Figure 8-3. As a result, the Sn-Ag-Cu ternary alloy deposition can result in a fine-grained Sn+Ag+Cu layer which is formed above the layer of Ag+Cu shown in Figure 8-4.

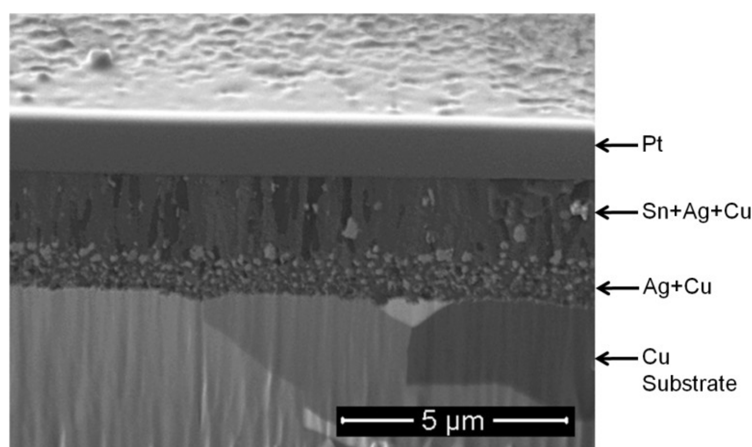

Figure 8-4 SEM/FIB processed cross-sectional ISE images of the sample produced after the cathodic polarisation test (Figure 8-3, curve 2) from bath C, Table 8-1.

8.2 Electrodeposition of Sn-Ag-Cu Alloy

8.2.1 Surface Morphology of Electrodeposits

The surface morphology of Sn-Ag-Cu alloy films deposited at room temperature without agitation is discussed. Figure 8-5 shows the SEM micrographs of electrodeposited Sn-Ag-Cu films from bath B (Table 8-1) at individual galvanostatic current densities of 5, 10, 15, 20 and 25 mA/cm^2 respectively and the corresponding chronopotentiometry curves are shown in Figure 8-6. As can be observed, relatively smooth and compact surface morphologies are achieved at low current densities, i.e. 5, 10 and 15 mA/cm^2 in images (a), (b) and (c), although they tend to be more grainy as the current density is increased. Nodular and even dendritic deposits appear at higher current densities of 20 and 25 mA/cm^2 in images (d) and (e). In other studies from the literature, it has been shown that a similar correlation between surface roughness and

the applied current densities exists, indicating the close dependency of morphology on the process current conditions in specific systems [88, 108].

The chronopotentiometry curves in Figure 8-6 explain this surface evolution in morphology. Although the driving potentials decrease with increasing galvanostatic current density, they remain relatively stable while the current density is low (curves (a), (b) and (c) for 5, 10 and 15 mA/cm^2 respectively in Figure 8-6). Owing to this, relatively smooth deposit morphologies are achieved (Figure 8-5, images (a), (b) and (c)). However, when the current densities are approaching, or even above the limiting current density (approximately 20 mA/cm^2 as revealed in Figure 8-1), the driving potentials required for Figure 8-5 images (d) and (e) have to be so negative (Figure 8-6, curves (d) and (e)) at the beginning (around -1.6 V) to reach the applied current density that hydrogen evolution is dominant, thus achieving nodular or dendritic morphologies.

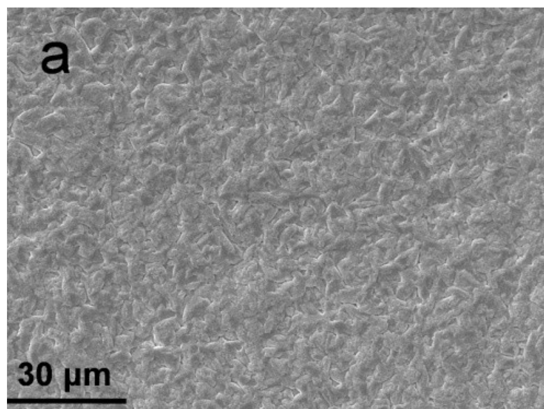

(a) current density = 5 mA/cm^2

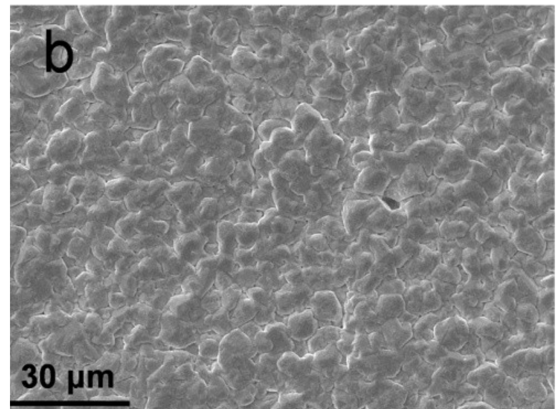

(b) current density = 10 mA/cm^2

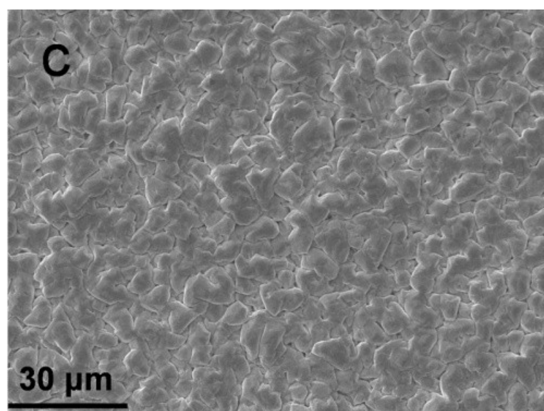

(c) current density = 15 mA/cm^2

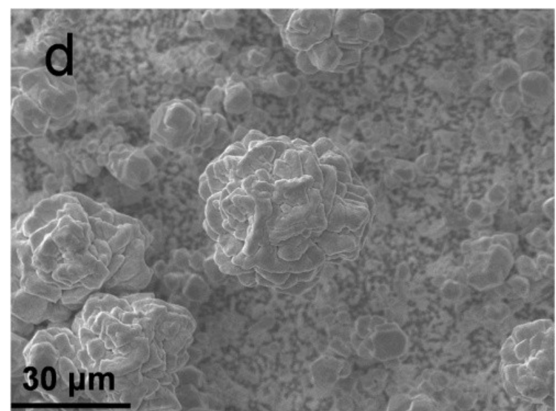

(d) current density = 20 mA/cm^2

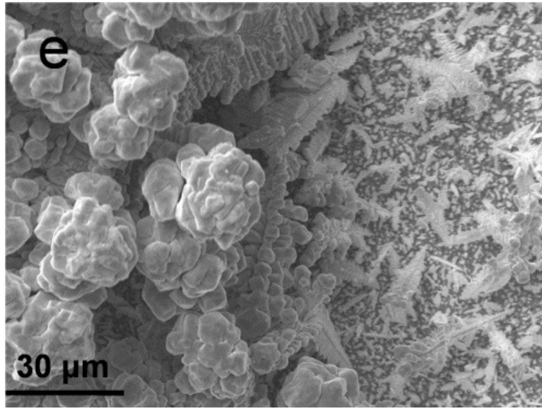

(e) current density = 25 mA/cm^2

Figure 8-5 SEM micrographs of Sn-Ag-Cu films electrodeposited under galvanostatic conditions from bath B, Table 8-1, electrical charge passed = 1500 C/dm^2.

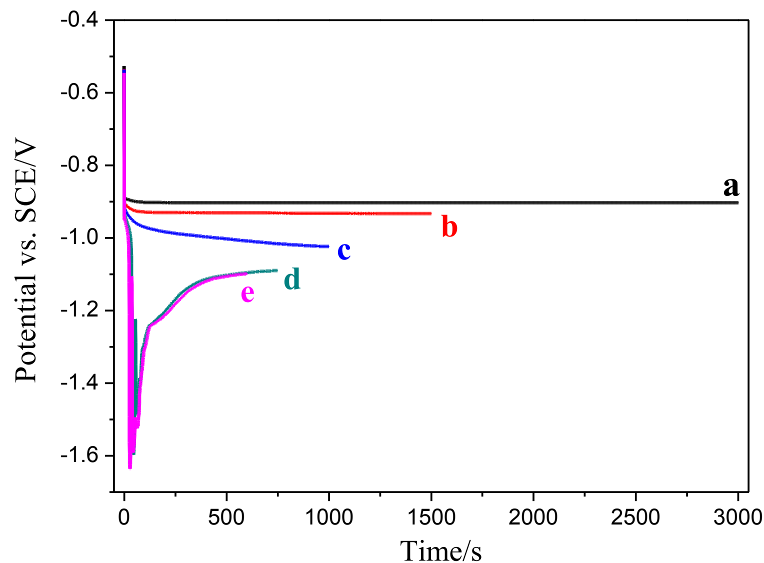

Figure 8-6 Chronopotentiometry of Sn-Ag-Cu alloys electrodeposition from bath B, Table 8-1 recorded under galvanostatic conditions, electrical charge passed = 1500 C/dm^2. Curves (a), (b), (c), (d) and (e) represent 5, 10, 15, 20 and 25 mA/cm^2 respectively.

8.2.2 Compositional Analysis

The compositions of the Sn-Ag-Cu deposits presented in Figure 8-5 were analysed by WDX, with results shown in Figure 8-7. Generally, the Ag contents in all the samples tend to decrease steadily as the current density increases, i.e. from 4.2wt.% at 5 mA/cm^2 to as low as 1.3wt.% at 25 mA/cm^2. Similarly, the Cu content shows a descending tendency from 1.7wt.% at 5 mA/cm^2 to only 0.8wt.% at 15 mA/cm^2.

However, the Cu content increases sharply at higher current densities (e.g. 20 and 25 mA/cm^2). It is speculated that the deposits have such a porous microstructure (Figure 8-5, images (d) and (e)) that the Cu substrates are not uniformly covered by the Sn-Ag-Cu electrodeposits (copper substrate evident by visual observation of the sample shown in Figure 8-5, image (e)). Consequently, WDX measurements have, in all probability, detected information from the Cu substrates through the porous and uneven deposits, resulting in the abnormal increase in Cu content generated in the results. However, with compact microstructures (dendrite and nodule free), it is believed that the films are so thick (~11 μm by SEM/FIB cross-sectional measurement) that the Cu substrate should not be interfering with the Cu contents in the electrodeposits as WDX results illustrate. It is important to notice that near-eutectic compositions (2.5–4.2wt.% Ag and 0.7–1.5wt.% Cu) are achievable for the relative compact and smooth Sn-Ag-Cu electrodeposits as shown in Figure 8-5, images (a), (b) and (c).

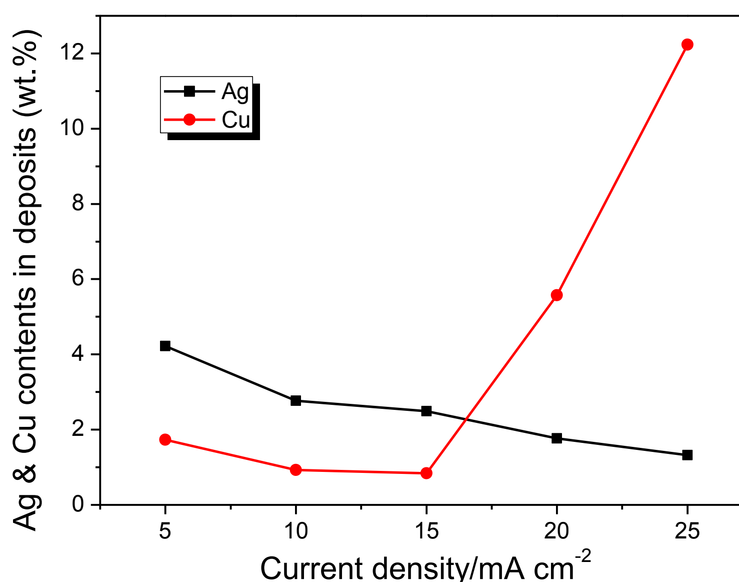

Figure 8-7 Ag and Cu contents (wt.%) in the electrodeposited Sn-Ag-Cu films vs. galvanostatic current density utilising bath B from Table 8-1. Measurements carried out by WDX.

8.3 Effects of Agitation on Sn-Ag-Cu Alloy Electrodeposition

8.3.1 Surface Morphology of Electrodeposits

The cathodic potentiodynamic polarisation curves in Figure 8-1 have demonstrated a different deposition process when agitation is applied. It is therefore presumed that electrodeposits should present distinct characteristics accordingly under the effects of agitation. Figure 8-8 shows the SEM micrographs of the electrodeposited Sn-Ag-Cu films under galvanostatic conditions plus agitation by magnetic stirring at 300 rpm, with the examined current density ranging from 5 mA/cm^2 up to 80 mA/cm^2. At the lower end (5 mA/cm^2), unlike the smooth surface in Figure 8-5 image (a) from a quiescent electrolyte, the deposit shows a rough and nodular microstructure. With the current densities increased, the deposits tend to grow smooth and compact again. This feature remains over a relatively wide current density range (10–70 mA/cm^2). A typical nodular microstructure appears when the current density reaches 80 mA/cm^2, as shown in Figure 8-8 image (i). This is because agitation largely enhances the mass transport (of metal ions) to the cathode surface and consequently increase the limiting current densities of the alloy [76], enabling much higher deposition rates as evidenced by the cathodic polarisation study and hence nodular crystals are only observed when the current density is reaching the increased limiting level.

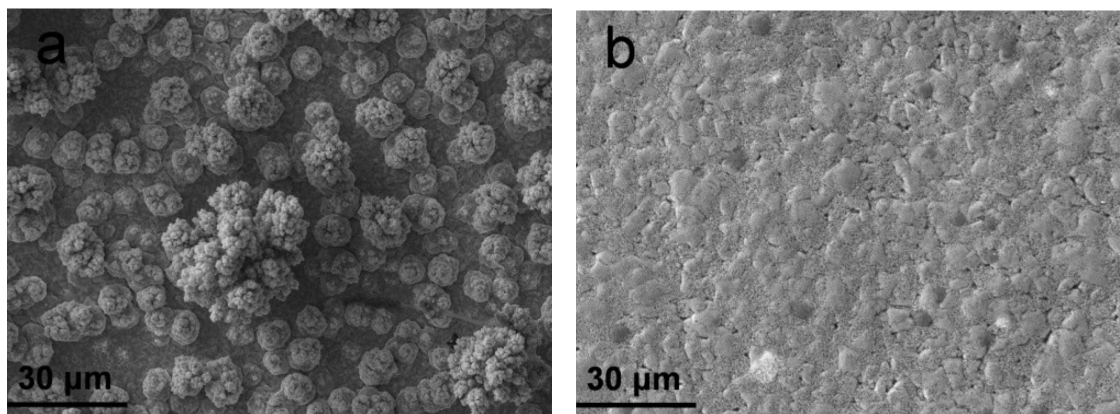

(a) current density = 5 mA/cm^2 (b) current density = 10 mA/cm^2

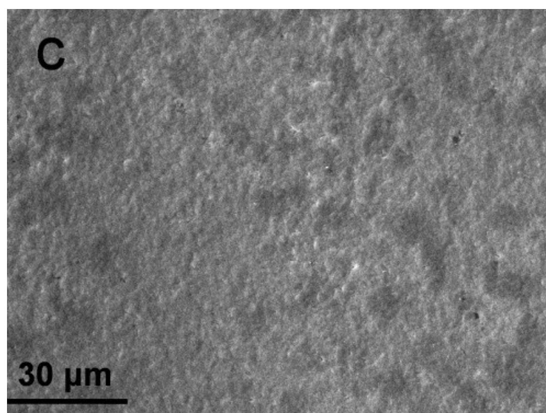

(c) current density = 15 mA/cm^2

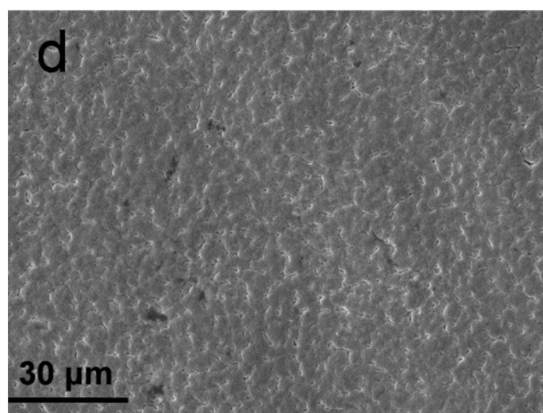

(d) current density = 20 mA/cm^2

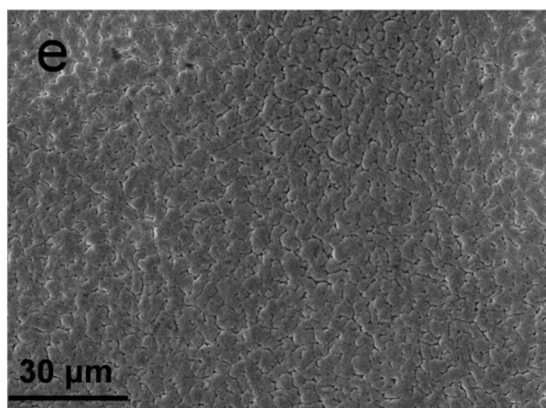

(e) current density = 25 mA/cm^2

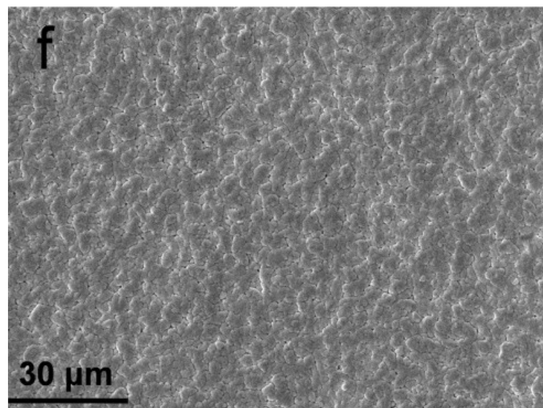

(f) current density = 30 mA/cm^2

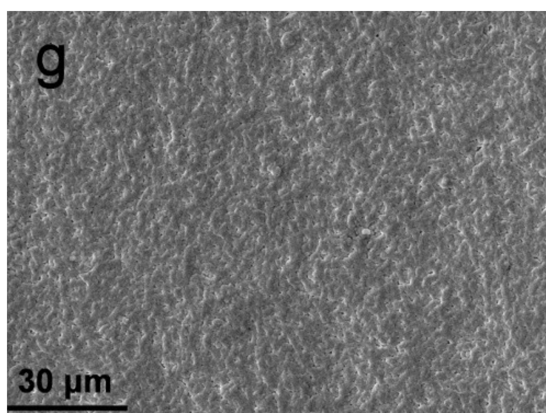

(g) current density = 50 mA/cm^2

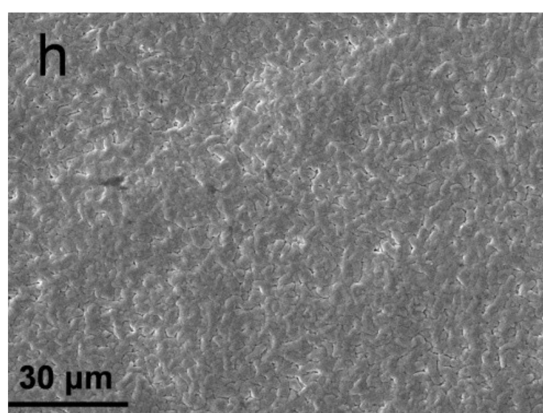

(h) current density = 70 mA/cm^2

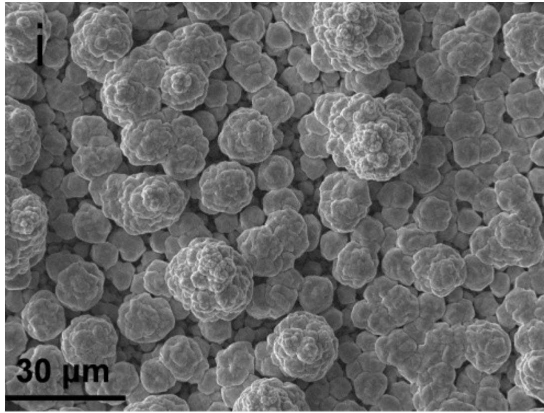

(i) current density = 80 mA/cm^2

Figure 8-8 SEM micrographs of Sn-Ag-Cu films electrodeposited under galvanostatic conditions from bath B, Table 8-1, electrical charge passed = 1500 C/dm^2, with agitation by magnetic stirring at 300 rpm.

Corresponding to the samples in Figure 8-8, chronopotentiometry curves in Figure 8-9 are relatively stable except for curve (i), the highest current density of 80 mA/cm^2 examined. The deposition potentials become lower (more negative) with increasing galvanostatic current density. It is noted that the severe fluctuation of potential in curve (i) occurs in line with a nodular and porous characteristic morphology as Figure 8-8 image (i) shows. Such a low potential (-1.8 V) required has involved hydrogen evolution, which contributes to the porous microstructure formation. This phenomenon (low potential leading to porous deposits) matches the cases (Figure 8-6, curves (d) and (e)) previously analysed without agitation. Therefore, it is concluded that stable chronopotentiometry is likely an indication of a smooth morphology, whilst fluctuations involving low potentials tend to suggest a porous microstructure with concurrent hydrogen evolution, as was also found in Kim *et al*'s study [108].

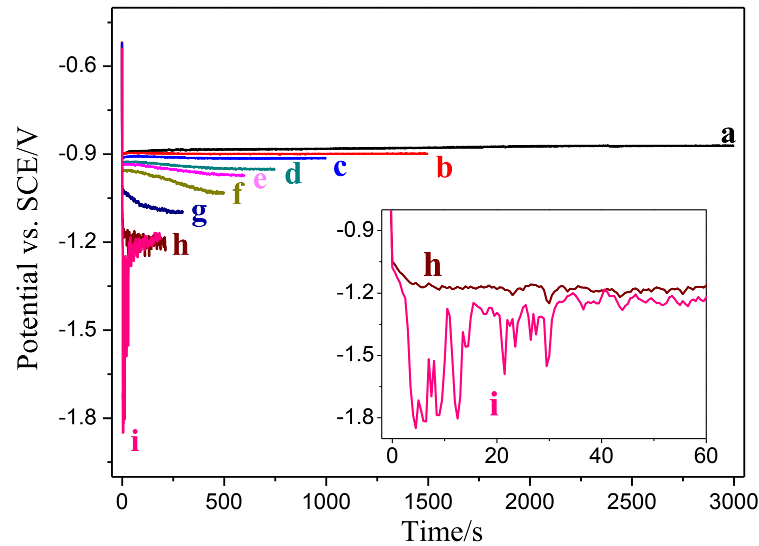

Figure 8-9 Chronopotentiometry of Sn-Ag-Cu alloys electrodeposition recorded under galvanostatic conditions from bath B, Table 8-1 with agitation by magnetic stirring at 300 rpm, electrical charge passed = 1500 C/dm^2. Curves (a), (b), (c), (d), (e), (f), (g), (h) and (i) represent 5, 10, 15, 20, 25 30, 50, 70 and 80 mA/cm^2 respectively.

8.3.2 Compositional Analysis

The composition of the Sn-Ag-Cu electrodeposits obtained over this wide current density range (5–80 mA/cm^2) under the effects of agitation has shown a similar descending trend for both Ag and Cu contents as illustrated in Figure 8-10. At 5 mA/cm^2, the Ag and Cu contents in the nodular deposits (Figure 8-8, image (a)) are as high as 26.9wt.% and 17.2wt.% respectively. This means that Ag and Cu, deposited at their agitation-enhanced limiting current densities, contributed largely to the total current applied, resulting in this nodular morphology which is typical in such occasions. At the higher current density end, the content of Ag comes close to the eutectic range (from 3.9wt.% to 3.2wt.% over 60–80 mA/cm^2), while Cu is relatively constant at approximately 1.1wt.% over this current density range.

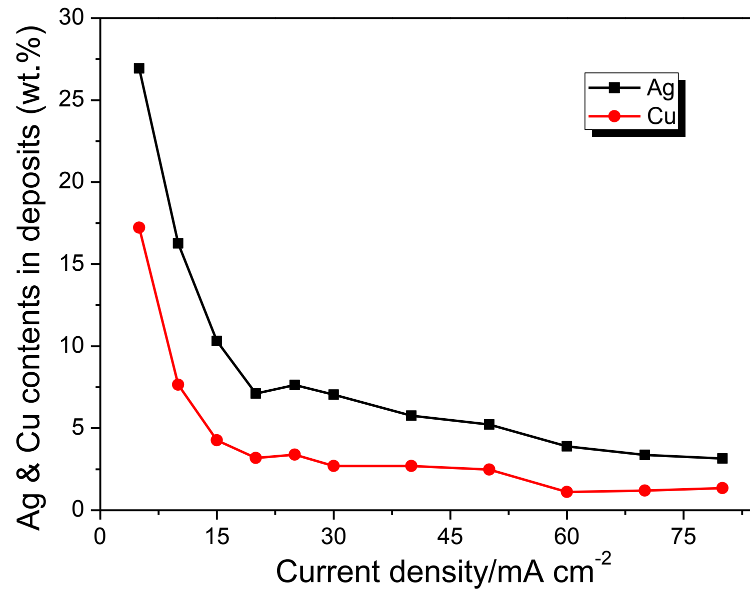

Figure 8-10 Ag and Cu contents (wt.%) in the electrodeposited Sn-Ag-Cu films vs. galvanostatic current density utilising baths B from Table 8-1 with agitation by magnetic stirring at 300 rpm. Measurements carried out by WDX.

8.4 Effects of Temperature on Sn-Ag-Cu Alloy Electrodeposition

8.4.1 Surface Morphology of Electrodeposits

Figure 8-11 demonstrates SEM micrographs of Sn-Ag-Cu alloy electrodeposits in bath B from Table 8-1 at 20°C, 40°C and 60°C at individual current densities (5, 15 and 25 mA/cm^2, specifically). In images (a), (b) and (c) investigated at 5 mA/cm^2, only image (c) at 60°C shows a distinctive dendritic deposit, whilst smooth surfaces are seen with images (a) and (b). This distinctive difference is partly attributed to the large compositional differences shown in Figure 8-13 from sample (c) to (a) and (b). In image (c), the total content of Ag and Cu is greater than 40wt.%, therefore, dendrites are the typical morphology when the significant constituents of the deposits (Ag and Cu) are deposited at their limiting current densities, although such current densities have already been largely enhanced by the increased bath temperature as presented in Figure 8-2. Electrodeposits generated at 15 mA/cm^2 (Figure 8-13, images (d), (e) and (f)) show some grainy but relatively smooth morphologies, regardless of the bath temperature investigated. However, the largely increased mass transport at 60°C has made the morphology in image (i) different from (g) and (h), although all

films were deposited at the same current density (25 mA/cm^2). Dendrites and nodules are dominant in images (g) and (h), but a relatively smooth and compact surface is evident in image (i), with limited crevices observed.

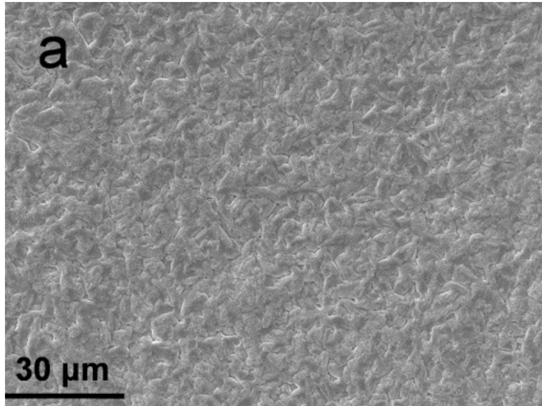

(a) bath temperature=20°C, current density = 5 mA/cm^2

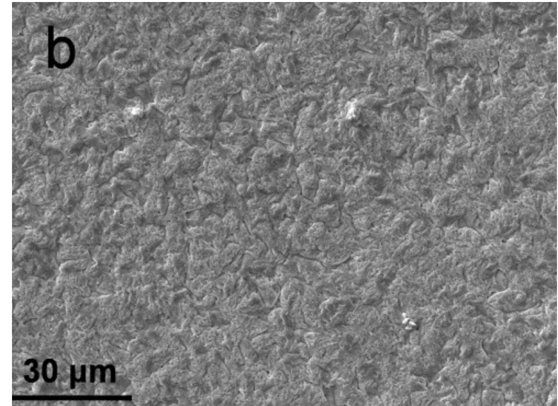

(b) bath temperature=40°C, current density = 5 mA/cm^2

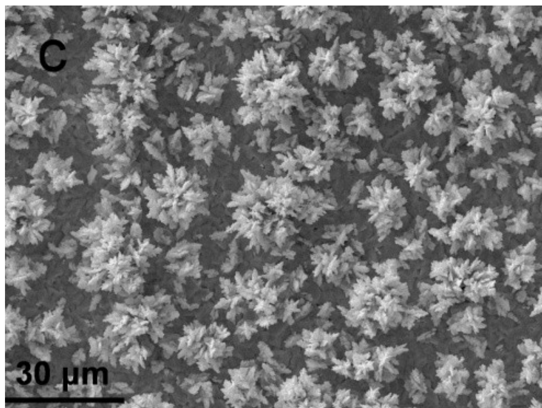

(c) bath temperature=60°C, current density = 5 mA/cm^2

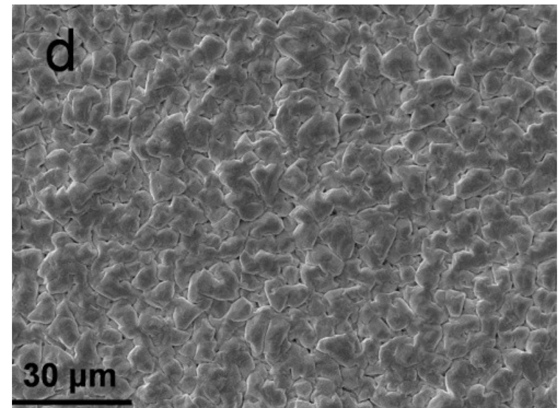

(d) bath temperature=20°C, current density = 15 mA/cm^2

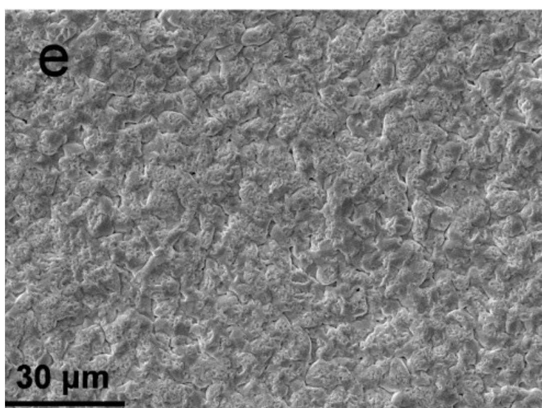

(e) bath temperature=40°C, current density = 15 mA/cm^2

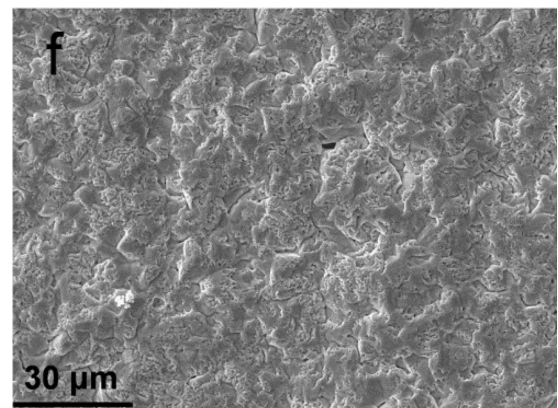

(f) bath temperature=60°C, current density = 15 mA/cm^2

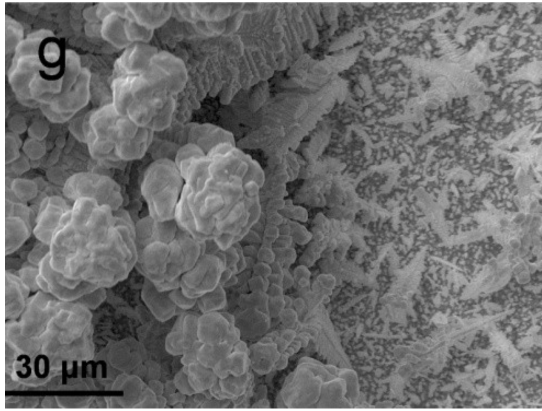

(g) bath temperature=20°C, current density = 25 mA/cm^2

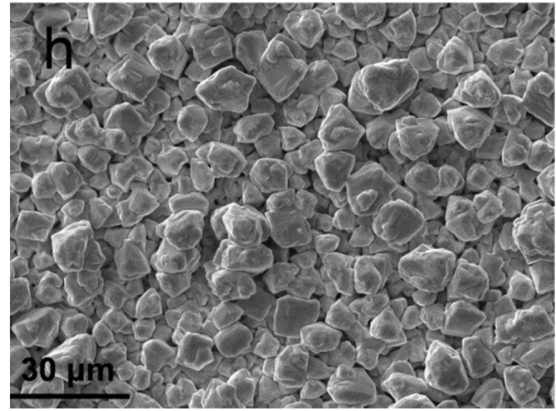

(h) bath temperature=40°C, current density = 25 mA/cm^2

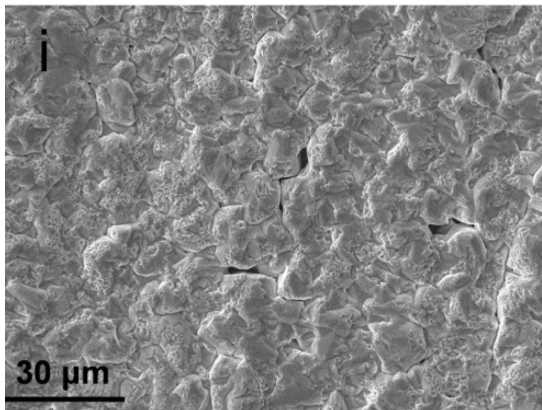

(i) bath temperature=60°C, current density = 25 mA/cm^2

Figure 8-11 SEM micrographs of Sn-Ag-Cu films electrodeposited under galvanostatic conditions from bath B, Table 8-1, electrical charge passed = 1500 C/dm^2. Bath temperatures of 20, 40 and 60°C, at current densities of 5, 15 and 25 mA/cm^2, respectively.

Chronopotentiometric data for elevated bath temperatures are given in Figure 8-12. Compared to the chronopotentiometry at 20°C (Figure 8-6), over the examined current density range (5 to 25 mA/cm^2), the potential curves only show significant fluctuations at 25 mA/cm^2 (Figure 8-12, diagram (a), curve (e)) when the bath temperature is increased to 40°C, generating nodular deposits as a result (Figure 8-11, image h). The curves stay stable over the whole current density range investigated (Figure 8-12, diagram (b)) at a higher bath temperature of 60°C. These stable curves are prone to produced dendrite and nodule free deposits, as Figure 8-11 indicates (images (c), (f) and (i)), except for the lowest current density examined (image (c)) with the reason already discussed above.

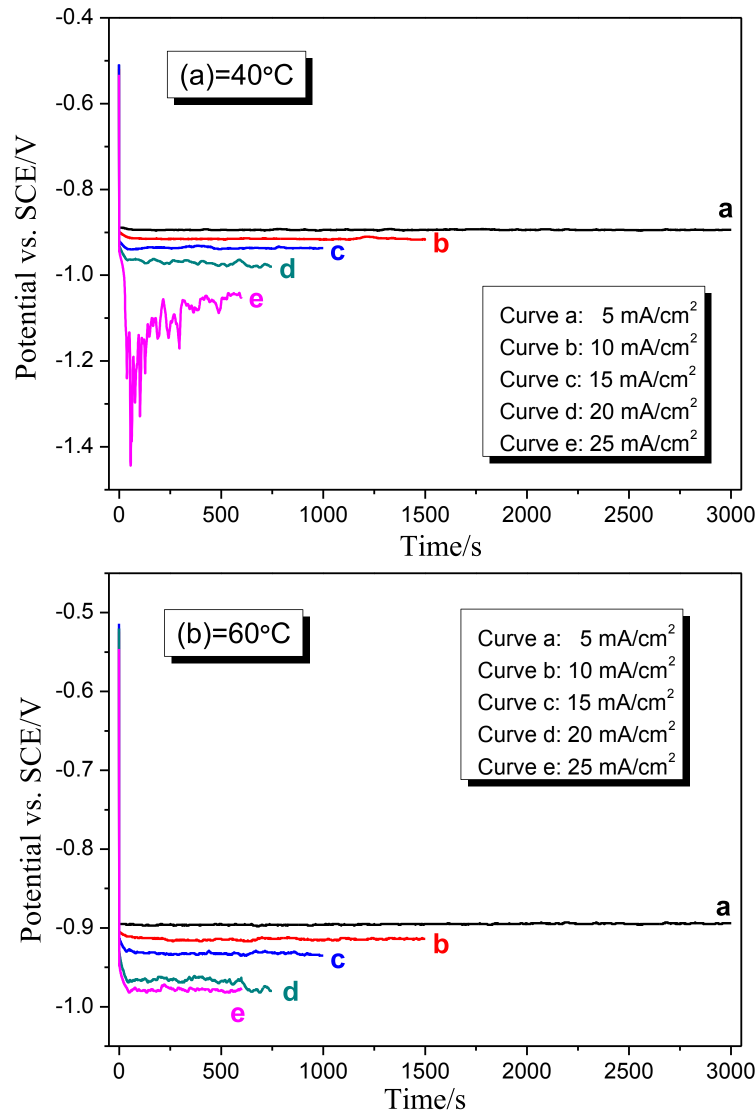

Figure 8-12 Chronopotentiometry of Sn-Ag-Cu alloys electrodeposition from bath B, Table 8-1 recorded under galvanostatic conditions, electrical charge passed = 1500 C/dm^2. Bath temperature=40°C (diagram (a)) and 60°C (diagram (b)). Curves (a), (b), (c), (d) and (e) represent 5, 10, 15, 20 and 25 mA/cm^2 respectively.

8.4.2 Compositional Analysis

The effects of bath temperature on the composition of Sn-Ag-Cu alloy electrodeposits are illustrated in Figure 8-13. It is clearly seen that there is an obvious decrease for both Ag and Cu contents as the current density increases, regardless of bath temperature, although this is more evident at the lower current densities for 60°C. The abnormal increase in Cu content in Figure 8-13, diagram (b), curve 1 is most likely due to the porous dendritic microstructure revealing the Cu substrate, as mentioned in Section 8.2.2. Generally, as can be concluded from Figure 8-13, for the same current

density, the contents of both Ag and Cu tend to be higher at a higher bath temperature. However, this tendency gradually diminishes as the current density increases.

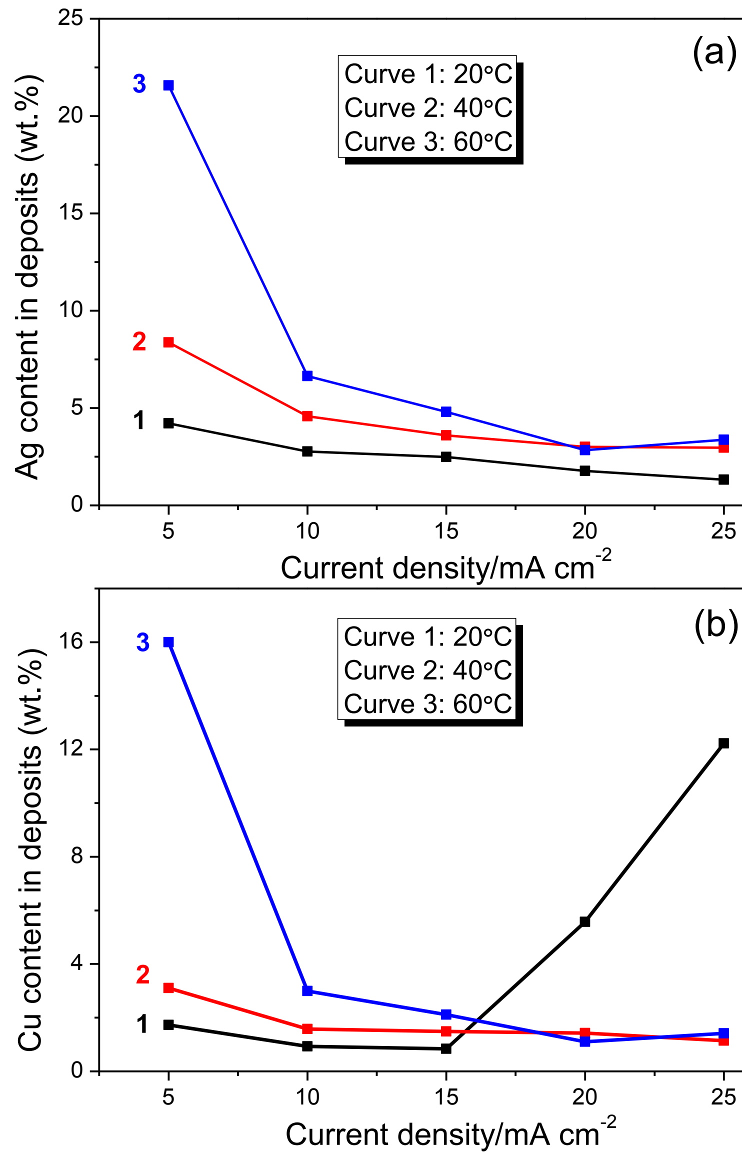

Figure 8-13 Ag (diagram (a)) and Cu (diagram (b)) contents (wt.%) in the electrodeposited Sn-Ag-Cu films vs. galvanostatic current density at varying bath temperature utilising bath B from Table 8-1. Measurements carried out by WDX. Curve 1, 2 and 3 represent 20, 40 and 60°C respectively.

8.5 Effects of Additives on Sn-Ag-Cu Alloy Electrodeposition

8.5.1 Surface Morphology of Electrodeposits

The surface morphology of electrodeposited Sn-Ag-Cu films, characterised by SEM in Figure 8-14, has been modified with the addition of PEG 600 and formaldehyde as

additives. As the current density increases from 5 to 15 mA/cm^2, there is a tendency for the surface to get smoother as shown in images (a), (b) and (c). This is due to the gradually increasing influence of the additives (PEG 600 and formaldehyde) on the deposition process, as the driving potential changes from -1.35 V to approximately -1.45 V shown in the chronopotentiometry curves (from (a) to (c)) in Figure 8-16. The reason for this morphology modification can be attributed to the potential-dependent characteristics of additives used, as discussed in Figure 7-3.

It is known that the additives (PEG and formaldehyde) operate synergistically and result in a smooth shiny surface, as shown in Figure 8-14, image (c). However, a rough and porous surface is observed in images (d) and (e). This is again due to the current densities approaching or exceeding the limiting value, as indicated by the noisy "V" shaped potential curves (Figure 8-16, curves (d) and (e)), including -1.7 V which is in the hydrogen evolution range as the polarisation curve indicates (Figure 8-3, curve 2).

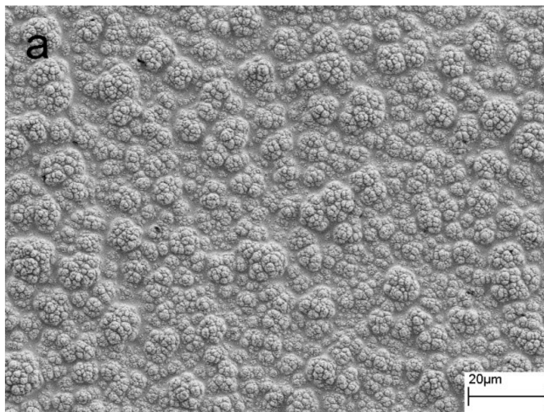

(a) current density = 5 mA/cm^2

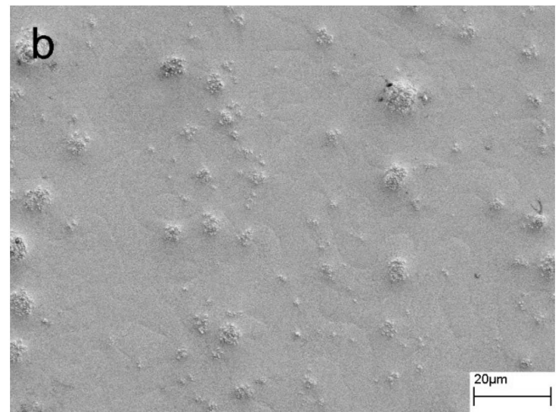

(b) current density = 10 mA/cm^2

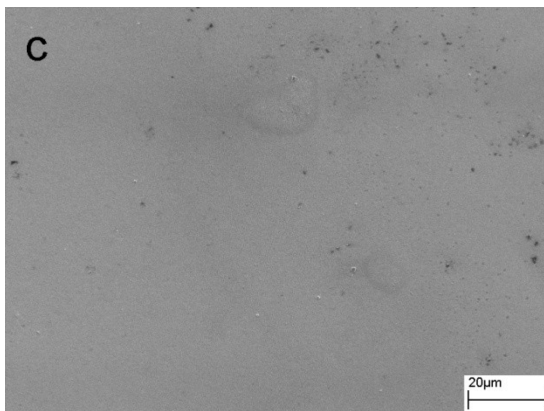

(c) current density = 15 mA/cm^2

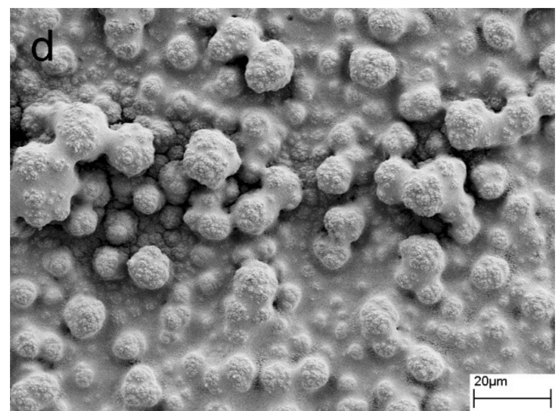

(d) current density = 20 mA/cm^2

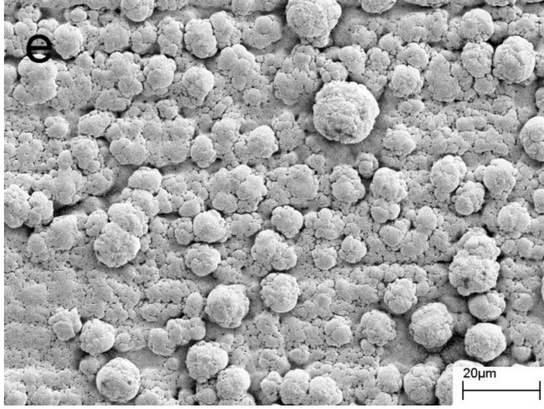

(e) current density = 25 mA/cm^2

Figure 8-14 SEM micrographs of Sn-Ag-Cu films electrodeposited under galvanostatic conditions from bath D, Table 8-1, electrical charge passed = 1500 C/dm^2.

In order to further reveal the bright surface generated as a result of the additives, an AFM morphological study was performed on the sample produced in bath D from Table 8-1 at a current density of 15 mA/cm^2 (Figure 8-14, image (c)). Figure 8-15 presents the AFM image obtained over a 3 μm × 3 μm scanned area. More details of the surface morphology can be achieved in this image, compared to the almost feature-free SEM figure (Figure 8-14, image (c)). As can be estimated from Figure 8-15, the size of the nodular clusters are of nano-scale (ca. 100 nm on average). This may explain the bright appearance as presented, which is a result of such fine structures resulting from the effects of the additives. More specifically, the quantified surface roughness from the AFM measurement shows a root-mean-square value (Rq) of only 18.6 nm.

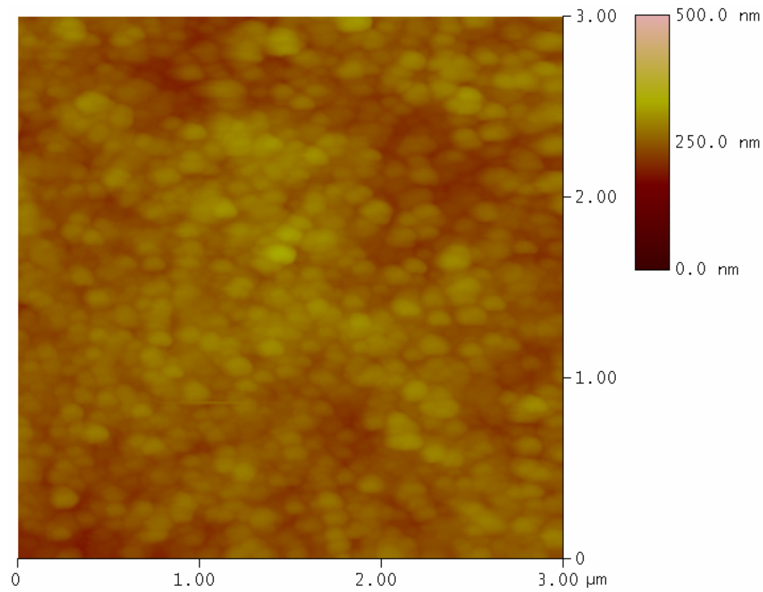

Figure 8-15 AFM image (3 µm × 3 µm) of the as-electrodeposited Sn-Ag-Cu film electrodeposited under galvanostatic conditions (15 mA/cm^2, electrical charge passed = 1500 C/dm^2, Figure 8-14, image (c)) from bath D, Table 8-1.

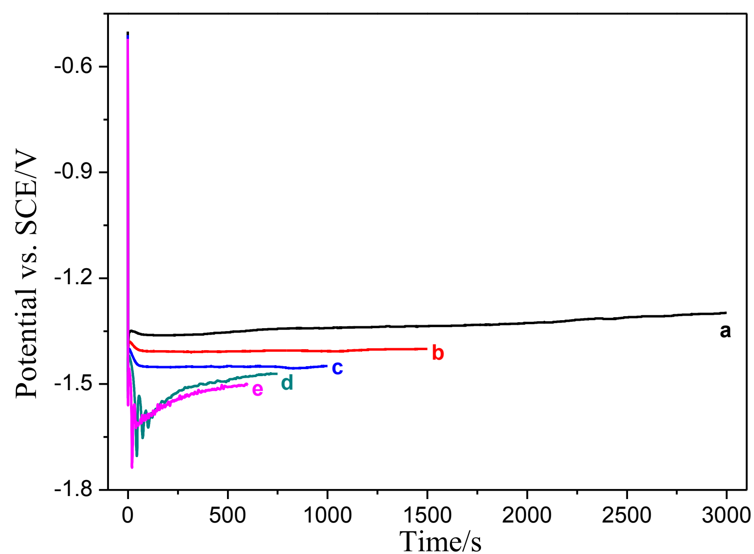

Figure 8-16 Chronopotentiometry of Sn-Ag-Cu alloys electrodeposition from bath D, Table 8-1 recorded under galvanostatic conditions, electrical charge passed = 1500 C/dm^2. Curves (a), (b), (c), (d) and (e) represent 5, 10, 15, 20 and 25 mA/cm^2 respectively.

8.5.2 Compositional Analysis

The compositions of the electrodeposited Sn-Ag-Cu films shown in Figure 8-14 at individual galvanostatic conditions are plotted in Figure 8-17 accordingly. The sample produced at a galvanostatic current density of 5 mA/cm^2 (Figure 8-14, image (a))

shows relatively high contents of Ag and Cu (Ag 4.9wt.% and Cu 1.7wt.%). With the current density increased, the compositions of Ag and Cu in the deposit remain relatively stable, particularly for Cu. This enables a relatively wide process window to produce deposits with the lowest fluctuations in composition and consequently achieves compositional uniformity over samples. For the electrodeposit with a smooth surface (Figure 8-14, image (c)), the result indicates a composition of Ag 3.8wt.% and Cu 0.8wt.%, which falls into the range of eutectic Sn-Ag-Cu compositions. Combined with the morphological analysis, it can be concluded that Sn-Ag-Cu alloy produced at a current density of around 15 mA/cm^2 gives a near-eutectic composition, whilst a smooth and fine-grained surface is also achievable.

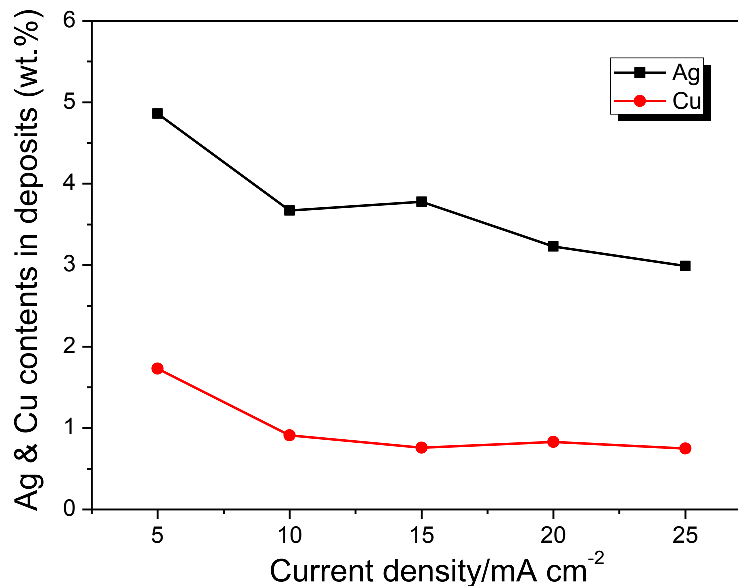

Figure 8-17 Ag and Cu contents (wt.%) in the electrodeposited Sn-Ag-Cu films vs. galvanostatic current density utilising bath D from Table 8-1. Measurements carried out by WDX.

8.6 Thermal Analysis of Electrodeposits

The differential scanning calorimetry (DSC) measurements were conducted to characterise the thermal property of the Sn-Ag-Cu electrodeposits.

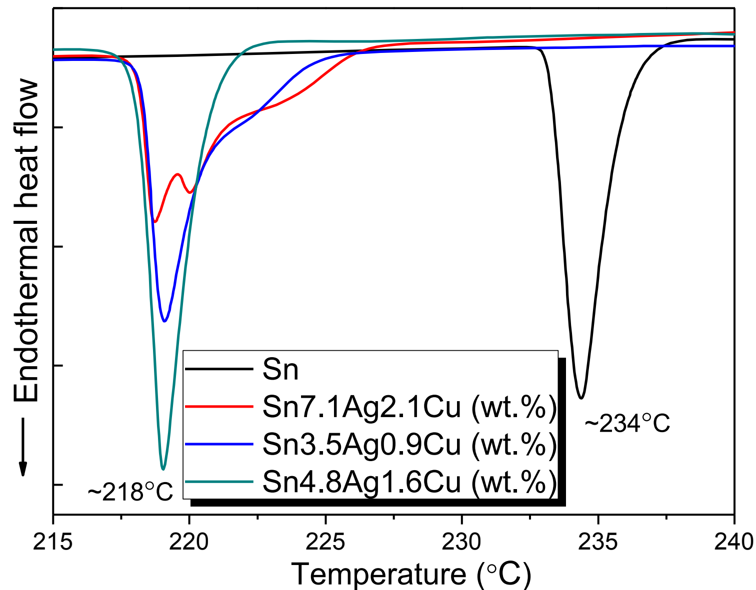

Figure 8-18 DSC measurements of Sn-Ag-Cu electrodeposits from bath F, Table 8-1. Scan rate at 10 K/min. Pure Sn presented as a reference.

Figure 8-18 compares the melting curves of three distinct Sn-Ag-Cu alloys with constituents characterised by WDX. As can be seen from this diagram, the sample with a measured composition of Sn-4.8wt.%Ag-1.6wt.%Cu shows a shape most similar to the reference pure tin, with only a single peak at ~218°C. This means, in terms of melting behaviour, this Sn-Ag-Cu electrodeposit has a melting property closer to the eutectic. This result to some extent agrees with the conclusions of Miller *et al* [127], who found a ternary eutectic melting temperature at 217°C and placed its composition at Sn-4.7wt.%Ag-1.7wt.%Cu. However, there are still discussions ongoing as to the eutectic point that is closely associated with the ternary alloy composition. Gebhardt and Petzow [128] proposed a composition of Sn-4.0wt.%Ag-0.5wt.%Cu whilst Moon *et al* [64], using thermal cycling experiments and Loomans *et al* [129] by thermal analysis of the signal from the monovariant binary eutectics concluded eutectic compositions of Sn-3.5wt.%Ag-0.9wt.%Cu and Sn-3.66wt.%Ag-0.91wt.%Cu respectively. For the other two alloys examined (Sn-7.1wt.%Ag-2.1wt.%Cu and Sn-3.5wt.%Ag-0.9wt.%Cu), widened endothermic processes can be observed. This should be attributed to their off-eutectic behaviour in terms of the melting process, such as widened solidus and liquidus temperature range, under the current testing conditions.

8.7 Microstructure of Electrodeposits

8.7.1 Phase Identification

The XRD analysis of the near-eutectic Sn-Ag-Cu film galvanostatically electrodeposited at a current density of 15 mA/cm^2 (Figure 8-14, image (c), Ag 3.8wt.% and Cu 0.8wt.%) is presented in Figure 8-19. As shown in this diagram, all the diffraction peaks are attributed to three phases: β-phase Sn, Ag_3Sn and Cu_6Sn_5 (except one from the Cu substrate as indicated). Kaneko [130] and Zhang [131] *et al* have reached similar results for phase analysis in their electrodeposited Sn-Ag-Cu films, which is in agreement with the phase structure from the Sn-Ag-Cu thermal equilibrium phase diagram [132]. The XRD analysis confirms the crystalline nature of the deposited film and the presence of Sn, Ag and Cu phases. Similar XRD patterns are also obtained for films deposited at other current densities examined.

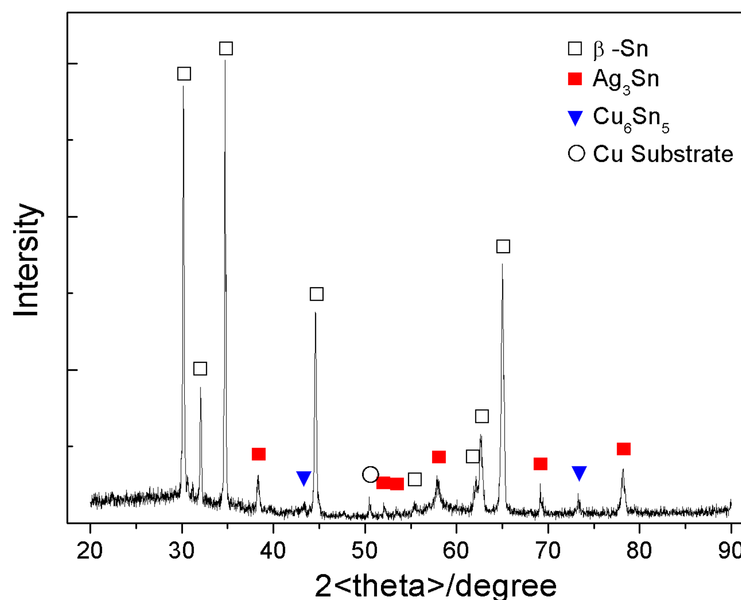

Figure 8-19 XRD spectrum of the Sn-Ag-Cu film galvanostatically electrodeposited from bath D (image (c)) from Table 8-1 at a current density of 15 mA/cm^2, electrical charge passed = 1500 C/dm^2.

8.7.2 Electrodeposits From A Bath Free of Additives

To further examine the microstructure of the Sn-Ag-Cu deposits, SEM/FIB micro-machining and TEM were used. Figure 8-20 shows the representative ISE micrograph of the cross-sectional as-electrodeposited Sn-Ag-Cu film from bath B (Table 8-1) free

of additives, with (image (b)) and without (image (a)) agitation. In both micrographs, the microstructure of the deposits is a compact aggregate of Sn grains, the sizes of which in image (b) are smaller than that in image (a) under the effects of agitation. Ag_3Sn and Cu_6Sn_5 intermetallic phases (bright contrast in the images) proven by XRD in Figure 8-19, are apparent both in Sn grains and along grain boundaries. These micrographs show the Ag_3Sn and Cu_6Sn_5 phases co-exist in the Sn-Ag-Cu electrodeposits. Moreover, TEM micrographs present more details as shown in Figure 8-21.

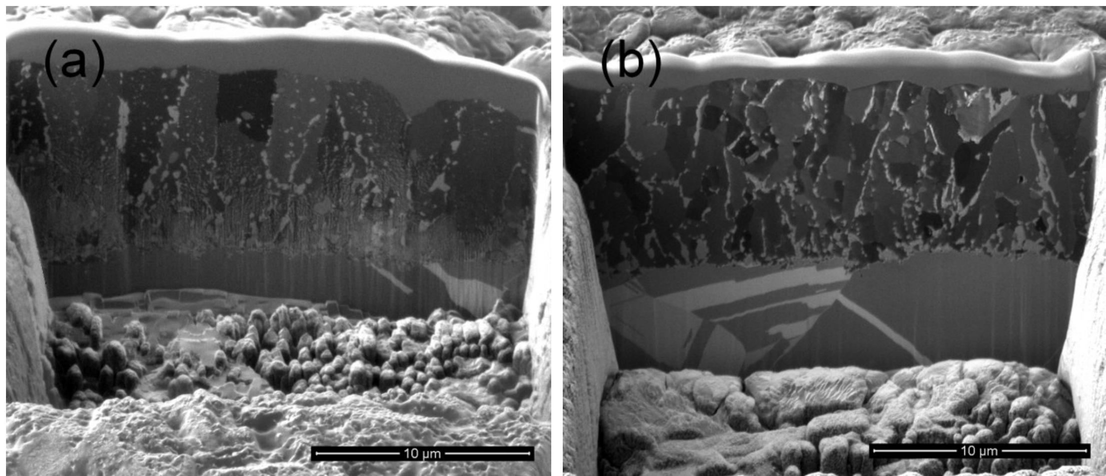

Figure 8-20 SEM/FIB processed cross-sectional ISE images of the as-electrodeposited Sn-Ag-Cu film produced under galvanostatic conditions from bath B, Table 8-1. Image (a) 10 mA/cm^2; Image (b) 70 mA/cm^2. Electrical charge passed = 1500 C/dm^2, with agitation by magnetic stirring at 300 rpm.

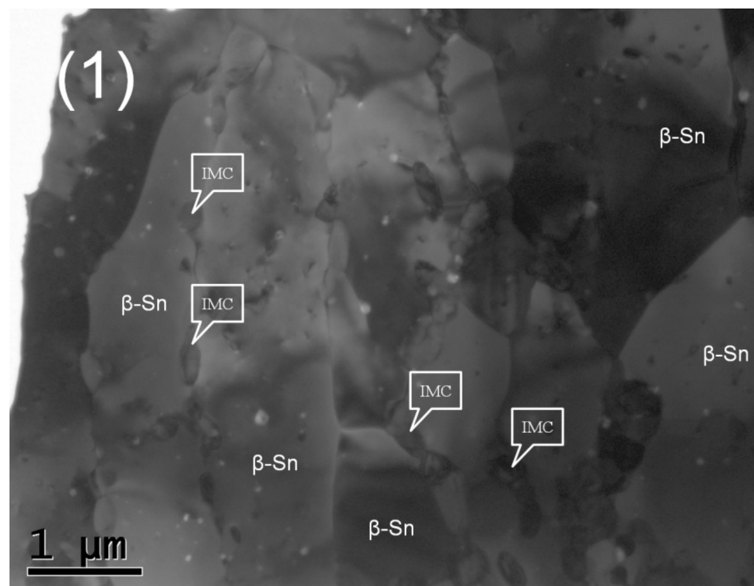

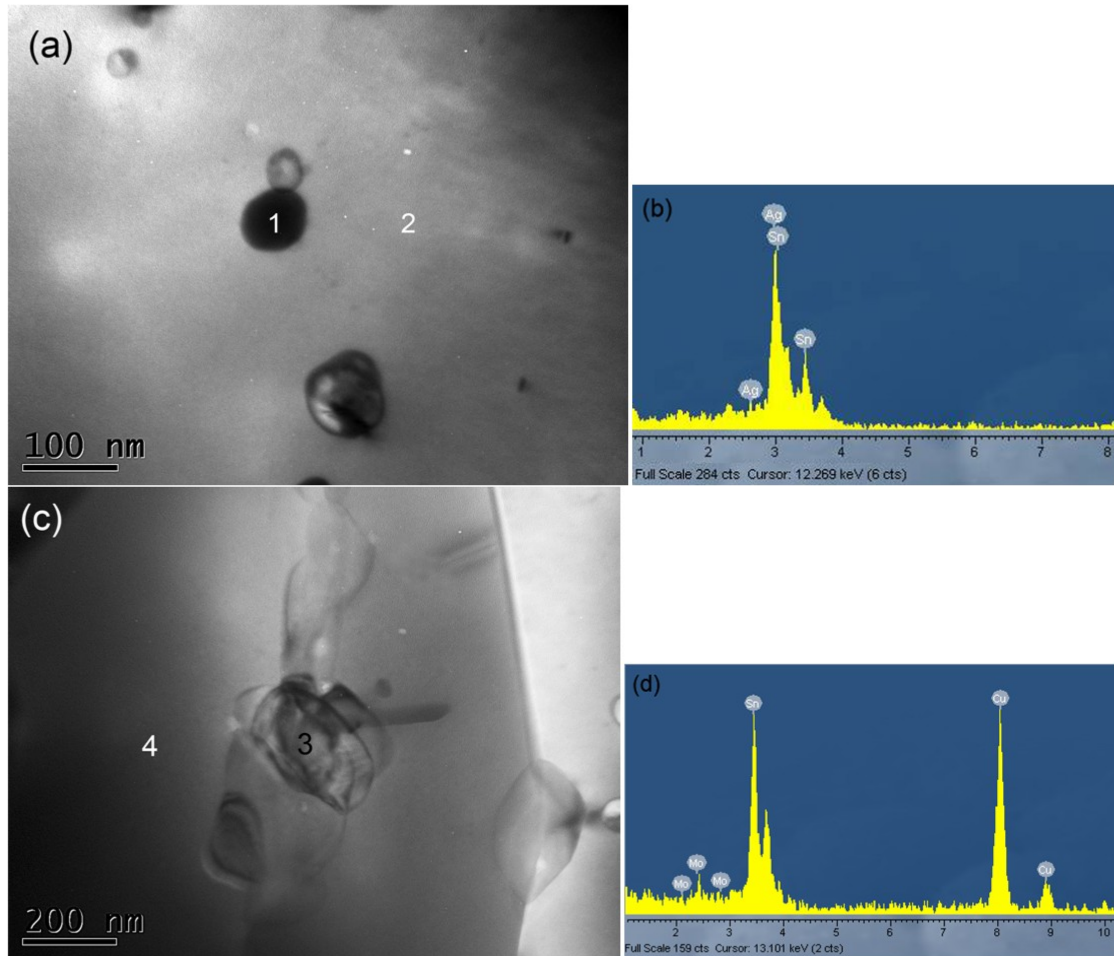

Figure 8-21 TEM micrographs and EDX spectra of Ag_3Sn (images (a) and (b)) and Cu_6Sn_5 (images (c) and (d)) in the Sn-Ag-Cu film electrodeposited under galvanostatic conditions (10 mA/cm^2, electrical charge pass = 1500 C/dm^2) from bath B, Table 8-1. Image (1) shows the general review. EDX analyses carried out at points "1", "2", "3" and "4", with resultant spectra for points "1" and "3" shown in images (b) and (d).

Ag_3Sn particles as marked in Figure 8-21 image (a), with sizes of less than 100 nm, are seen located in the Sn matrix. Kerr *et al* [133] also observed a similar structure in eutectic Sn-Ag alloys. Quantitative EDX measurements (spectrum (b)) show that point "1" has a composition of 72.6at.% Ag and 27.4at.% Sn. Referring to the phase structure from the Sn-Ag thermal equilibrium phase diagram [134], this result suggests a composition close to Ag_3Sn, whilst 100at.% Sn is measured at point "2", allowing the conclusion that Ag_3Sn intermetallic particles lie in a Sn matrix. Similarly, image (c) illustrates the morphology of Cu_6Sn_5 particles in the Sn matrix. These are larger in size than Ag_3Sn in the shown image. The EDX spectrum in image (d) shows constituents of Sn, Cu and Mo at point "3", with Mo peaks emanating from the Mo grid used for TEM foil mounting (instead of the commonly used Cu grid to eliminate

the potential compositional interference). Quantitative results show a composition of 42.9at.% Cu, 40.1at.% Sn and 17.0at.% Mo for point "3", which reveals a stoichiometry close to Cu_6Sn_5, whilst only Sn and Mo are detected for point "4", the electrodeposit matrix.

8.7.3 Electrodeposits in Bath With Additives

Figure 8-22 shows the representative SEM/FIB micrograph of the cross-section of as-electroplated Sn-Ag-Cu films with additives. Aggregation of fine and columnar Sn grains can be seen throughout the structure. It is such long Sn grains that make up the clusters on the smooth surface observed in Figure 8-15 from the AFM analysis.

Also clearly noticeable in this image are the widely but uniformly spread particles with bright contrast. As indicated in the XRD phase analysis in Figure 8-19, these particles show the Ag_3Sn and Cu_6Sn_5 phases probably co-exist in the as-electroplated deposits, as confirmed by the TEM analysis in Figure 8-23. Compared to Figure 8-20, the intermetallic particles (Ag_3Sn and Cu_6Sn_5) are also refined under the effects of additives.

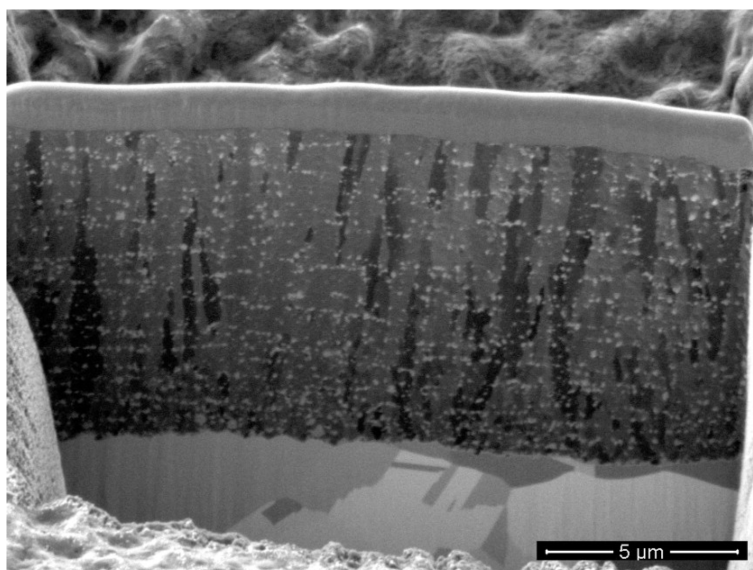

Figure 8-22 SEM/FIB processed cross-sectional ISE images of the as-electrodeposited Sn-Ag-Cu film produced under galvanostatic conditions from bath D, Table 8-1 (15 mA/cm^2, electrical charge pass = 1500 C/dm^2).

The cross-sectional TEM micrographs of the as-electroplated Sn-Ag-Cu deposits with additives is shown in Figure 8-23. As can be observed in image (a), the width of the

columnar Sn grains is about 200 nm, with a distinctive view of grain boundaries. Ag_3Sn and Cu_6Sn_5 particles, with a size of the order of tens of nanometres (images (b) and (c)), are dispersed homogeneously either within Sn grains or along grain boundaries in this near-eutectic structure. The EDX measurements in TEM show the compositions of points "1" to "7" with results summarised in Table 8-2. These compositional tests confirm the co-existence of Ag_3Sn and Cu_6Sn_5 particles in the structure of Sn-Ag-Cu electrodeposit.

Table 8-2 TEM-EDX quantitative compositional measurements of points shown in Figure 8-23

Point	Sn (L) at.%	Ag (L) at.%	Cu (K) at.%
1	27.9	72.1	–
2	100	–	–
3	100	–	–
4	46.5	–	53.5
5	45.8	–	54.2
6	100	–	–
7	100	–	–

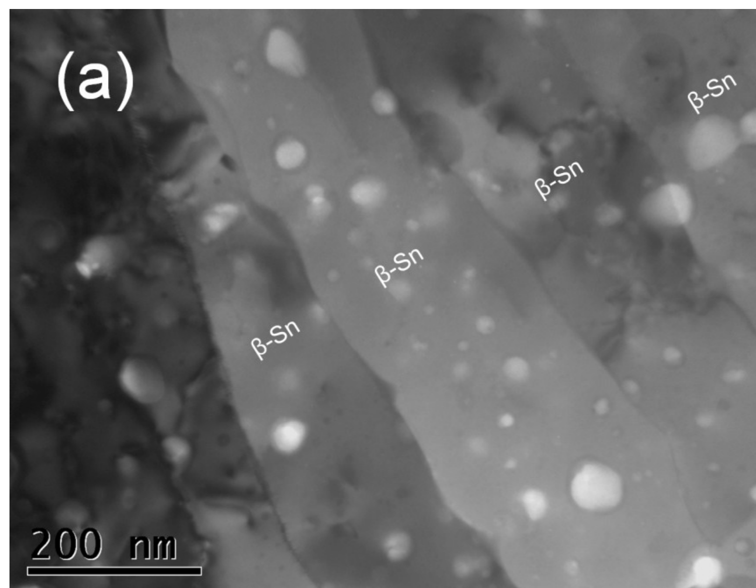

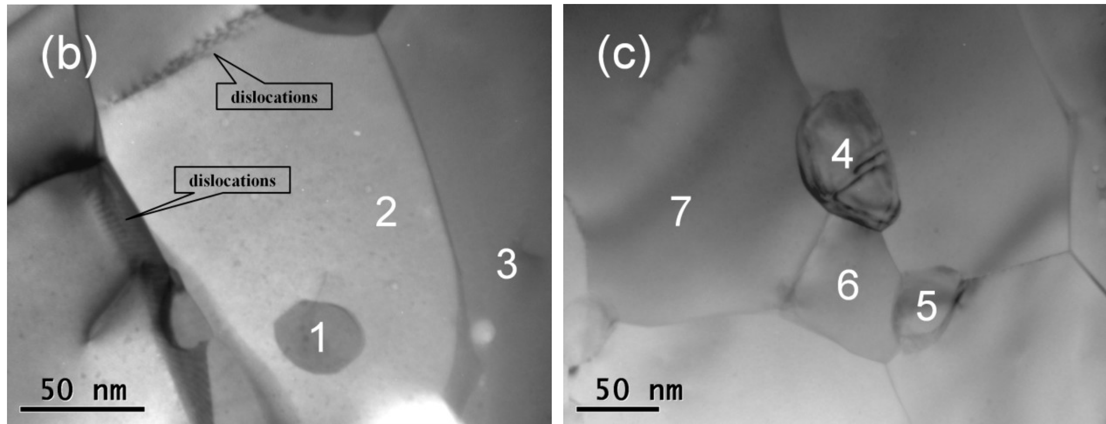

Figure 8-23 TEM micrographs of the Sn-Ag-Cu film electrodeposited under galvanostatic conditions (10 mA/cm^2, electrical charge pass = 1500 C/dm^2) from bath D, Table 8-1. Image (a) general view of Sn gains and Ag_3Sn, Cu_6Sn_5 particle; Image (b) magnified view of Ag_3Sn particle in-between Sn grains; Image (c) magnified view of Cu_6Sn_5 particles in-between Sn grains. EDX quantitative measurements of points "1" to "7" summarised in Table 8-2.

It can be noted in Figure 8-23, image (b), that ordered "stitch-like" structures can be found at the tin grain boundaries. There are believed to be dislocations similar to those seen in other studies [135, 136]. Figure 8-24 shows a highly magnified view of two other dislocation features found in the as-electrodeposited Sn-Ag-Cu alloy. However, these features are only found in the electrodeposit from bath D, under the effects of additives (PEG 600 and formaldehyde).

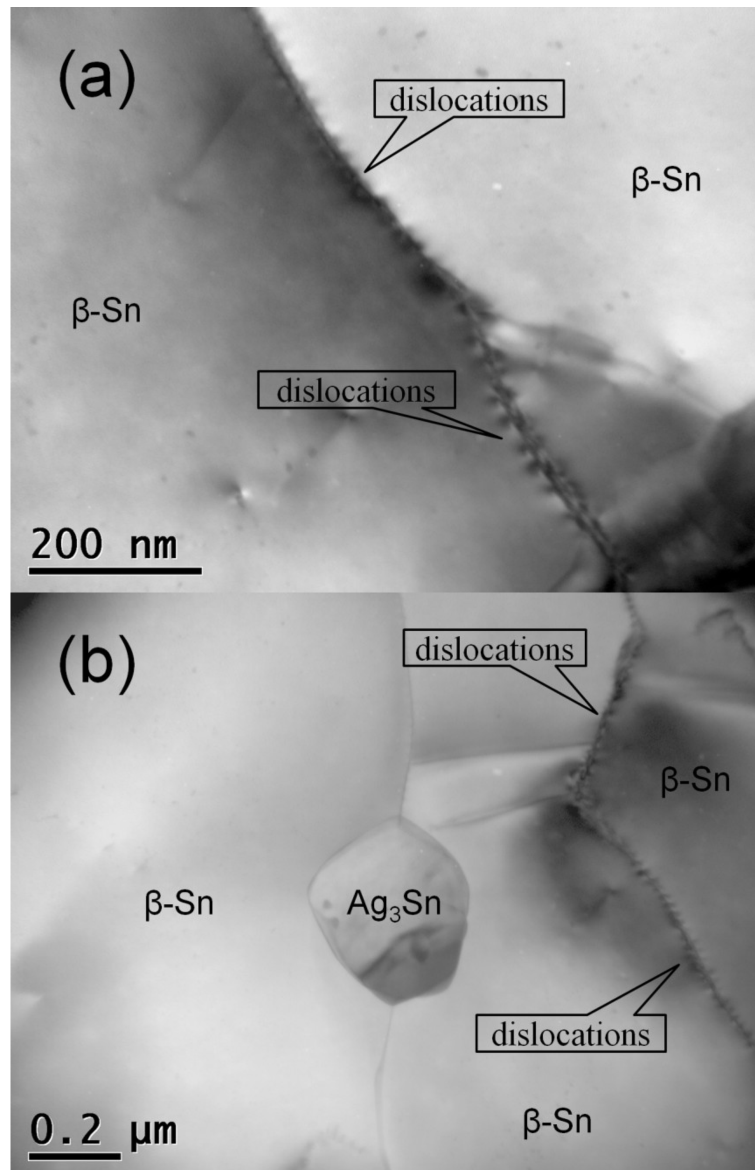

Figure 8-24 TEM micrographs of dislocations in the Sn-Ag-Cu film electrodeposited under galvanostatic conditions (10 mA/cm^2, electrical charge pass = 1500 C/dm^2) from bath D, Table 8-1 with the presence of additives.

Common reasons for dislocation formation include mechanical and thermal histories [137]. However, as the electrodeposit didn't undergo any mechanical deformation or thermal processing, it is believe that internal stress in the Sn-Ag-Cu electrodeposits, popularly existing in electrodeposits in baths with [138] or without the presence of additives [139], has caused the dislocations, as this is an efficient way to release the stress and potential energy. Therefore, the bright Sn-Ag-Cu electrodeposit under the effects of PEG 600 and formaldehyde might have been stressed during the

electrodeposition process. However, this needs to be confirmed by internal stress measurements.

8.8 Wafer Bumping of Sn-Ag-Cu Alloy

On the basis of previous study on Cu coupons, Sn-Ag-Cu solder bumps were produced potentiostatically on wafers from baths B and D from Table 8-1 to examine the process with and without the presence of additives and the resultant solder bumps. In bath B, free of additives, a potential of -1.1 V was used which equates to a current density of around 15 mA/cm^2 as indicated in both the polarisation and chronopotentiometry curves (Figure 8-1 and Figure 8-6 respectively). Figure 8-25 shows the as-electrodeposited bumps with a pitch size of 50 μm (25 μm diameter). It can be noticed that without additives, although having a compact microstructure, a rough surface on the bumps is typical, which has been indicated by studies on Cu coupons (Figure 8-5, image (a)).

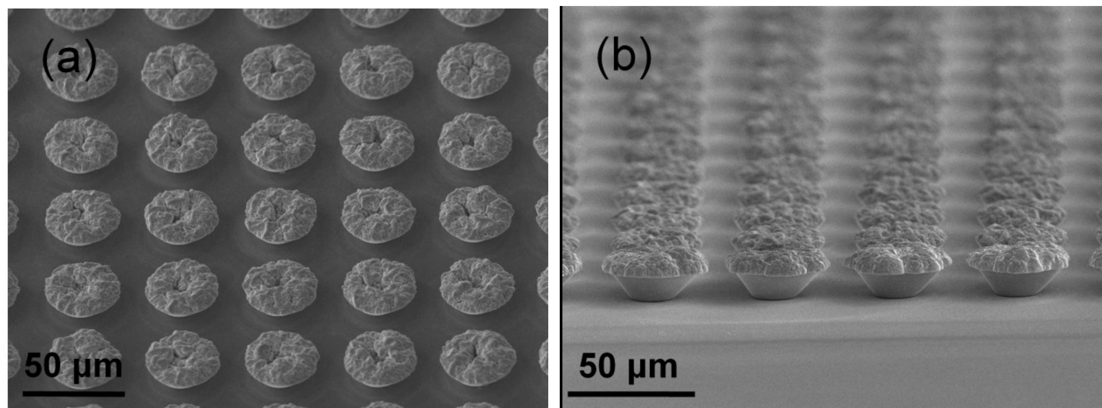

Figure 8-25 SEM micrographs of the as-electrodeposited Sn-Ag-Cu solder bumps formed under potentiostatic conditions at a potential of -1.1 V from bath B, Table 8-1, pitch size = 50 μm (25 μm bump diameter): (a) plan view; (b) magnified side view.

As PEG 600 and formaldehyde are included in the electrolyte, Sn-Ag-Cu solder bumps of a near eutectic composition were also produced potentiostatically at a potential of -1.45 V, which equates to a current density of approximately 15 mA/cm^2 as the polarisation and chronopotentiometry curves confirm (Figure 8-3 and Figure 8-16). Figure 8-26 shows the as-electroplated bumps with a pitch size of 50 μm (25 μm diameter). The plan view (image (a)) shows a good uniformity of bumps, which is critical for fine pitch chip scale packaging. From the side view of the bumps (image

(b)), the smooth surface resulting from the influence of additives remains consistent with the samples produced on Cu coupons. This result promises the possibility of generating consistent, uniform and high yield bumps of ultrafine pitch on a wafer scale. Consequently, this has demonstrated the feasibility of producing optimised fine pitch near-eutectic Sn-Ag-Cu solder bumps for miniaturised flip-chip application.

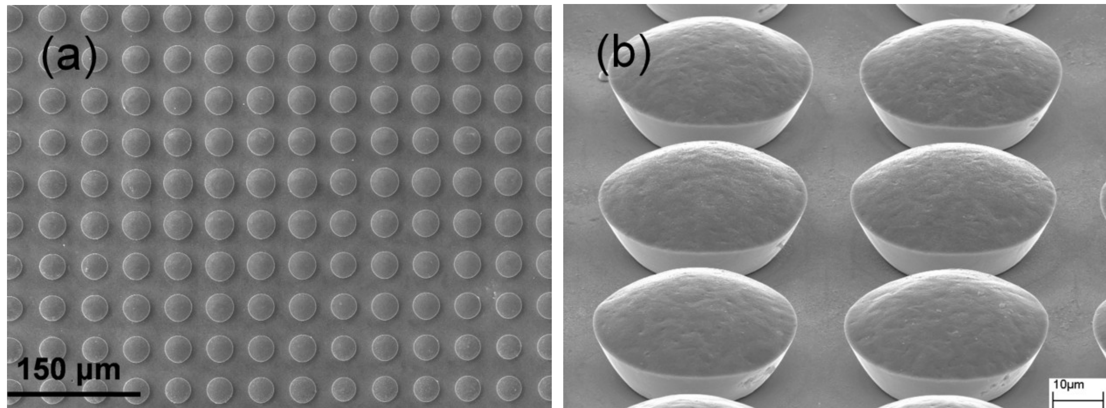

Figure 8-26 SEM micrographs of the as-electrodeposited Sn-Ag-Cu solder bumps formed under potentiostatic conditions at a potential of -1.45 V from bath D, Table 8-1 with the presence of additives, pitch size = 50 µm (25 µm bump diameter): (a) plan view; (b) magnified side view.

8.9 Summary

Pyrophosphate and iodide based baths and processes for the electrodeposition of near-eutectic Sn-Ag-Cu alloys were investigated through cathodic potentiodynamic polarisation and characterisation of electrodeposits under different process conditions. Ternary Sn-Ag-Cu alloys were produced when the driving potential for Sn electrodeposition was reached (-0.88 V vs.SCE) after the mass-transport limited stage for noble metals deposition (Ag and Cu). The morphologies of deposits tended to be relatively smooth at lower current densities (5 to 15 mA/cm^2) with a near-eutectic composition (2.5–4.2wt.% Ag and 0.7–1.5wt.% Cu), though the Ag and Cu contents tended to be lower with increasing current density. Nodular deposits were generated when the current density was approaching or above the limiting deposition current densities of the alloy. As agitation was applied during the electroplating process, the Ag and Cu contents were as high as 26.9wt.% and 17.2wt.% respectively when the current density was only 5 mA/cm^2. However, nodular deposits did not appear until the current density reached 80 mA/cm^2. This was because the agitation significantly enhanced the mass transport to the cathode surface and as a result, Sn grains produced

were smaller compared to the non-agitation process. It was also demonstrated that increased bath temperature had similar effects on the mass transport. With the addition of PEG 600 and formaldehyde, electrodeposits with bright surfaces were generated at a current density 15 mA/cm^2 while achieving a near-eutectic composition of Sn-3.8wt.%Ag-0.8wt.%Cu. AFM confirmed a root-mean-square value (*Rq*) of only 18.6 nm for this bright surface.

XRD analysis revealed that regardless of the process conditions, the deposited Sn-Ag-Cu alloy films included Sn, Ag_3Sn and Cu_6Sn_5 phases. TEM micrographs illustrated that Ag_3Sn and Cu_6Sn_5 intermetallic particles were present either in Sn grains or along grain boundaries. Under the effects of additives, Ag_3Sn and Cu_6Sn_5 intermetallic particles, with a size of tens of nanometres, were uniformly spread within the whole deposit. Dislocations were observed at tin grain boundaries under the effects of additives. This was probably owing to the internal stress induced in the electrodeposits. Fine pitch (50 μm) near-eutectic Sn-Ag-Cu solder bumps were produced on a wafer scale utilising the electrolyte and optimised process parameters. The surface morphology of the bumps obtained was significantly improved with the addition of additives and solder bumping with excellent consistency and uniformity on a wafer scale has been achieved.

Chapter 9

Conclusions and Future Work

9.1 Conclusions

Experimental investigations carried out in the current study have realised the electrodeposition of near-eutectic Sn-Ag, Sn-Cu and Sn-Ag-Cu alloys for solderable finishes on electronic components as well as for the fabrication of solder bumps for flip chip interconnection. The following conclusions can be drawn from those studies:

9.1.1 Electrodeposition of Sn-Cu System

As one of the recognised lead-free candidates, near-eutectic Sn-Cu solder alloy system was achieved by electrodeposition as one of the objectives for the current study. The electrolyte was formulated and Sn-Cu electrodeposits characterised. The summary of the results is as follows:

1. Based on a methanesulphonate system, the electrolyte was formulated using tin methanesulphonate and copper sulphate as the ion sources for tin and copper respectively. Tin methanesulphonate has proved an efficient source providing tin ions which were the main constituent of the objective near-eutectic Sn-Cu solder alloy.

2. The effects through the addition of thiourea, OPPE and MSA to the tin methanesulphonate and copper sulphate electrolyte were analysed through cathodic potentiodynamic polarisation investigations. Forming complexes with Cu ions (Cu^{2+}), thiourea facilitated the co-deposition of Sn-Cu alloy by bringing their deposition potentials close, although not showing any significant contribution to electrodeposit microstructural improvement. OPPE demonstrated strong inhibitive effects on Sn deposition and rough electrodeposit surface morphologies, such as

dendrites and nodules, were effectively eliminated with its presence and characteristic crystalline facets were seen on the electrodeposits as observed by SEM. While improving the bath's shelf life owing to its reducing acid attribute, MSA not only gave benefits of achieving uniform Sn-Cu coating by significantly enhancing the conductivity of the electrolyte, it also refined the electrodeposited tin grains as evidenced by SEM/FIB cross-sectional observation.

3. From a bath consisting of tin methanesulphonate at 70 g/L and copper sulphate at 0.007 mol/L respectively with the presence of thiourea, OPPE and MSA, compositional analyses, by WDX measurements, demonstrated that the objective near-eutectic Sn-Cu alloys (0.6–0.8wt.%Cu) were achievable over a current density range of 10–20 mA/cm^2, generating relatively smooth and compact electrodeposits. DSC thermal scanning results showed that all the Sn-Cu electrodeposits exhibited a melting peak commencing at approximately 227°C, matching the melting temperature of eutectic Sn-Cu alloy as seen from the equilibrium Sn-Cu phase diagram. Another melting peak at around 233°C, resembling the melting behaviour of pure tin, was also evident for samples with copper composition below the eutectic point (0.7wt.%Cu). This was probably owing to the insufficient copper content in the electrodeposits.

4. XRD investigations indicated two phases, β-Sn and Cu_6Sn_5, in the electrodeposits. This was further confirmed by SEM/FIB and TEM observations, as well as EDX analysis. Cross-sectional TEM micrographs showed that with sizes typically no more than 100 nm, column packed Cu_6Sn_5 intermetallics were predominantly spread along Sn grain boundaries.

9.1.2 Electrodeposition of Sn-Ag and Sn-Ag-Cu System

A pyrophosphate-iodide based electrolyte system was established for the electrodeposition of near-eutectic Sn-Ag solder alloy. With modifications, this system was further extended to the electrodeposition of ternary eutectic Sn-Ag-Cu alloy, one of the most promising lead-free alternatives. The main conclusions utilising this electrolyte system for Sn-Ag and Sn-Ag-Cu alloys are as follows:

1. As well as using tin pyrophosphate and silver iodide as the sources for tin and silver ions respectively, potassium pyrophosphate at a concentration of 1.0 mol/L was included in the electrolyte to fully complex with the tin ions (Sn^{2+}). This, therefore, effectively reduced the concentration of free tin ions, inhibited the tin ion oxidation from Sn^{2+} to Sn^{4+} (by ambient oxygen) and significantly improved the bath shelf-life as a result. Potassium iodide at 2.0 mol/L was also added to the bath for complexation with silver ions and consequently brought the deposition potential of silver closer to that of tin for Sn-Ag co-deposition.

2. From cathodic potentiodynamic polarisation data and depending on the objective alloy, binary/ternary Sn-Ag/Sn-Ag-Cu alloys were produced when the driving potential for Sn electrodeposition was reached (-0.88 V vs. SCE) after the mass-transport limited stages for noble metals' deposition (Ag for Sn-Ag and Ag-Cu for Sn-Ag-Cu systems). Polyethylene glycol (PEG) 600 and formaldehyde were employed in the system as additives to improve the properties of the electrodeposits. PEG showed strong inhibitive effects on tin deposition as the reduced current density in cathodic polarisation curves demonstrated. Formaldehyde was found to reduce to methanol from a potential of -1.2 V vs. SCE, after which synergetic effects with PEG were evident on the alloy electrodeposition process.

3. As observed by SEM, regardless of the alloy composition, the morphology of electrodeposits tended to evolve from compact and flat feather-like to nodular and dendritic characteristics as the current density was increased to approach the limiting levels. The sole addition of PEG 600 did not produce a smooth surface, but instead long protrusions were observed owing to limited locations for deposition outgrowth as a result of the adsorptive behaviour of PEG. However, the synergetic effects of both PEG and formaldehyde achieved bright surface, with AFM confirming a root-mean-square roughness value (Rq) of only 18.6 nm. The surfaces of samples from the absence of additives were so rough that appropriate AFM measurements were disqualified.

4. Cross-sectional microstructural analysis of Sn-Ag and Sn-Ag-Cu electrodeposits of different surface morphologies under varying conditions were carried out by SEM/FIB and TEM observations. As confirmed by XRD spectra and in-depth

observation in TEM micrographs, Ag_3Sn particles, as well as Cu_6Sn_5 for Sn-Ag-Cu alloys, were widely spread within β-Sn grains or along grain boundaries in the electrodeposits, regardless of the deposits being compact, nodular or dendritic. Under the effects of additives (PEG and formaldehyde), Ag_3Sn and Cu_6Sn_5 intermetallic particles, with a size of tens of nanometres, were uniformly spread within the whole Sn-Ag-Cu deposit and the long-shape fine Sn grains had a width of 200 nm or less. Such a fine grained microstructure explained the bright surface of the deposited films. Dislocations were observed at tin grain boundaries in TEM micrographs under the effects of additives. This was probably owing to the internal stress in the electrodeposits.

5. The effects of other process parameters, including agitation and bath temperature, were investigated for the ternary Sn-Ag-Cu system. As agitation was applied to the electroplating process, the Ag and Cu contents were as high as 26.9wt.% and 17.2wt.% respectively when the current density was relatively low, 5 mA/cm^2. However, nodular deposits did not appear until the current density reached 80 mA/cm^2. This was because the agitation significantly enhanced the mass transport to the cathode surface, with another effect being smaller Sn grains produced compared to the non-agitation process as revealed by SEM/FIB observations. Increased bath temperatures had similar effects on mass transport in the current system. At 5 mA/cm^2, 60 °C, mainly silver dendrites were observed, which was due to the increased Ag limiting deposition current density produced by the elevated bath temperature. Higher bath temperatures, i.e. 40 and 60 °C, also achieved increased limiting current density for tin, although less effectively than agitation.

6. Compositional analysis by WDX revealed that, in general, the contents of Ag and Cu in the electrodeposits tended to decrease with increasing current density applied. However, with the presence of additives (PEG and formaldehyde) promising a fine-grained compact microstructure, near-eutectic Sn-Ag (3.1–4.3wt.%Ag) alloys were achievable over a current density range of 10 to 20 mA/cm^2. Regarding the ternary Sn-Ag-Cu alloy, with a near-eutectic composition (2.5–4.2wt.% Ag and 0.7–1.5wt.% Cu) achievable at current densities from 5 to

15 mA/cm^2, a composition of Sn-3.8wt.%Ag-0.8wt.%Cu was recorded with the presence of additives.

7. Through DSC thermal scanning revealing the melting behaviour, electrodeposits of Sn-3.6wt.%Ag and Sn-4.8wt.%Ag-1.6wt.%Cu, measured by WDX, showed single peak curves with the peaks recorded at 222°C and 228°C respectively. Electrodeposits with other measured compositions showed widened endothermic processes.

9.1.3 Lead-Free Wafer Level Solder Bumping

As one of the main objectives and applications for the current project, lead-free (Sn-Ag, Sn-Cu and Sn-Ag-Cu) solder bumps were produced on test wafers utilising the electrolyte systems developed and characterised.

1. Regardless of the lead-free alloy employed, the developed processes demonstrated two most important merits of using electrodeposition as the wafer bumping methodology: efficiency and fine pitch. All the solder bumps were fabricated with high yield across the whole wafer in one operation. Pitch size of 50 μm, bump diameter of 25 μm were demonstrated, which could be further scaled down depending on the photoresist pattern produced on the wafer.

2. Near-eutectic Sn-Cu solder bumps were produced on the wafer through the methanesulphonate electrolyte system developed. With a bath including all the required constituents, Sn-Cu solder bumps were produced with fine β-Sn grains and Cu_6Sn_5 particles predominantly and uniformly existing along tin grain boundaries.

3. Utilising the pyrophosphate-iodide based electrolyte system and under the effects of PEG and formaldehyde, both near-eutectic Sn-Ag and Sn-Ag-Cu solder bumps with smooth surfaces were demonstrated on test wafers. Such bumps were of refined grain structure, also with Ag_3Sn and Cu_6Sn_5 particles uniformly spreading within the whole bump. This process was helpful to achieve solder bumping with excellent consistency and uniformity on wafers, which is important for producing reliable solder joints at later fabrication stages.

9.2 Recommendations for Future Work

1. Because of the oxidation of tin ions, the shelf life of the developed tin methanesulphonate solution remains a issue. Proper steps, such as finding appropriate anti-oxidants, should be taken for improvement, whilst any other addition to the electrolyte should be comprehensively characterised in terms of its potential effects on the electrochemical process as well as the properties of the electrodeposits.

2. Owing to its brittle nature, over growth of IMC, such as Ag_3Sn and Cu_6Sn_5, could be detrimental to the reliability of solder joints [140]. Since Ag_3Sn and Cu_6Sn_5 widely exist in the as-electrodeposited solder bumps as proven, it is worth studying their impact on IMC formation during later stages, such as during the reflow process and over the service life of the electronic devices.

3. Owing to electrochemical heterogeneity over the cathode surface resulting from factors such as complex geometry of the work piece (cathode) and localised electrochemical environment in the bath, non-uniform electrodeposition could commonly happen and result in un-even deposition, such as non-uniform bump height and composition in terms of wafer level lead-free solder bumping [141]. Specially designed bath jigs are normally required to properly accommodate the work piece, such as a wafer with specific size and deposition pattern. An appropriate method of agitation should also be considered to improve the uniformity across the wafer [142].

4. Copper pillars have been an option for wafer level bumping in situations where the requirement for fine pitch is so strong that even the spherical geometry of solder bumps after reflow is not acceptable [143]. Compared to solder materials, other advantages of using copper as the bumping materials include greater electrical and thermal conductivity, as well as better resistance to electromigration. Figure 9-1 shows a copper pillar on wafers with a solderable cap that can be reflowed and therefore connected to the substrate. After the copper pillar is produced (normally by electrodeposition), lead-free solder caps, i.e. Sn-Ag, Sn-Cu and Sn-Ag-Cu alloys, depending on requirements, can be electrodeposited on to the copper pillars from the developed process in the current study.

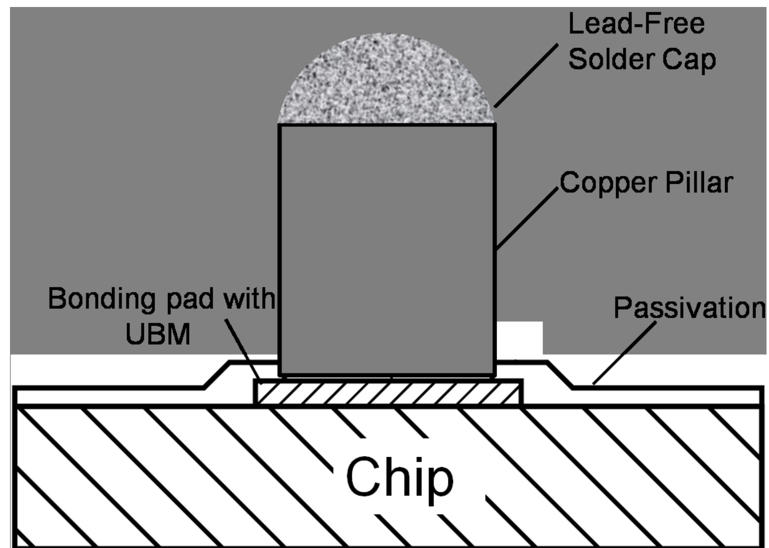

Figure 9-1 Illustration of a copper pillar on a wafer with a lead-free solder cap for flip chip interconnection

References

1. J. Orton, *Birth of the Transistor: Point Contacts and P-N Junctions*, in *Semiconductors and the Information Revolution*. 2009, Academic Press. p. 57-94.

2. R. Asthana, A. Kumar and N. B. Dahotre, *Semiconductor Manufacturing*, in *Materials Processing and Manufacturing Science*. 2006, Academic Press. p. 485-550.

3. G. Marsh, *Moore's law at the extremes.* Materials Today, 2003. 6 (5): p. 28-33.

4. R. R. Tummala, *Introduction to Microsystems Packaging*, in *Fundamentals of Microsystems Packaging*. 2004, McGraw-Hill. p. 8.

5. H.-M. Tong, *Microelectronics packaging: present and future.* Materials Chemistry and Physics, 1995. 40 (3): p. 147-161.

6. J. H. Lau, *Integrated Circuit Packaging Trends*, in *Low Cost Flip Chip Technologies for DCA, WLCSP, and PBGA Assemblies*. 2000, McGraw-Hill. p. 1-2.

7. R. R. Tummala, *Introduction to Microsystems Packaging*, in *Fundamentals of Microsystems Packaging*. 2004, McGraw-Hill. p. 18.

8. O. Brand, *Microsensor Integration Into Systems-on-Chip.* Proceedings of the IEEE, 2006. 94 (6): p. 1160-1176.

9. O. Brand, *Packaging*, in *Comprehensive Microsystems*, G. Yogesh, T. Osamu and Z. Hans, Editors. 2008, Elsevier. p. 437.

10. J. L. Young. *Wafer level and substrate level chip scale packaging*. in International Symposium on Advanced Packaging Materials: Processes, Properties and Interfaces. 1999. Braselton, GA. p. 232 - 235.

11. R. Arnold. *Chip scale package versus direct chip attach (CSP vs. DCA)*. in Electronic Components and Technology Conference 50th. 2000. Las Vegas, NV. p. 822 - 828.

12. R. R. Tummala, *Fundamentals of IC Assembly*, in *Fundamentals of Microsystems Packaging*. 2004, McGraw-Hill. p. 344.

13. R. R. Tummala, *Fundamentals of IC Assembly*, in *Fundamentals of Microsystems Packaging*. 2004, McGraw-Hill. p. 391.

14. S. K. Prasad, *Introduction*, in *Advanced Wirebond Interconnection Technology*. 2004, Kluwer Academic Publishers. p. 1-3.

15. C. Lopez, L. Chai, A. Shaikh and V. Stygar, *Wire bonding characteristics of gold conductors for low temperature co-fired ceramic applications.* Microelectronics Reliability, 2004. 44 (2): p. 287-294.

16. B. Gehman, *Bonding Wire Microelectronic Interconnections.* IEEE Transactions on Components, Hybrids, and Manufacturing Technology, 1980. 3 (3): p. 375 - 383.

17. H. Reichl. *Tape-automated-bonding*. in Electronic Manufacturing Technology Symposium, 1990, IEMT Conference., 8th IEEE/CHMT International. 1990. p. 460-471.

18. S. K. Kang, *Tape-automated Bonding: Materials and Technologies*, in *Encyclopedia of Materials: Science and Technology*, K.H.J. Buschow, W.C. Robert, C.F. Merton, I. Bernard, J.K. Edward, M. Subhash and V. Patrick, Editors. 2001, Elsevier. p. 9088-9093.

19. J. H. Lau, S. J. Erasmus and D. W. Rice, *Overview of tape automated bonding technology.* Circuit World, 1993. 16 (2): p. 5-24.

20. http://www.ami.ac.uk/courses/topics/0258_tab/index.html. October 27, 2010.

21. D. L. Barton, K. Bernhard-Höfer and E. I. Cole, *Flip-chip and "backside" techniques.* Microelectronics Reliability, 1999. 39 (6-7): p. 721-730.

22. C. L. Wong and J. How. *Low cost flip chip bumping technologies*. in Electronic Packaging Technology Conference, 1997. Proceedings of the 1997 1st. 1997. p. 244-250.

23. G. Humpston and A. P. Needham, *Advanced flip-chip solder bonding.* Nuclear Instruments and Methods in Physics Research Section A: Accelerators, Spectrometers, Detectors and Associated Equipment, 1997. 395 (3): p. 375-378.

24. T. Y. Tee, X. Fan and Y.-S. Lai, *Advances in Wafer Level Packaging (WLP).* Microelectronics Reliability, 2010. 50 (4): p. 479-480.

25. R. R. Tummala, *Fundamentals of Multichip Packaging*, in *Fundamentals of Microsystems Packaging*. 2004, McGraw-Hill. p. 302.

26. R. Islam, C. Brubaker, P. Lindner and C. Schaefer. *Wafer level packaging and 3D interconnect for IC technology*. in Advanced Semiconductor Manufacturing IEEE/SEMI Conference and Workshop 2002. p. 212 - 217.

27. *Assembly and Packaging.* International Technology Roadmap for Semiconductors, 2007.

28. J. H. Lau, *A Brief Introduction to Flip Chip Technologies for Multichip Module Applications*, in *Flip Chip Technologies*, J.H. Lau, Editor. 1995, McGraw-Hill. p. 25-28.

29. W. J. Greig, *Flip Chip-The Bumping Processes*, in *Integrated Circuit Packaging, Assembly and Interconnections*, W.J. Greig, Editor. 2007, Springer US. p. 143-167.

30. P. Gupta, *Effect of Intermetallic Compound on Thermomechanical Reliability of Lead-Free Solder Interconnects for Flip-Chips*. MSc Thesis, 2004. Georgia Institute of Technology.

31. Z. S. Karim and R. Schetty. *Lead-free bump interconnections for flip-chip applications*. in Electronics Manufacturing Technology Symposium, 2000. Twenty-Sixth IEEE/CPMT International. 2000. p. 274-278.

32. A. Huffman, R. LaBennett, S. Bonafede and S. C. *Fine-pitch wafer bumping and assembly for high density detector systems*. in Nuclear Science Symposium Conference Record, 2003 IEEE. 2003. p. 3522-3526 Vol.5.

33. J. Kloeser, P. Coskina, R. Aschenbrenner and H. Reichl, *Bump formation for flip chip and CSP by solder paste printing.* Microelectronics Reliability, 2002. 42 (3): p. 391-398.

34. J. H. Adriance, M. A. Whitmore and J. D. Schake. *Bumping of silicon wafers by stencil printing*. in Electronics Manufacturing Technology Symposium, 1999. Twenty-Fourth IEEE/CPMT. 1999. p. 313-319.

35. P. A. Gruber, L. B. Langer, G. P. Brouillette, D. H. Danovitch, J. L. Landreville, D. T. Naugle, V. A. Oberson, D. Y. Shih, C. L. Tessler and M. R. Turgeon, *Low-cost wafer bumping.* IBM Journal of Research and Development, 2005. 49: p. 621-639.

36. G. Jing-Feng, E. W. C. Yau, P. C. H. Chan, R. S. W. Lee and M. M. F. Yuen. *Optimization of stencil printing wafer bumping for fine pitch flip chip applications*. in Electronic Components and Technology Conference, 2003. Proceedings. 53rd. 2003. p. 1724-1730.

37. F. Andres, C. Lee and G. Pham-Van-Diep. *Bumping wafers via ultrasonically enhanced stencil printing*. in Electronics Manufacturing Technology Symposium, 2003. IEMT 2003. IEEE/CPMT/SEMI 28th International. 2003. p. 331-334.

38. K. Seyama, H. Yamamoto, K. Satou, H. Yoshimura, H. Ota and Y. Usui. *Transcription solder bump technology using the evaporation method*. in International Conference on Multichip Modules and High Density Packaging. 1998. Denver, CO. p. 314-318

39. M. Datta, T. Osaka and J. W. Schultze, *Microelectronic Packaging*, in *New Trends in Electrochemical Technology Series*. 2005, CRC Press LLC. p. 36-39.

40. M. Kelly and J. Lau, *Low Cost Solder Bumped Flip Chip MCM-L Demonstration.* Circuit World, 1995. 21 (4): p. 14-17.

41. H. Sunil, *Green Electronics through Legislation and Lead Free Soldering.* CLEAN - Soil, Air, Water, 2008. 36 (2): p. 145-151.

42. T. C. May and M. H. Woods, *Alpha-particle-induced soft errors in dynamic memories.* Electron Devices, IEEE Transactions on, 1979. 26 (1): p. 2-9.

43. D. S. Yaney, J. T. Nelson and L. L. Vanskike, *Alpha-particle tracks in silicon and their effect on dynamic MOS RAM reliability.* Electron Devices, IEEE Transactions on, 1979. 26 (1): p. 10-16.

44. A. Sharif, *A Study on Interfacial Interaction Behavior Between Lead-Free Solders and Electroless Nickel Metallization for Advanced Electronic Packaging*. PhD Thesis, 2005. City University of Hong Kong.

45. C. F. Luk, *The Characterization and Reliability Analysis of Green Electronics Manufacturing Processes for Hard Disk Drive Head Assembly*. PhD Thesis, 2006. City University of Hong Kong.

46. B. H. Robinson, *E-waste: An assessment of global production and environmental impacts.* Science of The Total Environment, 2009. 408 (2): p. 183-191.

47. R. Widmer, H. Oswald-Krapf, D. Sinha-Khetriwal, M. Schnellmann and H. Böni, *Global perspectives on e-waste.* Environmental Impact Assessment Review, 2005. 25 (5): p. 436-458.

48. V. Eveloy, S. Ganesan, Y. Fukuda, J. Wu and M. G. Pecht, *Are you ready for lead-free electronics?* . IEEE Transactions on Components and Packaging Technologies, 2005. 28 (4): p. 884-894.

49. http://www.inemi.org/cms/. October 27, 2010.

50. http://www.epa.gov/tri/guide_docs/. October 27, 2010.

51. M. Abtew and G. Selvaduray, *Lead-free Solders in Microelectronics.* Materials Science and Engineering: R: Reports, 2000. 27 (5-6): p. 95-141.

52. C. Handwerker, U. Kattner and K.-W. Moon, *Fundamental Properties of Pb-Free Solder Alloys*, in *Lead-Free Soldering*, J. Bath, Editor. 2007, Springer Science+Business Media, LLC. p. 22.

53. K. Suganuma, *Future of Lead-Free Soldering*, in *Lead-Free Soldering in Electronics: Science, Technology and Environmental Impact*, K. Suganuma, Editor. 2004, Marcel Dekker, Inc. p. 330.

54. I. Anderson, *Development of Sn-Ag-Cu and Sn-Ag-Cu-X alloys for Pb-free electronic solder applications*, in *Lead-Free Electronic Solders*, K.N. Subramanian, Editor. 2007, Springer US. p. 55-76.

55. K. J. Puttlitz, *Overview of Lead-Free Solder Issues Including Selections*, in *Handbook of Lead-Free Solder Technology for Microelectronic Assemblies*, K.J. Puttlitz and K.A. Stalter, Editors. 2004, Marcel Dekker, Inc. p. 20.

56. C. Handwerker, U. Kattner and K.-W. Moon, *Fundamental Properties of Pb-Free Solder Alloys*, in *Lead-Free Soldering*, J. Bath, Editor. 2007, Springer.

57. T. B. Massalski, H. Okamoto, P. R. Subramanian and L. Kacprzak, *ASM Binary Alloy Phase Diagrams*. 1996: ASM International.

58. W. Yang, R. Messler and L. Felton, *Microstructure evolution of eutectic Sn-Ag solder joints.* Journal of Electronic Materials, 1994. 23 (8): p. 765-772.

59. M. McCormack and S. Jin, *New, lead-free solders.* Journal of Electronic Materials, 1994. 23 (7): p. 635-640.

60. K. G. Snowdon, C. G. Tanner and J. R. Thompson. *Lead-free soldering electronic interconnect: Current status and future developments*. in Electronic Components and Technology Conference. 2000. Las Vegas, NV. p. 1416-1419.

61. D. R. Frear, J. Jang, J. K. Lin and C. Zhang, *Pb-free solders for flip-chip interconnects.* JOM, 2001. 53 (6): p. 28-32.

62. S. Huh, K. Kim and K. Suganuma, *Effect of Ag addition on the microstructural and mechanical properties of Sn-Cu eutectic solder.* Materials Transactions, 2001. 42 (5): p. 739-744.

63. I. E. Anderson, J. C. Foley, B. A. Cook, J. Harringa, R. L. Terpstra and O. Unal, *Alloying Effects in Near-eutectic Sn-Ag-Cu Solder Alloys for Improved Microstructural Stability.* Journal of Electronic Materials, 2001. 30: p. 1050-1059.

64. K. Moon, W. Boettinger, U. Kattner, F. Biancaniello and C. Handwerker, *Experimental and thermodynamic assessment of Sn-Ag-Cu solder alloys.* Journal of Electronic Materials, 2000. 29 (10): p. 1122-1136.

65. I. Ohnuma, M. Miyashita, K. Anzai, X. Liu, H. Ohtani, R. Kainuma and K. Ishida, *Phase equilibria and the related properties of Sn-Ag-Cu based Pb-free solder alloys.* Journal of Electronic Materials, 2000. 29 (10): p. 1137-1144.

66. K. Suganuma, *Advances in lead-free electronics soldering.* Current Opinion in Solid State and Materials Science, 2001. 5 (1): p. 55-64.

67. J. Jiang, J.-E. Lee, K.-S. Kim and K. Suganuma, *Oxidation behavior of Sn-Zn solders under high-temperature and high-humidity conditions.* Journal of Alloys and Compounds, 2008. 462 (1-2): p. 244-251.

68. L. Zhang, S.-b. Xue, L.-l. Gao, Y. Chen, S.-l. Yu, Z. Sheng and G. Zeng, *Microstructure and creep properties of Sn-Ag-Cu lead-free solders bearing minor amounts of the rare earth cerium.* Soldering & Surface Mount Technology, 2010. 22 (2): p. 30-36.

69. C. M. L. Wu, D. Q. Yu, C. M. T. Law and L. Wang, *Properties of lead-free solder alloys with rare earth element additions.* Materials Science and Engineering: R: Reports, 2004. 44 (1): p. 1-44.

70. M. Jordan, *The Electrodeposition of Tin and its Alloys*. 1995: Eugen G.Leuze Publishers. p22-38.

71. M. Schlesinger and M. Paunovic, *Modern Electroplating*, 4th. 2000: John Wiley & Sons, Inc.

72. P. Vanýsek, *Electrochemical Series*, in *Handbook of Chemistry and Physics*, 88th Edition, D.R. Lide, Editor. 2007, Chemical Rubber Company.

73. M. Jordan, *The Electrodeposition of Tin and its Alloys*. 1995: Eugen G.Leuze Publishers. 22-38.

74. J. Y. Kim, J. Yu, J. H. Lee and T. Y. Lee, *The Effects of Electroplating Parameters on the Composition and Morphology of Sn-Ag Solder.* Journal of Electronic Materials, 2004. 33 (12): p. 1459-1465.

75. E. K. Yung and L. T. Romankiw, *Fundamental Study of Acid Copper Through-Hole Electroplating Process.* Journal of The Electrochemical Society, 1989. 136 (3): p. 756-767.

76. Q. Chen, Z. Wang, J. Cai and L. Liu, *The influence of ultrasonic agitation on copper electroplating of blind-vias for SOI three-dimensional integration.* Microelectronic Engineering, 2010. 87 (3): p. 527-531.

77. C. T. Walker and R. Walker, *Effect of ultrasonic agitation on some properties of electrodeposits.* Electrodeposition and Surface Treatment, 1973. 1 (6): p. 457-469.

78. M. Lisinenkova, K. Bade, L. Hahn and J. Schulz, *Development of a sonovoltammetric cell for mass transport investigations in the LIGA-process under megasonic agitation.* Electrochimica Acta, 2007. 53 (2): p. 312-318.

79. E. Castellani, J. Powers and L. Romankiw, U.S. Patent 4,102,756 Nickel-Iron (80:20) Alloy Thin Film Electroplating Method and Electrochemical Treatment and Plating Apparatus, 1978.

80. T. M. Tam, *Electrodeposition Kinetics for Tin, Lead, and Tin-Lead Fluoborate Plating Solutions.* Journal of The Electrochemical Society, 1986. 133 (9): p. 1792-1796.

81. P. A. Kohl, *The High Speed Electrodeposition of Sn/Pb Alloys.* Journal of The Electrochemical Society, 1982. 129 (6): p. 1196-1201.

82. Y.-H. Yau, *The Effect of Process Variables on Electrotinning in a Methanesulfonic Acid Bath.* Journal of The Electrochemical Society, 2000. 147 (3): p. 1071-1076.

83. C. Rosenstein, *Methane Sulfonic Acid as an. Electrolyte for Tin, Lead and Tin-Lead Plating for. Electronics.* Metal Finishing, 1990. 88 (1): p. 17-21.

84. M. Goodenough and K. J. Whitlaw, *The Suppression of Sn, Pb, and Sn-Pb by organic Compounds.* Transactions of the Institute of Metal Finishing, 1987. 67: p. 44.

85. C. T. J. Low and F. C. Walsh, *Electrodeposition of tin, copper and tin-copper alloys from a methanesulfonic acid electrolyte containing a perfluorinated cationic surfactant.* Surface and Coatings Technology, 2008. 202 (8): p. 1339-1349.

86. C. T. J. Low and F. C. Walsh, *Normal and anomalous electrodeposition of tincopper alloys from methanesulphonic acid bath containing perfluorinated cationic surfactant.* Transactions of the Institute of Metal Finishing, 2008. 86: p. 315-325.

87. N. M. Martyak and R. Seefeldt, *Additive-effects during plating in acid tin methanesulfonate electrolytes.* Electrochimica Acta, 2004. 49 (25): p. 4303-4311.

88. S. Joseph and G. J. Phatak, *Effect of surfactant on the bath stability and electrodeposition of Sn-Ag-Cu films.* Surface and Coatings Technology, 2008. 202 (13): p. 3023-3028.

89. J. Dini, *Electrodeposition of Copper*, in *Modern Electroplatin*, 4th Edition, M. Schlesinger and M. Paunovic, Editors. 2000, John Wiley & Sons. p. 68.

90. S. D. Beattie and J. R. Dahn, *Single-Bath Electrodeposition of a Combinatorial Library of Binary $Cu_{1-x}Sn_x$ Alloys.* Journal of The Electrochemical Society, 2003. 150 (7): p. C457-C460.

91. A. N. Correia, M. X. Facanha and P. de Lima-Neto, *Cu-Sn coatings obtained from pyrophosphate-based electrolytes.* Surface and Coatings Technology, 2007. 201 (16-17): p. 7216-7221.

92. B. Neveu, F. Lallemand, G. Poupon and Z. Mekhalif, *Electrodeposition of Pb-free Sn alloys in pulsed current.* Applied Surface Science, 2006. 252 (10): p. 3561-3573.

93. S. Arai, H. Akatsuka and N. Kaneko, *Sn-Ag Solder Bump Formation for Flip-Chip Bonding by Electroplating.* Journal of The Electrochemical Society, 2003. 150 (10): p. C730-C734.

94. W. M. Murray and N. H. Furman, *Studies of the Reducing Action of Mercury. III. Hydrogen Peroxide Formation and the Copper-Catalyzed Autoxidation of Quinquivalent Molybdenum and Other Strong Reductants in Acid Solution.* Journal of the American Chemical Society, 1936. 58 (10): p. 1843-1847.

95. C. T. J. Low and F. C. Walsh, *The stability of an acidic tin methanesulfonate electrolyte in the presence of a hydroquinone antioxidant.* Electrochimica Acta, 2008. 53 (16): p. 5280-5286.

96. T. Kondo, K. Obata, T. Takeuchi and S. Masaki, *Bright Tin-Silver Alloy Electrodeposition from an Organic Sulfonate Bath Containing Pyrophosphate, Iodide & Triethanolamine as Chelating Agents.* Plating & Surface Finishing, 1998. 85 (2): p. 51-55.

97. N. Kubota and E. Sato, *Conductivity and ion transport in silver-tin pyrophosphate baths.* Electrochimica Acta, 1984. 29 (3): p. 361-364.

98. P. Dixit, C. W. Tan, L. Xu, N. Lin, J. Miao, J. H. L. Pang, P. Backus and R. Preisser, *Fabrication and characterization of fine pitch on-chip copper interconnects for advanced wafer level packaging by a high aspect ratio through AZ9260 resist electroplating.* Journal of Micromechanics and Microengineering, 2007. 17 (5): p. 1078.

99. A. Ul-Hamid, H. M. Tawancy, A.-R. I. Mohammed, S. S. Al-Jaroudi and N. M. Abbas, *Quantitative WDS analysis using electron probe microanalyzer.* Materials Characterization, 2006. 56 (3): p. 192-199.

100. S. J. B. Reed, *Optimization of Wavelength Dispersive X-Ray Spectrometry Analysis Conditions.* Journal of Research of the National Institute of Standards and Technology, 2002. 107 (6): p. 497-502.

101. C.A.Volkert and A. M. Minor, *Focused Ion Beam Microscopy and Micromachining.* MRS Bulletin, 2007. 32 (5): p. 389-399.

102. C. P. Warner and R. A. Corbett. *The Impact of Testing Methodology on Breakdown Potentials*. in International Conference on Shape Memory and Superelastic Technologies. 2006. California, USA. p. 253-264.

103. N. Kaneko, M. Seji, S. Arai and N. Shinohara, *Sn-Cu Solder Bump Formation from Acid Sulfate Baths Using Electroplating Method.* Electrochemistry, 2003. 71 (9): p. 791.

104. O. Khaselev, I. S. Zavarine, A. Vysotskaya, C. Fan, Y. Zhang and J. Abys, *Electroplating and properties of SnBi and SnCu for lead-free finishes.* Transactions of the Institute of Metal Finishing, 2002. 80: p. 200-204.

105. Y. Kong, J. Shao, W. Wang, Q. Liu and Z. Chen, *Electroless Sn-Ni alloy plating with high Sn content free of activation pretreatment.* Journal of Alloys and Compounds, 2009. 477 (1-2): p. 328-332.

106. W. Sun and D. G. Ivey, *Development of an electroplating solution for codepositing Au-Sn alloys.* Materials Science and Engineering B, 1999. 65 (2): p. 111-122.

107. L. W. Flott, *Quality control : The electroplating process.* Metal Finishing, 1996. 94 (3): p. 55-58.

108. B. Kim and T. Ritzdorf, *Electrochemically Deposited Tin-Silver-Copper Ternary Solder Alloys.* Journal of The Electrochemical Society, 2003. 150 (2): p. C53-C60.

109. M. Fukuda, K. Imayoshi and Y. Matsumoto, *Effects of Thiourea and Polyoxyethylene Lauryl Ether on Electrodeposition of Sn-Ag-Cu Alloy as a Pb-Free Solder.* Journal of The Electrochemical Society, 2002. 149 (5): p. C244-C249.

110. C.-C. Hu, Y.-D. Tsai, C.-C. Lin, G.-L. Lee, S.-W. Chen, T.-C. Lee and T.-C. Wen, *Anomalous growth of whisker-like bismuth-tin extrusions from tin-enriched tin-Bi deposits.* Journal of Alloys and Compounds, 2009. 472 (1-2): p. 121-126.

111. Y.-D. Tsai, C.-C. Hu and C.-C. Lin, *Electrodeposition of Sn-Bi lead-free solders: Effects of complex agents on the composition, adhesion, and dendrite formation.* Electrochimica Acta, 2007. 53 (4): p. 2040-2047.

112. F. J. Barry and V. J. Cunnane, *Synergistic effects of organic additives on the discharge, nucleation and growth mechanisms of tin at polycrystalline copper electrodes.* Journal of Electroanalytical Chemistry, 2002. 537 (1-2): p. 151-163.

113. H. Nishikawa, Y. Hamada and T. Takemoto, *Estimation Method for Liquidus Temperature of Lead-Free Solder Using Differential Scanning Calorimetry Profiles.* Journal of Electronic Materials, 2009. 38 (12): p. 2610-2616.

114. J. í. Sopoušek, M. Palcut, E. Hodúlová and J. Janovec, *Thermal Analysis of the Sn-Ag-Cu-In Solder Alloy.* Journal of Electronic Materials, 2010. 39 (3): p. 312-317.

115. N. Duan, J. Scheer, J. Bielen and M. van Kleef, *The influence of Sn-Cu-Ni(Au) and Sn-Au intermetallic compounds on the solder joint reliability of flip chips on low temperature co-fired ceramic substrates.* Microelectronics Reliability, 2003. 43 (8): p. 1317-1327.

116. J. R. Duffield, D. R. Williams and I. Kron, *Speciation studies of the solubility and aqueous solution chemistry of tin(II)- and tin(IV)-pyrophosphate complexes.* Polyhedron, 1991. 10 (3): p. 377-387.

117. V. I. Kravtsov and V. V. Kondratiev, *Kinetics and mechanism of pyrophosphate metal complexes electroreduction.* Electrochimica Acta, 1991. 36 (3-4): p. 427-434.

118. F. Fourcade and T. Tzedakis, *Study of the mechanism of the electrochemical deposition of silver from an aqueous silver iodide suspension.* Journal of Electroanalytical Chemistry, 2000. 493 (1-2): p. 20-27.

119. M. R. S. Oliveira, D. A. A. Mello, E. A. Ponzio and S. C. de Oliveira, *KI effects on the reversible electrodeposition of silver on poly(ethylene oxide) for application in electrochromic devices.* Electrochimica Acta, 2010. 55 (11): p. 3756-3765.

120. H.-Y. Chen, C. Chen, P.-W. Wu, J.-M. Shieh, S.-S. Cheng and K. Hensen, *Effect of Polyethylene Glycol Additives on Pulse Electroplating of SnAg Solder.* Journal of Electronic Materials, 2008. 37 (2): p. 224-230.

121. M. E. H. Garrido and M. D. Pritzker, *Inhibition of Copper Deposition by Polyethylene Glycol and Chloride.* Journal of the Electrochemical Society, 2009. 156 (5): p. D175-D183.

122. S. Arai and T. Watanabe, *Electrodeposition of Sn-Ag Alloy with a Non-Cyanide Bath.* Electrochemistry, 1997. 65 (12): p. 1097-1101.

123. P. G. Russell, N. Kovac, S. Srinivasan and M. Steinberg, *The Electrochemical Reduction of Carbon Dioxide, Formic Acid, and Formaldehyde.* Journal of the Electrochemical Society, 1977. 124 (9): p. 1329-1338.

124. K. Zeng and K. N. Tu, *Six cases of reliability study of Pb-free solder joints in electronic packaging technology.* Materials Science and Engineering: R: Reports, 2002. 38 (2): p. 55-105.

125. J. R. Selman and C. W. Tobias, *Mass-Transfer Measurements by the Limiting-Current Technique*, in *Advances in Chemical Engineering*, G.R.C.J.W.H. Thomas B. Drew, Jr. and V. Theodore, Editors. 1978, Academic Press. p. 211-318.

126. A. M. Rashidi and A. Amadeh, *The effect of saccharin addition and bath temperature on the grain size of nanocrystalline nickel coatings.* Surface and Coatings Technology, 2009. 204 (3): p. 353-358.

127. C. Miller, I. Anderson and J. Smith, *A viable tin-lead solder substitute: Sn-Ag-Cu.* Journal of Electronic Materials, 1994. 23 (7): p. 595-601.

128. E. Gebhardt and G. Petzow, *The Constitution of the System Ag-Cu-Sn.* Zeitschrift Fur Metallkunde, 1959. 50: p. 597-605.

129. M. Loomans and M. Fine, *Tin-silver-copper eutectic temperature and composition.* Metallurgical and Materials Transactions A, 2000. 31 (4): p. 1155-1162.

130. N. Kaneko, M. Komatsu, T. Kurashina, S. Arai and N. Shinohara, *Sn-Ag-Cu Alloy Electroplating from Acid Sulfate Baths for Pb-free Solder.* Electrochemistry, 2005. 73 (11): p. 951-956.

131. J. Zhang, M. An, L. Chang and G. Liu, *Effect of triethanolamine and heliotropin on cathodic polarization of weakly acidic baths and properties of Sn-Ag-Cu alloy electrodeposits.* Electrochimica Acta, 2008. 53 (5): p. 2637-2643.

132. T. B. Massalski, H. Okamoto and P. R. Subramanian, *Binary Alloy Phase Diagrams, 2nd ed.* 1990: ASM International. 265.

133. M. Kerr and N. Chawla, *Creep deformation behavior of Sn-3.5Ag solder/Cu couple at small length scales.* Acta Materialia, 2004. 52 (15): p. 4527-4535.

134. T. B. Massalski, J. L. Murray, L. H. Bennett and H. Baker, *Binary Alloy Phase Diagrams*. Vol. 1. 1996, Ohio: ASM International. 71.

135. M. Azzaz, J. P. Michel, V. Feregotto and A. George, *TEM observations of dislocations in aluminium nitride after high temperature deformation.* Materials Science and Engineering B, 2000. 71 (1-3): p. 30-38.

136. D. L. Medlin, S. M. Foiles and D. Cohen, *A dislocation-based description of grain boundary dissociation: application to a 90° <110> tilt boundary in gold.* Acta Materialia, 2001. 49 (18): p. 3689-3697.

137. G. Dehm, D. Weiss and E. Arzt, *In situ transmission electron microscopy study of thermal-stress-induced dislocations in a thin Cu film constrained by a Si substrate.* Materials Science and Engineering A, 2001. 309-310: p. 468-472.

138. R. Walker, *Stress in copper electrodeposits made with benzotriazole as addition agent.* Electrochimica Acta, 1968. 13 (8): p. 1861-1866.

139. S. E. Hadian and D. R. Gabe, *Residual stresses in electrodeposits of nickel and nickel-iron alloys.* Surface and Coatings Technology, 1999. 122 (2-3): p. 118-135.

140. D. Li, C. Liu and P. P. Conway, *Characteristics of intermetallics and micromechanical properties during thermal ageing of Sn-Ag-Cu flip-chip solder interconnects.* Materials Science and Engineering A, 2005. 391 (1-2): p. 95-103.

141. Y.-J. Tan and K. Y. Lim, *Understanding and improving the uniformity of electrodeposition.* Surface and Coatings Technology, 2003. 167 (2-3): p. 255-262.

142. B. Kim and T. Ritzdorf, *Electrodeposition of Near-Eutectic SnAg Solders for Wafer-Level Packaging.* Journal of The Electrochemical Society, 2003. 150 (9): p. C577-C584.

143. P. Dixit, J. Miao and R. Preisser, *Fabrication of High Aspect Ratio 35 mu m Pitch Through-Wafer Copper Interconnects by Electroplating for 3-D Wafer Stacking.* Electrochemical and Solid-State Letters, 2006. 9 (10): p. G305-G308.

PUBLICATIONS

1. Y. Qin, G. D. Wilcox and C. Liu. "Electrodeposition of Sn-Ag solder alloy for electronics interconnection". in Electronics System-Integration Technology Conference, ESTC 2008. 2nd. London. p. 833-838.

2. Y. Qin, G. D. Wilcox and C. Liu, "Electrodeposition and characterization of eutectic Sn-Ag Alloy as solder bumps for flip-chip interconnection". Journal of The Electrochemical Society, 2009. 156(10): p. D424-D430.

3. Y. Qin, A. Wassay, C. Liu, G. D. Wilcox, K. Zhao and C. Wang. "Electrodeposition of Sn-Cu solder alloy for electronics interconnection". in International Conference on Electronic Packaging Technology & High Density Packaging, ICEPT-HDP 2009. Beijing. p. 772-777.

4. Y. Qin, C. Liu, G. D. Wilcox, K. Zhao and C. Wang. "Electrodeposition of Sn-Ag-Cu solder alloy for electronics interconnection". in Electronics Packaging Technology Conference, EPTC 2009. 11th. Singapore. p. 398-402.

5. Y. Qin, C. Liu, G. D. Wilcox, K. Zhao and C. Wang. "Near-eutectic Sn-Ag-Cu solder bumps formation for flip-chip interconnection by electrodeposition". in Electronic Components and Technology Conference, ECTC 2010. 60th. Las Vegas. p. 144-150. Winner of “IEEE CPMT Society Student Travel Award”.

6. Y. Qin, G. D. Wilcox and C. Liu, "Electrodeposition and characterisation of Sn-Ag-Cu solder alloys for flip-chip interconnection". Electrochimica Acta (2010), *in press*, doi:10.1016/j.electacta.2010.08.102.

7. Y. Qin, G. D. Wilcox and C. Liu, "The effects of polyethylene glycol and formaldehyde on the electrodeposition of Sn-Ag-Cu solder alloys from a pyrophosphate bath". Electrochimica Acta, in preparation.

8. Y. Qin, G. D. Wilcox and C. Liu, "Electrodeposition and characterisation of near-eutectic Sn-Cu solder alloy for electronics interconnection". Journal of The Electrochemical Society, in preparation.

9 Y. Qin, G. D. Wilcox and C. Liu, "The potentiodynamic polarisation behaviour of electrodeposited tin-based lead-free solder alloys in NaCl solution". Corrosion Science, in preparation.